Riassunto

Supermassive Black Holes: a spectroscopic and photometric study on the connection with their host galaxies

I Buchi Neri Supermassicci: uno studio fotometrico e spettroscopico sulla connessione con le galassie ospiti

Studente di Dottorato: **Elena Tundo**

Uno dei più promettenti temi nell'astronomia extragalattica per i prossimi decenni sarà l'evoluzione delle galassie. E' divenuto sempre più chiaro come le loro proprietà e la loro evoluzione siano intimamente collegate alla crescita dei buchi neri supermassicci (SMBH) nei loro nuclei. Per capire la formazione delle galassie, e la loro successiva evoluzione, bisognerà chiarire la connessione tra i SMBH e le loro galassie ospiti.

I SMBH sono presenti in quasi tutti i nuclei delle galassie; la loro formazione, il loro accrescimento, e il loro impatto sulla materia circostante rappresentano alcuni dei problemi ancora irrisolti nella storia della formazione delle strutture cosmiche.

Per capire l'evoluzione delle galassie, è necessario studiare questo soggetto da più punti di vista.

Abbiamo bisogno sia di strumenti che permettano di tracciare il comportamento dei SMBH e delle loro galassie ospiti anche ad alto redshift o in galassie attive, sia di comprendere come agisca il cosiddetto AGN "feedback" all'interno delle singole galassie.

Nella prima parte di questo lavoro il nostro obiettivo è determinare un tracciante per la dispersione di velocità stellare σ_*, allo scopo di offrire uno strumento nello studio della relazione tra la massa dei SMBH $M_\bullet$ e σ_* anche in galassie attive o ad alto redshift, dove σ_* non può essere misurata direttamente. Proponiamo uno studio estensivo della cinematica del gas descritta dalle tre righe d'emissione di [OIII], [NII] e Hα utilizzando l'archivio della Sloan Digital Sky Survey (SDSS), in modo da stabilire quale sia il miglior tracciante per σ_* e in modo da capire come l'AGN influenzi la cinematica del gas. Sono stati presi in considerazione tre sottocampioni di galassie, rispettivamente AGN, Star Forming (SF) e Transition (TR).

Abbiamo effettuato una nuova analisi degli spettri SDSS; poichè gli assorbimenti stellari possono influenzare o addirittura sopraffare le emissioni del gas ionizzato, è stato necessario sottrarre il continuo stellare.

Una attenzione particolare è stata dedicata a stabilire la qualità dei programmi usati nel fit, e all'analisi statistica dell'idoneità delle tre righe d'emissione prese in considerazione come possibili traccianti della dispersione di velocità stellare.

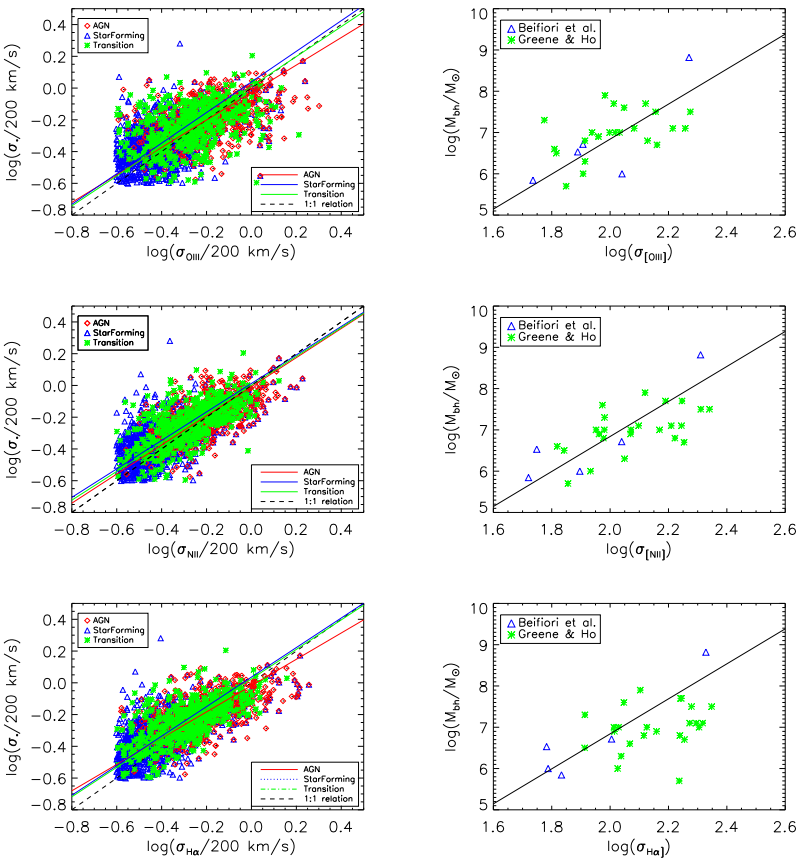

Figura 1: *Figura in alto a sinistra*: σ_* verso $\sigma_{[OIII]}$. I diamanti rossi rappresentano gli AGN, i triangoli blu le galassie SF e gli asterischi verdi le galassie TR (vedi legenda). Le linee continue rappresentano i fit della relazione $\sigma_* - \sigma_{[OIII]}$, rossa per gli AGN, blu per le SF e verde per le TR. La linea tratteggiata rappresenta una relazione unitaria. *Figura in alto a destra*: $M_\bullet$ contro $\sigma_{[OIII]}$ usando i campioni di Beifiori et al. (2009) –triangoli blu– e di Greene & Ho (2006) –asterischi verdi. La linea continua rappresenta la relazione trovata in Tremaine et al. (2002). *Figura in mezzo a sinistra e figura in mezzo a destra*: come sopra, usando le misure di [NII]. *Figura in basso a sinistra e figura in basso a destra*: come sopra, usando le misure di Hα.

I risultati principali di questa prima parte possono essere riassunti nei seguenti punti:

- Abbiamo dimostrato che la σ della riga d'emissione dell'[OIII], $\sigma_{[OIII]}$, correla con σ_*; tuttavia la correlazione è debole, con un coefficiente di correlazione di Pearson che varia tra 0.42 a 0.55 nei tre sottocampioni di galassie AGN, SF e TR. La pendenza della relazione è statisticamente più bassa dell'unità, e nel campione degli AGN si registra la pendenza più bassa.

- Le relazioni $\sigma_* - \sigma_{[NII]}$ e $\sigma_* - \sigma_{H\alpha}$ sono piu' strette della $\sigma_* - \sigma_{[OIII]}$, e il coefficiente di correlazione di Pearson diventa di 0.60 e 0.62, rispettivamente per [NII] e Hα, nel campione delle galassie AGN. Tutti i risultati delle nostre misure di scatter intrinseco e di correlazione mostrano che le righe d'emissione di [NII] and Hα sono meglio correlate alla dispersione di velocità stellare rispetto all'[OIII].

- In tutti i casi troviamo una pendenza b <1, anche se le righe d'emissione di [NII] and Hα mostrano pendenze generalmente maggiori di quelle trovate con la relazione $\sigma_* - \sigma_{[OIII]}$ (si veda la Figura 1, pannelli di sinistra).

- Le pendenze e i coefficienti di correlazione sono simili usando qualunque delle tre righe di emissione nel sottocampione delle galassie SF; osserviamo invece che la pendenza nel campione degli AGN risulta piu' bassa nella relazione $\sigma_* - \sigma_{[OIII]}$ rispetto a quella trovata nei campioni SF e TR, con $b_{AGN} < b_{TR} < b_{SF}$. Nella relazione $\sigma_* - \sigma_{[NII]}$ vediamo che le pendenze nei campioni AGN, TR e SF concordano entro le incertezze di misura, mentre per la relazione $\sigma_* - \sigma_{H\alpha}$ otteniamo che $b_{SF} \simeq b_{TR}$, con $b_{AGN} < b_{SF}, b_{TR}$.

- Abbiamo determinato le equazioni per le relazioni σ_{gas}/σ_* per ognuna delle tre righe d'emissione, nei tre sottocampioni, usando diversi metodi di regressione.

Questi risultati indicano che nelle galassie StarForming o Transition il gas ionizzato è meno perturbato dagli effetti non gravitazionali del meccanismo centrale degli AGN, con la conseguenza che σ_{gas} è subviriale così come osservato nelle galassie quiescenti.

La ragione per cui la pendenza della relazione $\sigma_* - \sigma_{[OIII]}$ risulta minore della pendenza delle relazioni $\sigma_* - \sigma_{[NII]}$ e $\sigma_* - \sigma_{H\alpha}$ risiederebbe così nel fatto che l'[OIII] è confinato nelle NLR, ed è di conseguenza più soggetto alle accelerazioni non gravitazionali; $\sigma_{[OIII]}$ risulta più allargata rispetto a $\sigma_{[NII]}$ e $\sigma_{H\alpha}$, e nei grafici $\sigma_* - \sigma_{gas}$ la sua posizione "migra" verso valori più alti in σ_{gas}, abbassando di conseguenza la pendenza.

Un test conclusivo del fatto che [NII] è un tracciante migliore per la dispersione di velocità stellare è rappresentato dal fatto che in un grafico di $M_\bullet$ contro σ_{gas} (si veda la Figura 1, pannelli di destra) la relazione $M_\bullet - \sigma_{[NII]}$ presenta lo scatter minore.

Nella seconda parte di questo lavoro di tesi l'attenzione è dedicata agli effetti dell' AGN feedback sulle galassie centrali di cluster. Circa un terzo dei cluster presenta una caduta della temperatura centrale del gas, e un tempo di raffreddamento inferiore all'età del cluster stesso; in tali cluster si dovrebbe instaurare

un massiccio flusso di gas in fase di raffreddamento. Tuttavia questo non è osservato, e si richiede quindi un qualche meccanismo per restituire al gas l'energia persa, irradiata prevalentemente sotto forma di raggi X.

L'AGN feedback è invocato per risolvere questo problema, detto del "cooling flow"; tuttavia, mentre i modelli teorici che prevedono l'AGN feedback producono galassie ellittiche completamente rosse, prive di popolazione stellare giovane, recenti osservazioni mostrano che le galassie al centro dei "Cool Core Cluster" (CCC) presentano una certa formazione stellare.

Lo scopo di questa seconda parte della tesi è di stabilire se i CCC e i "Non Cool Core Clusters" (NCCC) sono caratterizzati da un diverso tasso di formazione stellare, e se questa differenza possa essere quantificata utilizzando i colori in banda ottica, NIR e UV.

Il lavoro svolto è partito dall' "extended Highest X-ray Flux Galaxy Cluster Sample" (HIFLUGCS), un campione di cluster sia CCC che NCCC; questo campione iniziale è stato incrociato con gli archivi SDSS, 2MASS e GALEX. E' stato necessario procedere a una attenta rianalisi fotometrica delle immagini Sloan, poiché i dati SDSS per galassie vicine e brillanti sono affetti da una sottrazione del cielo erronea, e poiché diverse galassie sono parzialmente sovrapposte e necessitano quindi di una accaurata analisi specifica.

I risultati principali di questa seconda parte possono essere riassunti nei seguenti punti:

- Abbiamo ricavato la relazione colore-magnitudine per tutti i punti del nostro campione al fine di derivare la pendenza b per ciascuno dei colori usati. Il punto zero per le galassie di CCC e NCCC è stato calcolato separatamente come $\mathrm{zp} = \langle \mathrm{color} \rangle - \langle \mathrm{mag} \rangle * \mathrm{b}$. L'ipotesi di base è che le galassie in CCC e NCCC condividano la stessa relazione colore-magnitudine, e che differiscano solo per il punto zero, ovvero per il colore medio.

- Osserviamo che le differenze di colore medio trovate sono sistematicamente positive, cosa questa che suggerisce una differenza fisica tra galassie di CCC e NCCC, essendo le galassie di CCC leggermente più blu (si veda la Figura 2).

- In un modello detto di "pure cooling flow" si dovrebbe osservare una correlazione tra i tassi di massa di gas che si deposita al centro del cluster per via della perdita di energia per raffreddamento (ricavate dalle osservazioni X) e i colori delle galassie, dal momento che la formazione stellare dovuta al gas che si condensa risulterebbe in colori più blu in galassie con flussi di gas più intensi. Nel nostro lavoro, non osserviamo alcuna correlazione di questo tipo.

- Le differenze di colore medio trovate in questo lavoro sono compatibili con l'idea che le galassie centrali in CCC abbiano avuto della formazione stellare recente o attualmente in corso. Tuttavia, dai nostri risultati, un modello di "pure cooling flow" è escluso.

I nostri calcoli preliminari sul tasso di formazione stellare medio nelle galassie di CCC, partendo da un colore $M_g - M_r$ ipotetico, indicano valori non superiori alle 2-5 $\mathrm{M}_\odot/\mathrm{yr}$.

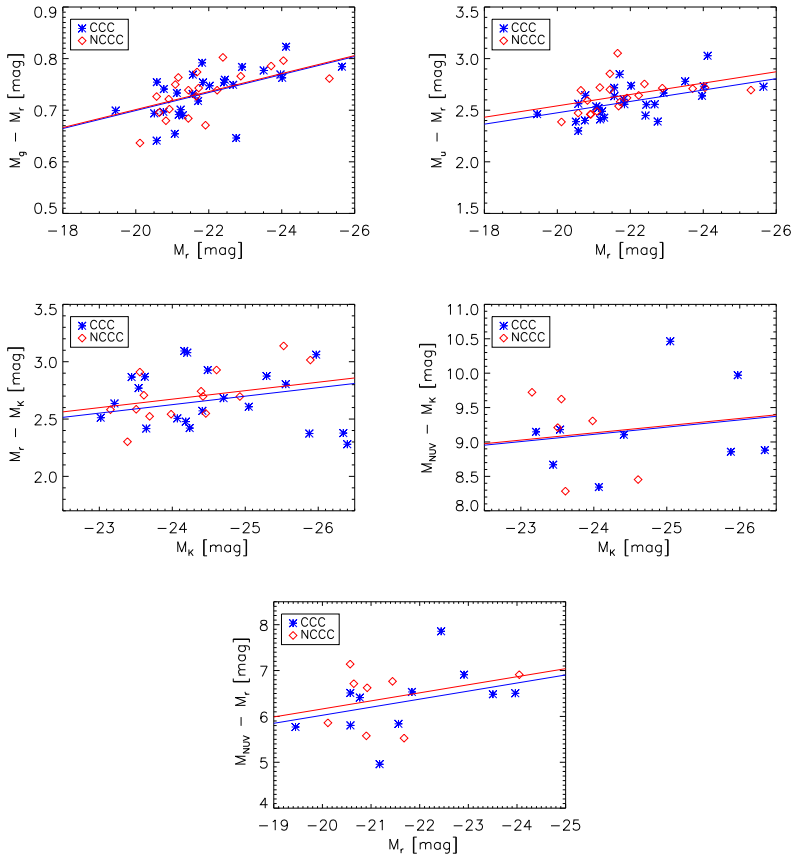

Figura 2: *Figura in alto a sinistra*: Diagramma colore magnitudine $M_g - M_r$ verso M_r. Le galassie in CCC sono rappresentate dagli asterischi blu, mentre le galassie in NCCC sono rappresentate dai diamanti rossi. Le linee continue rappresentano la relazione colore-magnitudine, rispettivamente, per le galassie di CCC (blu) e di NCCC (rosso). Lo stesso codice di colore è usato in tutti i pannelli. *Figura in alto a destra*: $M_u - M_r$ versus M_r. *Figura in mezzo a sinistra*: $M_r - M_K$ verso M_K. *Figura in mezzo a destra*: $M_{NUV} - M_K$ verso M_K. *Figura in basso*: $M_{NUV} - M_r$ verso M_r.

Abstract

Supermassive Black Holes: a spectroscopic and photometric study on the connection with their host galaxies

Ph.D. Student: **Elena Tundo**

One of the main themes in extragalactic astronomy for the next decade will be the evolution of galaxies over cosmic time. It has, however, become clear that the properties and the evolution of galaxies are intimately linked to the growth of their Supermassive Black Holes (SMBH). Understanding the formation of galaxies, and their subsequent evolution, will therefore be incomplete without clearifing the connection between the SMBHs and their host galaxies.

The formation, assembly history, and environmental impact of the SMBHs that are ubiquitous in the nuclei of luminous galaxy remain today some of the main unsolved problems in cosmic structure formation studies.

To understand galaxy evolution we need to study this subject from a different point of view.

We need tools that can help us to trace the behavior of SMBHs and their host galaxies at high redshift and in active galaxies, and we need to understand how AGN feedback acts.

In the first part of this thesis work we seek to find a tracer for the stellar velocity dispersion σ_* in order to give a tool in the study of the $M_\bullet - \sigma_*$ relation even in active or high redshift galaxies, were σ_* cannot be measured directly. We perform an extensive study on the kinematics of the gas as described by the three gas emission lines [OIII], [NII] and Hα using the SDSS database, in order to find the best tracer for σ_* and to get some clues concerning the effect of AGN on the gas kinematic. We will study three subsamples of AGN, Star Forming (SF) and Transition (TR) galaxies.

A new analysis of the SDSS spectra was required due to the need of a robust stellar continuum subtraction, in order to take into account the stellar absorption features on the gas emission lines.

A particular attention has been devoted in establishing the quality of the line fitting program, and the statistical analysis of the suitability of the gas emission lines was rigorous.

The main results of this first part can be summarized as follows:

- We show that [OIII] line do have a correlation with σ_*; this correlation is poor, with a Pearson correlation coefficient ranging from 0.42 to 0.55 in the different subsamples. The slope of the relation is statistically *less* than unity, and the AGN sample shows the lowest value.
- Hα and [NII] show a tighter relation, with a Pearson correlation coefficient of 0.60 and 0.62, respectively, in the AGN subsample. All results from our measures of the intrinsic scatter and of the correlation coefficient show that [NII] and Hα lines are more tightly tied to σ_* than [OIII].

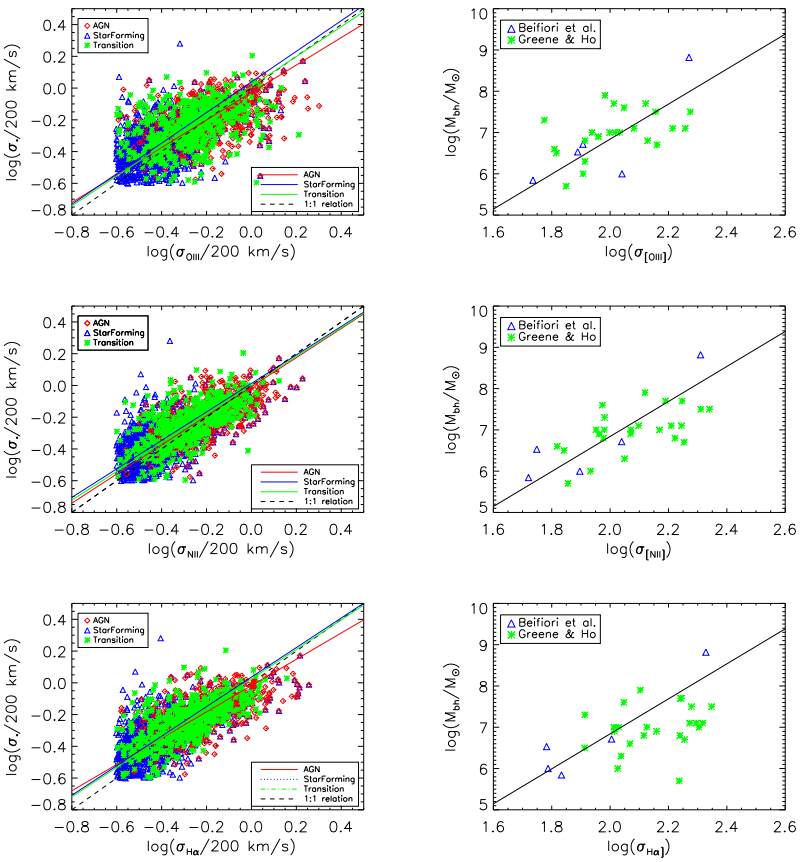

Figure 1: *Upper Left Panel*: σ_* versus $\sigma_{[OIII]}$. Different symbols refer to different class of objects. As in the legend, red diamonds are AGN, blue triangles are SF and green asteriscs are TR. The solid lines represent the best fit of the $\sigma_* - \sigma_{[OIII]}$ relation, red for AGN, blue for SF and green for TR. The black dashed line represent an unitary relation, shown for comparison. *Upper Right Panel*: $M_\bullet$ plotted versus $\sigma_{[OIII]}$ for the samples of Beifiori et al. (2009) –blue triangles– and of Greene & Ho (2006) –green asterisks. The black line represent the $M_\bullet - \sigma_*$ relation from Tremaine et al. (2002). *Middle Left and Right panels*: As in the upper left and upper right panels, using [NII] data. *Bottom Left and Right Panels*: As in the upper left and upper right panels, using Hα data.

- In any case the slope of the relation between the gas and the stars is lower than unity, even if Hα and [NII] lines show slopes that are usually steeper than the slope of the $\sigma_* - \sigma_{[OIII]}$ relation (see Figure 1, left panels).

- The slope, scatter, correlation coefficient are similar using the three emission lines in the SF sample, while they differ in the TR and AGN samples. Particularly, we observe the slope in the AGN sample to be shallower in the $\sigma_* - \sigma_{[OIII]}$ relation with respect to the slope in the TR and SF, with b_{TR} showing an intermediate value between b_{SF} and b_{AGN}. On the other side, the slope of the $\sigma_* - \sigma_{[NII]}$ relation for the three AGN, TR and SF samples agree within uncertainties. Hα emission line shows $b_{SF} \simeq b_{TR}$, while b_{AGN} results to be shallower as in the case of [OIII].

- We propose an equation for the σ_{gas}/σ_* for each of the three line, in the different subsamples, using different regression methods.

In our opinion these findings indicate that in StarForming or Transition galaxies the ionized gas is less perturbed by non-gravitational effects from the central engine than in AGNs, so the measured σ_{gas} is subvirial as observed in quiescent galaxies.

The reason for the slope in the $\sigma_* - \sigma_{[OIII]}$ relation to be lower than in the cases of [NII] or Hα lines could reside in the fact that [OIII] is nearer to the central engine in AGN, and consequently is more subject to its non gravitational acceleration; $\sigma_{[OIII]}$ is then more broadened respect to $\sigma_{[NII]}$ or $\sigma_{H\alpha}$ and its position in a $\sigma_* - \sigma_{gas}$ plot migrate toward higher values of σ_{gas}, therefore decreasing the slope of the relation.

A conclusive test of [NII] being a better tracer for the stellar velocity dispersion respect to the [OIII] line is represented by the fact that in a $M_\bullet - \sigma_{gas}$ plot (see Figure 1, right panels) the $M_\bullet - \sigma_{[NII]}$ presents the lowest scatter.

In the second part of this thesis work we will look at the effects of AGN feedback in galaxy clusters. About one third of clusters present a central drop in the core gas temperature, with central cooling time shorter than the cluster age; it should be observed in these cases a massive flow of cooling gas. This is not, and some heating mechanism is required.

AGN feedback is so invoked to solve the so called "cooling flow problem"; anyway, while theoretical models still presents AGN feedback that produces red and dead ellipticals recent observations suggest that AGN feedback cannot be as efficient as to completely suppress star formation.

The goal of this Section of the Thesis is to establish whether the Cool Core Clusters (CCC) and Non Cool Core Clusters (NCCC) are characterized by a different star formation rate, and if this difference can be assessed with the use of broad band optical, NIR and UV colors.

The work was carried out using the extended Highest X-ray Flux Galaxy Cluster Sample (HIFLUGCS) of both CCC and NCCC clusters, matched with the SDSS, 2MASS and GALEX surveys. We first performed a careful photometrical re-analysis of SDSS data, since SDSS data are affected by a wrong sky subtraction and because several targets are partially blended and needed a careful ad-hoc analysis.

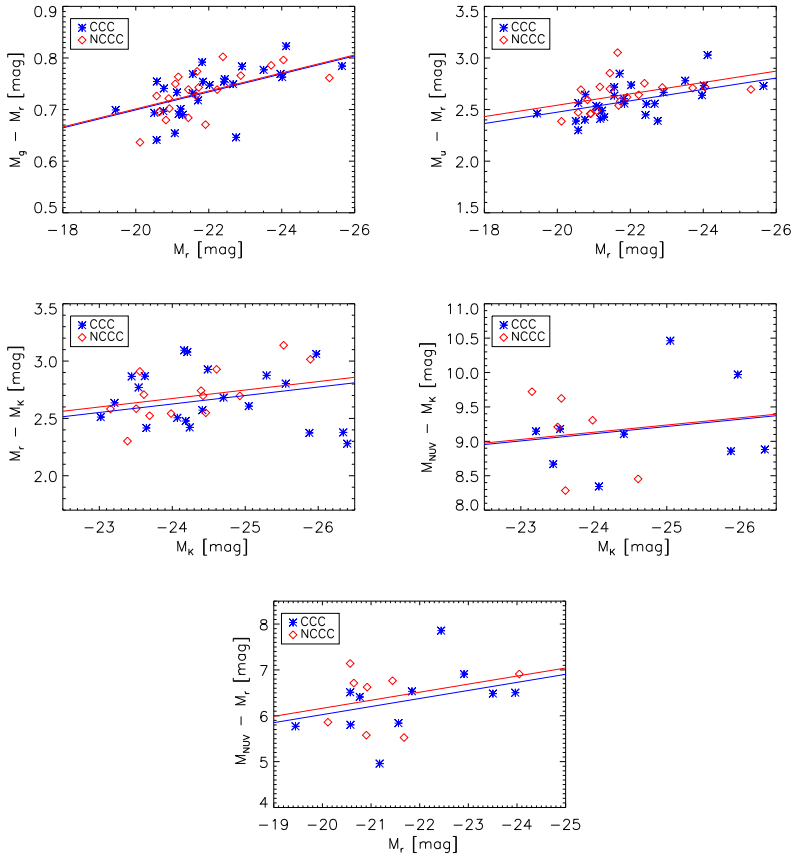

Figure 2: *Upper Left Panel*: $M_g - M_r$ color versus M_r diagram for our sample. Blue asterisks represent galaxies in Cool Core Clusters, while red diamonds represent galaxies in Non Cool Core Clusters. The lines represent the fitted color-magnitude relations for the CCC (blue line) and NCCC (red line) samples. The same color code is used in the upper right, middle left, middle right, and bottom panels, showing respectively the $M_u - M_r$ versus M_r, the $M_r - M_K$ versus M_K, the $M_{NUV} - M_K$ versus M_K, and the $M_{NUV} - M_r$ versus M_r diagram.

The main results of this first part can be summarized as follows:

- We fitted the color-magnitude relation for all the data points to retrieve the slopes b for each color-magnitude relations, and then derived the zero points using the zp $= \langle \text{color} \rangle - \langle \text{mag} \rangle * \text{b}$ separately for the two CCC and NCCC sample, under the hypothesis that galaxies both in CCC and NCCC follow the same color-magnitude relation, and that the two samples differ just for the mean colors.
- We observe that the mean color differences are systematically positive, so indicating that they are probably physically different in our samples (see Figure 2).
- In a pure cooling flow model, we should observe a correlation between the mass deposit rate calculated from X-ray observations and the colors of galaxies, since the star formation due to the cooling gas falling on the central galaxies should give bluer colors in galaxies undergoing stronger star formation. In our case, we don't see any correlation.
- The differences we found are compatible in our opinion with CCC central galaxies to have recent or ongoing SF. Still, a pure cooling flow model is excluded by our findings.

Our preliminary calculation to find the mean difference in SFR between CCC and NCCC galaxies from $g-r$ color indicates SFR of no more than 2-5 $\text{M}_\odot/\text{yr}$.

Contents

Chapter 1

Introduction

One of the main themes in extragalactic astronomy for the next decade will be the evolution of galaxies over cosmic time. It has, however, become clear that the properties and evolution of galaxies are intimately linked to the growth of their Supermassive Black Holes (SMBH). Understanding the formation of galaxies, and their subsequent evolution, will therefore be incomplete without clearifing the connection between the SMBHs and their host galaxies.

The formation, assembly history, and environmental impact of the SMBHs that are ubiquitous in the nuclei of luminous galaxy today remain some of the main unsolved problems in cosmic structure formation studies.

In this thesis work we want to give our contribution to this exciting frontier of astronomy.

1.1 SMBHs and their host galaxies

1.1.1 Local relations

There are no other objects that fashinated the imagination of astronomers as supermassive black holes. They were studied well before their existence was proved. It is of 1783 the idea of an "obscured star" so massive that the light couldn' t escape from it's surface, idea exposed from the Rev. John Mitchell in a paper submitted to the *Royal Society* of London.

The way that would lead to the discovery of SMBHs was not easy, or straightforward, or short, but since that date to our days step by step the way were covered, even if sometimes it were done while studing something entirely different -or when we thought it was entirely different.

Nowadays we know that there is one super massive black holes in almost each galaxy; this conclusion was found by Soltan (1982) with a simple consideration on the density of quasars and active galaxies at high redshift, and calculating, assuming the efficency coeffient for the trasformation of the mass in energy, ϵ, the mass needed to produce such amount of energy.

The implied number density of SMBHs means that we have an high number of hidden, relic quasars, in the Local Universe. And if the energetic phenomena happening inside Quasar and Seyfert galaxies, are happening inside the host galaxies, the natural consequent idea is that at least the more massive galaxies

all presented such phenomena in the past, and that the fuel mechanism somehow were exhausted.

We have nowadays more or less one hundred of well measured SMBHs mass in the Local Universe, measured via the proper motion of stars (only in our Galaxy), or via the dinamics of stars and gas.

It is of the 1995 the first relation suggested (Kormendy & Richstone 1995, e then Richstone et al. 1998, Magorrian et al. 1998, van der Marel 1999) between the mass of the SMBH and the blu luminosity of the host galaxy.

It is more recent the relation proposed (Ferrarese & Merrit 2000, Gebhardt 2000, Tremaine et al. 2002, Tundo et al. 2007) between the SMBH mass and the stellar velocity dispersion σ_* of the host galaxy, the $M_\bullet - \sigma$ relation.

Other empirical derivations of relationships between the BH mass and several different properties of its host galaxy were proposed, such as bulge mass (Häring & Rix 2004), bulge luminosity (Kormendy 1993; McLure & Dunlop 2002; Marconi & Hunt 2003; Bettoni et al. 2003), and galaxy light concentration (Graham et al. 2001).

The existence of the above correlation strongly suggests that formation and evolution of galaxies happen *togheter with* that of their supermassive black holes.

These correlations pose a theoretical challenge because the mass accretion onto BHs takes place on extremely small spatial scales compared to the scales corresponding to these global properties of galaxies.

In the semi analytical model of Haehnelt & Kauffmann (2000), Kauffmann & Haehnelt (2000), bulges and supermassive black holes both form during major mergers, and the slopes of the relations between SMBHs and galaxy properties are determined by how much gas cools, forms stars or is funneled to the centre in dark matter halos of different mass/velocity dispersion. With the hypothesis that black holes in progenitor galaxies coalesce, and that they accrete by a fixed fraction of the available gas of the galaxies, they can find relations between the galaxy luminosity and velocity dispersion, and the mass of the SMBH, that match the ones actually found in the local universe.

Several models are based on black hole accretion influencing star formation and gas dynamics in the host galaxy; this feedback can occur through ionization, mechanical work, and heating (e.g., Ciotti & Ostriker 1997; Blandford 1999; Silk & Rees 1998). The model of Blandford (1999) gives $M_\bullet < \eta\sigma^{5/3}$ whereas Silk & Rees (1998) predict $M_\bullet \propto \sigma^5$. Finally, the accretion of collisional dark matter indicates the scaling relation $M_\bullet \propto \sigma^{4-4.5}$ (Ostriker 2000).

Adams et al. (2001) propose a model to describe a collapse flow that produces galactic bulges and SMBHs, in which the initial condition state is a slowly rotating isothermal sphere. In this model, characterized by an effective sound speed, correlated to the velocity dispersion, and by an angular velocity, the pericenter of particles is determined, and the black hole final mass is constrained by the condition that the pericenter falls inside the Schwarzschild radius; even this model leads to the scaling law $M_\bullet \propto \sigma^4$, which is consistent with observations.

Several other groups have modeled the joint cosmological evolution of quasars and galaxies (see, e.g., Monaco et al. 2000; Granato et al. 2001; Cavaliere & Vittorini 2002; Cattaneo & Bernardi 2003; Haiman et al. 2004; Hopkins et al. 2006; Lapi et al. 2006).

1.1.2 AGN feedback and host galaxies evolution

Other pieces of evidence on an intimate relation between the evolution of galaxies and the accretion of SMBH, and on galaxies in the Universe spending a fraction of their lifetimes as active galactic nuclei (AGN), come from the fact that the growth of SMBHs during active accretion phases, traced by the cosmological evolution of the AGN luminosity function (Ueda et al. 2003, Hasinger et al. 2005,La Franca et al. 2005, Silverman et al. 2008), eventually matches the mass function of SMBHs in the local Universe (Marconi et al. 2004, Yu & Tremaine 2002, Shankar et al.2004).

This abundance of supermassive black holes is the subject of considerable current interest (e.g. McLure & Dunlop 2004; Yu & Lu 2004; Ferrarese & Ford 2005, Tundo et al. 2007).

Finally, both BH growth and star formation appear to follow the same "anti-hierarchical" behaviour over cosmic time. The peak activity of luminous QSOs occurs at z$\sim$2, where large galaxies were also forming most of their stars, while moderately luminous AGN are more common at the current epoch, where stars are forming is smaller galaxies. The role played by nuclear activity in modulating star formation processes in the host galaxies is commonly referred as **AGN feedback**.

The main idea is that radiative and mechanical energy from the AGN regulates both star formation and accretion during periods of galaxy growth.

This kind of black-hole driven feedback is thought to be essential in shaping the first galaxies. Current models propose that mergers of small gas-rich proto galaxies in deep potential wells at high redshift drive star formation and black hole growth (in proto-quasar active galaxies) until a luminous quasar forms. At this point, a black-hole driven wind evacuates gas from the nascent galaxy, limiting additional star formation and further black hole growth (Silk & Rees 1998). Further episodes of merger-driven star formation, accretion, and feedback are expected to proceed through cosmic time. This provides a plausible origin for the relations between BH mass and galaxy properties (e.g. King 2003), and explains many outstanding problems in galaxy evolution (e.g. Croton et al. 2006; Hopkins et al. 2006).

For example, using semi analytic models to attempt to understand the process for which galaxies form when gas condenses at the centres of a hierarchically merging population of dark haloes, have consistently run into problems stemming from a mismatch in shape between the predicted distribution of dark halo masses and the observed distribution of galaxy luminosities.

Most stars are in galaxies of Milky Way brightness; the galaxy abundance declines exponentially at brighter luminosities and increases sufficiently slowly at fainter luminosities that relatively few stars are in dwarfs. In contrast, the theory predicts a much broader halo mass distribution.

Another puzzling aspect of the galaxy population is the fact that the most massive galaxies, typically ellipticals in clusters, are made of the oldest stars and so finished their star formation earlier than lower mass galaxies. Confirming evidence for this comes from look-back studies which show that both starformation and AGN activity take place more vigorously and in higher mass objects at redshifts of 1 to 2 than in the present Universe (e.g. Shaver et al. 1996; Madau et al. 1996). Cowie et al. (1996) termed this phenomenon "downsizing", and it conflicts with hierarchical growth of structure in a ΛCDM cosmogony where

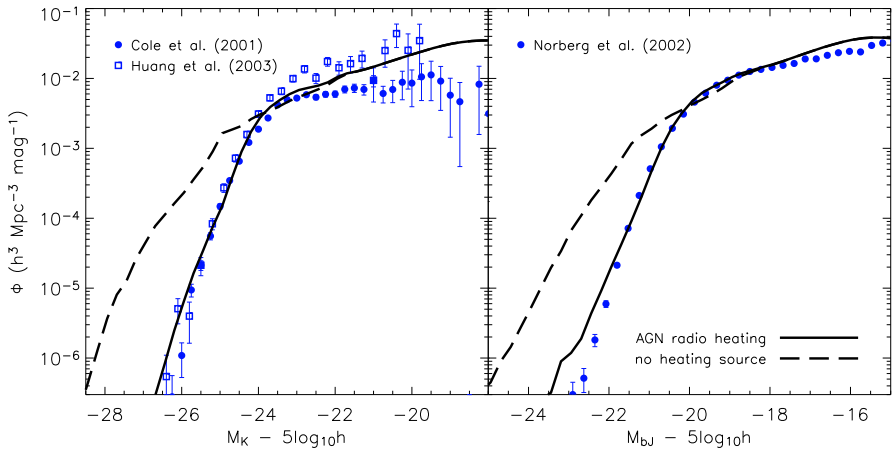

Figure 1.1: Figure 8 of Croton et al. (2006); galaxy luminosity functions in the K (left) and J (right) photometric bands, plotted with and without "radio mode" feedback. Symbols indicate observational results as listed in each panel.

massive dark haloes assemble at lower redshift than lower mass haloes (e.g. Lacey & Cole 1993).

AGN feedback, limiting the mass of the central galaxies and preventing them from forming stars at late times when their mass and morphology can still change through mergers, results in a galaxy luminosity function with a sharper high-mass cut-off in which the most massive systems are red, dead and elliptical.

Figure 1.1 (Figure 8 of Croton et al. 2006), shows that the inclusion of AGN heating produces a good fit to the data in both colours. Without this heating source the model overpredicts the luminosities of massive galaxies by about two magnitudes and fails to reproduce the sharp bright end cut-offs in the observed luminosity functions.

Similarly, Figure 1.2 (Figure 9 of Croton et al. 2006) shows that a clear bimodality in colour is seen in both panels, as requested by observations, but without a heating source the most massive galaxies are blue rather than red. Only when heating is included are massive galaxies as red as observed.

So, intense periods of star formation and black hole growth occur concurrently in the history of massive galaxies, possibly triggered by mergers (e.g. Sanders et al. 1988; Springel et al. 2005). Eventually, feedback from the AGN terminates star formation and extinguishes the AGN itself.

Despite the intense current interest in this topic, and its great importance, direct evidence for AGN feedback at high redshift is scarce and the details of the physical processes are unclear. It is thus certain to remain one of the most active topics in astrophysics during the next decade and beyond.

Moreover, it is still not clear what physical processes control the SMBH accretion rate, nor, for a given accretion rate, what form does the energy feedback take (photons, nuclear winds and jets), nor how do these three forms of feedback, in turn, affect the accretion rate. It is thought that the radiative form of feedback is most effective when the black hole is accreting close to its Edding-

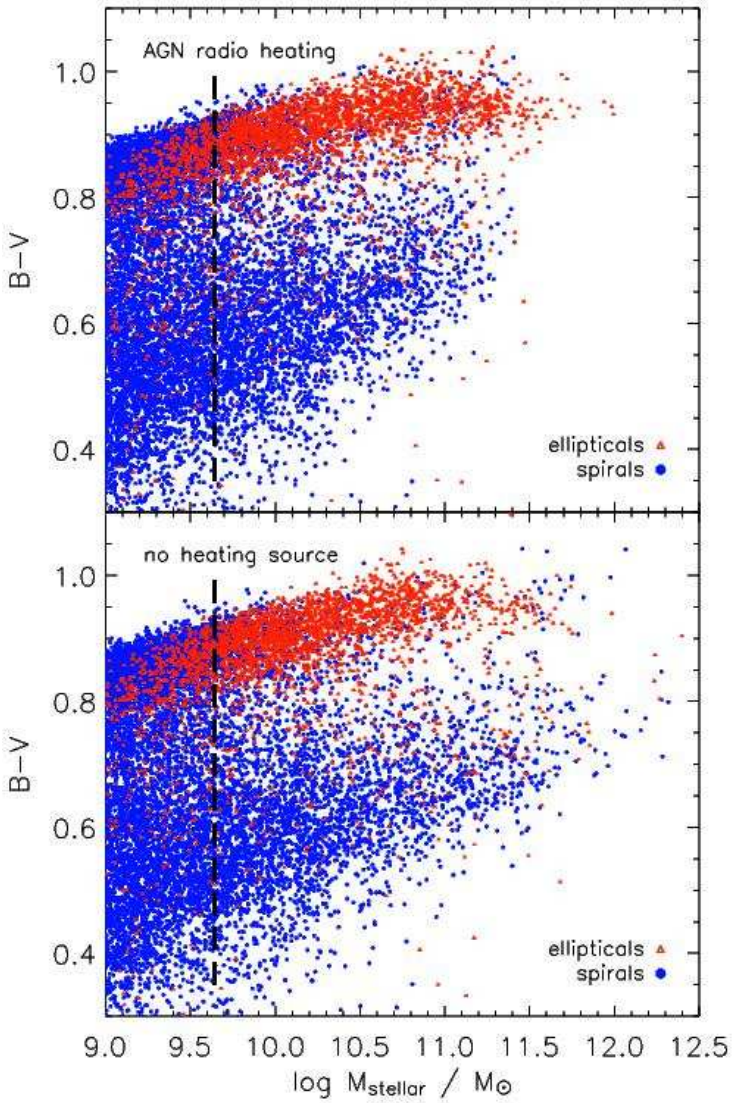

Figure 1.2: Figure 9 of Croton et al. (2006); the B-V colours of model galaxies plotted as a function of their stellar mass with (top) and without (bottom) "radio mode" feedback. Triangles (red) and circles (blue) correspond to early and late morphological types respectively; the thick dashed lines mark the resolution limit to which morphology can be reliably determined in the Millennium Run.

ton limit, and that the mechanical form associated with jets, on the other hand, operates at rates below the Eddington limit (see, e.g., Di Matteo, Springel & Hernquist 2005, Springel, Di Matteo & Hernquist 2005, Ciotti et al. 2009 and references therein), but the most one can say is that energy output (radiative or mechanical) from the central SMBH pushes matter out, the accretion rate drops precipitously and the expanding matter drives shocks into the galactic gas. Then the resulting hot bubble ultimately cools radiatively.

1.1.3 AGN feedback and the cooling flow problem

AGN feedback is invoked also to resolve the so called "cooling flow problem".

About one third of all clusters present a central drop in the core gas temperature; a cooling flow cluster is characterized by bright X-ray emission from cool, dense gas in the central region of the cluster. Within the cooling radius, where the cooling time of the gas is less than the time since the last major heating event, the cooling time decreases as the gas density increases and, eventually, the gas temperature drops rapidly to $< 10^4$ K, so that cooled gas condenses onto the central galaxy. The condensing gas is replenished by hot gas lying above, leading to a steady, long-lived, pressure-driven inward flow of gas.

To a first approximation the power radiated from the steady flow equals the sum of the enthalpy carried into it, so that the X luminosity gives an estimate of the mass deposit rate.

First observations with ROSAT revealed mass deposit rate of up to 1000 $M_\odot$/yr (Fabian 1994), but as soon as the first X-ray maps of clusters became available, and much more with the era of CHANDRA and XMM-Newton with their high resolution X-ray spectroscopy, it was revealed that few or none of the supposed gas were actually cooling.

AGN feedback can solve this problem. Observations showed (Burns et al. 1981) that every cluster with a strong cooling flow also contains a massive and active central radio galaxy.

A number of authors have suggested ways in which the radio source might replace the thermal energy lost to Xray emission (Binney & Tabor 1995; Churazov et al. 2002; Bruggen & Kaiser 2002; Ruszkowski & Begelman 2002; Kaiser & Binney 2003; Omma et al. 2004).

The most viable mechanism seems to be the energy injected into the intra cluster medium (ICM) by powerful radio jets emanating from AGNs. When these interact with the dense thermal plasma of the ICM, two bubble-like lobes of non-thermal plasma are inflated, which are filled with relativistic particles and magnetic field and thus become visible in radio observations.

Episodic (on-off) activity of radio jets injects non-thermal radio bubbles which may heat the ICM via weak shocks, and additionally these plasma bubbles are responsible for the mechanical (PdV) work done on the ICM for heating it, which is one of the favored mechanism of AGN-ICM feedback.

However, several recent studies have reported examples of ongoing star formation in the brightest cluster galaxies in cool core clusters (CCC) (Cardiel et al. 1998, Crawford et al. 1999, Edge 2001, Goto 2005, McNamara et al. 2006, Wilman et al. 2006, O'Dea et al. 2008, Bildfell et al. 2008, Cavagnolo et al. 2008, Rafferty et al. 2008).

The mounting evidence for active star formation poses a challenge for models that invoke strong AGN feedback.

So, the picture is still incomplete. While theoretical models still presents AGN feedback that produces red and dead ellipticals (De Lucia et al. 2006), recent observations suggest that AGN feedback cannot be as efficient as to completely suppress star formation.

1.2 The goals of this thesis work

To understand galaxy evolution we need different things.

We need tools that can help us to trace the behavior of SMBHs and their host galaxies at high redshift and in active galaxies, and we need to understand how AGN feedback acts.

This thesis work has two different goals, all pointing to the same main topic.

In Chapter 2 we seek to find a tracer for the stellar velocity dispersion σ_* in order to give a tool in the study of the $M_\bullet - \sigma_*$ relation even in active/far galaxies, were the σ_* cannot be measured directly. We perform an extensive study on the kinematics of the gas as described by the three gas emission lines [OIII], [NII] and Hα, in order to find the best tracer for σ_* and to get some clues on the effect of AGN on the gas kinematic.

In Chapter 3 we will look at the effects of AGN feedback in galaxy clusters; we will asses the mean color difference between galaxies in Cool Core Clusters and Non Cool Core Clusters using broad band magnitude from the Sloan Digital Sky Survey and from the 2MASS and GALEX surveys, in order to prove if and in what measure there are difference in star formation between galaxies at the core of clusters presenting cooling flows of collapsing gas and galaxies in clusters without such supply of cooling gas. This will help us in understanding to what extend AGN is able to re-heating the infalling gas.

In Chapter 4 we will summarize our conclusions.

Chapter 2

The relation between stellar and gas velocity dispersion

2.1 Introduction

Stars and gas are in motion inside galaxies; each star, each particle move under the gravitational potential of the matter that compose the galaxy itself.

Via the virial theorem it is possible to desume the galaxy mass from the velocity dispersion of stars.

Assuming spherical symmetry of the system, a stationary state, we find

$$M(r) = -\frac{r\sigma_r^2}{G}[\frac{d\ln\nu}{d\ln r} + \frac{d\ln\sigma_r^2}{d\ln r} + 2\beta] \tag{2.1}$$

where G is the gravitational constant, r is the radius, ν is the tracer of the gravitational potential and σ_r is the radial velocity dispersion. β is the anisotropy parameter $\beta = 1 - \frac{\sigma_\phi^2}{\sigma_r^2}$.

Assuming that the velocity field is isotropic and that we can trace the mass of the system from its luminosity, we can find from observations of the surface brightness and of the line of sight velocity dispersion σ_{los} the following:

$$\nu(r) = -\frac{1}{\pi}\int_r^\infty \frac{dI}{dR}\frac{dR}{R^2 - r^2} \tag{2.2}$$

$$\nu(r)\overline{v}_r^2(r) = -\frac{1}{\pi}\int_r^\infty \frac{d(I\sigma_{los}^2)}{dR}\frac{dR}{R^2 - r^2} \tag{2.3}$$

where R is the projected distance form the center of the galaxy. With these equations we can measure the mass of the galaxy via Formula 2.1.

When the hypothesis of isotropy is not confirmed, it is possible to assume that the ratio mass/luminosity is constant along the radius.

The degeneracy between anisotropy of the velocity dispersion and the ratio M/L can be solved by deriving not only σ_* but the whole line of sight velocity distribution (LOSVD), or at least the low order h3 and h4 parameters. The knowledge of the LOSVD allows to constraints the structure of the stellar orbits and therefore to constraints the β parameter. Anyway, even more complex models are available today.

With some prudence, also gas motion can be used to calculate galaxy mass, via the virial theorem $M(r) = r\sigma^2/G$. But unlike stars, that are a dissipationless system, gas particles represent a collisional one; this means that gas tend to reside in more flattened systems than stars, and that in presence of, for example, jets from the central engine, or radiative pressure giving momentum to the gas, at least some non gravitational acceleration is possible. In this case, the above equation cannot give the correct measure for the mass, representing instead an upper limit, since this acceleration broadens the emission line of the gas.

Nevertheless there is still debate around the possibility of using gas velocity dispersion as a proxy for the stellar velocity dispersion σ_*. Measuring σ_* in high redshift and/or active galaxies is very difficult, and using σ_{gas} would be of great help in studing, for esemple, SMBH demography.

In fact, the bulge stellar velocity dispersion is often difficult to measure directly, and in active galaxies the stellar absorption features are quickly swamped by nonstellar emission from the nucleus.

Since measuring SMBH masses is still possible only in a small sample of galaxies (there are about 49 direct dynamical measurements and 19 upper limits available today, see Gultekin et al. 2009), it is common to derive $M_\bullet$ from σ_* as given by the $M_\bullet - \sigma_*$ relation (Ferrarese & Merritt 2000; Gebhardt et al. 2000a; Tremaine et al. 2002, Tundo et al. 2007). Velocity dispersion distribution function $\phi(\sigma)$ is used to compute the mass function of SMBHs (Aller & Richstone 2002, Yu & Tremaine 2002, Shankar et al. 2004, McLure & Dunlop 2004, Salucci et al. 1999, Tundo et al. 2007).

So, in studing the formation and evolution of SBMHs and their host galaxies it would be useful to have a tool powerful as the $M_\bullet - \sigma_*$ relation even at high redshift, and every time it is non possible to measure the stellar velocity dispersion, like in active galaxies.

This tool can be given by the [OIII] line, a strong, ubiquitous line, almost present in every galaxy, and with an high ionization potential, assuring that the gas is near the central engine, in the Narrow Line Region (NLR).

The NLR is in a privileged position in galaxies: compact enough to be illuminated by the active nucleus and yet large enough to feel the gravitational forces of the bulge. Early studies of integrated line profiles determined that gravity, not nuclear activity, dominates the global kinematics of the NLR (Wilson & Heckman 1985; Whittle 1992a,b).

Nelson & Whittle (1996) compared [O III]λ5007 FWHM/2.35 (for a gaussian line profile σ=FWHM/2.35)and σ_* in a sample of 75 Seyfert galaxies, and found on average good agreement between $\sigma_{[OIII]}$ and σ_*, with considerable scatter. The correlation was poor (a Pearson correlation coefficient of 0.48), and using an OLS Bisector regression method they reported a slope less than 1.

They also shown that, as already known (Wilson & Willis 1980), there were a correlation between [OIII] line width and radio luminosity; strong linear radio source generally had supervirial line widths.

On the contrary when they excluded all objects with powerful linear radio sources or with morphological peculiarities, they found that the mean of FWHM[OIII]/2.35 was *lower* than that of σ_*, so that $FWHM_{[OIII]}/2.35 \sim 0.8\sigma_*$ in average.

Since then, the $\sigma_* - \sigma_{[OIII]}$ relation was tested both directly in samples of low luminosity AGN and indirectly in samples of moderate luminosity QSO, deriving BH masses from the size and velocity of BLR (Kaspi et al. (2000), and

in different class of AGN (Type 2 and Type 1 Seyfert galaxies, Narrow Line Seyfert 1 -NLS1).

Nelson (2000) tested the relation indirectly using a sample of AGN for which were available SMBH masses ($M_\bullet$) from reverberation mapping tabulated in Kaspi et al. (2000), plotted versus σ_* when available and versus $\sigma_{[OIII]}$ otherwise. he found that AGN followed the Tremaine et al. (2002) within uncertanties, but reported a somehow shallower slope.

Boroson (2003) used a sample of 107 low redshift radio quiet QSO and Seyfert1 galaxies from the Early Data release of the Sloan Digital Sky Survey (SDSS). He derived Black Hole masses from the kinematics of the Broad Line Region (BLR) using $M_\bullet = v^2 R_{BLR}/G$ (Kaspi et al. 2000) where $v = \sqrt{3}/2 FWHM\ H\beta$ and where the size of the BLR were obtained from the continuum luminosity at λ =5100 Å using $R_{BLR} = 32.9(\lambda L5100/10^{44}\ \mathrm{erg\ s^{-1}})^{0.7}$ lt days.

Compared with the [OIII] width he found that his sample described the same relation of Tremaine at al. (2002) within the uncertainties, but he reported a lower slope ($b_T = 4.02 \pm 0.32; b_B = 3.59 \pm 0.47$).

Another indirect study was made by Shields et al. (2003); in their sample of high luminosity QSO (reaching z =3.3) he retrieved BH masses from reverberation mapping (Kaspi et al. 2000) and his $M_\bullet - \sigma_{[OIII]}$ relation resulted in agreement with that of Tremaine et al. (2002) in radio quiet objects while radio loud QSO settled *above* the Tremaine et al. relation. They commented the trend for [OIII] line width to correlate with AGN luminosity (Brotherton 1996 b, McIntosh et al. 1999, Véron-Cetty et al. 2001) as a consequence of both the increasing mass of the SMBH with the luminosity of the galaxy, and of the $M_\bullet - \sigma_*$ relation. Still, the problem with radio loud QSO can be interpreted not with galaxies having SMBHs with higher mass than usual, but with [OIII] not tracing the stellar velocity dispersion.

Another class of AGN, the Narrow Line Seyfert1 (NLS1) began to show a peculiar behavior respect to the $M_\bullet - \sigma_*$ when using the [OIII] line width.

Grupe & Mathur (2004) used 75 soft X-ray selected AGN with 32 NLS1 and found that their NLS1 galaxies lain *below* Tremaine et al. (2002) relation.

The study of Botte et al. 2005 confirmed that the NLS1 didn't describe the Tremaine et al. (2002) relation if [OIII] is used instead of σ_*. They supplied a new stellar σ through direct measures of the [CaII] triplet ∼8550 Å and found that these measures are overestimate by $\sigma_{[OIII]}$.

It was suggested by Green & Ho (2005) that the [OIII] line should be fitted not by a single Gaussian, and that in the $\sigma_* - \sigma_{[OIII]}$ it should be used the *core* of the line. It is known in fact (Heckman et al. 1981; De Robertis & Osterbrock 1984; Whittle 1985a; Wilson & Heckman 1985, Komossa et al. 2008) that [OIII] emission line can presents blue asymmetries (blueshift and blue wings).

Green & Ho (2005) selected a sample of AGN from the SDSS and fitted, when needed, the profile of the [OIII] line with a double Gaussian. They measure the mean of the ratio $\frac{\sigma_{[OIII]}}{\sigma_*}$ using the $\sigma_{[OIII]}$ as fitted with a single Gaussian, and the core of the line. They found in fact that in the former case the mean ratio was 1.34±0.66 while in the latter was 1.00±0.35; in their work the authors found also that the Eddington ratio L_{bol}/L_{EDD} of the galaxy, that measure the accretion rate of the central engine, acts as a third parameter, so that at increasing L_{bol}/L_{EDD} corresponds an increasing $\Delta\sigma = \sigma_{[OIII]} - \sigma_*$. The authors

tested also other lines of the NLR, namely the [SII] $\lambda\lambda$ 6716, 6731 Å doublet and the [OII] λ3727 Å line, but they found that they were to weak, and the scatter in the $\sigma_* - \sigma_{gas}$ relation was even higher than in the case of [OIII].

Nevertheless Bian, Yuan & Zhao (2006) showed in a sample of 150 NLS1 that even the choice of the core of the [OIII] line doesn't change the fact that NLS1 seem outliers respect to the Tremaine et al. (2002) relation.

Another study of Gu et al. (2006) in 79 nearby galaxies, of which 65 was Seyfert2 galaxies, showed again a slope in the $\sigma_* - \sigma_{[OIII]}$ of 0.84±0.08.

The debate around the possibility of using $\sigma_{[OIII]}$ instead of σ_* has not yet a resolutive answer. It is pressing to find the solution of this problem, since the interest on distribution function of SMBH mass is arising, and this is not the only point of interest in the study of the [OIII] line.

In fact, the kinematics and structure of the gas itself, compared with the stellar ones, give interesting clues for understanding the structure and the dynamic history of the host galaxy.

A new analysis is needed; in this study we want to compare the emission lines [OIII], [NII] and Hα to test the $\sigma_* - \sigma_{gas}$ relation, and to find the best tracer for the σ_* stellar velocity dispersion.

The disadvantages of using the [OIII] emission line are quite evident; first of all the huge amount of intrinsic scatter, and the fact that a class of AGN, namely, the NLS1 galaxies, seems to obey to a different $M_\bullet - \sigma$ relation when [OIII] is used.

A possible explanation of this behavior resides in the blue asymmetries that may affect [OIII] line width.

Since it is known (de Robertis & Osterbrock 1984, Komossa et al. 2008, Rice et al. 2006) that blueshift and blue wings correlate with the ionization potential of the line, we want to test the feasibility of a lower ionization potential line in tracing the stellar velocity dispersion.

In effect, since we are willing to trace the bulge gravitational potential, we asked ourselves *why* should we relay on the [OIII] line. Authors agree that [OIII] originates in the NLR, since its high ionization potential (35.1 eV), and that it's kinematics, although dominated by the gravitational potential of the bulge, should be also affected by the turbulences of the nucleus.

The reasons that lead scientist to use [OIII] emission line consists mainly on the fact that this line is almost ubiquitous in galaxies, and that it is quite strong, so it is easy to measure. The fact that it originate in the NLR it is somehow seen as a *pro*, since [OIII] is used as a proxy for the stellar velocity dispersion mainly in studies on supermassive black holes (SMBHs), but if we really want a tracer for the bulge potential we should prefer a line as Hα, that is even stronger than the [OIII] line, has a lower IP (13.6 eV) so that is less affected by blue asymmetries and that is *not* confined in the NLR. Even [NII] forbidden line is strong, easy to measure, it is not absorbed, and has low ionization potential (14.5 eV). Also, being a nebular line, it is less affected by stellar features than Hα (we are not saying that it is not affected at all, because its proximity with Hα may cause its involvement with the same stellar feature).

The use of the [NII] emission line in estimating the stellar velocity dispersion was proposed recently by Ho (2009), that showed in a sample of 345 bright galaxies form the Palomar spectroscopic survey of nearby galaxies that the gas dispersion correlate with the stellar velocity dispersion. As for the [OIII] emission

line they find that in mean the ratio σ_{gas}/σ_* is lower then unity in non active galaxies, while the value increase with nuclear luminosity or Eddington ratio.

I will show that Hα and [NII] emission line offers a relation with higher correlation respect to [OIII], and that is less subject to the non-gravitational effects of the central engine in AGN.

I will use a sample of both active and starforming galaxies selected from the SDSS Data Release 6th (DR6)

2.2 The sample

2.2.1 The Sloan Digital Sky Survey

We select our sample from the Sloan Digital Sky Survey (SDSS) 6th Data Release (DR6) database (Adelman-McCarthy et al. 2006).

The SDSS (York et al. 2000, Stoughton et al. 2002) is one of the most ambitious and influential surveys in the history of astronomy. Over eight years of operations (SDSS-I, 2000-2005; SDSS-II, 2005-2008), it obtained deep, multi-color images covering more than a quarter of the sky and created 3-dimensional maps containing more than 930,000 galaxies and more than 120,000 quasars.

The SDSS uses a dedicated 2.5-meter telescope (Gunn et al. 2006) at Apache Point Observatory, New Mexico, equipped with two powerful special-purpose instruments. The 120-megapixel camera imaged 1.5 square degrees of sky at a time, about eight times the area of the full moon. A pair of spectrographs fed by optical fibers measured spectra of more than 600 galaxies and quasars in a single observation.

The SDSS survey is magnitude limited (with 95% detection repeatability for point sources) with limiting magnitudes of 22.0 (u band), 22.2 (g), 22.2 (r), 21.3 (i) and 20.5 (z) mag.

The Main Galaxy Sample targets, moreover, are selected to have a minimum Petrosian r magnitude of 17.7 mag (even if, since the target selection flags used in order to create the spectroscopic plates were based on an earlier processing of the data, for the Main Galaxy Sample this amounts to changes in the r band flux limit, and in fact our final sample have an apparent -model- magnitude between 10.8 and 19.5 mag in r band).

In our subsequent analysis we will ignore any selection effects due to the magnitude limits. We just notice that since the bulk of our selected sample, due to our constraints, consist in galaxies with mean redshift of z$\sim$0.09, we are missing galaxies fainter than about -18.5 mag. Even if our maximum redshift is z=0.36, we observe in our sample a drop in the galaxy number at z=0.16; at that distance we are missing galaxies fainter than about -20 mag.

One can find detailed information about SDSS project at the internet address http://www.astro.princeton.edu/PBOOK/welcome.htm

Funding for the SDSS and SDSS-II was provided by the Alfred P. Sloan Foundation, the Participating Institutions, the National Science Foundation, the U.S. Department of Energy, the National Aeronautics and Space Administration, the Japanese Monbukagakusho, the Max Planck Society, and the Higher Education Funding Council for England. The SDSS was managed by the Astrophysical Research Consortium for the Participating Institutions.

The SDSS is managed by the Astrophysical Research Consortium (ARC) for the Participating Institutions. The Participating Institutions are the American Museum of Natural History, Astrophysical Institute Potsdam, University of Basel, University of Cambridge, Case Western Reserve University, The University of Chicago, Drexel University, Fermilab, the Institute for Advanced Study, the Japan Participation Group, The Johns Hopkins University, the Joint Institute for Nuclear Astrophysics, the Kavli Institute for Particle Astrophysics and Cosmology, the Korean Scientist Group, the Chinese Academy of Sciences (LAMOST), Los Alamos National Laboratory, the Max-Planck-Institute for Astronomy (MPIA), the Max-Planck-Institute for Astrophysics (MPA), New Mexico State University, Ohio State University, University of Pittsburgh, University of Portsmouth, Princeton University, the United States Naval Observatory, and the University of Washington.

The 6th Data Release of the SDSS, with 375,000 galaxy spectra, enables us to compare nuclear gas and stellar kinematics with a large, homogeneous sample.

Spectroscopic candidates are selected based on imaging in the u, g, r, i, and $z$bands (Fukugita et al. 1996; Smith et al. 2002; Strauss et al. 2002) with a drift-scan camera (Gunn et al. 1998). Spectra are acquired with a pair of fiber-fed spectrographs.

The spectrographs

In the spectral range $3800 - 9200$ Å, divided between two cameras around 6150 Å, the spectral resolution $R = \lambda/\Delta\lambda$ variates around 1800 and 2000 depending on wavelength. This resolution is enought to measure velocities in a galactic spectrum with uncertanties better than ± 20 km s^{-1} for σ_* greater than $\sim$70 km s^{-1}.

The 640 fibers subtend a diameter of 3" each, and cannot be positioned nearer than 55" each other.

The fixed 3" aperture is large enough to let through not only the light from the nucleus in AGN but also substantial amounts of stellar light from the host galaxy. For example, at the median redshift of the sample $z = 0.1$, a 3" aperture subtends about 4 h^{-1} kpc. Moreover, galaxies with higher redshift will have a larger host galaxy component in the observed spectra. Thus, the nuclear emission lines are often contaminated by the stellar absorption lines of the host galaxy. For weak AGNs, this contamination can be so severe that the interesting emission lines are completely submerged in the absorption lines.

The spectra have an instrumental resolution of $\lambda\ \Delta\lambda \sim 1800$ ($\sigma_{inst} \sim 71$ km s^{-1}). Integration times are determined for a minimum signal-to-noise ratio (S/N) of 4 at $g = 20.2$ mag. The spectroscopic pipeline performs basic image calibrations, as well as spectral extraction, sky subtraction, removal of atmospheric absorption bands, and wavelength and spectrophotometric calibration (Stoughton et al. 2002).

The data reduction is performed automatically by a number of pipelines that work interdependently.

2.2.2 The Princeton reduction

The Princeton spectra are an alternative reduction of the SDSS spectra. These reductions are improved respect to that of SDSS in various way; determination of redshifts and classifications uses an independent code doing direct chi-squared fitting of templates to spectra. The point that make them attractive to us is that the measures of the stellar velocity dispersion are made explicitly masking the emission lines, so giving the possibility to have a bigger sample of galaxies with both σ_* and σ_{gas} measured respect to the SDSS.

The Princeton re-reductions of the "public release" data is available from the web site http://spectro.princeton.edu/. The data are grouped into disjoint samples of when the data became available.

The spectroscopic pipeline (SPECTRO) is a large data reduction software package that automatically reduce all spectroscopic observations made by the SDSS. It is formed by two distinct pipelines. The first one (2D SPECTRO) reduces the raw bidimensional spectra and gives the monodimensional calibrated spectra; it interpolates over bad pixels and performs bias and dark subtraction, flat-fielding and applies wavelength calibration and sky subtraction. It combines the three individual exposures for each object.

The second one (1D SPECTRO) combines the red and blue halves of the spectrum together, masks all bad pixels, fits the continuum of the spectrum, finds and fits emission lines. It determines all emission-line redshift and classify all detected emission lines. It also classifies the spectrum using a set of template spectra ranging from stars to quasars, using a principal component analysis similar to that of Connolly et al. (1995). The spectrum is cross-correlated with the templates to obtain the absorption-line redshift and the internal velocity dispersion of galaxies is estimated using the width of the Cross Correlation Function peak. It is also performed flux calibration of the spectrum using the calibrated photometric images.

2.3 Measuring the emission lines

With the SDSS pipeline the continuum is fitted using a median/mean filter. A sliding window is created of length 300 pixels for galaxies and stars or 1000 pixels for quasars. Pixels closer than 8 pixels (560km/s) for galaxies and stars or 30 pixels (2100 km/s) for QSOs to any reference line are masked and not used in the continuum measurement. The remaining pixels in the filter are ordered and the values between the 40th and 60th percentile are averaged to give the continuum. In this way, emission lines such as Hα can be strongly affected by the stellar absorption. For this reason we decided to fit again our galaxies.

2.3.1 The continuum subtraction

A first selection from the Main Galaxy Sample was made by choosing all galaxies presenting positive measured $\sigma_{[OIII]}$,$\sigma_{[NII]}$, $\sigma_{H\alpha}$, $\sigma_{H\beta}$ and σ_*, and a mean signal to noise ratio greater than 5 in the Princeton reduction. We need a positive measured $\sigma_{H\beta}$ to distinguish galaxies in AGN and Star Forming (Kewley et al. 2006).

To have both the emission lines *and* the stellar velocity dispersion reduced the original sample to about 6780 galaxies.

In order to measure emission lines, we need to remove the stellar continuum. The stellar continuum dramatically affects lines as $H\beta$, while forbidden lines as $[OIII]$ and $[NII]$ should be quite unaffected.

We decided to test these two different ways for the continuum subtraction to quantify how much the measure of the width of an emission line can differ when the contamination from an absorption line is taken into account and when it is not.

Consequently, the subtraction was performed:

- fitting a linear continuum to the spectrum
- using a Principal Component Analisys (PCA)

The Principal Component Analisys (PCA)

The PCA was performed following the procedure outlined in Hao et al.(2005).

Principal component analysis (PCA) involves a mathematical procedure that transforms a number of possibly correlated variables into a smaller number of uncorrelated variables called principal components. The first principal component accounts for as much of the variability in the data as possible, and each succeeding component accounts for as much of the remaining variability as possible.

Much has been written about the use of PCA in studies of the multivaiate distribution of astronomical data (Efstathiou & Fall 1984, Connolly et al. 1995, Lahav et al. 1996; Bromley et al. 1998; Eisenstein et al. 2003; Yip et al. 2004)).

Given a set of spectral energy distribution (SED), each SED can be thought of as an axis within a myltidimensional hyperspace, $f_{\lambda i}$, where λ is the wavelength and i the spectral type. From this hyperspace we can construct normal spectra, $e_{\lambda i}$, that represent an orthogonal basis or eigenspectra.

The basic idea of stellar continuum subtraction is to build a library of stellar absorption-line spectra templates and use them as building blocks to simulate the stellar spectrum of the object in question. The library needs to be complete in the sense that it must contains enough information on various absorption features to be able to simulate the stellar components of various galaxies with widely spread metallicities, ages, and velocity dispersions.

We achieve this using a sample of pure absorption-line spectra taken from the SDSS, as delineated in Hao et al.(2005).

In practice we require the $H\alpha$ equivalent width, EW($H\alpha$), to be less than 0 (positive equivalent width corresponds to emission lines) and that [OII] λ3727 not be detected. [OII] λ3727 is used because it is always present even in very weak emission-line galaxies.

By limiting ourselves further to high-S/N spectra, we decided to use galaxies in the redshift range $z < 0.25$. Our sample includes, at this stage, more than 1600 galaxies.

Prior to analysis, all the spectra were reported to a common rest frame.

The SDSS spectra are binned log-linear. Units are 10^{-17} erg/cm/s^2/ Å. The pixel size is fixed in velocity space at 69 km/s = $\ln(10) * c * 0.0001$, where 0.0001 is the log 10 dispersion per pixel.

From the header of the spectra we recover the redshift z, the mean λ of the initial pixel λ_{start} and the number of the pixels n_{pixel}. With these data we obtain the logarithm of the wavelength as

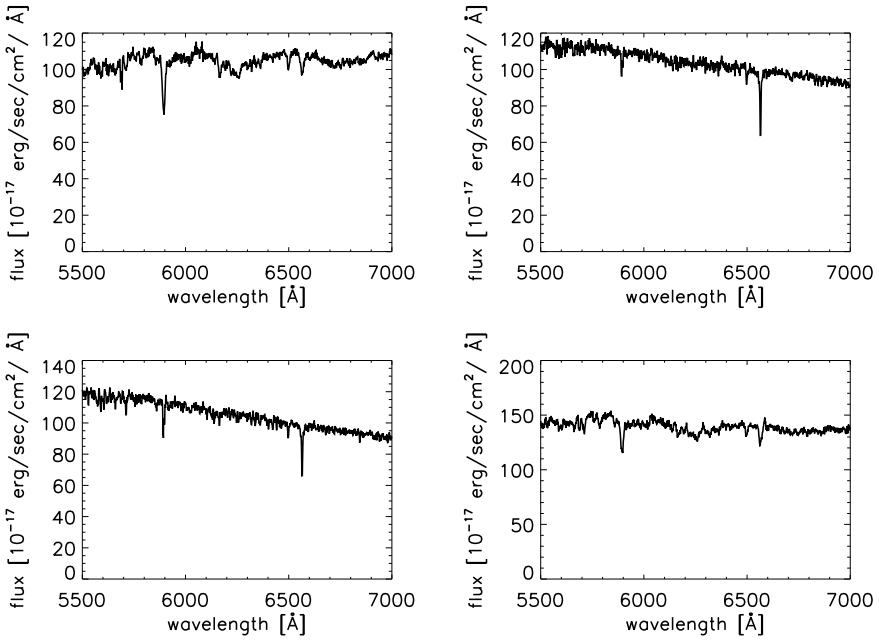

Figure 2.1: Some of the pure absorption-line SDSS spectra used in the PCA analysis

$$\log(\lambda) = \lambda_{start} + 0.0001 * (n_{pixel}) \tag{2.4}$$

and the wavelength reported to $z = 0$ are

$$\lambda_{z=0} = \lambda/(1+z) \tag{2.5}$$

Spectra was now cutted between $\lambda = 4500$ and $\lambda = 7000$ Å, and reported with a spline function to the same reference wavelengths.

Some of these spectra are showed as an example in Fig 2.1.

With these spectra we constructed the correlation matrix S of dimension $M \times M$, in which M is the total number of galaxies (while N is the total number of common wavelength bin).

Each {ij} element is given by the correlation coefficient between the ith and the jth variable.

The problem of finding the matrix that reduces the correlation matrix to its diagonal form Λ, such is

$$R^{\dagger} S R = \Lambda \tag{2.6}$$

is solved with the *pcomp* routine of IDL. This gives a number of eigenvector equal to the number of imput spectra, with the main features of the absorption-line galaxies concentrated in the first few; in just the first eight eigenspectra it is contained more than 90 % of the informations, as one can compute looking at the diagonal component of Λ, that are the eigenvalues of the system. The eigenvalues

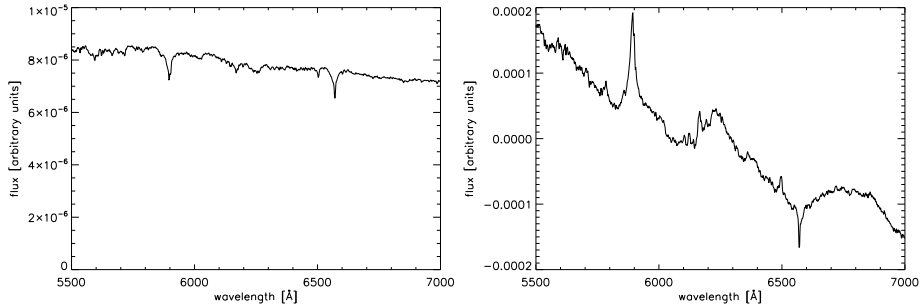

Figure 2.2: The first (left) and the second (right) eigenspectra in the wavelength range $5500 - 7000$ Å. This first eigenspectra accounts for more than 90% of the informations.

represent infact the statistical relevance of the corresponding eigenspectra in the galaxy sample.

The eigenbasis is given now by

$$e_{\lambda i} = R^{\dagger}_{ij} f_{\lambda i} \tag{2.7}$$

and each SDSS spectrum in the our pure absorption-line sample can be represented, without errors, by a linear combination of the eigenspectra:

$$f_{\lambda i} = \sum_{j=1}^{m} y_{ij} e_{\lambda j} \tag{2.8}$$

where m is the total number of eigenspectra and y_{ij} is the weight of the jth eigenspectrum in the ith galaxy.

Since we have found that the first 8 eigenspectra represent more than 99 % of the information, we can reproduce our spectra using a linear combination of these ones.

We used the *curvefit.pro* IDL routine to perform a non-linear least squares fit of our spectra to a linear combination of our eight eigenspectra, after masking the emission lines.

We shows in the following figures some examples of the whole procedure applied to the spectra of our pure absorption-line galaxies, chosen to test the reliability of the procedure prior to use the PCA in the stellar continuum subtraction of our emission-line galaxy sample.

Subtracting a linear fit

In our procedure we selected the regions around the emission lines of interest (each region has at least 200 wavelength bin), $H\alpha$, $[OIII]$, $[NII]$, choosing zones free from absorption or emission features. We fitted the selected area to a straight line using the the *mpfitfun* IDL routine.

The best fit parameters given by *mpfitfun* are used to build a straight line of length equal to the one of the spectra; this line is finally subtracted to our spectra.

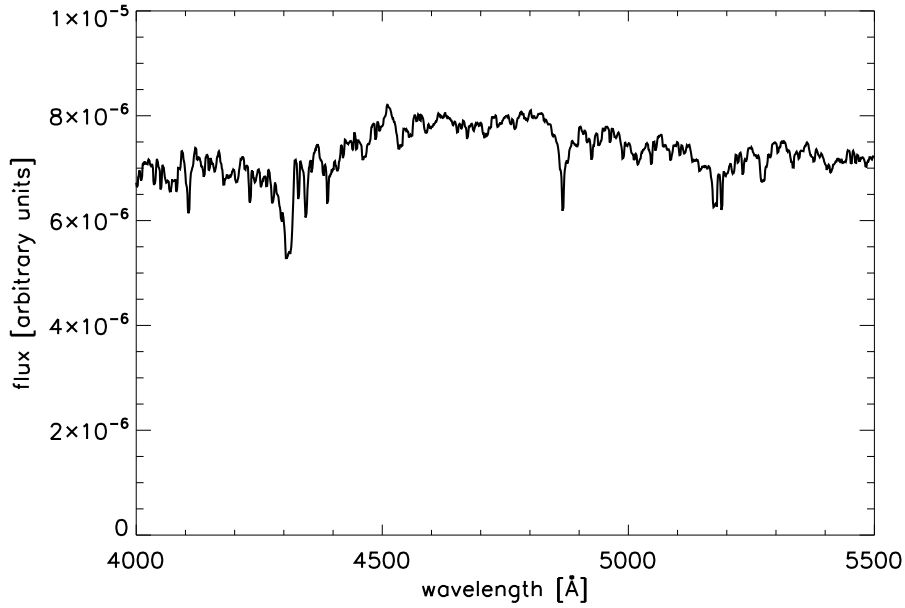

Figure 2.3: The first eigenspectra in the wavelength range $4000 - 5500$ Å. This first eigenspectra accounts for more than 90% of the informations.

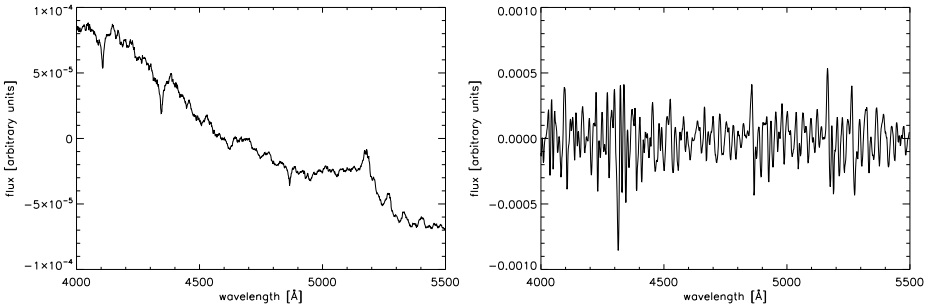

Figure 2.4: The second (left) and the third (right) eigenspectra in the wavelength range $4000 - 5500$ Å. We see that this third eigenspectra already represent just noise in the spectrum.

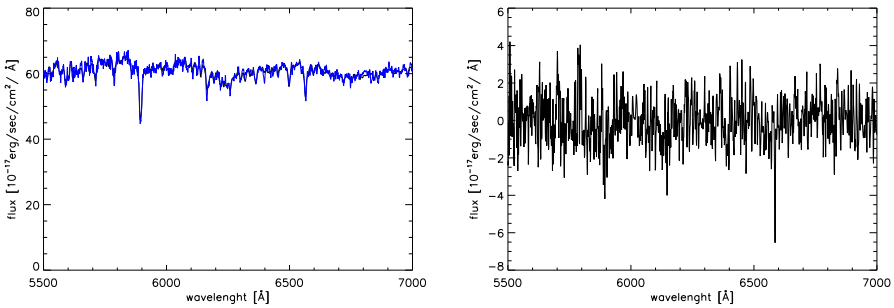

Figure 2.5: *Left*: A spectrum (black line) and the sintetic spectrum (blue line) builted with a linear fitting of the 8 eigenspectra, in the range $5000 - 6500$ Å. *Right*: Residuals in the subtraction of the stellar continuum.

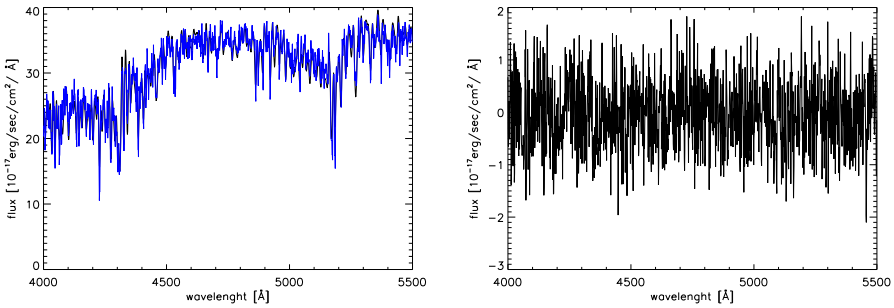

Figure 2.6: *Left*: A spectrum (black line) and the sintetic spectrum (blue line) builted with a linear fitting of the 8 eigenspectra, in the range $4000 - 5500$ Å. *Right*: Residuals in the subtraction of the stellar continuum.

2.3.2 The line fitting

In the two different continuum-subtracted spectra we fitted the emission lines of interest with the *mpfitfun* routine; in particular we used, in the case of the [OIII] line, a single Gaussian, while for the complex of the Hα and [NII] doublet we performed at the same time a fit on the three line, with the [NII]λ6548 line binded to have its height equal to one third of the [NII]λ6583 line height, and to have the same σ.

We performed two fit, the first one with starting guesses fixed to be $\lambda_{start} = \lambda_{line}$, σ_{start} =1 and height$_{start}$ =1. The second fit were performed on the same region, but with the starting guesses given by the parameters found in the previous fit. We retrieved in this way the λ, the σ, the height of the fitted Gaussian.

We derived also the χ^2 of the fit and the uncertainties reported by *mpfitfun*.

Assuming that the true reduced χ^2 value is unity, the estimated parameters uncertainties are computed by scaling the formal 1-sigma error in each parameter, computed from the covariance matrix, by the measured chi-squared value.

The observed σ is the convolution of the intrinsic line width and the instrumental response. To first order, the intrinsic line σ can be approximated by

$$\sigma = \sqrt{\sigma_{obs}^2 - \sigma_{inst}^2} \tag{2.9}$$

In the case of the SDSS data, σ_{inst} varies not only as a function of wavelength, but also of the location of the object on the plate and the temperature on the night of the observations. For this reason, the SDSS pipeline measures the instrumental response using an arc lamp spectrum, and returns the resolution at every pixel.

The dispersion is found in the *fits* files of the SDSS, and it is given in pixel space. To convert to resolution in wavelength units, we have to multiply it by the local pixel size in wavelength units, which is $\ln(10) * \lambda * 0.0001$ where λ is the wavelength of the pixel and 0.0001 is again the log dispersion. We applied the following equation

$$\sigma_{inst}[\text{Å}] = \sigma_{inst}[\text{pix}] * (\ln(10) \times \lambda_{line} \times 0.0001) \tag{2.10}$$

When we remove the effects of instrumental resolution, some line width resulted lower than the resolution limit of $\sim$70 km s$^-$1; this means that on such galaxies the uncertainty on the line measure will increase. Still, the selection effects due to the rejection of galaxies with low σ can change the parameters we are looking for (see Bernardi et al. 2003a and Hyde & Bernardi 2009 for discussion of biases introduced by eliminating objects based on their σ_*) so we decided to take all objects with $\sigma > 50$ km s^{-1}.

σ_* correction

SDSS fibers have a fixed aperture of 3". This means that for galaxies at different distances the fiber will take a different portion of the galaxies itself. If the velocity dispersion were a constant inside a galaxies, this would'nt give any differences. Instead, we know that the radial velocity dispersion profile variates inside an early type galaxy, and it generally decreases with radius. This is not

the case of spiral galaxies (Pizzella et al. 2004). So σ_* for distant early galaxies sistematically underestimate the velocity dispersione that would be measured in a fixed *phisical* aperture, as, for example, the effective radius R_e. We overcome this problem by applying the correction for the aperture as in Jørgensen et al. (1995):

$$\sigma_*[R_e/8] = 10^{\log\sigma_* + 0.04\times(\log(1.5) - \log(0.125\times R_e))} \tag{2.11}$$

were $\sigma_*[R_e/8]$ is the stellar velocity dispersione reported to the effective radius R_e divided by 8.

The effective radius is taken from SDSS database; it is calculated by SDSS routines as a parameter in the fit to the radial surface brightness profile (given as the average surface brightness in a series of annuli).

It is given, in each band, both for a de Vaucouleurs (deVRad$_r$) and an exponential (expRad$_r$) model fit.

We identified the type of our galaxies. We retrieved the parameters **fracDev**$_r$, **eclass** and **ci** from the SDSS database. fracDev$_r$ is the weight of the de Vaucouleur model for the galaxy, and give an idea of how close is the radial surface brightness profile to the de Vaucouleur fit. *eclass* give a classification of the galaxy based on its spectrum, using Principal Component Analysis (Connolly et al. 1995). Its value range between ∼-0.35 and ∼0.5 passing from early type galaxies to late type. *ci* is the concentration index, given as the ratio $\frac{P_{90}}{P_{50}}$ of the radii containing 90% and 50% of the Petrosian flux of the galaxy.

An early type galaxy will have (Bernardi et al. 2003a) at the same time

$$fracDev_r > 0.8 \quad \sigma_* > 0 \quad eclass < -0.05 \quad ci > 2.75 \tag{2.12}$$

Anyway, our subsequent results don't change depending on this correction.

2.3.3 Comparation between measurements

In the following figures we compare our measures of $\sigma_{[OIII]}$, $\sigma_{[NII]}$ and $\sigma_{H\alpha}$, obtained subtracting the stellar continuum with the PCA and with the linear fit, with SDSS measures. For simplicity, we will call our different measures σ_{PCA}, σ_{fit} and σ_{SDSS}, and we will talk about PCA measures, fit measures, and SDSS measures, for the three cases.

We expect than for the [OIII] emission line σ measurements, the stellar continuum subtraction using the PCA should not give different results with respect to that using a linear fit of the continuum, because there are no strong stellar features at that wavelength.

The case is different for the [NII] and Hα lines. For the Hα line this is evident because of the complex stellar absorption feature, while in the case of the [NII] emission line, even if there are no stellar absorption at that wavelength, the line itself is involved in the feature of the Hα line, since their positions are so close.

In Figure 2.7, left, we compare the SDSS [OIII] measures with ours fit measures; in the right panel we plot PCA measures versus fit measures. In both plots we see that the three measurements agree; the mean and the scatter of the differences between the different measures are

$$\overline{\sigma_{fit} - \sigma_{SDSS}} = -0.04 \pm 0.4$$

$$\overline{\sigma_{fit} - \sigma_{PCA}} = 0.02 \pm 0.2$$

so while the mean value of the difference between measures are comparable in the two cases, the scatter between PCA and fit measures is smaller than the one between fit and SDSS data.

We see in Figure 2.8, left, the relative differences $(\sigma_{fit} - \sigma_{PCA})/\sigma_{PCA}$. Overplotted in black dots are the mean values of the relative differences in bin of $\sigma_{[OIII]PCA}$. The dashed and dotted lines represent the 1-σ and 2-σ confidence in the mean values.

We notice that when $\sigma_{PCA} >\sim 1.3$ Å the mean relative difference is well constrained around zero, with a 1-σ confidence well under a 10% There are some problem when $\sigma_{PCA} <\sim 1.3$ Å: the relative difference increases while σ_{PCA} gets lower, but this behavior does not matter us, because even if there are not stellar absorption at the [OIII] wavelength, still even a smooth feature in the stellar continuum can affect a very narrow emission line, as we can see in Figures 2.13, 2.14 . We will explain this more plainly in the next paragraph.

In the right panel of Figure 2.8 we show the relative differences $(\sigma_{fit} - \sigma_{SDSS})/\sigma_{SDSS}$. In this case we notice a somehow more caothic behavior, but this does not surprise us since this information is yet in the fact that the scatter in the differences between fit and SDSS measures is bigger than the one between fit and PCA measures. Again, there is an enhancement of the relative difference at small σ_{SDSS}. SDSS recommends not to use measures below the resolution limit of 70 km s^{-1}, and in effect if we stay beyond that limit (corresponding to $\sigma = 1.17$ Å for the [OIII] line, to $\sigma = 1.54$ Å for the [NII] line and to $\sigma = 1.53$ Å for the Hα line), the problem is mostly reduced.

In the case of the [NII] emission line we have that (Figure 2.9)

$$\overline{\sigma_{fit} - \sigma_{SDSS}} = -0.08 \pm 0.3$$
$$\overline{\sigma_{fit} - \sigma_{PCA}} = 0.1 \pm 0.2$$

and so even in this case the scatter between fit and SDSS measures are higher respect to the one between PCA and fit measures, but we notice that the first is lower that in the case of [OIII] line, probably because [NII] line is stronger and easier to measure, and the second is higher, probably because, as yet said, the [NII] emission line is easy to be involved in the stellar feature at the wavelength of the Hα line.

We see,in fact in Figure 2.10 that the relative differences between fit and SDSS data (right panel) have a more regular distribution around zero than in the case of the [OIII] line, while the relative difference between fit and PCA measures (left panel) reveals to be higher, at short σ_{PCA}, than for [OIII].

The Hα line shows a similar behavior. We have that

$$\overline{\sigma_{fit} - \sigma_{SDSS}} = -0.2 \pm 1.0$$
$$\overline{\sigma_{fit} - \sigma_{PCA}} = 0.001 \pm 0.5$$

and we see in Figure 2.11 and 2.12 the same enhancement of the relative difference between fit and PCA data, and the good agreement between fit and SDSS data.

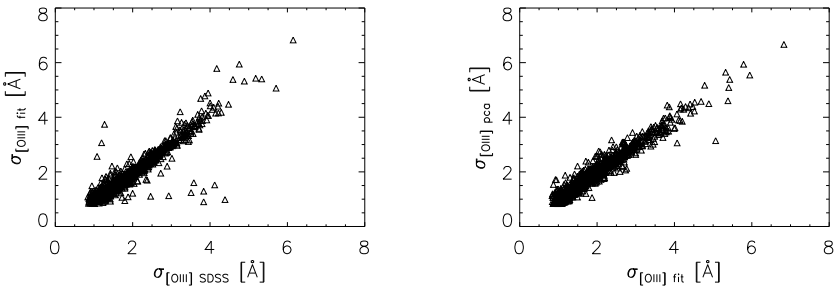

Figure 2.7: *Left*: fit measures plotted versus SDSS measure for the [OIII] line. *Right*: PCA measures plotted versus fit measure for the [OIII] line.

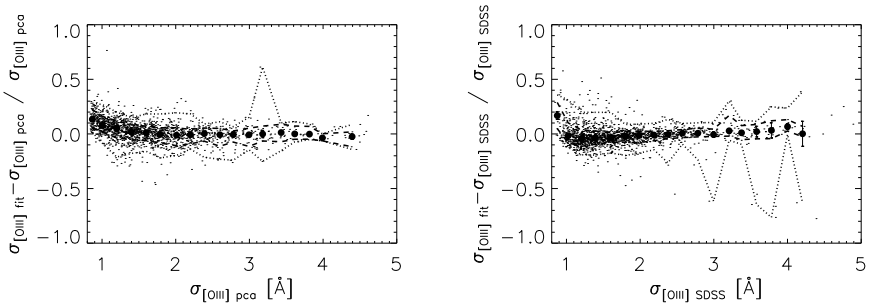

Figure 2.8: *Left*: Relative difference $(\sigma_{fit} - \sigma_{PCA})/\sigma_{PCA}$ between fit and SDSS measures of the [OIII] line plotted versus PCA measures. measures. *Right*: Relative difference $(\sigma_{fit} - \sigma_{SDSS})/\sigma_{SDSS}$ between fit and SDSS measures of the [OIII] line plotted versus SDSS

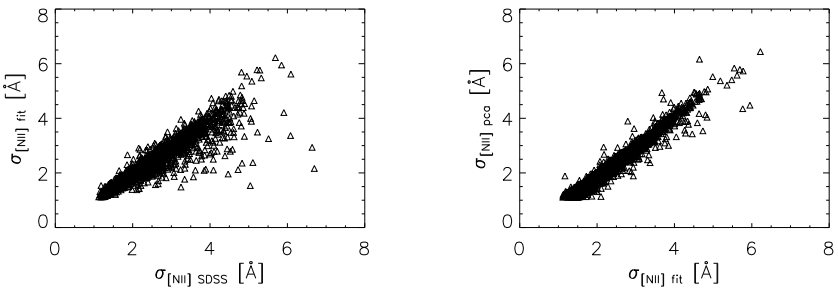

Figure 2.9: *Left*: fit measures plotted versus SDSS measure for the [NII] line. *Right*: PCA measures plotted versus fit measure for the [NII] line.

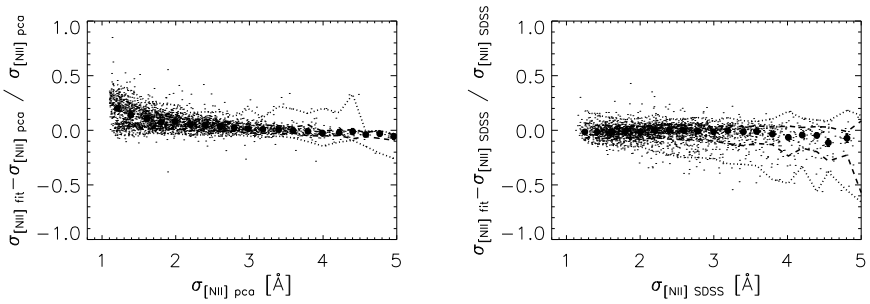

Figure 2.10: *Left*: Relative difference $(\sigma_{fit} - \sigma_{PCA})/\sigma_{PCA}$ between fit and SDSS measures of the [NII] line plotted versus PCA measures. *Right*: Relative difference $(\sigma_{fit} - \sigma_{SDSS})/\sigma_{SDSS}$ between fit and SDSS measures of the [NII] line plotted versus SDSS measures.

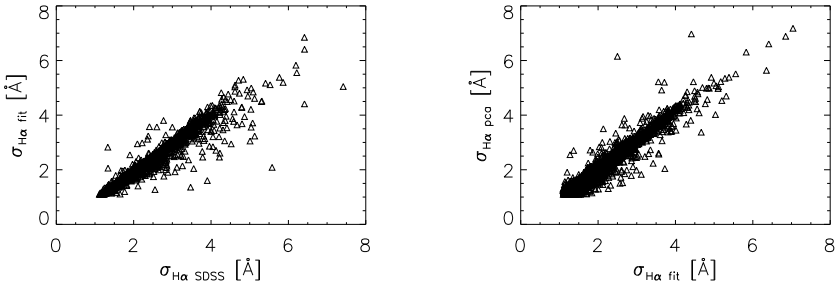

Figure 2.11: *Left*: fit measures plotted versus SDSS measure for the Hα line. *Right*: PCA measures plotted versus fit measure for the Hα line.

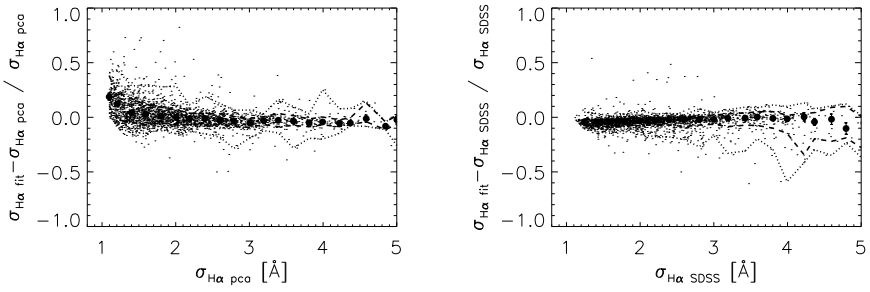

Figure 2.12: *Left*: Relative difference $(\sigma_{fit} - \sigma_{PCA})/\sigma_{PCA}$ between fit and SDSS measures of the $H\alpha$ line plotted versus PCA measures. *Right*: Relative difference $(\sigma_{fit} - \sigma_{SDSS})/\sigma_{SDSS}$ between fit and SDSS measures of the Hα line plotted versus SDSS measures.

Simulation

Before proceeding in the analisys of the $\sigma_{gas} - \sigma_{star}$ relation we asked ourselves how should be the σ measured after subtracting the stellar continuum with a PCA respect to the ones measured subtracting a continuum with a linear fit, to test conclusively the goodness of our stellar continuum subtraction.

To perform this test, we built a simulation in which we imposed an absorption line to an emission line.

We fixed the σ, λ, flux of the emission line, and we simulated five different series of 100 absorption lines.

These absorption lines had a σ that could deviate from that of the emission line with a normal distribution, and their fluxes was fixed to be in proportion to the flux of the emission line of, respectively, $1:2$, $1:5$, $1:7$, $1:10$, $1:15$.

We simulated the noise using a normal distribution with mean value of 0.6, that is a mean value of the noise of the spectra we effectively used. The emission and absorption lines were convolved with an instrumental dispersion σ_{inst} of 1.5 Å, that is a tipical value for our spectra.

We performed this test three times, using an emission line, respectively:

- with $\sigma = 6.$ Å and a flux of 450 [10^{-17} erg s^{-1} cm^{-2} Å^{-1}]
- with $\sigma = 1.5$ Å and a flux of 110 [10^{-17} erg s^{-1} cm^{-2} Å^{-1}]
- with $\sigma = 1.5$ Å and a flux of 25 [10^{-17} erg s^{-1} cm^{-2} Å^{-1}]

In this way we can observe the influence of a stellar feature on a strong line, with a high flux and a value of σ well far from the resolution limit, and for emission lines at the SDSS resolution limit, both with an high and a low flux.

We performed the fit of the resulting lines with a single Gaussian. Figures 2.13 and 2.14 show the results of our simulation.

Different colors refers to different series of absorption lines, as in the legend.

We plotted the relative difference $(\sigma_{obs} - \sigma_{em})/\sigma_{em}$ versus the σ_{abs}/σ_{em}, where σ_{obs} is the σ of the resulting line, while σ_{em} is the σ of the original emission line and σ_{abs} is the one of the absorption line.

What we see from our plots is that:

- if the line is strong and far from the resolution limits, only in the case of an absorption line with a flux comparable to that of the emission lines we notice a strong relative difference between the observed line and the original emission line.
- if the line is near the resolution limit of the spectrum but is still strong enought, we will measure a line σ greater than σ_{em} just if $\sigma_{abs} < \sigma_{em}$.
- if the line is both near the resolution limit and with a low flux, then we can measure a line σ greater than σ_{em} even if $\sigma_{abs} > \sigma_{em}$.

This is to point out that the behavior of our data in Figures 2.8 , 2.10 , 2.12 is what we expect.

In any case, even if we do have an amount of uncertanty in the measurement of our data via the Principal Component Analysis, we will see that this uncertantiy is lower than the intrinsic scatter in the $\sigma_{gas} - \sigma_{star}$ relation.

We conclude that our PCA measurement is of good quality, and we proceed in the calibration of the $\sigma_{gas} - \sigma_{star}$ relations.

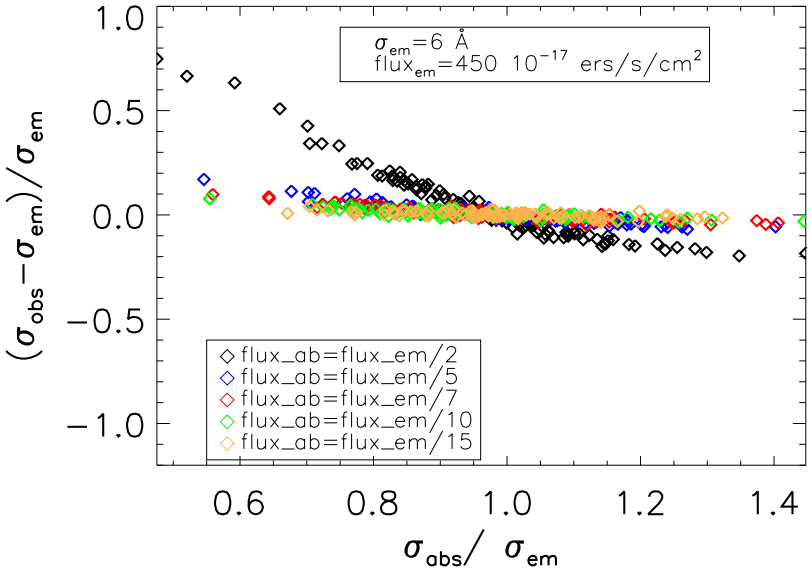

Figure 2.13: Relative difference $(\sigma_{obs} - \sigma_{em})/\sigma_{em}$ between the measured σ_{obs} of an emission line that is superimposed on an absorption line and the σ_{em} of the unabsorbed emission line, plotted versus the ratio σ_{abs}/σ_{em} of the σ_{abs} of the absorption line over the σ_{em} of the emission line (see text). The emission line is fixed to have a σ_{em} of 6 Å and a flux of 450 [10^{-17} erg s^{-1} cm^{-2}]. Different colors refer to 5 different series of simulated absorption lines, as in the legend. In each series of 100 simulation the absorption lines have a σ_{abs} that can deviate from σ_{em} with a normal distribution. Their fluxes are fixed to be in a ratio with the flux of the emission line of, respectively, 1 : 2 (black symbols), 1 : 5 (blue), 1 : 7 (red), 1 : 10 (green), 1 : 15 (orange).

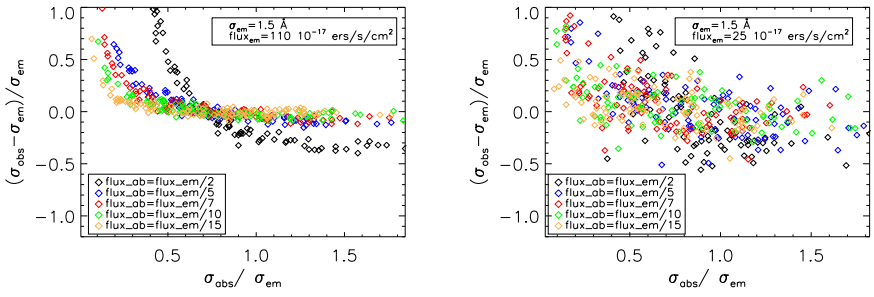

Figure 2.14: *Left*: The same as in Figure 2.13, with an emission line fixed to have σ_{em} =1.5 Å and a flux of 110 [10^{-17} erg s^{-1} cm^{-2}] *Right*: The same as in Figure 2.13, with an emission line fixed to have σ_{em} =1.5 Å and a flux of 25 [10^{-17} erg s^{-1} cm^{-2}]

2.4 The $\sigma_* - \sigma_{gas}$ relation

2.4.1 The sample selection and the methodology

We now want to compare the stellar and gaseous kinematics as traced by σ_*, $\sigma_{[OIII]}$, $\sigma_{[NII]}$ and $\sigma_{H\alpha}$.

Galaxies were selected to have a medium signal to noise S/N greater than 5, and a stellar velocity dispersion between 50 and 420 km s^{-1}. As already said, SDSS recommends to ignore measures of σ_* lower than 70 km s^{-1}, given that the instrumental resolution is $\sim$70 km s^{-1}, still, we decided to keep galaxies with σ_* >50 km s^{-1} to avoid selection effects (see discussion in Bernardi et al. 2008c and Hyde & Bernardi 2008).

Our final sample consist of about 2230 galaxies, with a maximum $\sigma_* \sim 380$, and with $0.002 < z < 0.27$. We want to point out again that the drastic reduction of the initial number of galaxies is principally due to the request to have galaxies with both emission lines and a measured σ_*.

In our sample the mean uncertainties represent, respectively, the 13% in the σ_*, as given by the Princeton reduction, while in our measurements we have a mean uncertainty of the 5% in the [NII] and Hα emission line width, and of the 13% in $\sigma_{[OIII]}$ measures.

We want to divide our resulting sample in AGN and Star Forming (SF) galaxies to test, if possible, if the mechanism that produce the large scatter in the $\sigma_* - \sigma_{[OIII]}$ relation found in previous studies really arise from the central engine of AGN.

Testing the influence of the choice of the diagnostic

We initially divided our sample in three subsamples according to their classification based upon their emission lines given by Princeton/MIT reduction .

Galaxies are classified as AGN if their fluxes are such that

$$\log([OIII]/H\beta]) > 0.7 - 1.2 * (\log([NII]/H\alpha) - 0.4) \tag{2.13}$$

as StarForming (SF) if

$$\log([OIII]/H\beta]) > 0.7 - 1.2 * (\log([NII]/H\alpha) - 0.4) \tag{2.14}$$

and as StarBurst (SB) if the EW of the Hα line was greater than 500 Å.

We asked ourselves if a different diagnostic could influence our subsequent results, since we compare the behavior of the relation in the three different subsamples; if different diagnostics define different subsamples even the results can differ.

Moreover, we know that the stellar continuum subtraction can be made using the PCA but also using synthetic stellar models; we want to investigate if these two methods can give slightly different vales of the flux, so influencing the diagnostic of galaxies.

To test this hypothesis we use the fluxes from the public Garching SDSS catalog, from the Princeton reduction and from the SDSS database.

Derived galaxy properties from the Garching emission line analysis (Kauffmann et al. 2003a; Brinchmann et al. 2004; Tremonti et al. 2004) can be found at http://www.mpa-garching.mpg.de/SDSS/DR4/.

In Garching database the stellar continuum subtraction is performed by fitting the emission line-free regions of the spectrum with a model galaxy spectrum computed using the population synthesis code of Bruzual & Charlot (2003).

As already said, the SDSS pipelines fit the stellar continuum using a median/mean filter. A sliding window is created of length 300 pixels for galaxies and pixels closer than 8 pixels to any reference line are masked. The remaining pixels in the filter are ordered and the values between the 40th and 60th percentile are averaged to give the continuum.

In the Princeton reduction, the stellar continuum subtraction is performed using a Principal Component Analysis technique.

The three data sets were matched, giving a total of 5100 galaxies; we will refer to these three samples of measure, for simplicity, as SDSS, Princeton and Garching data.

We plot in Figure 2.15 the ratio between [OIII] and Hβ fluxes versus the ratio of [NII] and Hα fluxes for the three sets of data, black for Garching, red for Princeton and green for SDSS.

To allow a better comprehension of the differences between the three data sets, we plotted all the data as a whole in the upper panel, to clearly show where the three plots disagree, while in the middle and bottom panels we show the Princeton, Garching and SDSS data separately.

As we see looking at the left edge of the data points in the upper panel, SDSS tend to measure higher ratio of [OIII]/Hβ and [NII]/Hα fluxes. This is what we expect, because, as we showed in the previous paragraph, not taking into account the stellar absorption gives emission lines weaker than the intrinsic ones; this effect will influence only lines that are superimposed to stellar features, as Hα and Hβ, while lines as [OIII] and [NII] will be almost unaffected. Consequently, Hα and Hβ fluxes in the SDSS data are lower than in Princeton and Garching reduction, and the ratio [OIII]/Hβ and [NII]/Hα are higher.

It is quite plain to explain even the behavior of SDSS data at the right end of the plot. The right "wing" of the figure seems narrower than in the cases of Princeton and Garching data, but this is because Hβ is a weak line and in consequence (see even Figure 2.14 and the discussion on the influence of stellar absorption on emission lines in the previous paragraph) much more affected by stellar absorption than Hα. So, we are just seeing that in SDSS data the ratio [OIII]/Hβ is much more enhanced than the [NII]/Hα ratio respect to the other two samples.

Overplotted in Figure 2.15 are the diagnostic adopted by Princeton (purple solid line) and the one elaborated by Kewley et al. (2006) (Equation 1) and 6) of Kewley et al. 2006, showed as the blue solid and dashed lines, respectively), so that galaxies are classified as Star Forming if

$$\log([\mathrm{OIII}]/\mathrm{H}\beta) < 0.61/[\log([\mathrm{NII}]/\mathrm{H}\alpha) - 0.05] + 1.3 \tag{2.15}$$

and as AGN if

$$0.61/[\log([\mathrm{NII}]/\mathrm{H}\alpha) - 0.47] + 1.19 < \log([\mathrm{OIII}]/\mathrm{H}\beta) \tag{2.16}$$

We consider first the problem of using different data, obtained with different methods of the stellar continuum subtraction, and using the same diagnostic; in this case, using the Kewley et al. diagnostic lead to small differences in the resulting subsamples of AGN and Star Forming galaxies.

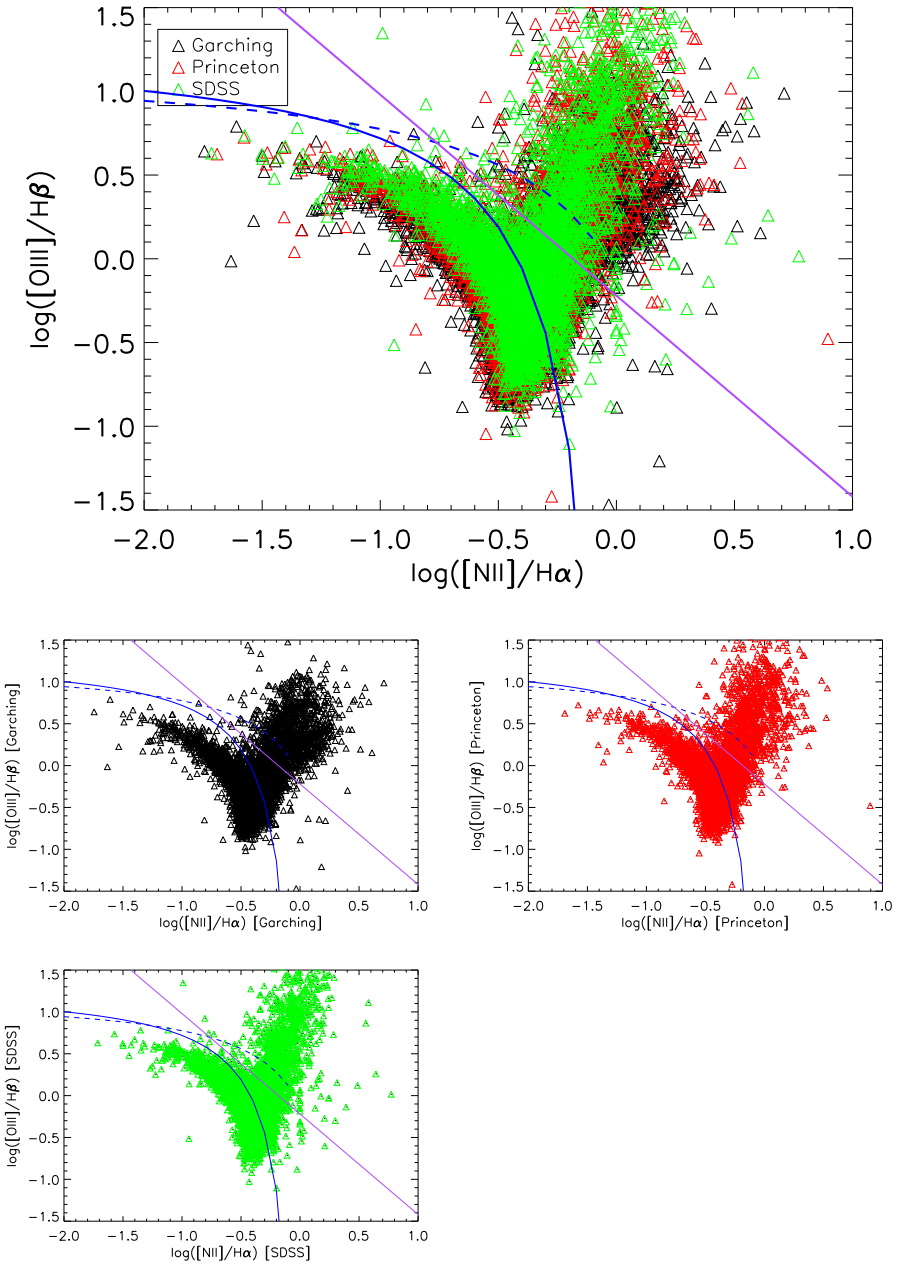

Figure 2.15: (*Upper panel*) We overplot the flux ratio of [OIII]/Hβ versus [NII/Hα] for Garching, Princeton and SDSS samples(see text); datapoints are represented by different colors, as in the legend, as black, red and green triangles. Purple solid line represent the diagnostic equation from the Princeton reduction (Equation 2.13) while the blue solid and dashed lines represent the classification from Kewley et al. (2003) (Equations 2.15 and 2.16). (*Middle panels*) Diagnostic diagram for Garching (left) and Princeton (right) data. (*Bottom panel*) Diagnostic diagram for SDSS sample. The purple solid line and the the blue lines represent the different classification as in the upper panel.

We have that 78% of the galaxies are classified as StarForming using the three different set of data, while the percentage reach the 97% when looking at galaxies that are classified as StarForming using just Princeton and Garching data.

In fact the SDSS data, measured after a continuum subtraction that don't take into account the stellar absorption features, are the ones that deviates more from the intrinsic fluxes.

Besides, we have that 82% of the galaxies share the AGN classification using the Princeton and the Garching data; Garching data give a bigger sample of AGN; even if its stellar continuum subtraction methods gives [OIII]/Hβ ratio lower than in Princeton reduction –and so galaxies should migrate from the AGN locus toward the transition locus– the Princeton reduction find a number of galaxies with Hβ negative flux –so, it finds Hβ in absorption.

Anyway, we can say that if we use Princeton reduction we will maybe miss a certain percentage of galaxies, but we will not have mismatched AGN respect to the Garching reduction.

We consider now the problem to use different diagnostics. We will refer to these two diagnostic as the Kewley and the Princeton diagnostic, for simplicity.

Using the same data (the Princeton reduction) we have that the Princeton diagnostic gives a 20% more AGN classified galaxies than the Kewley diagnostic, and this is evident from Figure 2.15, since the purple line –the Princeton diagnostic– is lower respect to the blue dashed line –the Kewley diagnostic.

In consequence, we have also a greater number of galaxies classified as StarForming, included a certain number of transition objects.

Since we are seeking both to find the best $\sigma_* - \sigma_{gas}$ relation *and* to understand the mechanism that cause the huge scatter in the relation, and since we want to compare the behavior of the relation in different samples of galaxies to have a hint on the possible involvement of the active nucleus , we decided to use the Kewley et al. (2006) classification, using the fluxes as given in the Princeton reduction.

With this diagnostic we will also be able to define a fourth sample, formed by the so called *transition* object, that we will refer to, from now on, as the TR sample.

The regression method

We will fit the data in the differents subsamples with the IDL code *sixlin.pro*, adapted from the FORTRAN program (Rev. 1.1) supplied by Isobe et al. (1990). This program allow the user to compute linear regression using each of the following methods:

1. Ordinary Least Squares Y vs. X (OLS Y|X) (c.f. linfit.pro)
2. Ordinary Least Squares X vs. Y (OLS X|Y)
3. Ordinary Least Squares Bisector (OLS Bisector)
4. Orthogonal Reduced Major Axis (OR)
5. Reduced Major-Axis (RMA)
6. Mean ordinary Least Squares

In the OLS (Y|X) the regression line is defined to be that line which minimize the sum of the square of the Y residuals. The inverse of OLS (Y|X), OLS (X|Y), minimize the sum of the square of the Y residuals.

To avoid specifying which is the "dependent" and indipendent" variable – for example when one is seeking the relation that lay upon two parameters, and it is not interested just in deriving one parameter from the other– there were proposed methods that treat the two variables symmetrically. The OLS Bisector is the line that bisect OLS (Y|X) and OLS (X|Y), while a second method use the geometric mean between OLS (Y|X) and OLS (X|Y), and it is the RMA. A third method gives the line that minimize the sum of the square of the perpendicular distances between the data points and the line, and it is the OR.

Since in our sample the intrinsic scatter of the data is much larger than uncertanties due to the measurements process, these 5 methods will give regression coefficients that are *theoretically* different (see Isobe et al. 1990).

In this case, the "right" choice does depend to what we are looking for. Since each method has its own advantages and disadvantages, and is more or less accurate in estimating its theoretical value, we decided to use all the methods that treat the two variables symmetrically, namely, the OLS Bisector and the OR and RMA methods.

Our subsequent discussion will take into account results from each of these three methods, but we anticipate that ours conclusions will not change depending on the regression method used.

A special discussion with regard to the intrinsic scatter in the relation. To this aim, we must fit $\langle \sigma_* | \sigma_{gas} \rangle$ using something like OLS Y|X, rather than treating the two variables symmetrically. In this case, we do *not* care about the actual value of the slope (unless it is very shallow), but we do care about the scatter. The relation with the smaller scatter is the preferred indicator of σ_*. However, we cannot really use OLS Y|X from Isobe et al because they do *not* allow one to include the effects of measurement error. To remove the bias from measurement error, we use the method in the Appendix of Tundo et al. (2007). This accounts for the measurement errors in both σ_* and σ_{gas}.

Now we can proceed in the analisys of the relation between the gas and stellar kinematics.

$\sigma_{[OIII]}$, $\sigma_{H\alpha}$, $\sigma_{[NII]}$ were transformed in km s^{-1} applying

$$\sigma[\text{km s}^{-1}] = c \times \frac{(\frac{\sigma}{\lambda_{line}} + 1)^2 - 1}{(\frac{\sigma}{\lambda_{line}}) + 1)^2 + 1} \tag{2.17}$$

were c is the velocity of light and λ_{line} is the wavelength of the line. This equation take into account relativistic effects; however, since in our sample $\sigma/\lambda_{line} << 1$, these don't change in any way our results, and we could have used as well the non relativistic equation $\sigma[\text{km s}^{-1}] = c \times \sigma/\lambda_{line}$.

Fist of all, we show that SF and SB galaxies have the same behavior respect to the $\sigma_* - \sigma_{gas}$ relation; in Figures 2.16 and 2.17 we see the best fit relations from the OLS Bisector, OR and RMA regression methods in the SF and SB galaxies using the three emission lines.

Blue triangles represent the SF galaxies, and light blue triangles represent SB galaxies. In each figure, the overplotted lines represent the best fit relations from the OLS Bisector (solid lines), OR (dotted lines) and RMA (dot-dashed

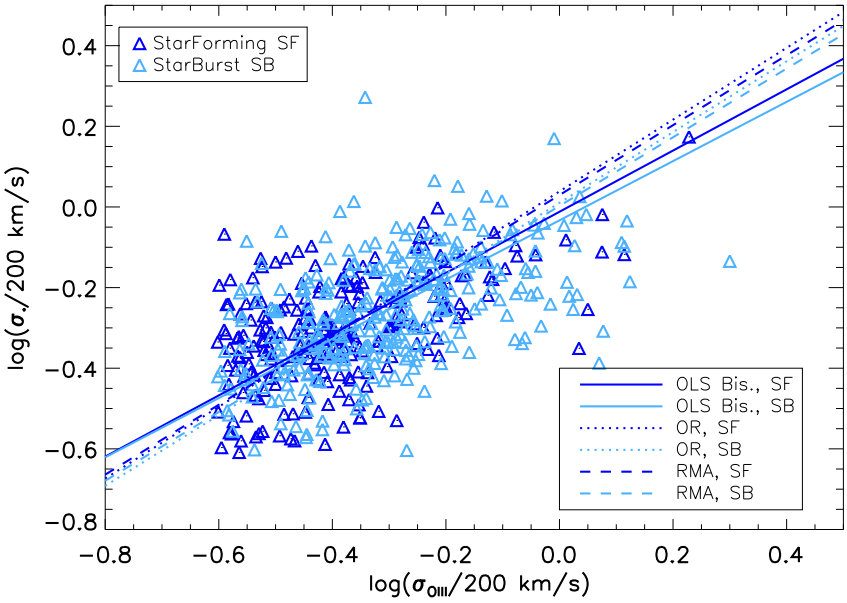

Figure 2.16: We compare the stellar velocity dispersion σ_* with the [OIII] line σ . Different colors refer to different class of objects. As in the legend, blue triangles are SF galaxies, and light blue triangles are SB galaxies . The lines overplotted represent the best fit of the $\sigma_* - \sigma_{[OIII]}$ relation from the OLS Bisector (solid lines), OR (dotted lines) and RMA (dot-dashed lines) regression methods. For each method, the blue line is the best fit in the SF sample and the light blue line is for the SB sample.

lines) regression methods. For each method, the blue line is the best fit in the SF sample and the light blue line is for the SB sample.

We summarize the best fit parameters of the relations showed in the previous plots in Table 2.4.1.

Table 2.1: Zero point and slope of the $\sigma_* - \sigma_{gas}$ relation in the SF and SB samples.

	OLS Bisector		**OR**		**RMA**	
	zero point	**slope**	**zero point**	**slope**	**zero point**	**slope**
			σ_* - $\sigma_{[OIII]}$			
SF	0.04±0.02	0.89± 0.04	-0.01± 0.03	0.76± 0.08	0.03± 0.02	0.86± 0.1
SB	0.01±0.02	0.87± 0.04	-0.03± 0.03	0.73± 0.08	0.002± 0.02	0.85± 0.09
			σ_* - $\sigma_{[NII]}$			
SF	0.02± 0.02	0.86± 0.04	-0.15± 0.02	0.77± 0.06	0.01± 0.02	0.85± 0.06
SB	0.02± 0.01	0.90± 0.04	0.002± 0.02	0.84± 0.05	0.02± 0.01	0.89± 0.07
			σ_* - $\sigma_{H\alpha}$			
SF	0.03± 0.02	0.87± 0.04	-0.0008± 0.03	0.78± 0.07	0.03± 0.02	0.86± 0.07
SB	0.02± 0.02	0.89± 0.04	0.004± 0.02	0.82± 0.06	0.02± 0.01	0.88± 0.07

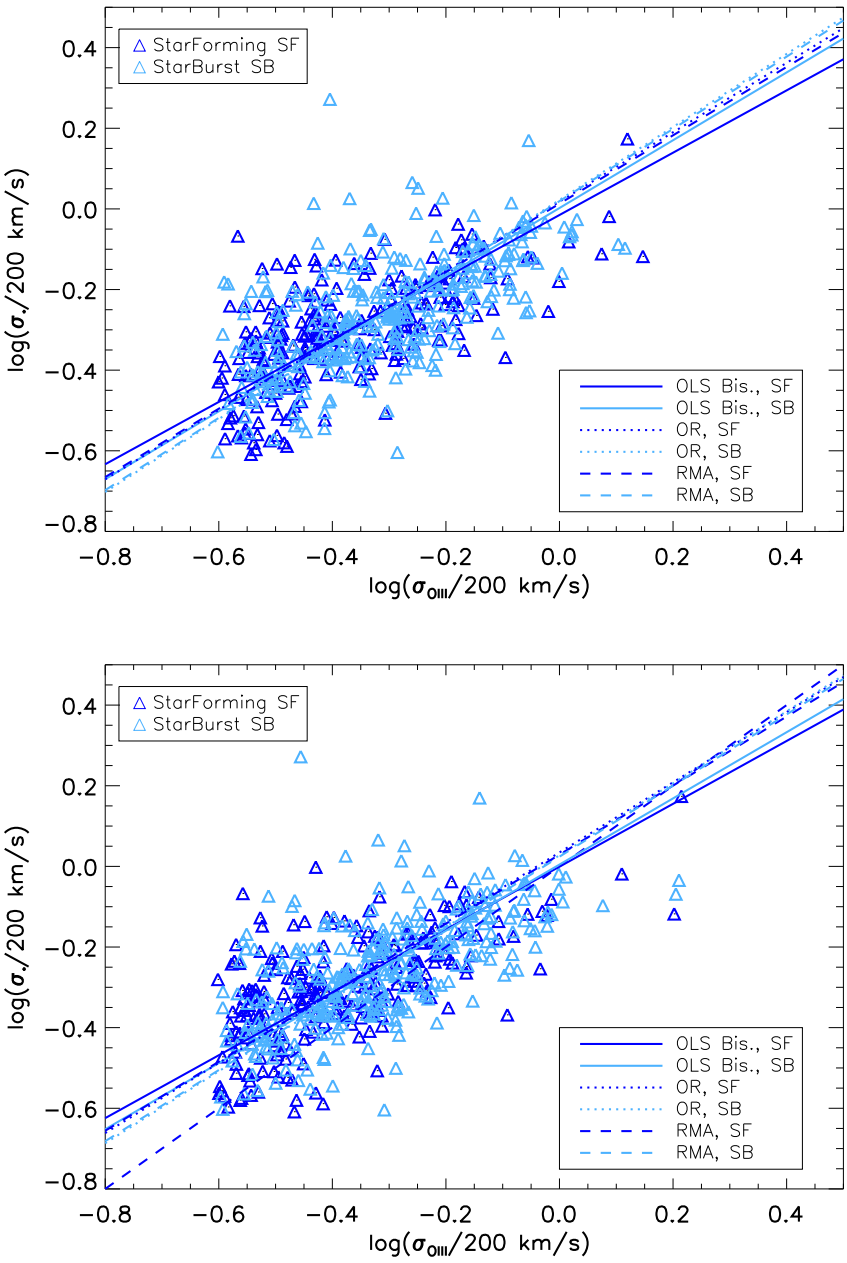

Figure 2.17: The same as in Figure 2.16, using the [NII] emission line (upper panel) and the Hα emission line (bottom panel).

Table 2.2: Ratio of stellar velocity dispersion to that of gas: $\langle \sigma_* / \sigma_{gas} \rangle$

Line	AGN	SF	TR
[OIII]	1.05± 0.01	1.18± 0.01	1.13± 0.02
Hα	1.08± 0.01	1.20± 0.01	1.15± 0.01
[NII]	1.05± 0.01	1.17± 0.01	1.10± 0.01

We notice that slopes and zero points in SF and SB samples agree within uncertainties for each of the three methods separately. We decide consequently to classify galaxies as AGN, SF and TR, and to include SB galaxies in the SF samples.

2.4.2 σ_*/σ_{gas} and non-gravitational motions

One measure of how well σ_{gas} traces σ_* is the ratio σ_*/σ_{gas}. Green & Ho (2005) report that, if one uses [OIII] to estimate σ_{gas}, then this ratio equals unity provided one is careful about the asymmetry of the line shape.

But, as showed by Komossa et al. (2008), the blue asymmetry correlates with the ionization potential (IP) of the line used. Since this is one of the reasons we wish to study the Hα and [NII] emission lines in the first place, we have also used them to estimate $\langle \sigma_* / \sigma_{gas} \rangle$. Table 2.4.2 shows the average $\langle \sigma_* / \sigma_{gas} \rangle$ ratio over our AGN, SF and TR samples when [OIII], [NII] and Hα are used to estimate σ_{gas}.

Putting aside for a moment the TR galaxies, the value of σ_*/σ_{gas} in the SF population is the "unperturbed" value. Gas in these objects is sub-virial due to its dissipative nature that lead the gas to lay in a more flattened distribution than stars (Gaskell 2009; Rice et al. 2006; Phillips et al. 1986). However, when the central engine is activated, several non-gravitational effects can accelerate the gas: compact radio jets, small-scale radio jets (e.g., Whittle 1992c found a correlation between [OIII] line width and radio luminosity), outflows, radiation pressure, tidal distortions. This increases σ_{gas}, thus decreasing σ_*/σ_{gas}. In this picture, Greene $ Ho's (2005) finding that $\sigma_* - \sigma_{[\mathrm{OIII}]}$ correlates with the Eddington ratio indicates that as the accretion rate on the central SMBH increases, so does the acceleration of the gas.

2.4.3 The $\sigma_* - \sigma_{gas}$ relation

We now transport our measures in a logarithmic system centered on 200 km s^{-1}. So, in the following, the $\sigma_* - \sigma_{gas}$ relation is actually a $\log(\sigma_*) - \log(\sigma_{gas})$ relation.

Since emission lines with different ionization potentials and different critical densities should have different widths (de Robertis & Osterbrock 1986), what we are really interested in, is the slope of the relation between σ_{gas} and σ_*.

In Figures 2.18 and following we show the relation between stellar and gaseous kinematics. Different symbols refer to different class of objects. As in the legend, red diamonds are AGN, blue triangles are Star Forming galaxies and green asteriscs are Transition galaxies, as explained above. The overplotted lines show the best fit relation from the OLS Bisector regression method (red

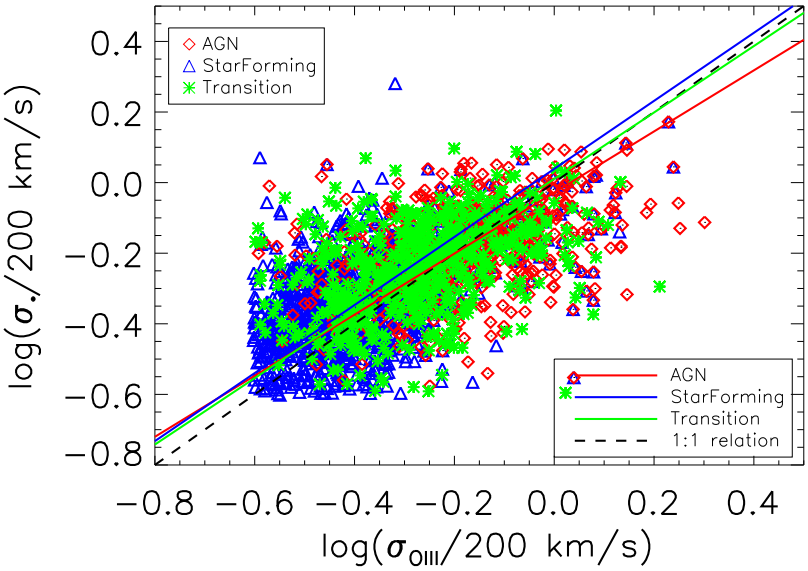

Figure 2.18: We compare the stellar velocity dispersion σ_* with the [OIII] line σ . Different symbols refer to different class of objects. As in the legend, red diamonds are AGN, blue triangles are Star Forming galaxies and green asteriscs are Transition galaxies (see text). The solid lines overplotted represent the best fit of the $\sigma_* - \sigma_{[OIII]}$ relation using the OLS Bisector regression method, performed using different subset of data, red for AGN, blue for Star Forming and green for Transition. The black dashed line represent an unitary relation, shown for comparison.

for the AGN sample, blue for the StarForming and green for the Transition sample). We show just the result from this method for simplicity. All the best fit parameters of the fitted relation from the three regression methods are shown in Table 2.4.3. The black dashed line represent an unitary relation, shown for comparison.

Figure 2.19 shows σ_* versus $\sigma_{H\alpha}$ and $\sigma_{[NII]}$.

It is evident that the rejection of galaxies with σ <50 km/s (both stellar and gaseous) resulted in a sharp cut in Figures 2.18 and 2.19. This cut affects mostly the SF galaxies, since TR and AGN usually have greater values of σ_{gas}. We tested, in fact, that using the OLS Bisector, the OR and RMA, the slope and zero points in the AGN and TR samples remain almost unchanged within uncertainties.

The slope in the SF sample, on the other side, become steeper; nevertheless we observe that values of σ <50 km/s usually have higher values of uncertainties than values above that limit, and that the uncertainties on slope and zero point of the best fit relation become larger than 100% the value itself of the parameters.

We show in Figure 2.20 how the SF sample is distributed in a $\log(\sigma_*) -$

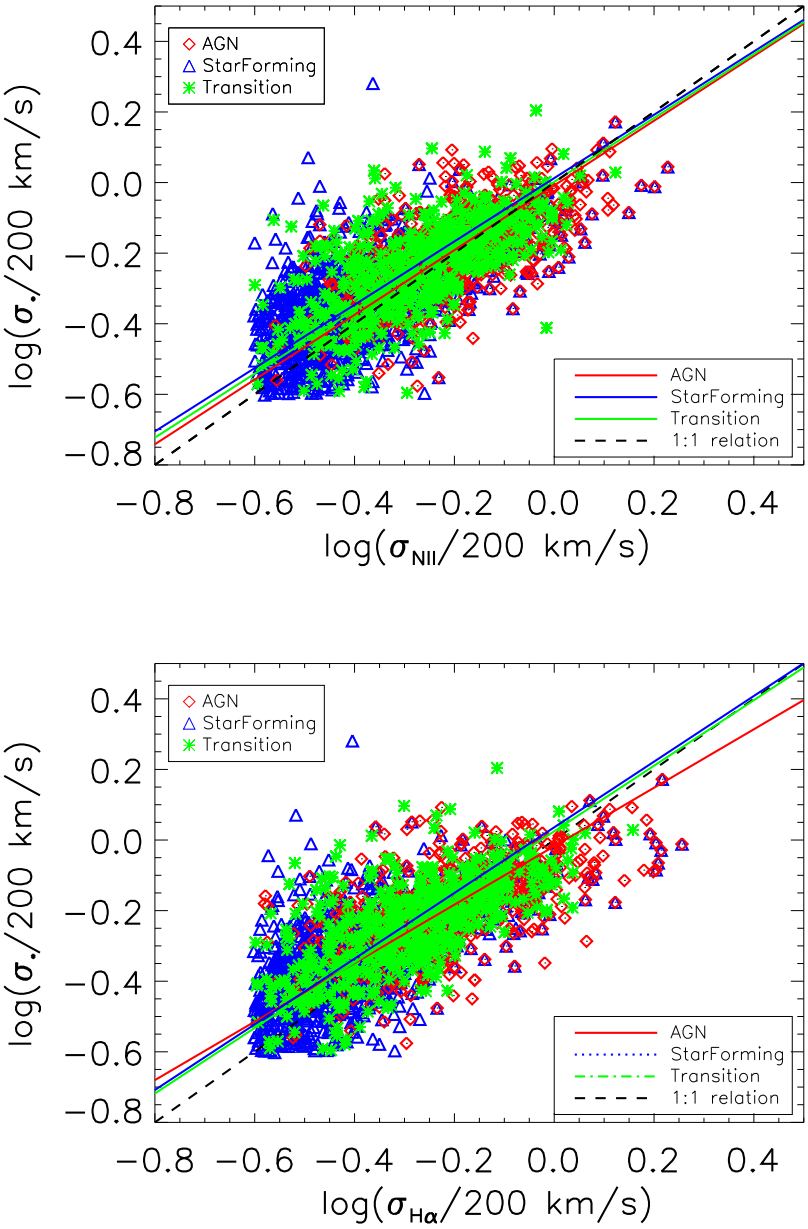

Figure 2.19: As in Figure 2.18 but plotting [NII] (upper panel) and Hα (lower panel) line σ.

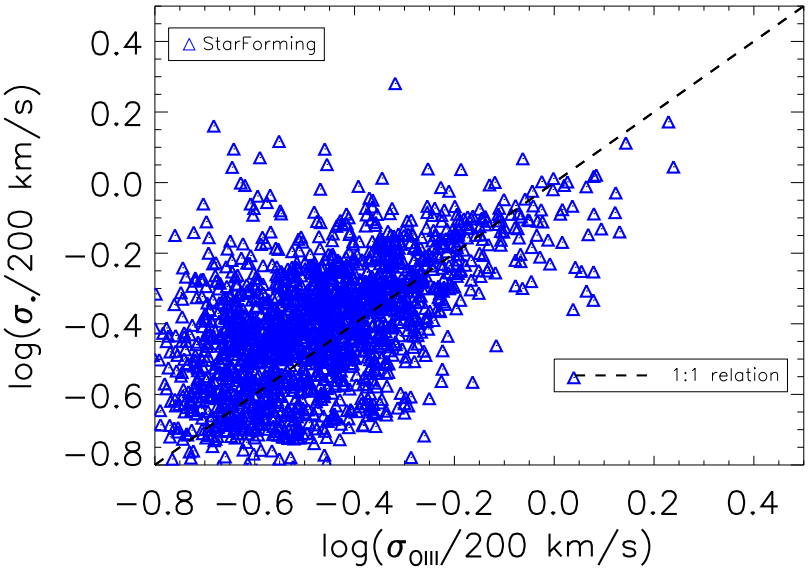

Figure 2.20: σ_* versus the [OIII] line σ for the SF sample when galaxies with σ <50 km/s are not removed. The black dashed line is an unitary relation, shown for comparison.

$\log(\sigma_{[OIII]})$ when we do not remove galaxies with σ <50 km/s.

So, the cut in both stellar and gaseous σ=50 km/s, in our opinion, just exclude galaxies for which the measures are unreliable.

In Figures 2.21 and 2.22 we show the normalized distribution of the residuals of the data with respect to the OLS Bisector relation. We show in Figure 2.21 the distribution in the AGN sample, for the three different emission lines, shown as the red line ([OIII]), the green line ([NII]) and the blue line (Hα).

We see that [OIII] shows the broadest distribution, so confirming the higher amount of scatter in the $\log(\sigma_*) - \log(\sigma_{[OIII]})$ for the AGN sample respect to the [NII] and Hα emission lines.

Figure 2.22 show the residual distribution for the TR sample (upper panel) and for the SF sample (bottom panel), with the same color code as in Figure 2.21. We notice that even in the TR sample the [OIII] shows the broadest distribution, while in the SF sample the differences between the three distributions are smaller. We will return on this point later in the Chapter.

In order to compare in a consistent way the robustness of the correlations using the three lines and in different samples, we computed the scatter of the data points with respect to the three fits using the OLS Bisector, OR and RMA method, as the standard deviation of $\sigma_* - \sigma_{fit}$ (note that we are using logarithmic quantities, actually), where σ_{fit} is the predicted σ_* value given the σ_{gas}, and the Pearson correlation coefficient in each case . We summarize these parameters in Table 2.3 .

As already said, each of the methods from Isobe et al. (1990) doesn't take

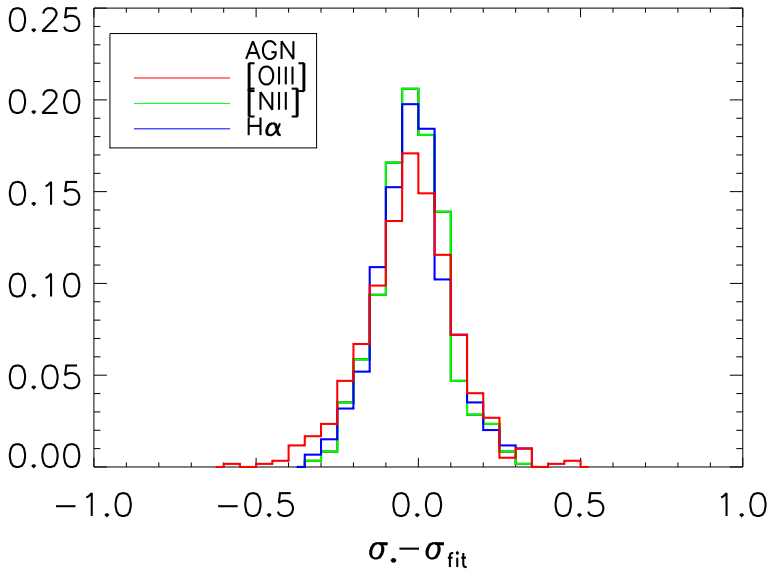

Figure 2.21: The normalized distribution of the residuals of the $\log(\sigma_*/200 \text{ km s}^{-1}) - \log(\sigma_{gas}/200 \text{ km s}^{-1})$ relation in the AGN sample, shown as the red ([OIII]), the green ([NII]) and the blue line (Hα).

into account measurements error in both coordinates, while the method in the Appendix of Tundo et al. (2007) do, so we computed the intrinsic scatter in Table 2.3 using our regression method.

The **Pearson correlation coefficient** r_P is defined by the equation

$$r_P = \frac{\Sigma_{xy}}{\Sigma_x \cdot \Sigma_y} \tag{2.18}$$

where $\Sigma_{xy} = \frac{1}{n}\Sigma(x_i - x)(y_i - y)$, and Σ_x and Σ_y represent the standard deviation for x and y datapoints. sono le deviazioni standard dei punti. This definition is equivalent to the following:

$$r_P = \frac{\Sigma xy - \frac{\Sigma x \Sigma y}{n}}{\sqrt{(\Sigma(x^2) - \frac{(\Sigma x)^2}{n})(\Sigma(y^2) - \frac{(\Sigma y)^2}{n})}} \tag{2.19}$$

Pearson correlation coefficient varies in the range [0,1], from a totally random distribution to a perfect linear relation. The r_P coefficient has a statistic distribution; we report this distribution to a normal one using a Fisher trasformation, described by the following:

$$z' = \frac{1}{2}[ln(1 + r_P) - ln(1 - r_P)] \tag{2.20}$$

In this way the standard deviation associated to the Pearson coefficient is simply given by

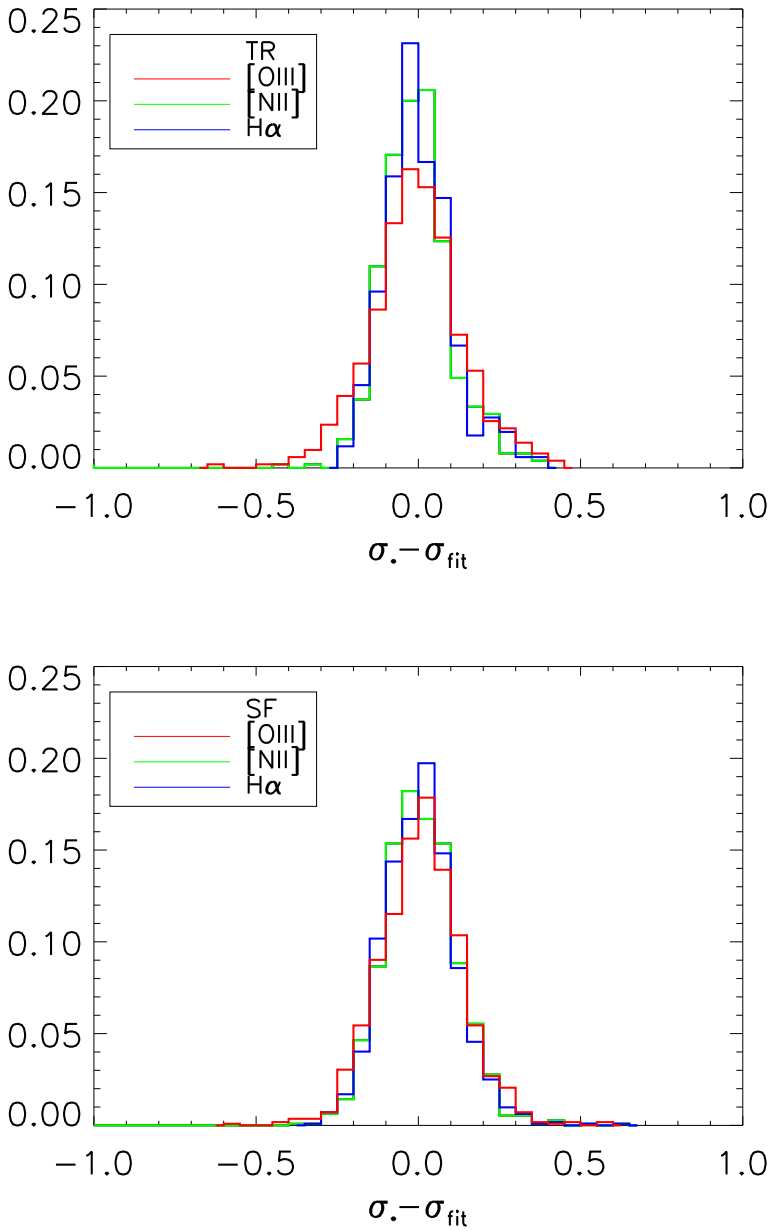

Figure 2.22: The same as in Figure 2.21 for the TR sample (upper panel) and the SF sample (bottom panel).

$$\sigma_{z'} = \frac{1}{\sqrt{n-3}} \tag{2.21}$$

In this way it is possible to compare the robustness of the correlation using different datasets, as in our case.

Looking at the results in Table 2.4.3 and 2.3 we notice that, as reported in previous studies, a correlation between the [OIII] and the stellar σ does exist. The correlation found in our study agrees with the ones measured by other authors. E.g, Nelson & Whittle (1996) found a Pearson correlation coefficient of r_P =0.48 in their sample of Seyfert galaxies while we measure in our AGN sample a Fisher transformed of the Pearson correlation coefficient of r_P=0.44 Our findings agree with the results of Gaskell (2009) that, using an OLS Bisector regression, found that the empirical calibration formula

$$\log \sigma_{[OIII]corr} = (0.82 \pm 0.11) * \log \sigma_{[OIII]} + (0.74 \pm 0.02)$$

would put his AGN data on an 1:1 relation.

We observe that using the [OIII] and [NII]emission line the slope of the $\sigma_* - \sigma_{gas}$ relation is lower in the AGN sample than in the TR or SF sample, while this behavior is not present at all in the case of Hα.

Also, we notice that the slopes in the SF and TR samples are usually in agreement within uncertainties.

We find an high amount of scatter, but in the case of [NII] and Hα it is highly reduced respect to the one measured in the $\sigma_* - \sigma_{[OIII]}$ relation.

The same if we look at the intrinsic scatter measured using the method from Tundo et al. (2007) which take into account the measurements error. In fact, since the uncertainties in [OIII] measures are higher than that in [NII] and Hα measures, to assess the real extent to which one emission line could be a better tracer for the stellar velocity dispersion, one have to take into account how much of the dispersion of the data points is due to the measurements uncertainties.

Comparing the data we notice that:

- In the case of the [OIII] and Hα emission lines the slope in the AGN sample is lower than the slope in the SF sample and in the TR sample
- The slopes of the three samples using the [NII] emission line usually agree within uncertainties
- The slopes in the SF and TR samples usually agree within uncertainties for [NII] and hα lines.
- In the case of the [OIII] line the slope in the TR samples is intermediate between the slope of the SF sample and of the AGN sample.
- The scatter of the data points with respect to the various regression methods in each of the AGN, SF and TR subsamples are lower when using [NII] and Hα emission lines
- The intrinsic scatter measured via the method of Tundo et al. (2007) is lower using [NII] and Hα emission lines both in AGN and TR subsample with respect to that obtained using [OIII].

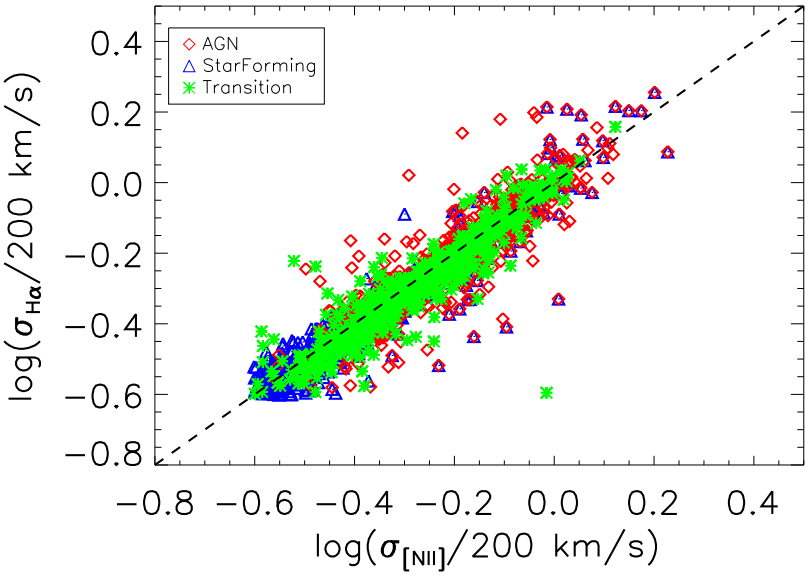

Figure 2.23: $\sigma_{H\alpha}$ values versus $\sigma_{[NII]}$ values. Colors and symbols are described in the legend: red triangles for the AGN sample, Blue triangles for the SF sample, and green asterisks for the TR sample. The dashed line represent an unitary relation, shown for comparison.

- The intrinsic scatter measured via the method of Tundo et al. (2007) is equal using [NII], Hα and [OIII] emission lines in the SF subsample.
- The Pearson correlation coefficient is higher using [NII] and Hα emission lines in each of the three subsamples.

We explore the hypothesis that the three lines does not describe the same kinematics comparing the three set of data.

In Fig. 2.23 we plot the Hα values versus the [NII] values; the dashed line represent an unitary relation, shown for comparison.

We notice that the values of $\sigma_{[NII]}$ are in good agreement with the measures of $\sigma_{H\alpha}$; the agreement between $\sigma_{[NII]}$ and $\sigma_{[OIII]}$ is good too (Figures 2.24, 2.25), but the scatter is higher.

We have that

$$\langle(\sigma_{[NII]} - \sigma_{H\alpha})\rangle = -0.009 \pm 0.0003 \qquad R_P = 0.91$$

$$\langle(\sigma_{[OIII]} - \sigma_{H\alpha})\rangle = 0.01 \pm 0.0005 \qquad R_P = 0.73$$

$$\langle(\sigma_{[OIII]} - \sigma_{[NII]})\rangle = 0.0006 \pm 0.0005 \qquad R_P = 0.74$$

in which R_P is the Pearson correlation coefficient.

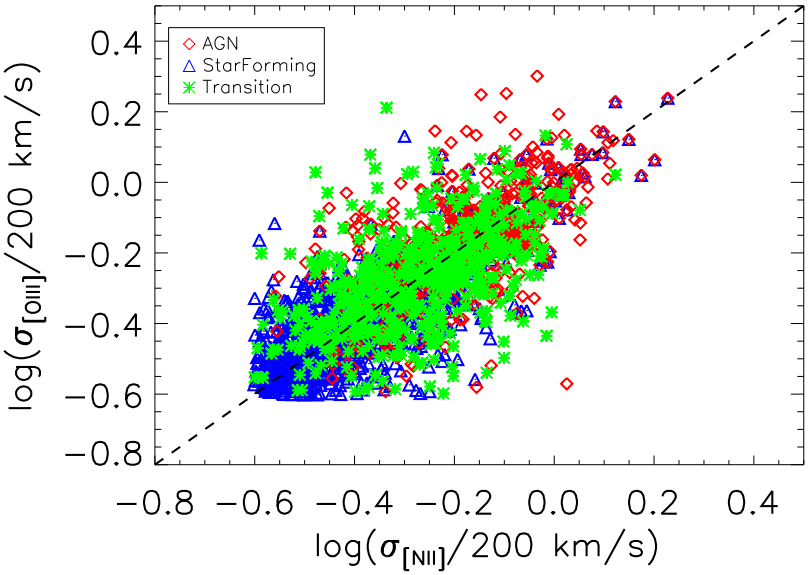

Figure 2.24: As in Figure 2.23, plotting $\sigma_{[OIII]}$ values versus $\sigma_{[NII]}$ values.

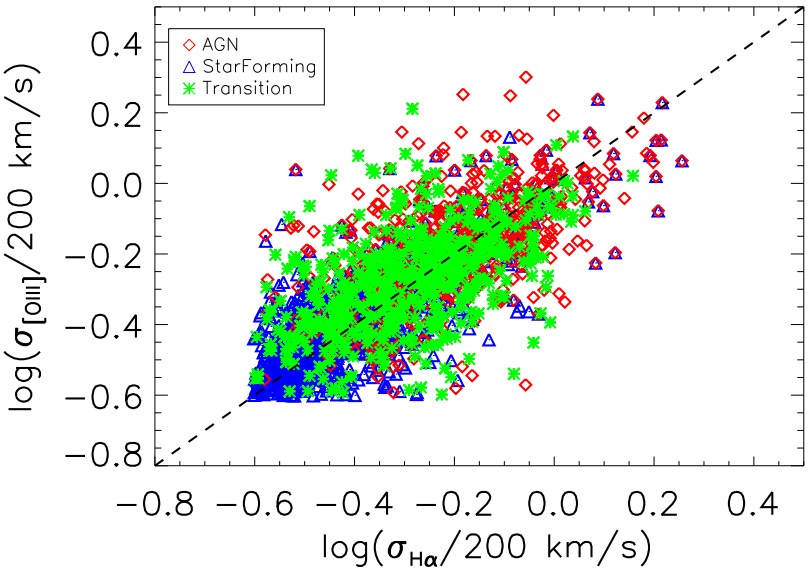

Figure 2.25: As in Figure 2.23, plotting $\sigma_{[OIII]}$ values versus $\sigma_{H\alpha}$ values.

	Σ_{OLS} (1)	Σ_{OR} (2)	Σ_{RMA} (3)	Σ_{Tundo} (4)	r_P (5)	z' (6)	$\sigma_{z'}$ (7)
σ_* - $\sigma_{[OIII]}$							
AGN	0.14	0.12	0.12	0.10	0.42	0.44	0.002
TR	0.13	0.13	0.13	0.07	0.55	0.61	0.001
SF	0.15	0.14	0.14	0.10	0.40	0.43	0.002
σ_* - $\sigma_{[NII]}$							
AGN	0.11	0.10	0.10	0.08	0.62	0.73	0.002
TR	0.12	0.11	0.11	0.06	0.64	0.77	0.001
SF	0.12	0.11	0.11	0.09	0.63	0.74	0.002
σ_* - $\sigma_{H\alpha}$							
AGN	0.11	0.10	0.10	0.09	0.60	0.69	0.002
TR	0.11	0.11	0.11	0.06	0.66	0.79	0.001
SF	0.11	0.11	0.11	0.08	0.67	0.81	0.002

Table 2.3: Parameters of the $\sigma_* - \sigma_{gas}$ relation in our samples. (1) Scatter using the OLS Bisector regression (2) Scatter using the OR regression (3) Scatter using the RMA regression (4) Scatter using the method in Tundo et al. (2007) (5) Pearson correlation coefficient (6) Fisher transformation (see text) (7) standard deviation relative to the Fisher transformation

So, the high correlation coefficient between $[NII]$ and Hα lines says that these two ionized gas are describing the same kinematics.

In the case of the [OIII] emission line, as already said in other works, we see that even if *in average* the ionized gas in the NLR *is* subject to the gravitational potential of the bulge, the non-gravitational effects of the central engine are, if not predominant, so important to dilute severely the correlation between $\sigma_{[OIII]}$ and $\sigma_{[NII]}$ and between $\sigma_{[OIII]}$ and $\sigma_{H\alpha}$.

Table 2.4: Best fit zero points and slopes for the $\sigma_* - \sigma_{gas}$ relation in our samples, given by OLS Bisector, OR and RMA regression methods.

	OLS Bisector		**OR**		**RMA**	
	zero point	**slope**	**zero point**	**slope**	**zero point**	**slope**
			σ_* - $\sigma_{[OIII]}$			
AGN	-0.02 ± 0.006	0.86 ± 0.02	-0.07 ± 0.01	0.62 ± 0.06	-0.03 ± 0.007	0.81 ± 0.09
TR	0.01 ± 0.009	0.94 ± 0.02	-0.02 ± 0.02	0.80 ± 0.08	0.003 ± 0.01	0.91 ± 0.10
SF	0.03 ± 0.009	0.96 ± 0.02	0.02 ± 0.01	0.92 ± 0.04	0.03 ± 0.01	0.96 ± 0.05
			σ_* - $\sigma_{[NII]}$			
AGN	-0.008 ± 0.006	0.92 ± 0.03	-0.01 ± 0.008	0.86 ± 0.04	-0.009 ± 0.006	0.91 ± 0.04
TR	0.001 ± 0.01	0.90 ± 0.06	-0.01 ± 0.03	0.84 ± 0.10	-0.0009 ± 0.02	0.89 ± 0.05
SF	0.01 ± 0.01	0.89 ± 0.04	-0.01 ± 0.02	0.83 ± 0.07	0.008 ± 0.01	0.89 ± 0.05
			σ_* - $\sigma_{H\alpha}$			
AGN	-0.01 ± 0.006	0.83 ± 0.02	-0.04 ± 0.008	0.70 ± 0.04	-0.02 ± 0.006	0.81 ± 0.04
TR	0.02 ± 0.009	0.93 ± 0.03	0.01 ± 0.01	0.89 ± 0.04	0.02 ± 0.009	0.92 ± 0.04
SF	0.03 ± 0.01	0.93 ± 0.02	0.01 ± 0.01	0.89 ± 0.03	0.03 ± 0.01	0.92 ± 0.04

Now we are interested in the physical reason of these findings. The answer to these questions will give us the possibility to single out the best tracer for the stellar velocity dispersion.

We started our investigation looking at the mean behavior of the data. In Figures 2.26 , 2.27 and 2.28 we show the mean values of σ_* in bin of, respectively, $\sigma_{[OIII]}$, $\sigma_{[NII]}$ and $\sigma_{H\alpha}$ for the various sample. In the upper left panel we show the data in the SF sample, and in the right upper panel the TR sample. In the lower panels we show, on the left, the mean values of σ_* in bin of σ_{gas} for the AGN sample, while in the right panel we see the mean values of σ_{gas} in bin of σ_* for the same sample. The black dashed line, representing an 1:1 relation, gives the feeling of how much the data deviates from an unitary relation.

We notice that in each case we pass through a situation, at lower σ_{gas}, in which the gas is subvirial, to a situation in which σ_{gas} tend to be greater than σ_*, around σ_{gas} $\sim$100 km s^{-1}.

In the AGN sample σ_{gas} reach higher maximum values respect to that in the SF and TR sample. This is expected as AGN occupy the higher part of the $\sigma_* - \sigma_{gas}$ relation (see Figures 2.18 ,2.19), while SF galaxies span a lower range of values.

Looking at Figures 2.26, 2.27 and 2.28 we see that, respect to [NII] and Hα, [OIII] shows values of σ that are more increased respect to σ_*. This is evident both in SF and TR sample, in which [OIII] show a greater number of galaxies with $\sigma_{gas} > \sigma_*$ respect to [NII] and Hα, and with an higher increase in value, and in the AGN sample, in which we see that $\sigma_{[OIII]}$ reaches higher values respect to $\sigma_{[NII]}$ and $\sigma_{H\alpha}$.

[NII] and Hα show a similar behavior (as it is expected since they are tightly correlated, see Figure 2.23). We still observe the mean values of σ_{gas} to deviate from the mean values of σ_*, but the amount of the deviation is smaller than in the case of the [OIII].

The plots in Figures 2.26, 2.27 and 2.28 show that the [OIII] emission line is not reproducing the stellar kinematics, and that even [NII] and Hα do show deviations from an unitary relation.

We observe also that in AGN and TR $\sigma_{[OIII]}$ at low σ_* have lower value respect to $\sigma_{[NII]}$ and $\sigma_{H\alpha}$. We see that below σ_* $\sim$100 km s^{-1} the mean value of $\sigma_{[OIII]}$ is almost independent from σ_*, remaining around a value of $\sigma_{[OIII]}$ $\sim$110 km s^{-1}, while [NII] and Hα still show a dependence from σ_* in the whole range of values.

We observe now the bottom right panels of Figures 2.26, 2.27 and 2.28. We plot the mean values of σ_* versus the mean values of σ_{gas} in the AGN sample. It is interesting that in this case the mean values appear to lay on the unitary relation, especially for [NII] and Hα emission lines.

This does not surprise us. We already know that $\langle\sigma_{gas}/\sigma_*\rangle$=1 within uncertainties in the AGN sample for each of the emission line, and we observe that in our samples the standard deviation of the datapoints are such that $\Sigma_x < \Sigma_y$ (with Σ_x and Σ_y being, respectively, the standard deviation of σ_{gas} and σ_*, and ρ being the correlation coefficient) so the theoretical slope given by the OLS (Y|X), for example (and for simplicity since it has a really simple expression) $\beta = \rho\frac{\Sigma_y}{\Sigma_x}$ will give, when using σ_* as independent variable, a slope greater than when used as dependent variable. We notice, nevertheless, that in this case the scatter in the relation is higher with respect to the scatter measured in the

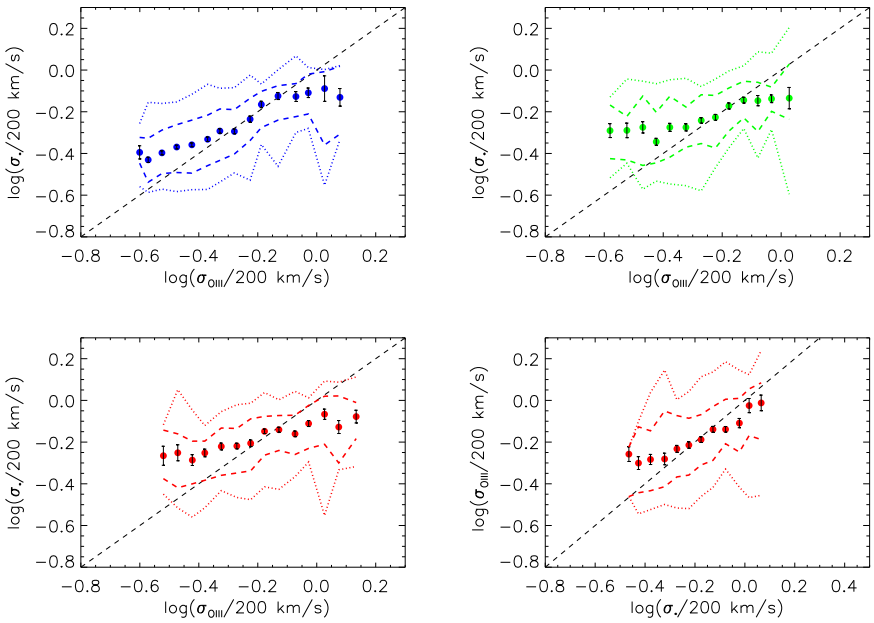

Figure 2.26: Mean value of σ_* data in bin of $\sigma_{[OIII]}$. The black dashed line represent an unitary relation. *Upper left*: SF sample. *Upper right*: TR sample. *Bottom left*: AGN sample. *Bottom right*: mean value of $\sigma_{[OIII]}$ in bin of σ_* in the AGN sample.

"direct" relation.

So, we want now to determine why there are these differences in the behavior of the $\sigma_* - \sigma_{gas}$ relation for the different subsamples, and for the different emission lines. For this reason, we considered the relative differences $\Delta\sigma/\sigma = (\sigma_* - \sigma_{gas})/\sigma_*$ versus the effective radius R_e and the inclination b/a, to explore the physical meaning of the relation and to search for possible secondary parameters in the relation.

The effective radius R_e and the inclination b/a are given by the SDSS database both for early (de Vaucouleur fit) and late type (exponential fit) galaxies; we retrieved, for each galaxy, the more appropriate value given its morphology.

In Figures 2.29, 2.30 and 2.31 we plot the mean values of the relative differences between gas and star velocity dispersion in bin of R_e and b/a, for the AGN, TR and SF sample. The dashed line represent the zero level for the relative difference.

We note that for the [OIII] emission line (Figure 2.29) the mean relative differences show a shallow trend with the effective radius, with bigger galaxies in AGN and TR samples having increasingly negative values of $\Delta\sigma/\sigma$.

When looking at the mean behavior of $\Delta\sigma/\sigma$ in bin of b/a, we do not observe any evident trend except that in the SF sample, with galaxies at lower b/a having increasingly negative values of $\Delta\sigma/\sigma$.

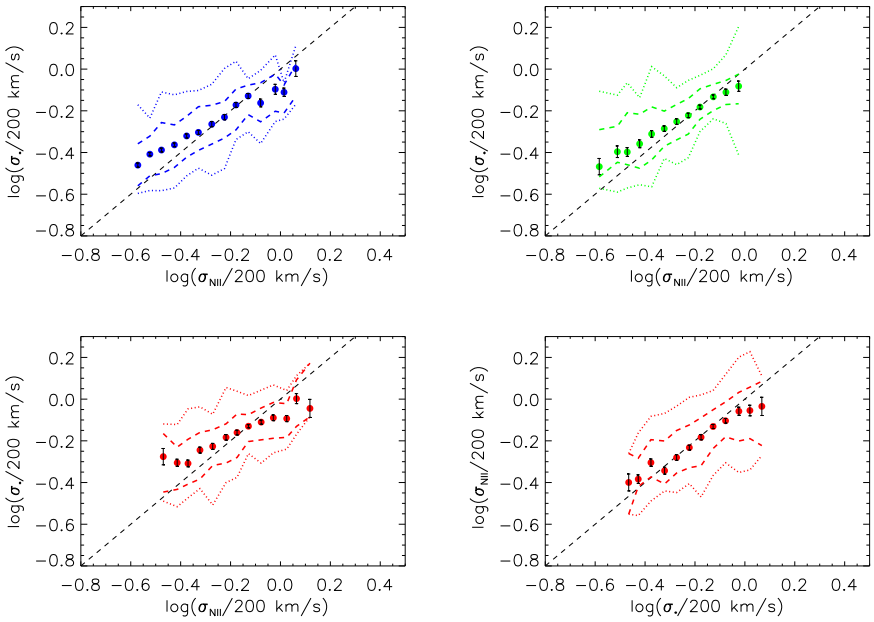

Figure 2.27: As in Figure 2.26 for [NII].

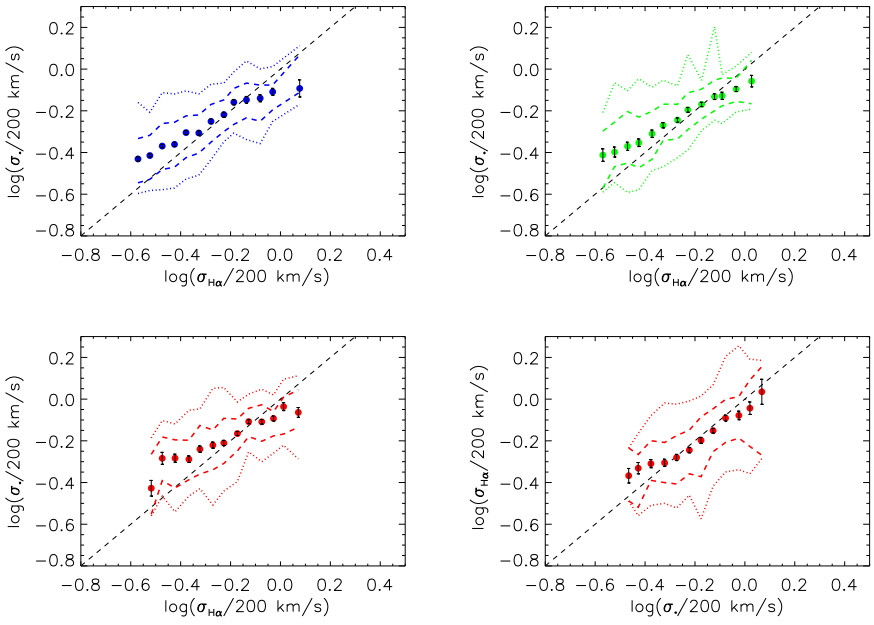

Figure 2.28: As in Figure 2.26 for Hα.

We also note that in the SF sample $\Delta\sigma/\sigma$ is usually lower than in the TR and AGN sample. We already know that from the study of the mean ratio of σ_*/σ_{gas}, that indicated how the gas in SF galaxies (and in TR, at a lower value) is usually subvirial.

From another point of view, we notice that $\sigma_{[OIII]}$ is enhanced in the AGN and TR sample with respect to the SF sample. We computed the mean value $\langle\Delta\sigma/\sigma\rangle$ of the relative difference in the three sample:

$$\langle\Delta\sigma/\sigma\rangle_{AGN} = 0.07 \pm 0.02$$
$$\langle\Delta\sigma/\sigma\rangle_{TR} = -0.002 \pm 0.02$$
$$\langle\Delta\sigma/\sigma\rangle_{SF} = -0.07 \pm 0.01$$

Using [NII] emission line we have:

$$\langle\Delta\sigma/\sigma\rangle_{AGN} = 0.01 \pm 0.02$$
$$\langle\Delta\sigma/\sigma\rangle_{TR} = -0.01 \pm 0.01$$
$$\langle\Delta\sigma/\sigma\rangle_{SF} = -0.06 \pm 0.01$$

While the mean value of the relative difference in the SF sample is at the same level than in the case of the [OIII], we notice that in the AGN the mean is slowly lower.

Using the Hα line we have:

$$\langle\Delta\sigma/\sigma\rangle_{AGN} = 0.003 \pm 0.01$$
$$\langle\Delta\sigma/\sigma\rangle_{TR} = -0.07 \pm 0.01$$
$$\langle\Delta\sigma/\sigma\rangle_{SF} = -0.10 \pm 0.01$$

Again, the mean value of the relative difference in the AGN sample (and, at a lower level, in the TR sample) are lower than in the case of the [OIII] emission line.

We do not observe, in the case of [NII] and Hα emission line, any trend of $\Delta\sigma/\sigma$ with the effective radius or with the inclination.

Now the fundamental question is which of the three tracers we are testing is better suited to be used as a proxy for the stellar velocity dispersion. Looking at the previous plots we started to think that [OIII] is not the best one of the three. But we need more tests to find an answer to our question. In fact, even if a relation has an high amount of intrinsic scatter, it can be safely used if the actual amount of the scatter is known.

In fact, consider two observables which we will call S, and s, with joint distribution $p(S, s)$. To make the discussion more concrete, suppose that this joint distribution is Gaussian, so that this distribution is completely specified by the means and variances of the two variables, and the cross-correlation coefficient $r_{\rm Ss}$. Then the distribution of S at fixed s is Gaussian with mean and variance

$$\langle S|s\rangle = \langle S\rangle + r_{Ss}\,\Sigma_S\,(s - \langle s\rangle)/\Sigma_s, \quad (2.22)$$
$$\Sigma^2_{S|s} = \Sigma^2_S\,(1 - r^2_{Ss}). \quad (2.23)$$

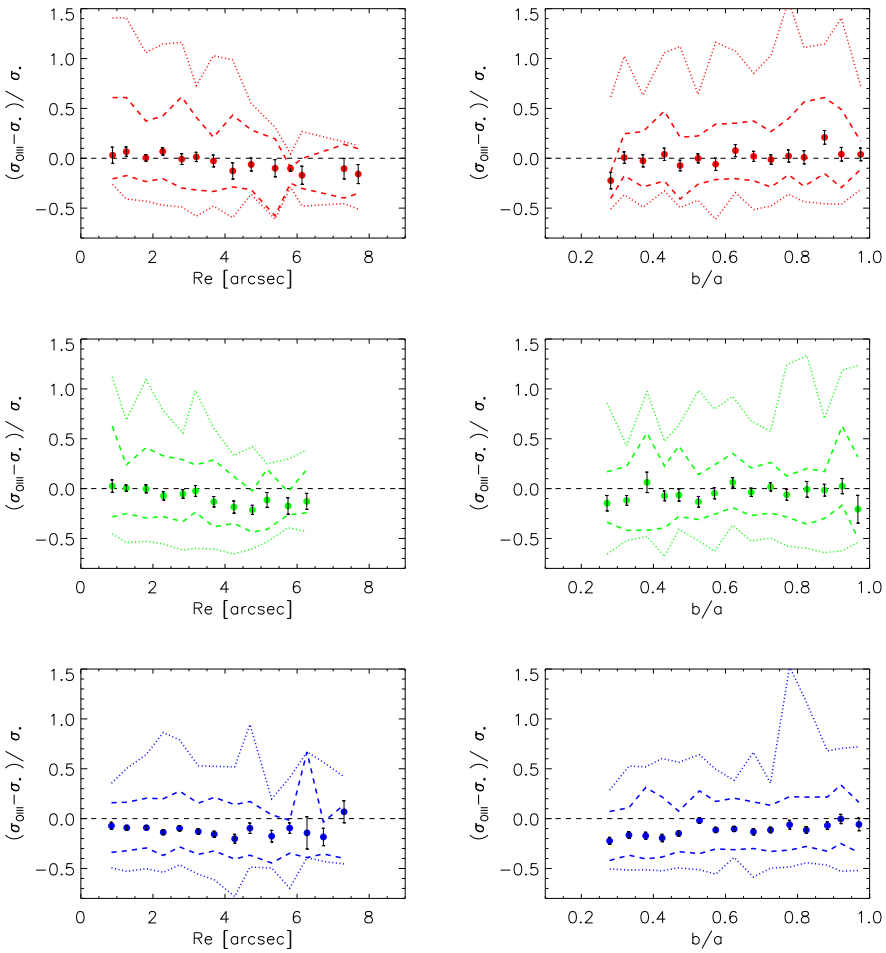

Figure 2.29: Mean value of the relative differences $(\sigma_{[OIII]} - \sigma_*)/\sigma_*$ in bin of the effective radius R_e (left panels) and of the inclination b/a (right panels) in the three samples. *Upper panels*: AGN sample. *Middle panels*: the TR sample. *Bottom panels*: the SF sample. The dashed line represent the zero level for the relative difference between gas and star velocity dispersion.

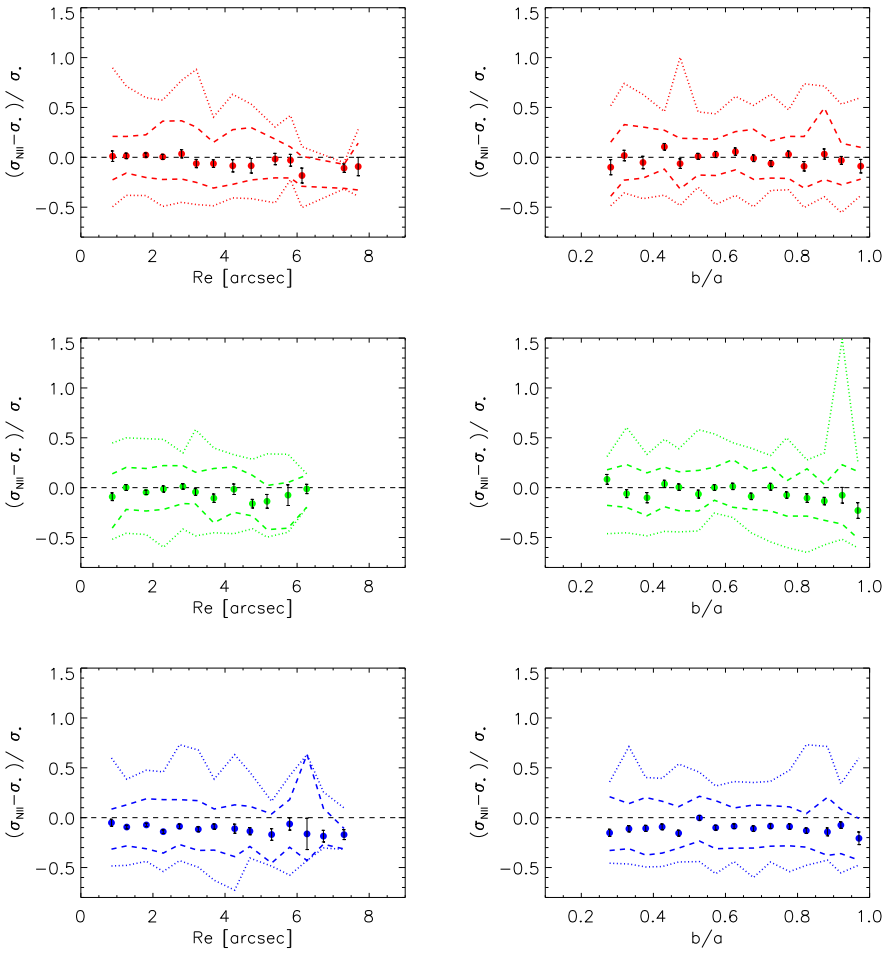

Figure 2.30: The same as in Figure 2.29 plotting the relative differences $(\sigma_{[NII]} - \sigma_*)/\sigma_*$

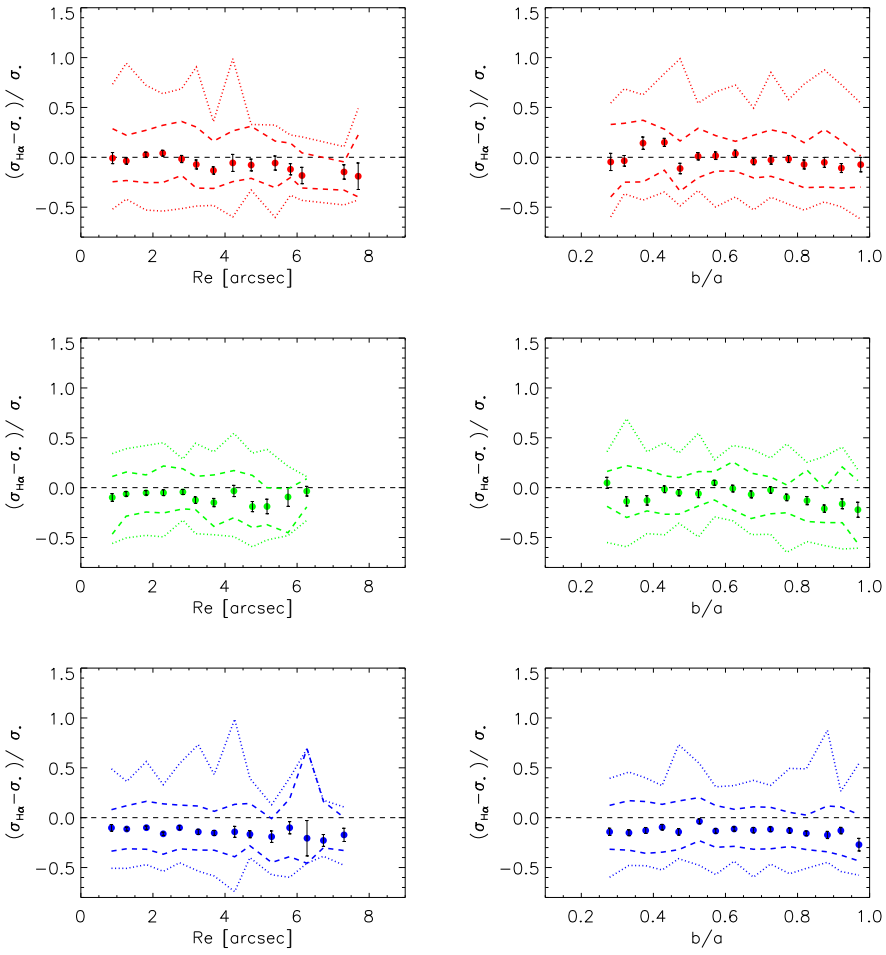

Figure 2.31: The same as in Figure 2.29 plotting the relative differences $(\sigma_{H\alpha} - \sigma_*)/\sigma_*$

Let $p_s(S)$ denote the result of predicting the distribution of S from the distribution of s by using $\langle S|s\rangle$ to change variables from $p(s)ds = p_s(S)dS$. Then $p_s(S)$ is a Gaussian centered on $\langle S\rangle$ with rms $= |r_{sS}|\Sigma_S$. Because this value will usually be smaller than Σ_S, we conclude that, in general, $p_s(S)$ will be more sharply peaked than the true $p(S)$ distribution.

In effect, the procedure just described ignores the scatter around the mean $\langle S|s\rangle$ relation. To include the effects of this scatter one must convolve $\phi(s)$ with the distribution $p(S|s)$ which has mean $\langle S|s\rangle$ and rms $\Sigma_{S|s}$:

$$\phi(S) \equiv \int ds\, \phi(s)\, p(S|s) \tag{2.24}$$

Provided $\langle S|s\rangle$ and $\Sigma_{S|s}$ are accurately known, it doesn't matter what s is, or how tightly correlated it is with S. That is to say, predicting the distribution of S from s using the expression above should give the same (correct) answer whatever emission line is used.

In Figures 2.32-2.39 we plot our data divided in bin of magnitude and in bin of σ_*.

Data were divided by their absolute magnitude and their σ_* values. In particular, the adopted bin in absolute magnitude are

- $M_r \leq$ -22
- -22 $\leq M_r \leq$ -21
- -21 $\leq M_r \leq$ -20
- $M_r \geq$ -20

while the bin in velocity dispersione were defined by

- $\sigma_* \leq$ -0.44
- -0.44 $\leq \sigma_* \leq$ -0.3
- -0.3 $\leq \sigma_* \leq$ -0.18
- $\sigma_* \geq$ -0.18

We remember again that we are actually working with logarithmic values reported to a system centered on σ =200 km s^{-1}.

These choice of bins in σ_* were made in order to have a similar number of objects in each bin.

Figure 2.32, upper panel, show the mean values of $\sigma_{[OIII]}$ in bin of b/a, divided by their values of absolute magnitude M_r, as in the legend.

In the other panels we plot the same data, but we show: in the middle left panel, the mean value of $\sigma_{[OIII]}$ in bin of b/a for the three AGN, TR and SF sample, represented by the red, green and blue symbols, and in the middle right, bottom left and bottom right panels, the mean value of $\sigma_{[OIII]}$ in bin of b/a divided by their values of M_r, respectively in the AGN, TR and SF sample.

We notice in Figure 2.32 (middle left panel) that AGN data have $\sigma_{[OIII]}$ higher than SF and TR, and TR galaxies have higher $\sigma_{[OIII]}$ than SF galaxies.

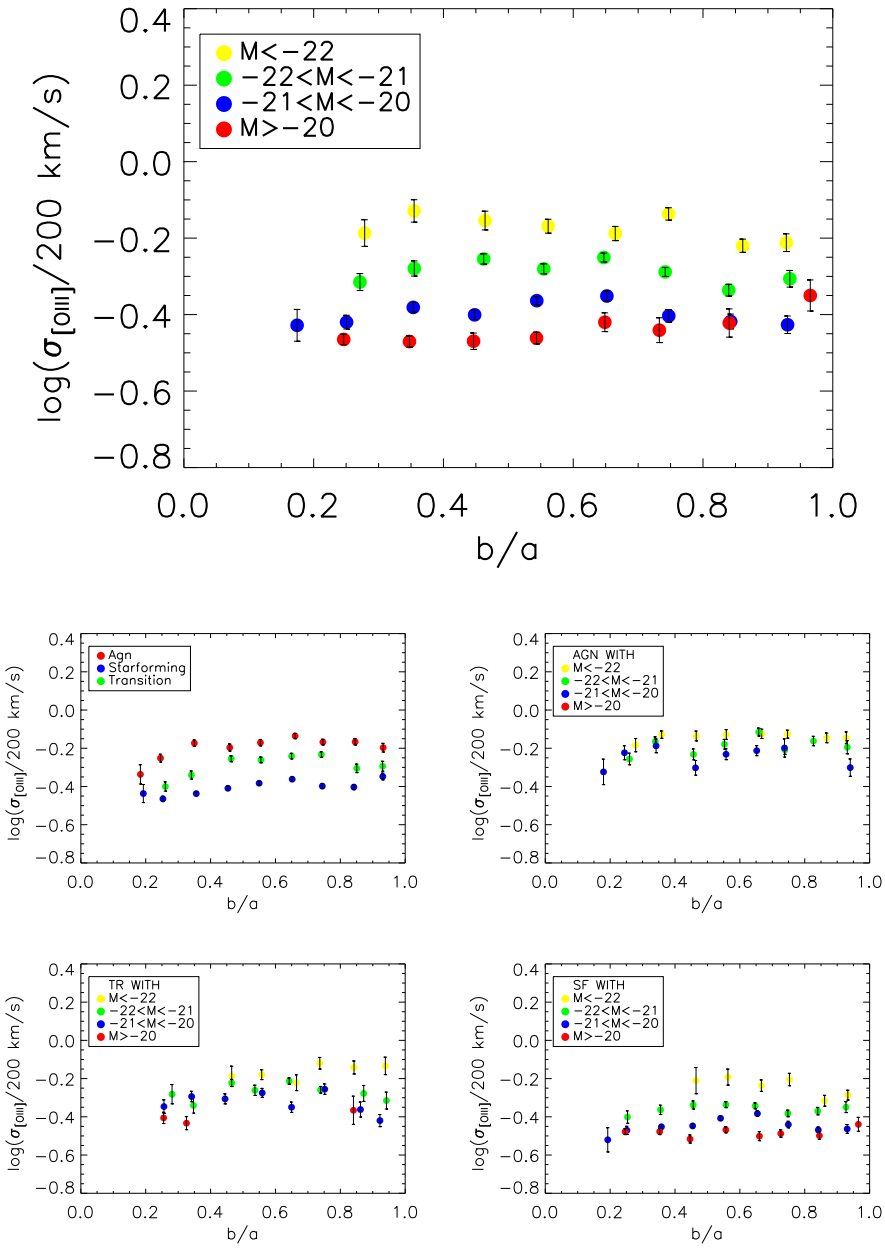

Figure 2.32: *Upper Panel*: $\overline{\sigma}_{[OIII]}$ in bin of b/a versus b/a. Yellow symbols represent galaxies with M_r <-22 mag, while green, blue, and red symbols represent galaxies with, respectively, -22< M_r <-21, -21< M_r <-20, and M_r >-20 mag. *Middle Left Panel*: the same data are plotted as in the upper panel, for AGN (red), SF (blue) and TR (green). *Middle Right Panel*: as in the upper panel, for the AGN sample. *Bottom Left Panel*: as in the upper panel, for the TR sample. *Bottom Right Panel*: as in the upper panel, for the SF sample.

Things get complicate when the sample is divided in magnitude bins, as we see in Figure 2.32. The mean values of $\sigma_{[OIII]}$ for more luminous –and consequently roughly bigger– galaxies tend to be higher, but we notice that in less luminous galaxies (with $M_r \geq$ -21 mag) the mean values of $\sigma_{[OIII]}$ almost overlap when the inclination is grater than b/a =0.6

So, big/luminous galaxies have bigger $\sigma_{[OIII]}$, and so have AGNs, while less luminous galaxies tend to have lower $\sigma_{[OIII]}$. Till now, nothin unexpected.

Nevertheless, when we look at the AGN data divided in bins of magnitude, as in Figure 2.32 middle right panel, we see that AGN of lower luminosity still have an high $\sigma_{[OIII]}$. In effect, while galaxies with a magnitude fainter than -21 mag show a mean value of $\sigma_{[OIII]}$ of $\sim$-0.4, AGN of the same luminosity show a mean value of $\sim$ -0.2

Even Transition galaxies show (Figure 2.32 bottom left panel) $\sigma_{[OIII]}$ values that are higher respect to those of galaxies of similar luminosity, but less markedly than in the AGN sample.

On the contrary, when we look at SF galaxies , we see that more luminous galaxies exhibit higher $\sigma_{[OIII]}$, and low luminous galaxies lower $\sigma_{[OIII]}$ as the whole sample do, and they do show an overlap of the mean values of $\sigma_{[OIII]}$ in less luminous galaxies. So, the AGN and TR samples have a $\sigma_{[OIII]}$ that is not correlated with magnitude –and hence, crudely, with mass.

We now explore the [NII] emission line behavior.

In Figure 2.33, upper panel, we show the mean value of $\sigma_{[NII]}$ versus b/a in bin of b/a, divided by their values of absolute magnitude M_r, as in the legend.

In the other panels we plot the same data, but we show: in the middle left panel, the mean value of $\sigma_{[NII]}$ in bin of b/a for the three AGN, TR and SF sample, represented by the red, green and blue symbols, and in the middle right, bottom left and bottom right panels, the mean value of $\sigma_{[NII]}$ in bin of b/a divided by their values of M_r, respectively in the AGN, TR and SF sample.

Even in this case we see, as expected, that the $\sigma_{[NII]}$ values for AGN are higer respect to the one of the SF and TR samples; this is expected, for a certain amount, since AGN tend to inhabit galaxies of higher masses.

As in the case of $[OIII]$ line, we see in Figure 2.33, middle right panel, that AGN of different luminosity shows similar mean $\sigma_{[NII]}$, while in the upper panel galaxies with lower luminosity have a lower mean value of $\sigma_{[NII]}$.

Looking at the behavior of SF galaxies in Figure 2.33, bottom right panel, we notice that in this case galaxies of different luminosity show differences in the mean value of $\sigma_{[NII]}$ that are slightly more pronounced that in the case of [OIII], but galaxies with $M_r \geq$ -21 mag do have mean values of $\sigma_{[OIII]}$ that overlap.

In the TR galaxies we see a behavior that is somehow in-between the AGN and SF galaxies, with galaxies exhibiting the same trend than in AGN sample, but with a mean value of $\sigma_{[NII]}$ that are closer to that of SF galaxies.

In Figure 2.34, upper panel, we show the mean value of $\sigma_{[NII]}$ versus b/a in bin of b/a, divided by their values of absolute magnitude M_r, as in the legend.

In the other panels we plot the same data, but we show: in the middle left panel, the mean value of $\sigma_{H\alpha}$ in bin of b/a for the three AGN, TR and SF sample, represented by the red, green and blue symbols, and in the middle right, bottom left and bottom right panels, the mean value of $\sigma_{H\alpha}$ in bin of b/a divided by their values of M_r, respectively in the AGN, TR and SF sample.

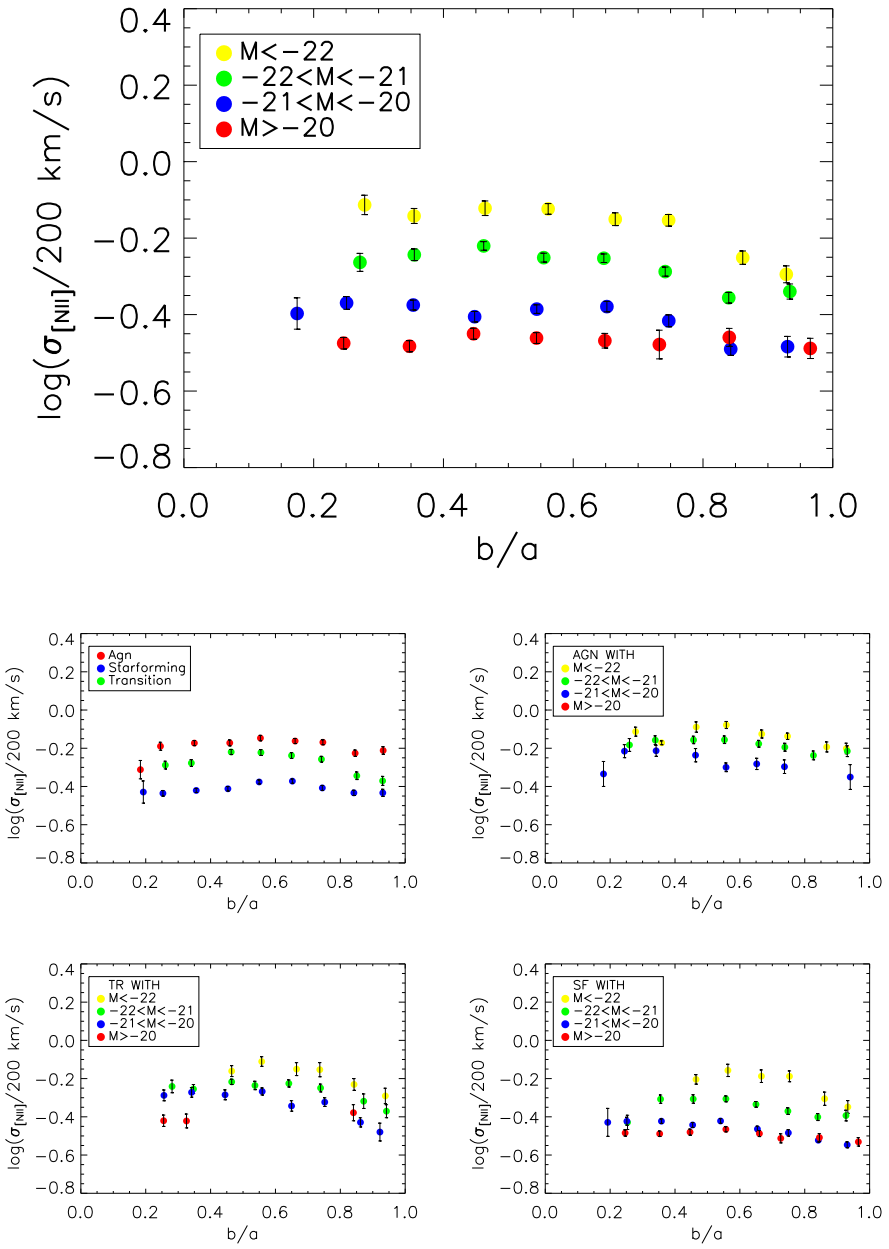

Figure 2.33: *Upper Panel*: $\overline{\sigma}_{[NII]}$ in bin of b/a versus b/a. Yellow symbols represent galaxies with M_r <-22 mag, while green, blue, and red symbols represent galaxies with, respectively, -22< M_r <-21, -21< M_r <-20, and M_r >-20 mag. *Middle Left Panel*: the same data are plotted as in the upper panel, for AGN (red), SF (blue) and TR (green). *Middle Right Panel*: as in the upper panel, for the AGN sample. *Bottom Left Panel*: as in the upper panel, for the TR sample. *Bottom Right Panel*: as in the upper panel, for the SF sample.

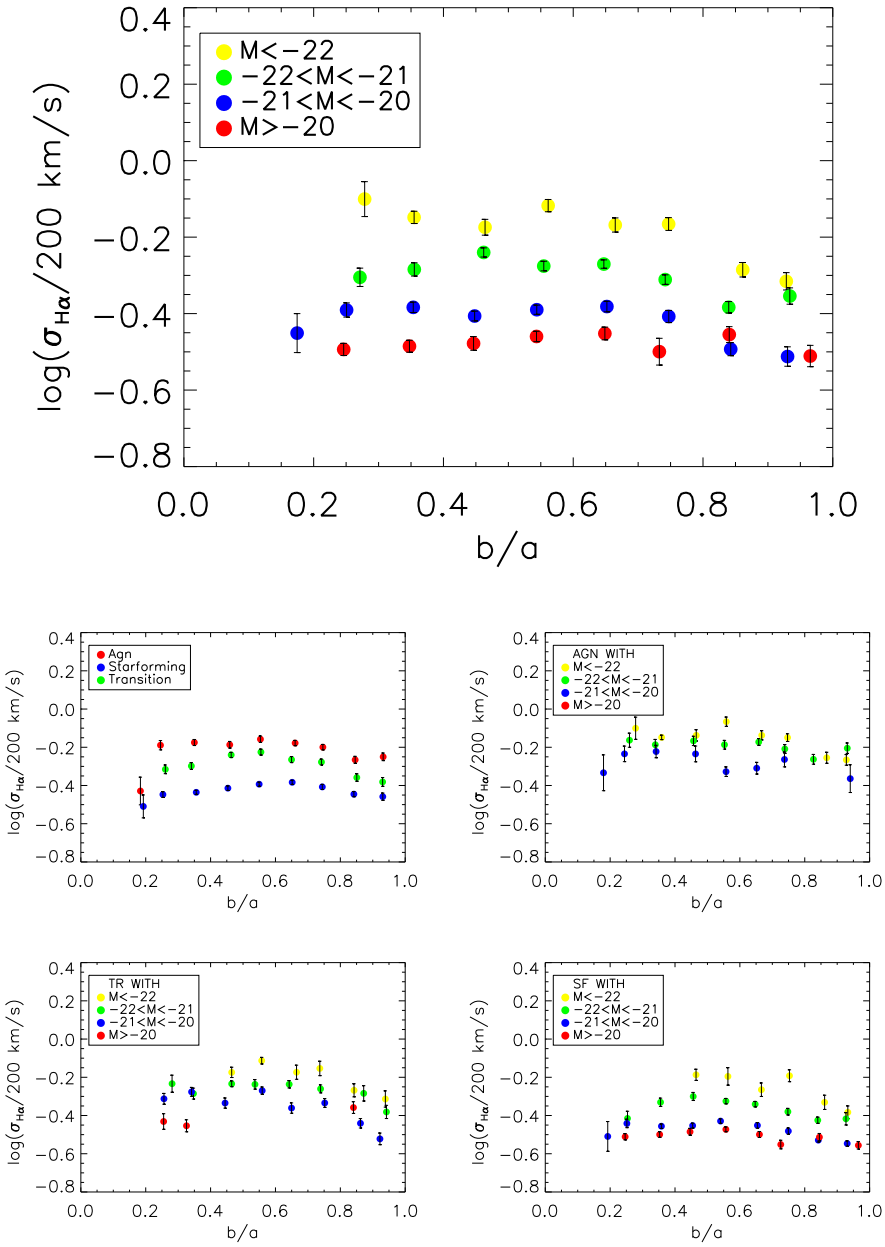

Figure 2.34: The mean Hα line σ in bin of b/a plotted versus the b/a parameter, divided by their magnitudes, as in the legend (see text). Yellow is for galaxies with M_r <-22, green for galaxies with -22< M_r <-21, blue for galaxies with -21< M_r <-20 and red for galaxies with M_r >-20 mag.

The Hα line reproduce the behavior of the $[NII]$ line when looking at the mean value of $\sigma_{H\alpha}$ in the three samples of AGN, StarForming and Transition (Figure 2.34, middle left panel).

This is expected, however, since $\sigma_{[NII]}$ is well reproduced by $\sigma_{H\alpha}$ with an high correlation (see Figure 2.23).

In AGNs, Figure 2.34, middle right panel, galaxies of different M_r show again similar mean $\sigma_{H\alpha}$.

To interpreter the trends we have showed till this point, we need to examine also the behavior of the stellar velocity dispersion σ_*.

Figure 2.35, upper panel, show the mean value of σ_* versus b/a in bin of b/a, divided by their values of absolute magnitude M_r, as in the legend.

In the other panels we plot the same data, but we show: in the middle left panel, the mean value of σ_* in bin of b/a for the three AGN, TR and SF sample, represented by the red, green and blue symbols, and in the middle right, bottom left and bottom right panels, the mean value of σ_* in bin of b/a divided by their values of M_r, respectively in the AGN, TR and SF sample.

Figure 2.35, middle left panel, indicate that the AGN sample shows a mean value of σ_* that is comparable to that of the gas as seen in Figures 2.32, 2.33 and 2.34 (middle left panes); $\overline{\sigma}_*$ in the TR subsample is closer to that in the AGN sample, than in the case of the ionized gas. Actually, the mean σ_* values in SF and TR samples are *higher* than in the case of the ionized gas.

Looking at Figure 2.35, upper panel, we notice that in galaxies of different luminosity the mean σ_* values are more clearly separated than in the case of the ionized gas, especially in the case of the [OIII]. Still, in SF galaxies we notice the usual overlap between galaxies with $M_r >$-21 mag.

In Figure 2.35, middle right panel, we see that even in this case AGNs with lower luminosity show an higher σ_* with respect to galaxies with the same M_r.

AGN and Transition galaxies show the same behavior; the mean values of σ_* for galaxies for the same luminosity is similar, while looking at $\sigma_{[OIII]}$, $\sigma_{[NII]}$ and $\sigma_{H\alpha}$ we see that in TR sample the mean values are usually lower, especially in the case of the [OIII] emission line.

In the SF sample galaxies of the lower magnitude bin ($M_r >$-21 mag, red and blue dots) present mean values of σ_* that are quite overlapping, as for the ionized gas.

What we are seeing in these plots is that the ionized gas tend to be sub-virial in SF galaxies, while in Transition objects, even if the gas is still sub-virial, it is already noted a tendency to an increase of the value of σ_{gas} respect to the values of an "unperturbed" situation.

We see this more clearly looking at the data in Table 2.4.3. The mean value $\langle\sigma_*\rangle$ is *higher* than that of the ionized gas if we look just at the whole sample galaxies divided in different magnitude bin; this is because the SF sample is the sample with more objects. In fact, we see that the mean value of σ_{gas} in SF galaxies is lower than the mean σ_*.

We see that the difference between $\langle\sigma_*\rangle$ and $\langle\sigma_{gas}\rangle$ is lower in AGN galaxies than in TR or SF galaxies. AGN galaxies show generally $\langle\sigma_{gas}\rangle$ close to the value of $\langle\sigma_*\rangle$.

The behavior of the TR galaxies deserve some attentions. We see that the ionized gas show mean values in the TR sample that are usually lower than in AGN sample with respect to the case of the stellar velocity dispersion.

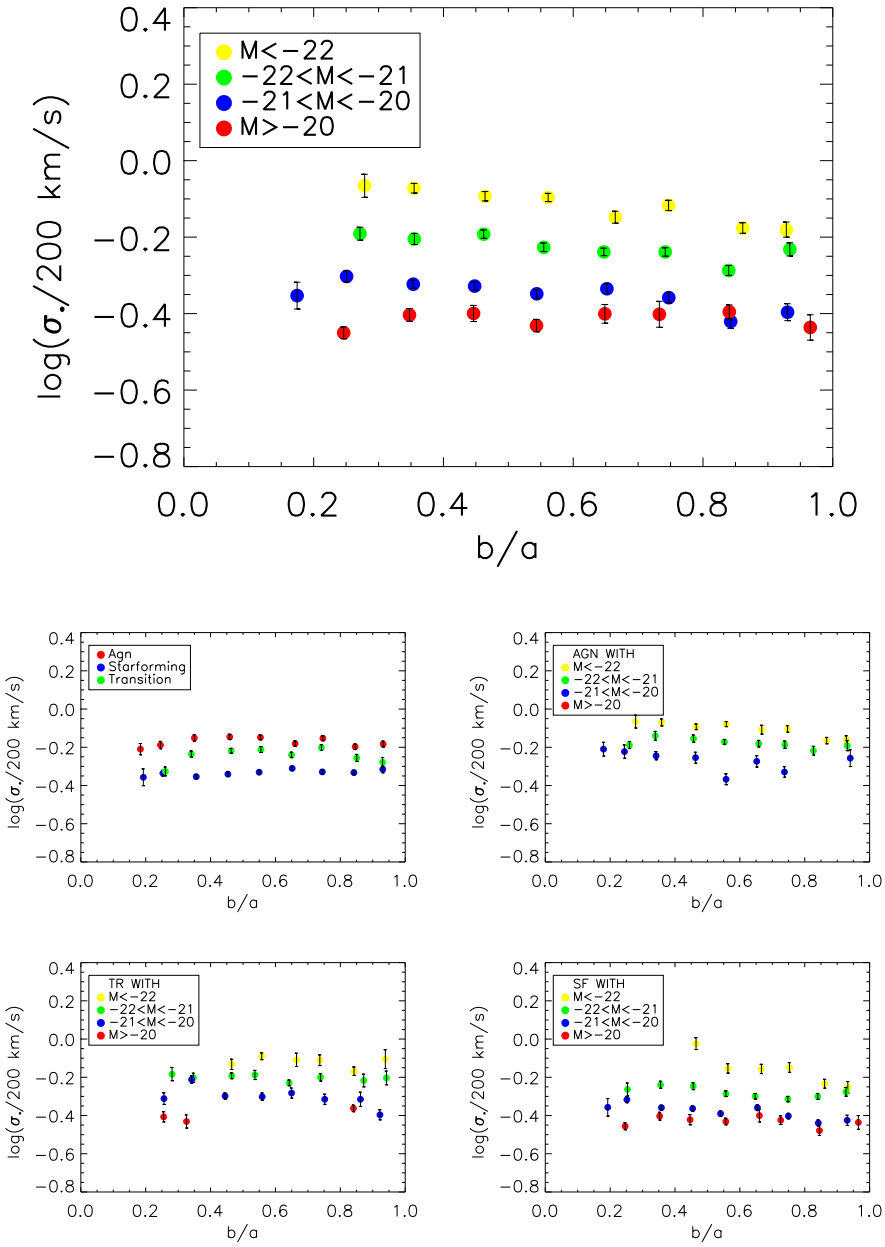

Figure 2.35: The mean stellar velocity dispersion σ_* in bin of b/a plotted versus the b/a parameter, divided by their magnitudes, as in the legend (see text). Yellow for galaxies with M_r <-22, green for galaxies with -22< M_r <-21, blue for galaxies with -21< M_r <-20 and red for galaxies with M_r >-20 mag.

Table 2.5: Mean values of the stellar velocity dispersion and of the emission line σ for [OIII], [NII] nd Hα in our samples, divided for bin of magnitude.

	$\overline{\sigma}_*$	$\overline{\sigma}_{[OIII]}$	$\overline{\sigma}_{[NII]}$	$\overline{\sigma}_{H\alpha}$
all galaxies				
AGN	-0.17± 0.02	-0.19± 0.06	-0.19± 0.05	-0.22± 0.08
TR	-0.24± 0.04	-0.29± 0.06	-0.28± 0.05	-0.29± 0.05
SF	-0.33± 0.01	-0.40± 0.04	-0.41± 0.02	-0.43± 0.04
all galaxies				
M<-22	-0.12± 0.04	-0.17± 0.03	-0.17± 0.07	-0.18± 0.08
-22<M<-21	-0.27± 0.03	-0.29± 0.03	-0.28± 0.05	-0.30± 0.05
-21<M<-20	-0.35± 0.04	-0.39± 0.03	-0.41± 0.04	-0.42± 0.05
M>-20	-0.41± 0.02	-0.44± 0.04	-0.47± 0.01	-0.48± 0.02
AGN sample				
M<-22	-0.11± 0.04	-0.14± 0.02	-0.14± 0.05	-0.15± 0.07
-22<M<-21	-0.18± 0.02	-0.19± 0.04	-0.18± 0.03	-0.19± 0.03
-21<M<-20	-0.27± 0.05	-0.25± 0.05	-0.28± 0.05	-0.29± 0.05
TR sample				
M<-22	-0.12± 0.03	-0.16± 0.04	-0.18± 0.06	-0.20± 0.07
-22<M<-21	-0.20± 0.01	-0.27± 0.04	-0.26± 0.05	-0.27± 0.05
-21<M<-20	-0.30± 0.05	-0.32± 0.05	-0.33± 0.08	-0.36± 0.08
M>-20	-0.40± 0.03	-0.40± 0.03	-0.40± 0.02	-0.41± 0.05
SF sample				
M<-22	-0.16± 0.08	-0.24± 0.05	-0.23± 0.08	-0.26± 0.08
-22<M<-21	-0.28± 0.03	-0.36± 0.02	-0.36± 0.05	-0.37± 0.05
-21<M<-20	-0.38± 0.04	-0.45± 0.04	-0.46± 0.05	-0.48± 0.04
M>-20	-0.44± 0.03	-0.48± 0.02	-0.49± 0.02	-0.51± 0.03

[NII] and Hα have usually the lowest mean values, while [OIII] is the closest to the values of the stellar velocity dispersion.

These differences generally become lower when looking at galaxies in the lower bin of magnitude.

If the ionized gas is accelerated from the central engine in AGNs the plots just shown are easily explained. In this picture the acceleration due to non gravitational forces that broaden the ionized gas lines is proportional to the strength of the central engine and so the Transition objects show an intermediate behavior between the SF galaxies, in which the gas is sub-virial, and the AGN, in which the gas reachs and eventually exceeds the value of σ_*.

As said in the Introduction, since [OIII] emission line is confined in the NLR, it is more subject to the effects of the central engine respect to Hα and [NII] lines. Even if Hα and [NII] can be accelerated by the AGN in the NLR, these effects will be diluted in the integrated spectra.

We conclude this section showing in Figures 2.36, 2.37, 2.38 and 2.39 the behavior of our galaxies when divided in bin of σ_*, as described at the beginning of this paragraph.

We plot in Figure 2.36 the mean stellar velocity dispersion σ_* in bin of b/a plotted versus the b/a parameter, divided by their stellar velocity dispersion

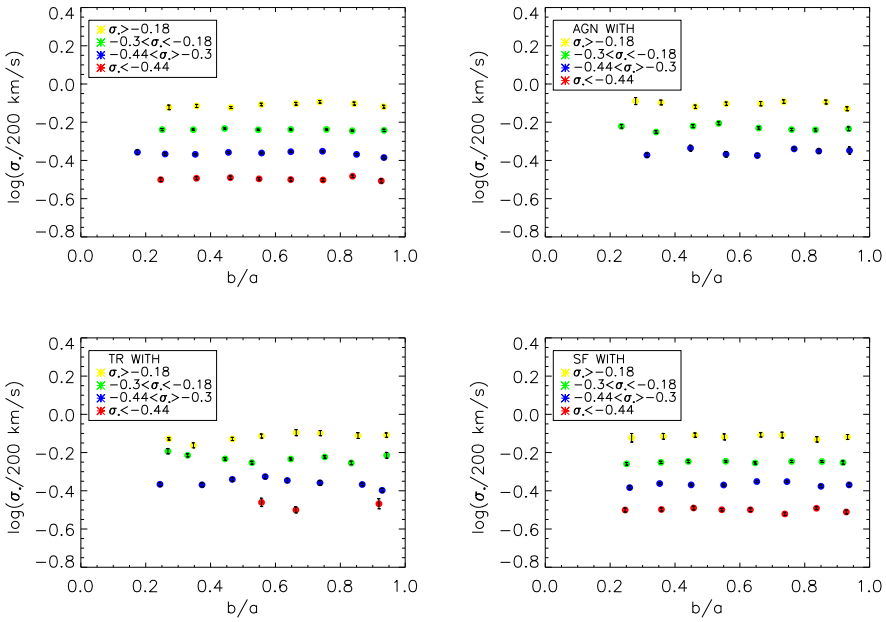

Figure 2.36: *Upper Left Panel*: the mean σ_* in bin of σ_* versus b/a. Yellow, green, blue, and red symbols are for galaxies with $\sigma_* \leq$ -0.44, -0.44 $\leq \sigma_* \leq$ -0.3, -0.3$\leq \sigma_* \leq$ -0.18 and $\sigma_* \geq$ -0.18 . Upper right, bottom left and bottom right panels are for the AGN, TR and SF samples.

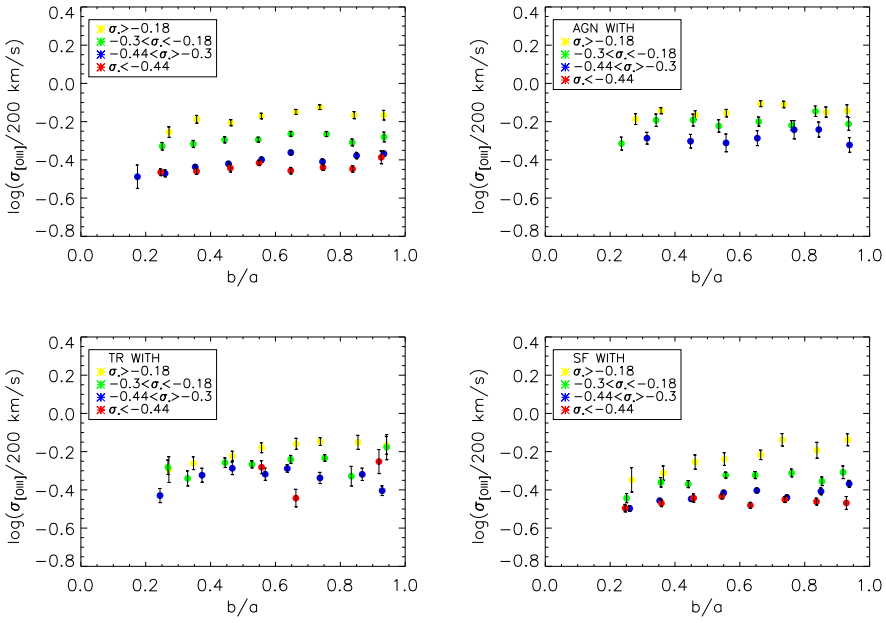

Figure 2.37: The same as in Figure 2.36 using [OIII] measures.

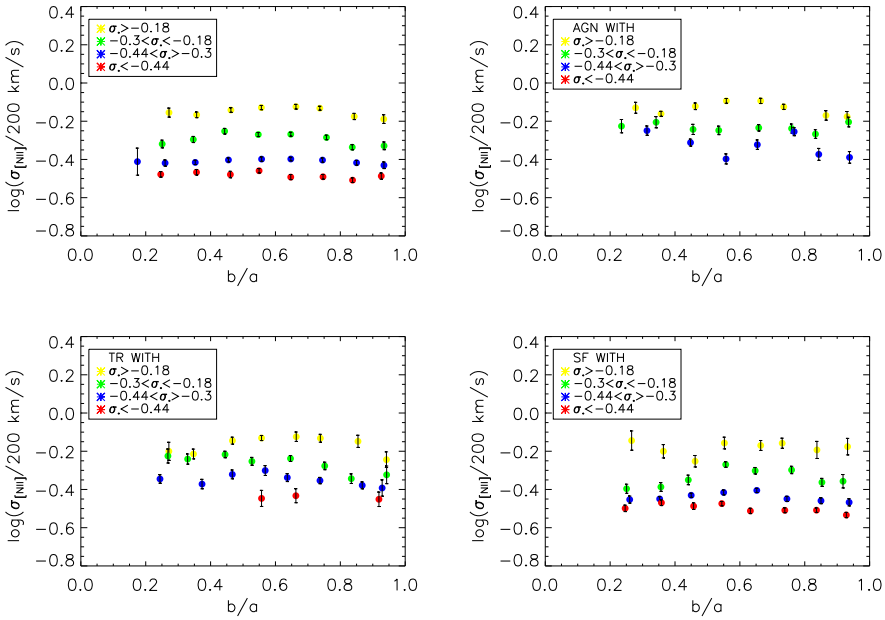

Figure 2.38: The same as in Figure 2.36 using [NII] measures.

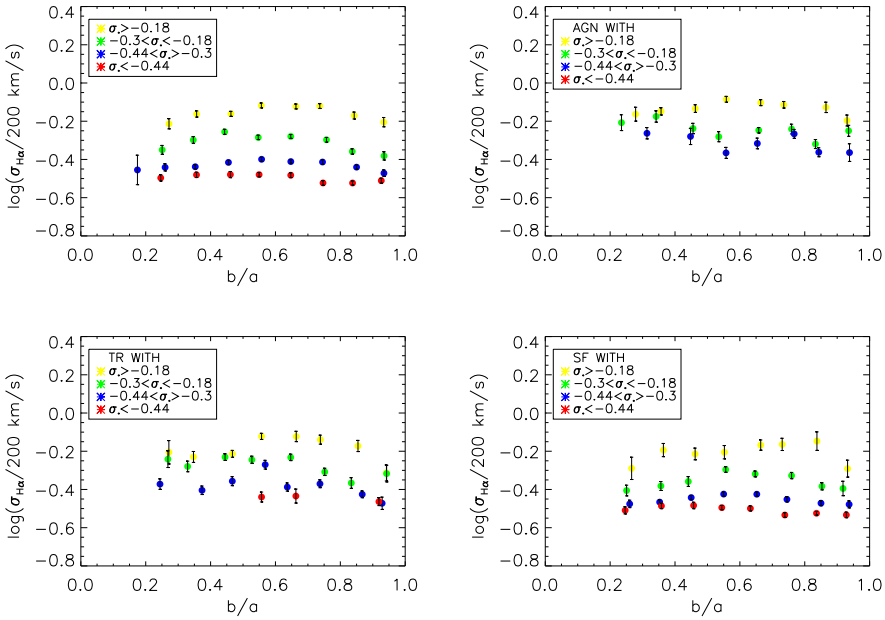

Figure 2.39: The same as in Figure 2.36 using Hα measures.

(upper left panels). In the upper right, bottom left, and bottom right panels we plot, respectively, the same data for the AGN, TR and SF sample.

In Figures 2.37, 2.38 and 2.39 we plot, respectively, the [OIII], [NII]and Hα lines.

It may look odd to plot the stellar velocity dispersion in bin of stellar velocity dispersion, but we chose to show these plots anyway to offer a comparison for the behavior of the ionized gas.

In fact, in this way it can easily appreciated how the [OIII] (Figure 2.37) really deviates from the kinematics described by the stellar velocity dispersion, and how it deviates *more* than [NII] or Hα ionized gas (Figures 2.38 and 2.39).

We see that [OIII] shows a smooth trend with b/a, with galaxies having higher values of $\sigma_{[OIII]}$ at increasing values of the inclination. We also observe that galaxies with σ_* <-0.3 share the same mean value of $\sigma_{[OIII]}$, while this is not in the case of the stellar velocity dispersion, and, at a lower extent, in the case of the [NII] and Hα lines.

Also, we observe how in the case of [OIII] the differences in the mean values of $\sigma_{[OIII]}$ for galaxies in different bin of σ_* at low value of b/a tend to decrease, and that in general differences between galaxies in different bin of σ_* are usually lower for [OIII] than for [NII] and Hα lines.

While we can say that each of the emission lines cannot describe exactly the same kinematic as the stellar velocity dispersion do, we notice that [OIII] is the one that show the greatest differences with σ_*.

2.4.4 The role of rotation

We explore now the role of the inclination, as parameterized by the axis ratio b/a.

Since we saw in Figure 2.37 that $\sigma_{[OIII]}$ exhibits a trend with b/a, we now want to divide our samples in bin of inclination and test the relation $\sigma_* - \sigma_{gas}$ in the different bins.

We plot in Figures 2.40, 2.41, 2.42 our σ_* versus σ_{gas} data, for the AGN, SF and TR samples, divided in bin of inclination b/a. These are the chosen bin:

- b/a<0.4
- 0.4<b/a<0.6
- 0.6<b/a<0.8
- b/a>0.8

From what we see from our plots, rotation seems not to be a key parameter in the $\sigma_* - \sigma_{gas}$ relation.

In no one of the AGN, TR or SF samples we notice a defined trend in the best fit slope when we divide galaxies in bin of b/a; sometime galaxies with the highest value of b/a show a steeper slope, while sometime they show a shallower one.

This happens in each of the three emission lines.

Nor we observe any improvement in the scatter of data points residuals respect to the best fit relation (see Table 2.6) in any of the bin. We are here showing just the OLS Bisector method results, for simplicity, but we obtain the same conclusions with the other regression methods.

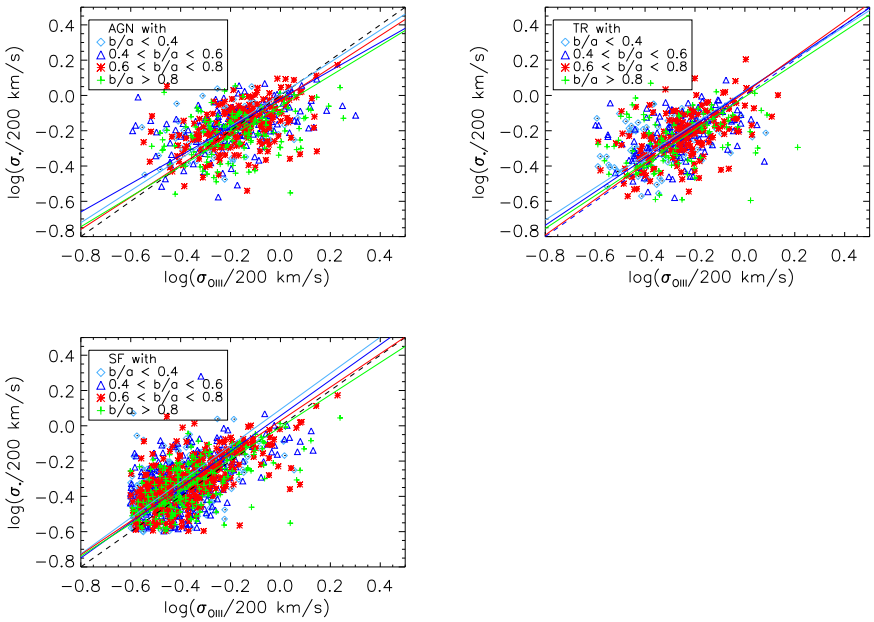

Figure 2.40: σ_* versus $\sigma_{[OIII]}$ data, for the AGN (upper left panel), TR (upper right panel) and SF samples (bottom panel), divided in bin of b/a (see text). Different symbols stand for: b/a <0.4 (light blue diamonds); 0.4< b/a <0.6 (blue triangles); 0.6< b/a <0.8 (red asterisks); b/a >0.8 (green plus signs).

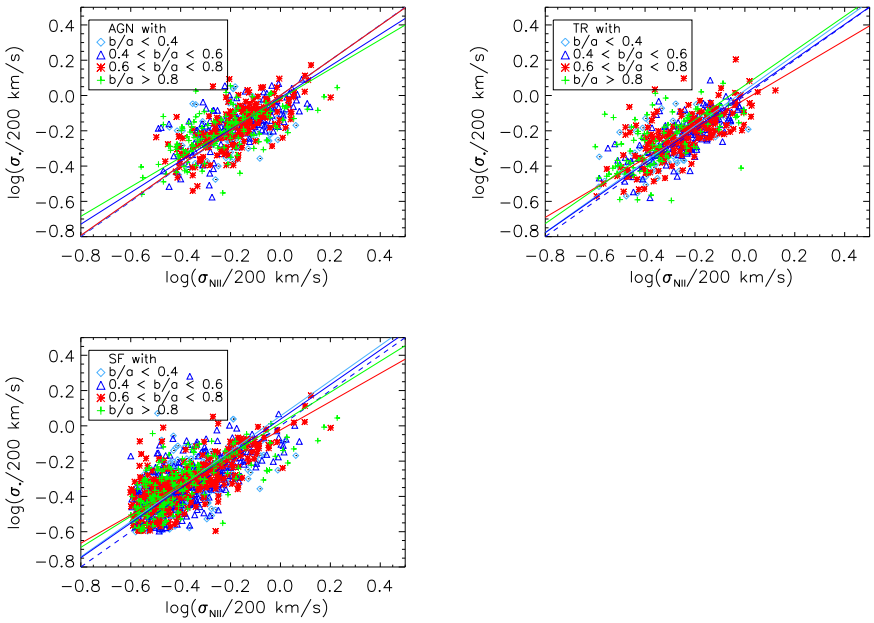

Figure 2.41: The same as in Figure 2.40 but using [NII] emission line.

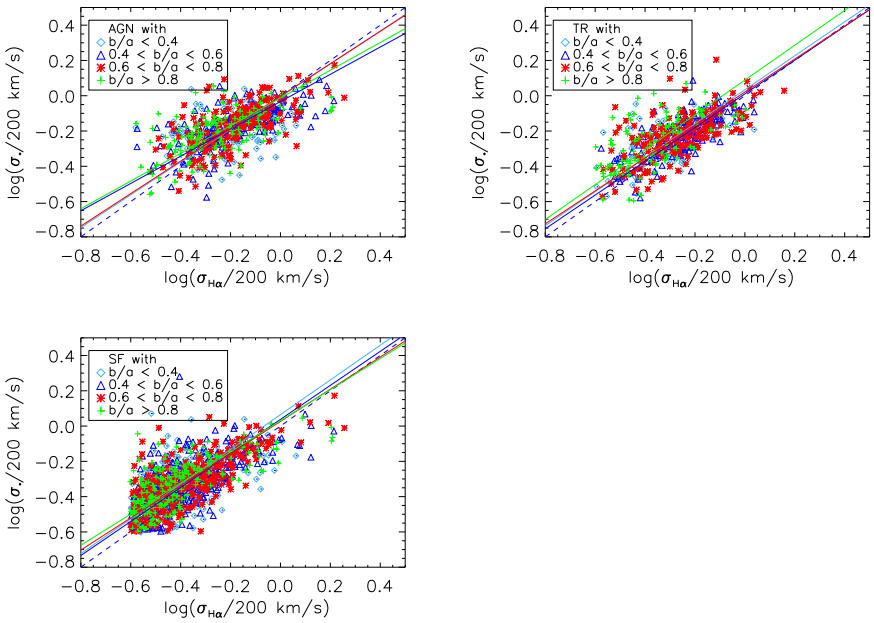

Figure 2.42: The same as in Figure 2.40 but using Hα emission line.

We observe instead that the scatter (measured as the standard deviation of the residual between the actual σ_* and the one expected from the fitted relation), with respect to the whole sample not divided in bin of b/a, gets worse, but this is mainly due to the fact that the amount of the scatter depends, also, on the number of data points, and so smaller set drawn from the same sample will have usually a bigger scatter.

We observe, nevertheless, that the scatter computed using the [NII] and Hα lines turn out again to be smaller than in the case of the [OIII].

This agrees with the results of Nelson & Whittle (1996). They studied the role of galaxy inclination in the scatter of the $\sigma_* - \sigma_{[OIII]}$ relation, and found no correlation.

If the [OIII] line widths were produced by rotation in the galaxy disk one would expect a correlation with b/a, with galaxies with higher b/a having lower $\sigma_{[OIII]}$, while if the NLR velocity field were completely random there should be no dependence on b/a at all (see Figure 11 of Nelson & Whittle).

In their sample they found that their data didn't conform to either case, but showed considerable scatter.

2.5 The $\sigma_* - \sigma_{gas}$ equations

It has now to be discussed which one of the best fit parameters has to be used.

In Isobe et al. (1990) it is pointed out that when the intrinsic scatter of the datapoints is bigger than the measurement uncertainties, as in our case, the theoretical values of the parameters of the 5 different regression methods

σ_* - $\sigma_{[OIII]}$			
	AGN	**TR**	**SF**
$b/a < 0.4$	0.13	0.15	0.14
$0.4 < b/a < 0.6$	0.13	0.14	0.13
$0.6 < b/a < 0.8$	0.13	0.13	0.12
$b/a > 0.8$	0.15	0.18	0.13
σ_* - $\sigma_{[NII]}$			
$b/a < 0.4$	0.13	0.11	0.13
$0.4 < b/a < 0.6$	0.09	0.09	0.12
$0.6 < b/a < 0.8$	0.10	0.12	0.11
$b/a > 0.8$	0.11	0.13	0.11
σ_* - $\sigma_{H\alpha}$			
$b/a < 0.4$	0.15	0.12	0.13
$0.4 < b/a < 0.6$	0.10	0.08	0.12
$0.6 < b/a < 0.8$	0.10	0.11	0.10
$b/a > 0.8$	0.11	0.13	0.11

Table 2.6: Scatters relative to the $\sigma_* - \sigma_{gas}$ relation using subsamples of galaxies with different values of b/a.

examined are different. Still, depending on what an astronomer is looking for, a choice between the methods is possible.

Isobe et al. performed an extensive series of Monte Carlo simulations to determine the accuracy and the size of the parameters uncertanties.

They found that OR is less accurate in approaching its theoretical value; the dispersion in the values of the slope in the various simulations results bigger than for the other methods. This is a disadvantage that can overcome the advantage of the method itself, that is to find the line that minimize the sum of the square of the *orthogonal* distances from the line.

They showed that the OLS Bisector has, on the contrary, a small standard deviation, and they suggest to use this method.

The RMA is discouraged because of the fact that the theoretical slope does not depend on the correlation between the data, and so is not a suitable method if one is willing to find the underlying relation between the data.

To test the performance of the three methods *in this case*, we applied to our σ_{gas}, for each of the subsamples, a transformation such that

$$\sigma_{gas}[\text{new}] = zp + slope * \sigma_{gas} \tag{2.25}$$

We then applied again the regression methods with this transformed σ_{gas} data; our results are summarized in Table 2.5.

We see that only the RMA method assure that after the calibration the data will lie on an unitary relation.

In fact, it is the only method between these three whose theoretical slope does not depend on the correlation between the variables. The theoretical RMA slope is given by $\beta = \frac{\Sigma_y}{\Sigma_x}$, where Σ_y and Σ_x are the standard deviation of the data point, the transformed x variables can be written $x_t = x\frac{\Sigma_y}{\Sigma_x}$.

The standard deviation of x_t will be now:

$$\Sigma_{xt} = \sqrt{\frac{\sum (x_t - \overline{x_t})^2}{n}} = \sqrt{\frac{\sum (x\frac{\Sigma_y}{\Sigma_x} - \overline{x\frac{\Sigma_y}{\Sigma_x}})^2}{n}}$$
$$= \frac{\Sigma_y}{\Sigma_x}\sqrt{\frac{\sum (x - \overline{x})^2}{n}} = \frac{\Sigma_y}{\Sigma_x}\Sigma_x = \Sigma_y$$

and so the resulting slope is $\beta_t = \frac{\Sigma_y}{\Sigma_{xt}} = 1$.

Also, we notice that if we use the equations with the best fit parameters given by the RMA to transform the data, and we fit again, we will find that even the best fit parameters given by the OLS Bisector and OR regression methods will give slopes equal to 1.

When using the $\sigma_* - \sigma_{gas}$ relation one should be aware that an OLS bisector best fit could still underestimate the correct σ_*.

This problem however is especially felt when the correlation is poorer, as in the case of the [OIII]. In the cases of Hα and [NII] lines the results of transforming the gas σ using the slope from OLS Bisector and RMA are similar, and so applying one or the other don't make much difference.

Since the OLS Bisector is the preferred method in such studies, we give our $\sigma_* - \sigma_{gas}$ equations for the transformation, in the AGN sample, according to that method, also to compare with other studies. Consequently:

$$\log(\sigma_*/200) = (-0.02 \pm 0.006) + (0.86 \pm 0.02) * \log(\sigma_{[OIII]}/200) \tag{2.26}$$

$$\log(\sigma_*/200) = (-0.008 \pm 0.006) + (0.92 \pm 0.03) * \log(\sigma_{[NII]}/200) \tag{2.27}$$

$$\log(\sigma_*/200) = (-0.01 \pm 0.006) + (0.83 \pm 0.02) * \log(\sigma_{H\alpha}/200) \tag{2.28}$$

We already noticed that the orthogonal methods are suitable when studying the underlying relation between two variables.

When, on the other side, the aim is to find the effective equation to transform the independent variable, a method like the OLS (Y|X) is more appropriate.

Still, this method, as given by Isobe et al. (1990), do not take into account measurements errors.

So, we give here the correct equation computed using the method in the Appendix of Tundo et al. (2007), that we describe briefly.

Let R be the "result" and O the "observable";we are seeking a relation like $y = a \times x + b$.

We report the data to a system centered on the means of the value: $y = R - \langle R \rangle$, e $x = O - \langle O \rangle$.

Minimizing the $\chi^2 \equiv \sum_{i=1}^{N}(y_i - ax_i - b)^2/N$ gives an expression like

$$a_{\min} = \frac{\sum_i x_i y_i}{\sum_i x_i^2} = \frac{\sigma_x \sigma_y r_{xy}}{\sigma_x^2 + \epsilon_x^2} = \frac{\sigma_x \sigma_y r_{xy}}{\sigma_x^2}\left(1 + \frac{\epsilon_x^2}{\sigma_x^2}\right)^{-1} = a_{y|x}\left(1 + \frac{\epsilon_x^2}{\sigma_x^2}\right)^{-1} \tag{2.29}$$

We see that $a_{\rm min}$ differs from the intrinsic slope $a_{y|x} = \frac{\sigma_x \sigma_y r_{xy}}{\sigma_x^2}$ due to the measurements uncertainties ϵ_x^2.

The scatter of the relation is given by

$$\chi^2_{\rm min} = \sigma_x^2 \left(1 - r_{xy}^2\right) + \epsilon_y^2 + a^2_{\rm min}\, \epsilon_x^2 \left(1 + \frac{\epsilon_x^2}{\sigma_x^2}\right) \tag{2.30}$$

The first term represents the *intrinsic* scatter of the relation, while the other terms are consequences of the measurements errors.

So, the intrinsic slope and scatter are given by

$$a_{\rm y|x} = a_{\rm min} \left(1 + \frac{\epsilon_x^2}{\sigma_x^2}\right) \qquad \text{e} \qquad \sigma^2_{\rm y|x} = \chi^2_{\rm min} - \epsilon_y^2 - a^2_{\rm min}\, \epsilon_x^2 \left(1 + \frac{\epsilon_x^2}{\sigma_x^2}\right) \tag{2.31}$$

The intrinsic slope $a_{y|x}$ can be computed even when the measurements uncertainties ϵ_y are big, while there are problems when the scatter in the observable values is much lower than the measurements error: $\sigma_x \ll \epsilon_x$. In this case measurements errors "delete" the relation between x e y and we measure a shallow slope, that need a big correction coefficient to be reported to the intrinsic value.

We report the parameters found with this method in Table 2.5.

Table 2.7: Parameters in the $\sigma_* - \sigma_{gas}$ relation from the method of Tundo et al. (2007). (1) Zero point (2) Slope (3) Intrinsic scatter (4) Correlation coefficient.

	zero point (1)	**slope** (2)	Σ (3)	ρ (4)
	σ_* - $\sigma_{[OIII]}$			
AGN	-0.11±0.01	0.41±0.04	0.10	0.46
TR	-0.10±0.02	0.53±0.07	0.11	0.48
SF	-0.06±0.01	0.71±0.05	0.07	0.75
	σ_* - $\sigma_{[NII]}$			
AGN	-0.06±0.01	0.62±0.04	0.08	0.68
TR	-0.07±0.01	0.64±0.03	0.09	0.70
SF	-0.09±0.01	0.62±0.03	0.06	0.84
	σ_* - $\sigma_{H\alpha}$			
AGN	-0.08±0.01	0.52±0.04	0.09	0.65
TR	-0.06±0.01	0.63±0.03	0.08	0.73
SF	-0.08±0.01	0.62±0.03	0.06	0.84

Table 2.8: Comparison between slopes fitted with OLS Bisector, OR and RMA methods in our original subsamples, and after transforming the $\sigma_{[OIII]}$ using the best fit parameters.

	OLS		**OR**		**RMA**	
	slope	**slope**$_{tr}$	**slope**	**slope**$_{tr}$	**slope**	**slope**$_{tr}$
			σ_* - $\sigma_{[OIII]}$			
AGN	0.86 ± 0.02	0.96 ± 0.03	0.62 ± 0.06	1.87 ± 0.2	0.81 ± 0.09	1.00 ± 0.1
TR	0.96 ± 0.02	0.97 ± 0.03	0.92 ± 0.04	0.99 ± 0.2	0.96 ± 0.05	1.00 ± 0.1
SF	0.94 ± 0.02	1.01 ± 0.03	0.80 ± 0.08	1.38 ± 0.08	0.91 ± 0.1	1.01 ± 0.07
			σ_* - $\sigma_{[NII]}$			
AGN	0.92 ± 0.03	1.01 ± 0.03	0.86 ± 0.04	1.09 ± 0.09	0.91 ± 0.04	1.00 ± 0.06
TR	0.89 ± 0.04	1.00 ± 0.03	0.83 ± 0.07	1.12 ± 0.06	0.89 ± 0.05	0.99 ± 0.05
SF	0.90 ± 0.06	0.98 ± 0.03	0.84 ± 0.1	1.09 ± 0.05	0.89 ± 0.05	1.00 ± 0.06
			σ_* - $\sigma_{H\alpha}$			
AGN	0.83 ± 0.02	0.98 ± 0.03	0.70 ± 0.04	1.23 ± 0.08	0.81 ± 0.04	0.99 ± 0.08
TR	0.93 ± 0.02	0.99 ± 0.03	0.89 ± 0.03	1.05 ± 0.06	0.92 ± 0.04	1.00 ± 0.05
SF	0.93 ± 0.03	0.99 ± 0.03	0.89 ± 0.04	1.05 ± 0.06	0.92 ± 0.04	1.00 ± 0.05

2.6 The $M_\bullet - \sigma_{gas}$ relation

We want now to prove that [NII] emission line can be a better tracer for the stellar velocity dispersion than the [OIII], by plotting the up-to-date available SMBH masses versus σ_{gas}.

We retrieved some of the nowadays available sample of galaxies with a measured SMBH mass. In many of these samples the SMBH masses are measured via the indirect method of Kaspi et al. (2000).

In the hypothesis that the BLR (Broad Line Region) is in virial equilibrium, the mass of the central black hole is given by $M_\bullet = v^2 R_{BLR}/G$, where v and R_{BLR} are the characteristic velocity and radius of the BLR, and G is the gravitational constant.

Kaspi et al. (2000) showed that a good correlation exists between BLR radius and the monochromatic luminosity L_{5100} with a power law index of 0.7 for their sample of reverberation-mapped AGNs, allowing this easily measured luminosity to be substituted for time lags derived from arduous monitoring campaigns. On the other side, v is deduced from the FWHM of the emission lines originated in the BLR, usually the Hβ or even the [OIII] emission lines, by assuming BLR clouds in random orbit motion.

In our selection we are limited by the fact that we want to retrieve galaxies observed by the SDSS, to measure the emission lines in a consistent way.

We describe in the following lines the chosen sample:

- Beifiori et al.(2009) measured the SMBH masses in 105 nearby (< 100Mpc) galaxies by modelling the emission line width of STIS/HST archival spectra in terms of gas motions following the method of Sarzi et al. (2002).
- Greene & Ho (2006) presented a study on 71 spectroscopically identified AGN from the SDSS 4DR. SMBH masses are computed using the radius-luminosity relation $R \propto L^{0.64}$ (Greene & Ho 2005b; Kaspi et al. 2005), and the BRL velocity is retrieved from the width of the Hα emission line.
- Boroson et al. (2003) presented a sample of 121 low redshift radio quiet QSO and Seyfert1 galaxies drawn from the SDSS EDR (Stoughton et al. 2002). SMBH masses are measured via the Kaspi et al. (2000) method. The velocity of the BLR is estimated from the Hβ emission line.
- Wang et al. (2006) selected their sample from the broad-line X-ray-emitting SDSS AGN catalog (Anderson et al. 2003) matched with the FIRST 20 cm radio survey (White et al. 1997). A total of 115 objects were retrieved, for wich the SMBH masses were measured using their Hβ emission line width as in Kaspi et al. (2000).
- Xu & Cao (2007) presented a sample of 110 low redshift bright X-ray selected ROSAT Seyfert1. SMBH masses were measured via the Hβ emission line and the optical luminosity at 5100Å (Kaspi et al. 2000).

We matched these samples with the SDSS database, and retrieved the spectra of the matched galaxies. We rejected galaxies with redshift z>0.36 to assure the detectability of the [NII] emission line.

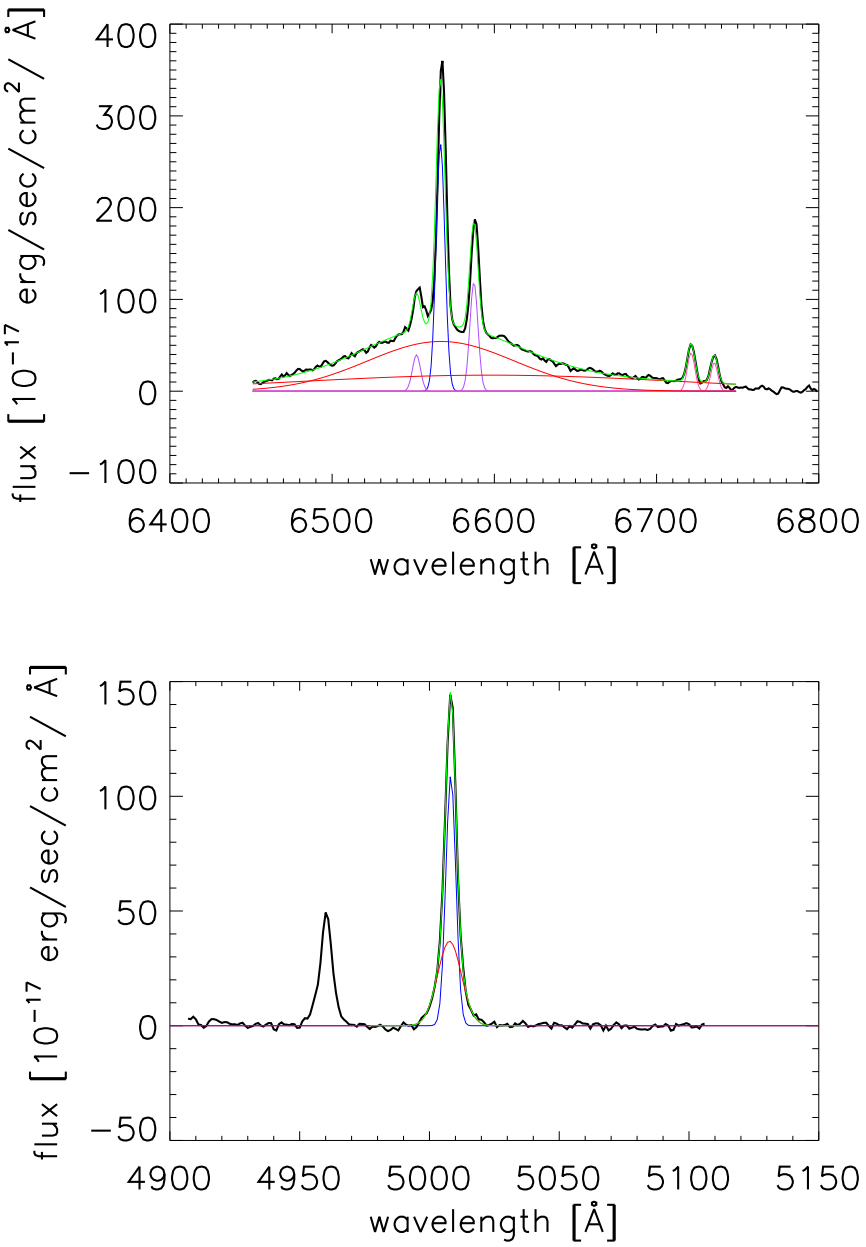

Figure 2.43: The rest frame spectrum (black line) of the galaxy SDSSJ093812.26+074340.0 around the Hα-[NII] emission lines (upper panel) and around the [OIII] emission line (bottom panel). In the upper panel the emissions are fitted with a narrow component (blue for Hα, purple for the [NII] doublet, and pink for the [SII] doublet) over imposed on two broad components (red lines). The resulting fitted spectra is drawn in green. In the bottom panel the [OIII] emission line is fitted with a narrow (blue line) component and a broad (red line) component. The resulting fitted spectra is drawn in green.

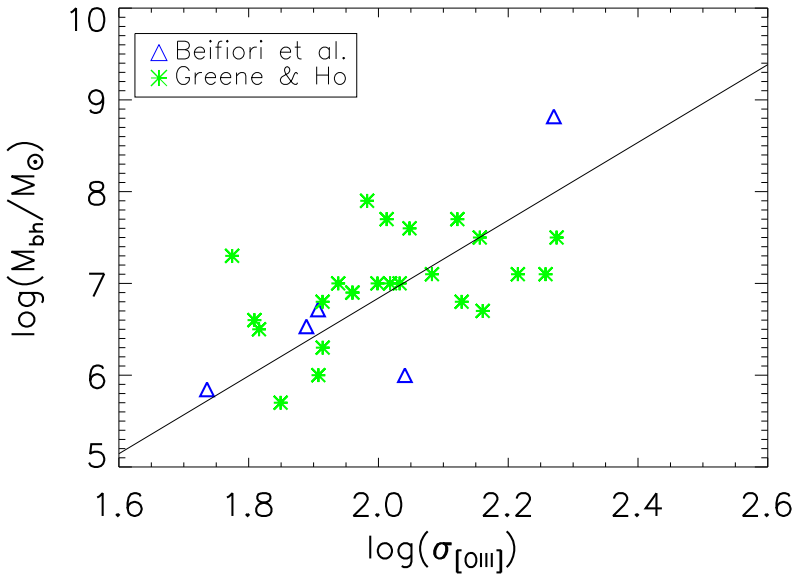

Figure 2.44: The SMBH masses plotted versus the $\sigma_{[OIII]}$ values for the samples of Beifiori et al. (2009) –blue triangles– and of Greene & Ho (2006) –green asterisks. The black line represent the $M_\bullet - \sigma_*$ relation from Tremaine et al. (2002).

In Figure 2.43 we show an example of the typical spectra of these object. Galaxies show intense broad components, and we modified our fitting routine to include such components.

The [SII]$\lambda\lambda$6719,6730 Å doublet was fitted to have an initial guess of the widths of the narrow components of the [NII] doublet and of the Hα lines.

For some galaxies more than one broad component were needed; we allowed our routine to use just one broad component up to three. The fit of the spectra were checked by eye, so to decide how many components were needed.

The situation for the [OIII] line is usually more straightforward, but we still usually need a broad component to fit the spectra, as we can see in Figure 2.43 (bottom panel).

Some of the galaxies showed a situation in which each of the emission line would have needed a separate broad component to fit the spectrum. In such situation, and generally when the fit were not satisfying, we rejected the object from our sample.

Our final sample consist of 68 galaxies.

We plot in Figure 2.44, 2.45 and 2.46 the $M_\bullet - \sigma_{gas}$ relation for the [OIII], [NII] and Hα emission line, respectively, using the galaxies from the sample of Greene & Ho (2006) –green asterisks– and from Beifiori et al. (2009) –blue triangles–

The correlation coefficient for these galaxies using the three emission lines are:

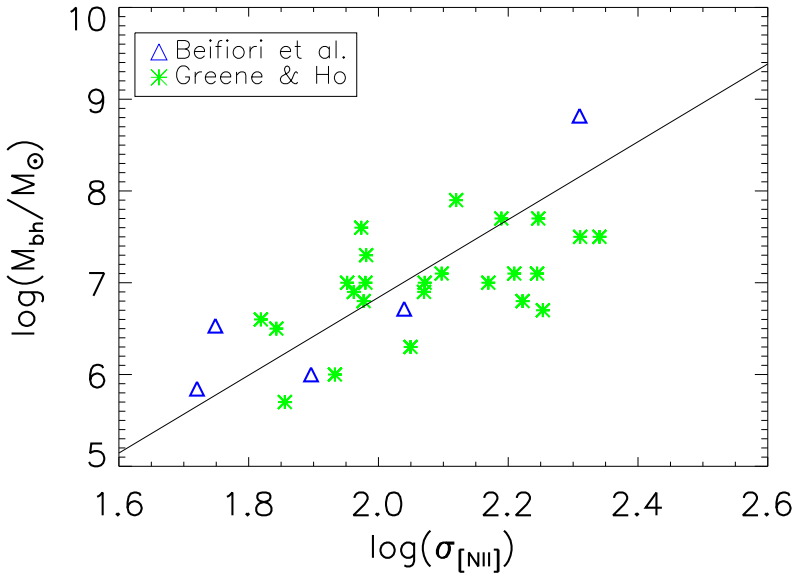

Figure 2.45: As in Figure 2.44 using the [NII] emission line.

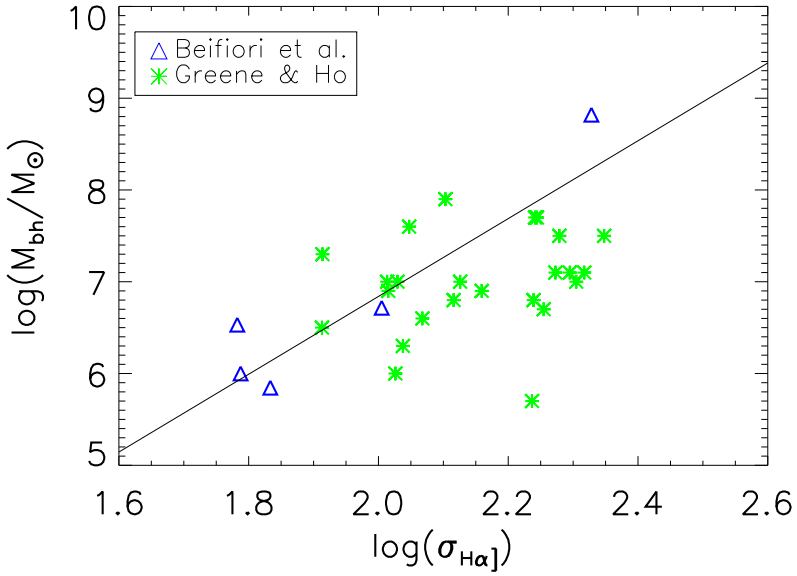

Figure 2.46: As in Figure 2.44 using the Hα emission line.

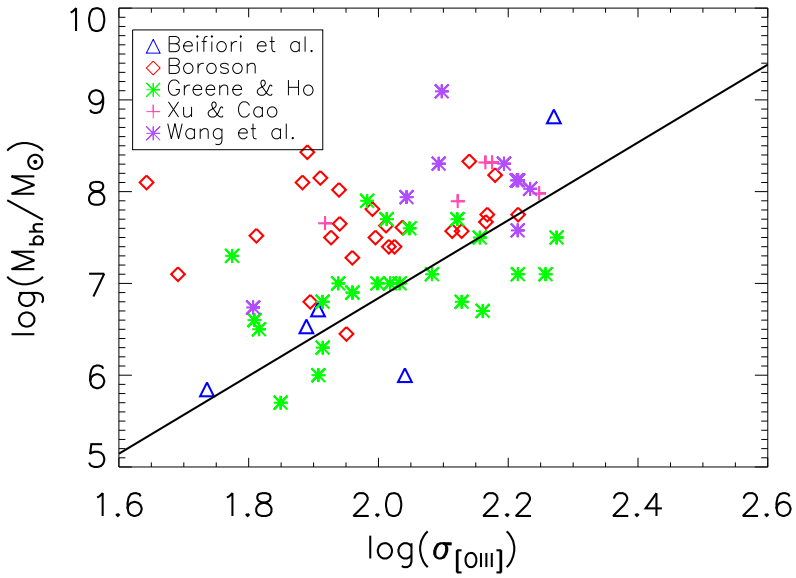

Figure 2.47: The SMBH masses plotted versus the $\sigma_{[OIII]}$ values for the samples of Beifiori et al. (2009), Boroson et al. (2003) Greene & Ho (2006), Wang et al. (2006), Xu & Cao (2007), shown respectively as blue triangles, green asterisks, red diamonds, purple asterisks and pink plus signs. The black line represent the $M_\bullet - \sigma_*$ relation from Tremaine et al. (2002).

$$r_P([OIII])_{G+B} = 0.58$$
$$r_P([NII])_{G+B} = 0.68$$
$$r_P(H\alpha)_{G+B} = 0.51$$

These values confirm the results obtained in this work, showing that [NII] can be a better tracer for the stellar velocity dispersion than [OIII].

Nevertheless, things complicate when we add galaxies from the other three sample, as we can see in Figures 2.47, 2.48 and 2.49.

X-ray selected galaxies (and hence with accreting SMBHs) and QSO do not appear to lie on the $M_\bullet - \sigma_*$ relation, showing instead grater $M_\bullet$ than expected, or, otherwise, smaller emission line width.

We report the correlation coefficients for the whole sample:

$$r_P([OIII])_{all} = 0.31$$
$$r_P([NII])_{all} = 0.33$$
$$r_P(H\alpha)_{all} = 0.26$$

This decrease in the overall correlation is due to the poor correlation in the Boroson (2003) sample:

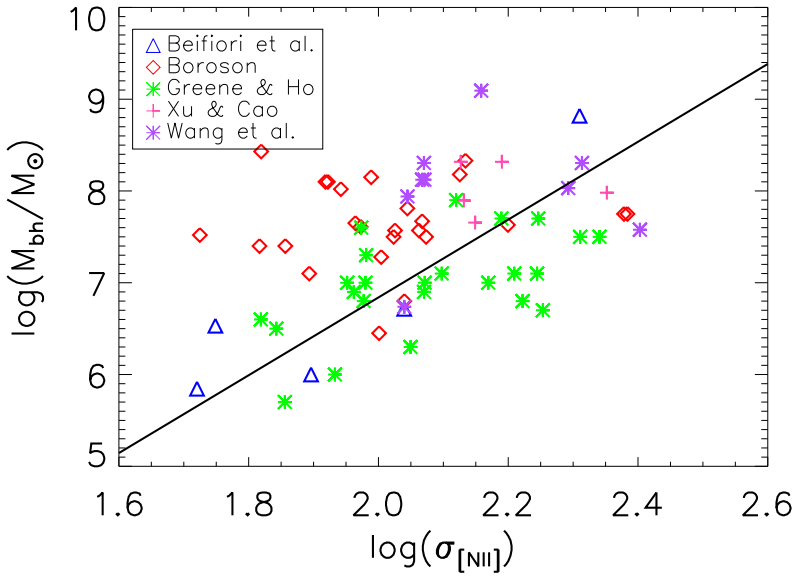

Figure 2.48: As in Figure 2.47 plotting the [NII] data.

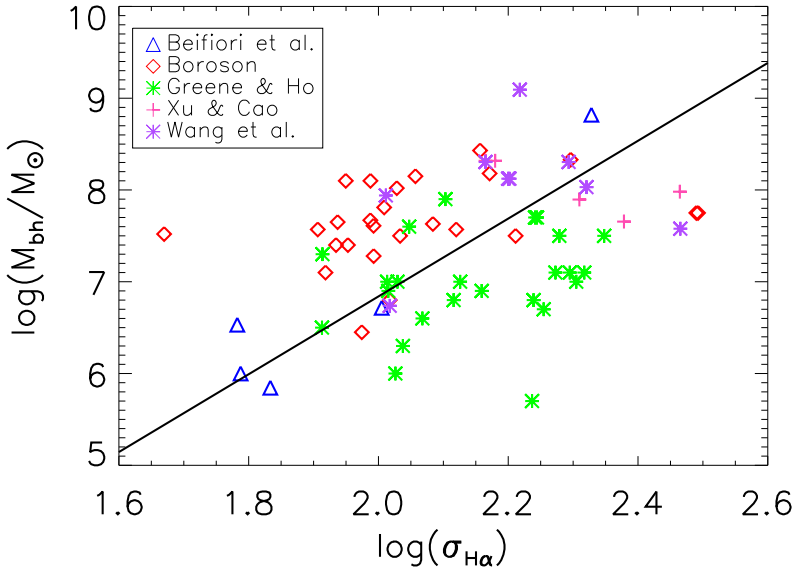

Figure 2.49: As in Figure 2.47 plotting the Hα data.

$$r_P([OIII])_B = 0.12$$
$$r_P([NII])_B = 0.07$$
$$r_P(H\alpha)_B = 0.31$$

While emission line measurement is particularly tricky with regard to the narrow component, so that we cannot rule out completely the hypothesis that we overestimated the broad component, so giving lower σ_{gas} for the narrow component, we note that this problem is not seen in the samples of Greene & Ho (2006) and Beifiori et al. (2009).

Xu & Cao (2007) showed in their sample a correlation between the SMBH masses and the FWHM of the broad component, and a correlation between the FWHM and the accretion rate $\dot{m}$, so that we can hypothesize that the $M_\bullet$ reported in these three sample are overestimated.

While this hypothesis needs further study, we can conclude at this point that in moderately active galaxies [NII] is actually a better tracer for $M_\bullet$, in consequence to the fact that it is a better proxy for σ_*, while in galaxies with stronger SMBH accretion we need to be careful about the use of secondary indicator of the stellar velocity dispersion.

2.7 Discussion and Conclusions

The width of the [OIII]emission line is often used as a proxy for the stellar velocity dispersion σ_*; σ_* is a key parameter in studying galaxies and galaxy evolution, since it trace the bulge stellar mass and the kinematics of stars inside the host galaxy, and since it is tightly connected with the mass of the super massive black hole at the center of galaxies, and with the circular velocity V_c (Pizzella et al. 2005).

Since it is difficult to measure σ_* in high redshift or active galaxies, we would miss such a key measure in the objects that are more important in the study of the evolution of galaxies.

To overcome this problem it was suggested to use [OIII]emission line as a tracer for σ_*; [OIII] is a strong and ubiquitous line, easy to measure, and whose high ionization potential assure that it is coming from the NLR.

This point is seen somehow as a *pro*, since the $\sigma_* - \sigma_{[OIII]}$ relation is used mostly in the study of the $M_\bullet - \sigma_*$ relation, but it is always noted that the fundamental hypothesis underlying this relation is that the NLR kinematic is dominated by the bulge gravity field and not by the SMBH's.

The use of σ_{OIII} revealed some problems. The high intrinsic scatter in the $\sigma_* - \sigma_{[OIII]}$ relation (with a Pearson correlation coefficient of $\sim$0.4) translate in a big uncertainty in the derived $M_\bullet - \sigma_{[OIII]}$ relation.

Also, a sub class of active galaxies, the Narrow Line Seyfert1 (NLS1), seem not to lie on the $M_\bullet - \sigma_*$ relation when using $\sigma_{[OIII]}$, and it was noted that the residuals $\Delta\sigma = \sigma_{[OIII]} - \sigma_*$ correlate with AGN luminosity and with the Eddington ratio.

Another problem in the use of [OIII] line width is given by the blue asymmetries (blue shifts and blue wings) that can affect [OIII].

Some correction was proposed; Green & Ho (2005) proposed to use just the core of the [OIII] line in the $\sigma_{[OIII]}/\sigma_*$, and a third parameter, the Eddington ratio, was added to the relation.

Still, even with these solutions, NLS1 were outliers respect to the $M_\bullet - \sigma_{[OIII]}$ relation.

Moreover, the *slope* of the relation is found to be lower than unity.

These problems are due to the influence of non gravitational forces coming from the active nucleus, that broaden the line width and perturb the kinematics of the NLR through radio jets, radiation pressure, tidal distortion, shocks.

In fact, it was showed (Gaskell 2009, Rice et al. 2006, Phillips et al. 1986) that the gas usually shows a line width lower than σ_*. This happens because gas is more subject to non-gravitational forces and dissipation, and tend to settle in a flattened distribution.

This translates, in AGN, in σ_{gas} that are in average lower than σ_* for σ_* below $\sim$100 km/s^{-1} , and that is bigger above. The deviation of σ_{gas} from its expected subvirial value is proportional to the AGN luminosity and to its Eddington ratio, so confirming the role of the central engine in the σ_{gas}/σ_* relation.

This happens because above that limits AGN effects tend to be stronger and the gas velocity may be increased by jets and other interaction between the central engine and the ionized gas.

We know (de Robertis & Osterbrock 1984, Komossa et al. 2008, Rice et al. 2006) that lines with higher Ionization Potential (IP) are more subject to asymmetries. Moreover, since the strong effects of AGN on the ionized gas in NLR, we want to test the reliability of other emission lines as tracers of the stellar velocity dispersion.

In this study we test [OIII], [NII] and Hα emission lines.

Since Hα and [NII] have a lower IP than [OIII] (IP$_{[OIII]}$=35.1, IP$_{[NII]}$=14.5, IP$_{H\alpha}$=13.6), we expect these lines to be less affected by the AGN and to be better tracer of the stellar kinematics. Also, [NII] and Hα are not confined in NLR, so the perturbations due to the AGN effects should be diluted in the integrated spectra. Moreover, [NII] and Hα are strong lines, even stronger than [OIII], so even easier to measure respect to [OIII].

We used the SDSS Main Galaxy Sample to select our sample of emission line galaxies, divided in three subsamples of AGN, Transition (TR) and Star Forming (SF) galaxies using the diagnostic of Kewley et al. (2006).

We performed a linear regression using three different methods, namely, the Orthogonal Least Square Bisector (OLS Bisector), the Orthogonal Reduction (OR), and the Reduced Major Axis (RMA) as delined in Isobe et al. (1990). Since in our sample the intrinsic scatter in the data is high, the different methods will give results that are *theoretically* different. Our subsequent discussion is nevertheless valid for each of the three methods.

We computed moreover the slope, zero point, intrinsic scatter and the correlation of the relations using the method outlined in Tundo et al. (2007), since the methods from Isobe et al. (1990) doesn't take into account measurements errors in both variables while our method does.

What's more, while orthogonal methods are the best choice when one is willing to understand the underling relation between two variables, when the aim of the work is to find the actual relation that enable to transform the

observed variable in another one, one should pick a method that minimize the residuals of the dependent variable at a fixed value of the independent one, as it does the OLS (Y|X) method –and our, with the advantage of including the effect of measurement errors in both variables.

We showed that [OIII] line do have a correlation with σ_*; this correlation is poor, with a Pearson correlation coefficient ranging from 0.42 to 0.55 in the different subsamples (see Table 2.3). The slope of the relation is statistically *lower* than unity, and the AGN sample shows the lowest value (see Table 2.4.3).

Our results agree with the findings of other studies, that indicated slopes less than unity. Gaskell (2009) proposes an equation for the $\sigma_{gas} - \sigma_*$ relation that appears to be in agreement with ours.

Hα and [NII] show a tighter relation, with a Pearson correlation coefficient of 0.60 and 0.62, respectively, in the AGN subsample (see Tables 2.3).

Nevertheless, even in the cases of Hα and [NII] lines we found slopes that are less than unity, even if they are usually steeper than the slope of the $\sigma_* - \sigma_{[OIII]}$ relation (Table 2.4.3).

While with [OIII] and Hα lines we find that the slopes in the SF and TR samples are usually steeper than in the AGN sample, with [NII] we find in the three subsamples slopes that agree within uncertainties.

All results from our measures of the intrinsic scatter and of the correlation coefficient do show that [NII] and Hα lines are more tightly tied to σ_* than [OIII].

In particularly, we find an intrinsic scatter using the [NII] emission line that is about 20% lower than in the case of [OIII].

We observe that the mean value of the ratio σ_{gas}/σ_* is enhanced in AGN rather than in StarForming or Transition galaxies, as reported in Table 2.4.2.

The fact that in the AGN sample the mean value of σ_{gas}/σ_* is close to unity must not confuse. We have $\sigma_{gas} < \sigma_*$ below $\sigma_{gas} \sim 100$ km s^{-1}, and $\sigma_{gas} > \sigma_*$ above, and this effect is much more evident in AGN than in StarForming or Transition galaxies.

This is caused by different reasons. One is the fact that StarForming and StarBurst galaxies reach lower values of magnitude –and so, very roughly, of mass and of velocity dispersion–, so that the numbers of points that are below the limits for which $\sigma_{gas}/\sigma_* < 1$ is greater than for AGN galaxies.

The more important reason is that in StarForming or Transition galaxies the ionized gas is probably less perturbed by non-gravitational effects from the central engine, so the measured σ_{gas} is subvirial as observed in quiescent galaxies.

The reason for the slope in the $\sigma_* - \sigma_{[OIII]}$ relation to be lower than in the cases of [NII] or Hα lines could reside in the fact that [OIII] is nearer to the central engine in AGN, and consequently can be more subject to its non gravitational acceleration; $\sigma_{[OIII]}$ is then more broadened respect to [NII] or Hα and its position in a $\sigma_* - \sigma_{gas}$ plot migrate toward higher value of σ_{gas}, so lowering the slope of the relation.

It is interesting to study the behavior of the Transition sample. $\sigma_{[NII]}$ and $\sigma_{H\alpha}$ show slopes that are similar than in the case of the StarForming , while for the [OIII] we see that the slope for the TR sample is intermediate between AGN and SF samples.

This is explained by the proximity of [OIII] to the AGN respect to [NII]

or Hα. Since TR galaxies can have a certain amount of nuclear activity, any acceleration effect on the ionized gas will be more efficient on the gas in the NLR. So, in TR galaxies we effectively see that [NII] and Hα lines are less affected by AGN activities.

We still see a slope less than unity in SF galaxies probably due to two effects. One is the perturbation to the gas kinematic due to the star formation itself. Shocks and heating from the burst of star formation can accelerate the gas even if the outcome of these accelerations will be obviously small respect to that of an AGN, and probably they would be diluted in an integrated spectrum.

The second reason is that in SF galaxies we could still see the effects of possible past nuclear activity. In fact, even if diagnostic diagram can assure us that a galaxy is undergoing star formation and in not an AGN *now*, nothing preclude that the galaxy could have experienced some activity in the past, since the idea that galaxies may have had multiple, periodic episode of AGN burst are nowadays commonly accepted.

We want to notice that the slope of the SF sample is higher in the case of the [OIII]. This effect is primarily due to our constraints in the minimum σ_{gas} and σ_* allowed (actually, 50 km s^{-1}). In fact, as we already noticed, lowering our limits results in steeper slopes, so we checked that *increasing* the limit to, e.g., 70 km s^{-1} causes the slopes in the SF sample to become shallower in the case of the [OIII] line, while they remain almost unchanged using [NII] and Hα lines.

Another clue of the fact that the differences in the slope and scatter in the $\sigma_{gas} - \sigma_*$ relation is due to the fact that [OIII] is more subject to acceleration from the AGN activity, come from the comparison of the [NII], Hα and [OIII] measures.

In effect, if we look at Figures 2.23 we see that [NII] and Hα clearly describe the same kinematics, with a Pearson correlation coefficient for the $\sigma_{[H\alpha]} - \sigma_{[]NII}$ relation of R_P =0.95, while the relation between $\sigma_{[OIII]}$ and $\sigma_{[NII]}$ or $\sigma_{H\alpha}$ shows a poorer correlation with R_P ~0.70 (see also Figures 2.25 and 2.24).

We would expect in Figures 2.29, 2.30 and 2.31, since rotation should tend to increase the σ of emission lines, an increase in the relative difference $(\sigma_{gas} - \sigma_*)/\sigma_*$ at higher b/a, so for galaxies seen face-on.

This is not observed. So, since b/a should be a parameter that play at least some role in the $\sigma_{gas} - \sigma_*$ relation we decided to test it.

Our samples were divided in four bin of inclination, and we derived the best fit parameters of the $\sigma_{gas} - \sigma_*$ relation in each bin.

As Nelson & Whittle (1996), we found that b/a is not correlated with σ_{gas}, as if the velocity field of the ionized gas is completely random respect to the inclination of the galaxy.

A conclusive test of [NII] being a better tracer for the stellar velocity dispersion respect to the [OIII] line is represented by the fact that in a $M_\bullet - \sigma_{gas}$ plot (see Figure 2.44, 2.45 and 2.46) the $M_\bullet - \sigma_{[NII]}$ presents the lowest scatter.

This is true when looking at moderately active galaxies, while in low redshift QSO and X-ray bright AGN (see Figure 2.47, 2.48 and 2.49) the correlation is poor in both [NII] and [OIII] lines, while it seems to be slightly stronger using Hα line.

This effect could be due to a correlation between the accretion of the SMBH and the FWHM of the broad emission lines, and hence of a correlation between

Table 2.9: Observed wavelengths of the emission lines at various redshifts.

Line	$\lambda_{z=0}$ [Å]	$\lambda_{z=0.5}$ [Å]	$\lambda_{z=1}$ [Å]
[OIII]	5006.8	7510.2	10013.6
Hα	6562.8	9844.2	13125.6
[NII]	6583.4	9875.1	13166.8

the activity of the AGN and the derived SMBH mass (Xu & Cao 2007), so that galaxies with an accreting SMBHs have $M_\bullet$ overestimated respect to galaxies with a moderately active nucleus.

Still, we cannot completely rule out the hypothesis that this effect is due instead to an underestimation of our line width measures, but if this is the case we should observe such bias even in the samples of quiescent or moderately active AGN.

This aspects needs further study.

We suggest that in using a ionized gas as a tracer for the stellar velocity dispersion, one should take into account two points.

The first one is that in any case the slope of the relation between the gas and the stars is less than unity, and that it must be calibrated depending on the class of galaxies studied.

The second point is that Hα and especially [NII] show less scatter and higher correlation with stars than [OIII], and a lower contamination from nuclear effects.

We propose an equation for the σ_{gas}/σ_* for each of the three line, in the different subsamples, using different regression methods.

It has to be noticed that due to its higher wavelength the [NII] line is observable in the optical up to a lower redshift than [OIII] line (see Table 2.7 for the observed wavelengths of the emission lines at various redshifts); nevertheless, [NII] can be also observable in NIR spectra.

2.7.1 Future work

Since the use of the [OIII] line was proposed to trace the stellar velocity dispersion in active and far galaxies, it has to be remembered that the tracer for σ_* should: 1-be observable in far galaxies 2-be used also in individual cases and not just statistically.

It would be interesting to put together the three emission lines and to perform a Principal Component Analysis to find if a combination of different lines could indicate a way to predict in a reliable way the stellar velocity dispersion.

Another point of interest is to find other lines that could be used as a tracer for the stellar velocity dispersion; in fact, since the need for a proxy for σ_* come for both active galaxies and high redshift galaxies, we will need different lines that could permit us to reach higher redshift.

In future studies we will also retrieve more samples of galaxies with measured $M_\bullet$; we will search for different types of galaxies to explore to which extent we can use the ionized gas as a tracer for the stellar velocity dispersion in different class of AGN, and to have some clues on the different behavior of the $M_\bullet - \sigma_{gas}$ relation in such galaxies.

Chapter 3

Cool Core Clusters and Con Cool Core Clusters

3.1 Introduction

3.1.1 Clusters of galaxies

Clusters of galaxies are the largest gravitationally bound structures in the Universe.

With diameters of several megaparsecs and masses up to 10^{15} $M_{\odot}$, they are often recognizable in images as distinct concentrations of galaxies centered on one or more brightest cluster members, and in fact they were seen first as overdensity in the projected distribution of galaxies in an optical image (Abell 1958).

Galaxy clusters are over-abundant in red, early-type galaxies compared to the field population (Oemler 1974; Butcher & Oemler 1978; Dressler 1980; Dressler et al. 1997; Treu et al. 2003; Balogh et al. 2004; Poggianti et al. 2006; Capak et al. 2007). Approximately 60% of bright galaxies located within the virial radii of cluster halos are bulge-dominated (E + S0) compared to $\sim$ 30% of similar luminosity galaxies located in very low-density environments (Whitmore & Gilmore 1991; Postman et al. 2005).

The fraction of weakly star-forming, early-type galaxies grows with the local galactic density, but even poor groups show differences compared to the general population (e.g., Postman & Geller 1984; Dressler et al. 1997; Zabludoff & Mulchaey 1998; Tran et al. 2001; Finn et al. 2008).

Galaxies in clusters typically experience more mergers than field galaxies (prior to their accretion), and this merger history bias plays a role in explaining population differences (Toomre & Toomre 1972). The fact that the overall mix of galaxies in clusters by type is known to evolve with redshift (Butcher & Oemler 1978; Ellingson et al. 2001; Tran et al. 2005; Gerke et al. 2007; Capak et al. 2007; Coil et al. 2008; Loh et al. 2008; Finn et al. 2008) suggests that the internal cluster processes play a major role in setting the differences between the cluster and field populations.

Galaxies in clusters and groups are subject to a number of processes that may suppress star formation or change the morphology of a galaxy. Ram-pressure

stripping (Gunn & Gott 1972; Quilis et al. 2000), galaxy-galaxy "harassment" within the cluster potential (Moore et al. 1996) and cold gas "strangulation" (Larson et al. 1980; Kauffmann et al. 1993), which cuts of the gas supply for ongoing star formation in cluster galaxies, are all effects that can contribute to the morphology of galaxies in clusters.

As tracers of the cosmic large-scale structure, galaxy clusters are also important probes for cosmology. It is the growth of structure in the matter distribution of the Universe that has a strong dependence on the cosmological model parameters and in particular on the nature of Dark Matter and Dark Energy. Since galaxy clusters are very sensitive tracers of structure growth, a census of the cluster population (via determination of the mass function of clusters) as a function of redshift can be used to test cosmological models (e.g. Borgani et al. 2001; Schuecker et al. 2003a,b; Henry 2004; Vikhlinin et al. 2003, 2009; Henry et al. 2009).

In fact, if we set the initial conditions and the cosmological parameters we can predict the redshift when virialized haloes of a given mass are expected to form.

Galaxy clusters are therefore very important giant astrophysical laboratories providing us with a well characterized physical environment compared to field galaxies, they also allow the study of large coeval galaxy populations and enable the investigation of their evolution in connection with the chemical and thermal evolution of the embedding intracluster medium; given moreover the importance of clusters as a test in cosmological models, they represent a key field of research in the modern studies of formation and evolution of galaxies.

Clusters of galaxies are searched in optical band, via the Sunayev-Zeldovich effect, via the gravitational lensing, but most informations on galaxy clusters come now from observations in X-ray .

Clusters in X-ray

The space between the galaxies is filled with a hot dilute plasma (with densities of 10^{-5} to 10^{-3} cm^{-3} from the cluster outskirts to the densest core regions) that emits X-rays and all is held in place by the gravity of a dark matter halo.

Gas temperatures typically lie in the range of 10^7-10^8 Kelvin, corresponding to X-ray luminosities of $L_X \sim 10^{43}$ erg s^{-1} to 10^{45} erg s^{-1} . The hot cluster plasma represent roughly the 90% of the baryons, while the rest are locked up in stars in galaxies (Lin et al. 2003). The hot gas forms a hydrostatic atmosphere, where the temperature and density distributions reflect the gravitating mass.

The warm baryons collapsed with the dark matter halo were subsequently heated to the virial temperature of the halo itself by accretion shocks and adiabatic compression. Mean gas temperatures reflect consequently the virial temperatures of halos, so that $T \propto \sigma^2$, where σ is the line of sight velocity dispersion of the cluster galaxies.

The electrons and ions of the thin plasma interact through Coulomb collisions and radiate mainly by thermal bremsstrahlung emission in the X-ray band (e.g., Sarazin 1988). Given the shape of the profile of the emissions, both of the continuum and of the recombination lines, the temperature and metallicity of the hot gas can be measured accurately with modern X-ray telescopes, since the shape of the spectrum for a thermal equilibrium plasma *is* determined by the plasma temperature and the elemental abundances.

Because the emission processes are collisional the power radiated per unit volume is proportional to the square of the density (so that the emission measure is $E = \int n_e n_H dV$). X-ray surface brightness can therefore be used to determine gas density, even when the temperature is poorly constrained.

The surface brightness profile can be fitted usually with a single β model (e.g., Cavaliere & Fusco-Femiano 1976; Branduardi-Raymont et al. 1981; Forman & Jones 1982)

$$S(r) = S_0\Big(1 + (r/r_c)^2\Big)^{-3\beta+1/2}, \tag{3.1}$$

where S_0 is central brightness and r_c is the core radius. Under the assumption of the gas and dark matter being isothermal, β is the ratio of the energy per unit mass in galaxies to that in the gas, and it is $\beta \sim 2/3$ for bright, relaxed clusters.

In the central regions of some clusters, where the gas temperature declines and the density rises rapidly, the fit is poorer and it is possible to use a double β model.

Assuming that the temperature is homogeneous in the cluster, it is possible to calculate the gas electron density profile as $n_e(r) = n_0[1+(r/r_c)^2]^{-3\beta/2}$ where n_0 is the central electron density. The errors introduced by this simplification in the presence of temperature variations is only on the order a few percent, which justifies this approximation.

Since galaxy clusters approach an equilibrium configuration characterized by a virial relation such as $E_{kin} = -2E_{pot} \propto \frac{\mathrm{GM}}{\mathrm{R}}$, and since analogously to the virial equilibrium of galaxies and dark matter particles, the ICM plasma thermalizes and attains a "virial temperature" which reflects the depth of the gravitational potential of the cluster, so in the collapse process the potential energy of the ICM is converted to internal heat, and if the gravitational potentials of clusters of different mass have a self-similar shape, as implied by numerical simulations of gravitational collapse (e.g. Navarro et al. 1995; Moore et al. 1999), then one finds the following self-similar relation between cluster mass and ICM temperature:

$$T \propto \sigma_{DM}^2 \propto M/R \propto M^{2/3} \tag{3.2}$$

where σ_{DM}^2 is the velocity dispersion of the dark matter particles.

The observed scaling relations make cluster temperatures and luminosities valuable proxies for the much less accessible masses of dark matter halos. Departures from these scaling relations reflect physics beyond pure gravitational dynamics.

Assuming that the gas is in hydrostatic equilibrium, and that the cluster has approximately spherical symmetry, the total mass of the cluster can be calculated from the temperature and density profile as

$$M(r) = -\frac{GkT}{\mu m_p} r\left(\frac{\log \rho_g}{\log r} + \frac{\log T}{\log r}\right) \tag{3.3}$$

where G is the gravitational constant, k the Boltzmann constant, ρ_g the gas density and m_p the proton mass. For a single β model, it take the form of

$$M(r) = \frac{3\beta kTr}{G\mu m_p} \frac{(r/r_c)^2}{1 + (r/r_c)^2}, \tag{3.4}$$

where μ is the molecular weight (μ=0.61).

Velocity dispersion and weak lensing masses generally agree with X-ray masses to within a few tens of percent, except perhaps in systems undergoing major mergers.

Chandra observations extending to large radii to measure the mass versus temperature relationship for relaxed clusters with temperatures in the range of 0.7- 9 keV, found $\mathrm{M}\propto\mathrm{T}^{1.5-1.6}$, which agrees with self-similar models (Vikhlinin et al. 2006).

The observed X-ray luminosity versus temperature relation for 3-10 keV clusters scales as $\mathrm{L}_X\mathrm{X}\propto\mathrm{T}^{2.6-2.8}$ which is steeper than expected for self-similar scaling (Markevitch et al. 1998; Arnaud & Evrard 1999). This departure may be due to excess entropy or preheating of the gas prior to virialization because of supernovae that enriched the gas with metals and AGN heating.

3.1.2 The cooling flow clusters and the cooling flow problem

The primary cooling process for intracluster gas is the emission of radiation. In assessing the role of cooling in the intracluster gas, it is useful to define a cooling time scale , that is the timescale in which the gas radiates away its thermal and gravitational energy if his luminosity is uncompensated by heating.

The cooling time of the gas is given by

$$t_{cool} = \frac{5}{2}\frac{n_e + n_i}{n_e}\frac{kT}{n_H \Lambda(A, T_m)}, \tag{3.5}$$

where $\Lambda(A, T_m)$ is the cooling function of the gas, and n_e, n_i, and n_H are the number densities of the electrons, ions, and hydrogen, respectively, and if the gas cools isobarically it can be written as

$$t_{cool} = 8.5 \times 10^{10} (\frac{n_p}{10^{-3}})^{-1} (\frac{T}{10^8})^{1/2} \text{ yr} \tag{3.6}$$

The hot gas in the cores of more than one third of clusters of galaxies, and most elliptical rich groups of galaxies, has a radiative cooling time shorter than the age of these systems, so the gas would develop into a cooling flow in the absence of additional heating. These clusters are commonly called Cool Core Cluster (CCC) against the Non Cool Core Clusters (NCCC) that don't exhibit such behavior.

If we define the cooling radius as the radius where the gas cooling time is equal to the age of the cluster assumed to be close to the Hubble time ($t_{age} \sim 1/H_0 = 13$ Gyr), we see that the physical meaning of the cooling radius within the classical cooling flow model is that, within that radius, the gas will loose all of its energy by X-ray emission and would be replaced by ambient hot gas from larger radii in a steady state inflow.

It is possible to calculate the energy loss rate from the integral of the X-ray emission inside the cooling radius and the mass inflow rate from the enthalpy influx necessary to compensate for this energy loss.

We have that

$$L_x \simeq \dot{M} \times (5kT)/(2\mu m_H) \simeq 1.3 \times 10^{44} T_5 \dot{M}_2 \text{ erg s}^{-1} \tag{3.7}$$

where $T_5 = (kT/5 \text{ keV})$ and $\dot{M}_2 = (\dot{M}/100 M_\odot/\text{year})$.

This implies that the ICM plasma should cool and condense in cool core clusters, in the absence of any heat source which could balance the cooling. The so-called "cooling flow" scenario (Fabian & Nulsen 1977; Fabian 1994) predicts mass deposition in the centers of some clusters at a rate of up to hundreds to thousands of solar masses a year. In general more than half of the clusters in the nearby Universe should have cooling flows in this model (Peres et al. 1998).

Still, since the cooling flow model leads to the prediction of very specific and testable spectral signatures of a steady state cooling flow (mainly Fe L complex), it could be seen that it fails to predict the observed amount and spatial distribution of star formation, line emission, and other expected products of cooling, which are generally observed only in the inner few tens of kpc.

In fact, even if first observations with the Einstein Observatory's Focal Plane Crystal Spectrometer [FPCS](Canizares et al. 1982, 1988) apparently detected the X-ray emission lines below 1 keV of various charge states of Fe L, that are the strongest spectroscopic signatures of cooling gas, the FPCS statistical significance, with an effective area of only one square centimeter, was very poor. Still, these results were bolstered by signatures of cooling at other wavelengths: filaments of Hα emission from warm, ionized gas (Heckman 1981); star formation (Johnstone et al. 1987; McNamara & O'Connell 1989); and pools of cold atomic and molecular gas (Edge 2001) provided support for a classical cooling flow model, albeit at lower rates.

With the advent of high quality spectra provided by XMM-Newton and Chandra, the cooling flow paradigm could be tested by spectroscopy. First evidence that the cluster cool cores are not consistent with the classical cooling flow model came from spectra analyzed with the Reflection Grating Spectrometers (RGS) on XMM-Newton.

These observations failed to confirm the line feature expected from cooling gas at $\sim$1 K, although there were some hint of lines consistent with a cooling rate much smaller then previous estimates. Ultraviolet line emission also suggests cooling rates about an order of magnitude smaller than in the pure cooling flow models (Oegerle et al. 2001; Bregman et al. 2006).

The absence of gas cooling below $\sim$1 K is confirmed in moderate spectral resolution CCD data from Chandra, XMM-Newton, and ASCA (e.g., McNamara et al. 2000; David et al. 2001; Fabian et al. 2003; Blanton et al. 2003; Peterson et al. 2003; Nulsen et al. 2005; Peterson & Fabian 2006; McNamara & Nulsen 2007 and references therein).

The spatial distribution of cool gas and star formation is more consistent with other, more complicated, cooling flow models, but at levels that fall orders of magnitude below the predictions. This failure implies that the gas is not condensing at the predicted rates, and that radiation losses are either being replenished, or the gas is condensing into an unseen state. Sensitive searches for the repository in optical, infrared, and radio bands have severely restricted the latter possibility, if not ruled it out entirely.

3.1.3 AGN feedback in cooling core clusters

The failure to find large quantities of cooling gas with the expected properties of a cooling flow implies that more than 90% of the energy radiated away is

being replenished. Only a few percent of the gas associated with the cooling flow forms stars and even less accretes onto the central supermassive black hole.

This "over-cooling" problem implies that feedback must have played a very important role in shaping galaxies. A number of feedback mechanisms have been proposed. For example, the heating by the UV background is expected to be effective only in small halos with masses M$< 10^{10} M_{\odot}$ at low redshift (Quinn et al. 1996; Gnedin 2000; Hoeft et al. 2006). The supernova (SN) feedback from instantaneous star formation may blow out gas from dwarf galaxies with halo mass less than M$< 10^{11} M_{\odot}$ but become much less effective in massive halos (MacLow & Ferrara 1999).

A clue to the solution may come from the observation (Burns, Gregory & Holman 1981) that every cluster with a strong cooling flow also contains a massive and active central radio galaxy. Tabor & Binney (1993) suggested that radio galaxies might regulate cooling flows, and this idea has gained considerable recent support from X-ray maps which show direct evidence for an interaction between radio lobes and the intracluster gas (McNamara et al. 2000, 2005; Fabian et al. 2003).

Croton et al. (2006) introduced a "radio mode" which is the result of the X-ray gas accretion on to the central SMBHs. The inclusion of this radio mode in their simulations allows suppression of both excessive cooling and growing of very massive galaxies. This AGN-heating mechanism is also found to be particularly effective in suppressing the star formation activity, that one expects to be prolific around the brightest cluster galaxies due to their preferential location in clusters. These BCGs should be accompanied by intense star formation activity and have blue colors, neither of which is observed and energy input from AGN outbursts in clusters may be especially needed to explain the observations.

AGN outbursts in the central dominant galaxy in groups and clusters can produce shocks, cavities and sound waves, all of which lead to re-heating of the cooling gas.

Buoyant bubbles and cavities in clusters

Although several mechanisms were discussed, the most promising heating process turned out to be the energy injected into the ICM by powerful radio jets emanating from AGNs in central galaxies of clusters and groups.

When the radio jets emerging from the central black hole interact with the dense thermal plasma of the ICM, two bubble-like lobes of non-thermal plasma should inflated, filled with relativistic particles and magnetic field and thus visible in radio observations. Such bubbles were first proposed by Gull & Northover (1973).

We know that the majority of cooling flow clusters contain powerful radio sources associated with central cD galaxies. Initial evidence of radio sources displacing, and evacuating cavities in, the X-ray-emitting intracluster medium was found with ROSAT observations of a few sources.

We now even know that about thirty cD clusters and a similar number of E galaxies and groups harbor cavities or bubbles in their X-ray halos (Fabian et al. 2000;McNamara et al. 2000, 2001; Schindler et al. 2001; Heinz et al. 2002;Mazzotta et al. 2002). Cavity systems are difficult to detect, so this is surely a lower limit to their numbers.

Like the radio lobes that created them, cavities are usually found in pairs of approximately elliptical X-ray surface brightness depressions, 20% to 40% below the level of the surrounding gas.

Cavity systems in clusters vary enormously in size, from diameters smaller than 1 kpc like those in M87 to diameters approaching 200 kpc in the Hydra A and MS0735.6+7421 clusters.

A correlation exists between radio luminosity and cavity power (Bîrzan et al. 2004; Dunn & Fabian 2006), but with a large scatter that is poorly understood.

Episodic (on-off) activity of radio jets should so injects these non-thermal radio bubbles which may heat in the end the ICM via weak shocks, and additionally these plasma bubbles are responsible for the mechanical (PdV) work done on the ICM for heating it, which is one of the favored mechanism of AGN-ICM feedback.

The work required to inflate the cavities against the surrounding pressure is up to pV = 10^{61} erg in rich clusters (e.g., Rafferty et al. 2006).

The total energy needed to create a cavity is the sum of its internal (thermal) energy, E, and the work required to inflate it, i.e., its enthalpy, H = E + pV . This is several times pV. The displaced gas mass is several 10^{10} $M_{\odot}$ in an average cluster system but can exceed 10^{10} $M_{\odot}$ in powerful outbursts such as those in MS0735.6+7421 and Hydra A.

In such sources the energy involved is 10^{60-62} erg, the most powerful radio outbursts known (e.g., McNamara et al. 2005; McNamara and Nulsen 2007). The energy involved is large enough to strongly affect or even quench any cooling flow, and to drive large-scale outflows that redistribute and heat the gas on cluster-wide scales.

A nearly empty cavity will rise into the cluster atmosphere like a buoyant weather balloon, traveling at a speed approaching the local free-fall velocity.

Studies of cavity populations should in principle yield information on the AGN duty cycle, the energy per AGN outburst, and outburst ages, once a reliable dynamical model has been established.

The Rafferty et al. (2006) sample is the most extensive cluster sample available, and thus provides a good representation of average cavity properties in clusters. The distribution of projected distances between the nucleus of the host cD and cavity centroid shows that the detection rate peaks in the inner 30 kpc or so and declines rapidly at larger distances. Only the rarest and most powerful outbursts produce detectable cavities beyond ∼100 kpc. Within 100 kpc the detection frequency declines formally as $\sim R^{-1.3}$, but is consistent with R^{-1} , the expected rate of decline for cavities launched on random trajectories.

The distribution of the ratio of projected nuclear distance to radius peaks at R/r∼ 2 and falls off rapidly beyond. Evidently, cavities travel roughly their own diameters before they disintegrate or become too difficult to detect.

Three estimates are commonly used for cavity ages: the buoyant rise time, the refill time, and the sound crossing time.

The first is the time taken for a bubble to rise at its buoyant terminal speed from the center of the cluster to its present location: $t_{buoy} \simeq R/v_t \simeq R\sqrt{SC/(2gV)}$ where S is the bubble's cross section, V its volume and C is the drag coefficient.

The "refill time" is the time required for gas to refill the displaced volume of the cavity as the bubble rises, so the time taken for a cavity to rise buoyantly through its own diameter:$t_r = 2\sqrt{r/g}$ for a spherical cavity of radius r, where g is the local gravitational acceleration.

Given the assumption that a bubble is launched from the nucleus and travels at approximately the sound speed, whereas it is likely to have a supersound speed at birth, and a subsonic speed when it travels buoyantly, the time it takes to rise to its projected position is then the sound crossing time, t_c=R/c_s, where c_s is the sound speed, and it is approximatively $c_s = \sqrt{kT/(\mu m_H)} \simeq 1100 T_5^{1/2}$ km s^{-1}.

Which timescale best approximates the true age depends on several unknown factors, and if the bubbles dynamics are still dominated by the AGN jets, all that age measures can be overestimated; still, it is an interesting measure of the last AGN episode.

But, even if AGN feedback scenario seems to be now widely accepted, the interest has shifted to the question: how is the ICM actually heated by AGN interaction? One of the most important earlier arguments in favor of cooling flows in the absence of feedback was that any possible heating mechanism has to be very well fine tuned, to exactly provide the balance to cooling. If too much heat is produced, it disperses the observed dense gas cores in cooling flows.

Also, there is little agreement on the rate of star formation in cooling core and non cooling core clusters.

Even if recent theoretical models predict that AGN feedback produces red and dead ellipticals (Croton et al. 2006, De Lucia et al. 2006), several recent studies have reported examples of ongoing star formation in the BCG in CCC (Cardiel et al. 1998, Crawford et al. 1999, Edge 2001, Goto 2005, McNamara et al. 2006, Wilman et al. 2006, O'Dea et al. 2008, Bildfell et al. 2008, Cavagnolo et al. 2008, Rafferty et al. 2008).

Additionally, Hicks & Mushotzky (2005) noted an excess in the UV flux as determined from the XMM-Newton Optical Monitor in many (but not all) the cooling flow clusters in their sample, which they interpreted as evidence for star formation.

Recently, Bildfell et al. (2008) undertook a comprehensive study of 48 clusters that span a wide range of X-ray characteristics. Specifically, they analyzed the surface brightness and color profiles of the BCGs hosted by these clusters, seeking to relate the resulting trends to the relative location of the BCGs within the clusters as well as to their global X-ray luminosity (L_X) and temperature (T_X). They found that 25% of their BCGs had bluer colors in their central regions, which they interpreted as evidence for ongoing star formation. They also found that these blue core systems only occurred in cool core clusters and then only if the BCG is located at the cluster center.

The mounting evidence for active star formation poses a challenge for models that invoke strong AGN feedback. Bildfell et al (2008) suggest that in the systems that they studied, heating by AGN feedback may be offsetting most of the radiative losses suffered by the hot gas surrounding the BCGs but not all. Therefore, the gas cools but at a significantly reduced rate. If this is indeed the case, it represents an important clue into how AGN feedback operates.

Rafferty et al. (2008) report the discovery of a sharp threshold for the onset of star formation in CCC, requiring a cooling time of less than $\sim 10^8$ yr and a cavity power lower than the X-ray cooling luminosity, implying again a direct link between AGN feedback and star formation suppression.

Pipino et al. (2009) present an analysis of near-ultraviolet (NUV) data from the GALEX mission and (optical) color profiles for a sample of 7 BCGs in the

Canadian Cluster Comparison Project, and find a one-to-one correspondence between blue cores and a NUV-enhancement. The implied star formation in the blue BCGs typically has an age less than 200 Myrs and contributes mass fractions of less than a percent. They suggest that any AGN heating of the intracluster medium in massive clusters only acts to reduce the magnitude of the cooling flow and that once this flow starts, it is nearly always active.

So, one of the nowadays problem is to understand how much are AGN effective in suppressing the star formation, a point that may depend on how and how much their power output varies over time, and on how efficiently cavity enthalpy and shock energy is converted to heat.

3.1.4 The aim of this work

With this work we want to to compare the mean optical, NIR and UV colors for a sample of both CC and NCC cluster galaxies.

We are interested in assessing if broad band colors are useful tools for detecting differences in the mean star formation rate between CC and NCC clusters – differences observed by other authors from e.g. the analysis of emission lines.

Although different methods can be used to measure the star formation rate in single objects, they are usually time consuming.

While such information is of vital importance for understanding galaxy cluster physics, we also need a tool that enables study of larger samples, so as to give a wider view of the "big picture".

This will also help us understand to what extent the AGN is able to re-heat the infalling gas.

3.2 Sample selection

We drawn our sample from the extended HIFLUGCS sample (HIghest X-ray FLUx Galaxy Cluster Sample; Reiprich 2001, Reiprich & Böhringer 2002) used by Chen et al. (2007); this is the largest X-ray flux limited galaxy cluster sample selected only by X-ray flux, irrespective of the cluster morphology.

Based on the ROSAT All-Sky Survey, the extended HIFLUGCS sample is composed of 63 galaxy clusters with galactic latitude |bII| $\geq$20 deg and a flux threshold of f_X(0.1-2.4 keV)$\geq$ 2 $\times 10^{-11}$ ergs s^{-1}cm^{-2}, and of 43 more clusters.

Another 6 clusters were added from the sample presented by Rafferty et al. (2008).

We have found the coordinates of the center of these 112 clusters as identified in X-ray observation in the BAX and XBACs database.

BAX, Base de Données Amas de Galaxies X is a multi-wavelength database dedicated to X-ray clusters and groups (http://webast.ast.obs-mip.fr/bax; Sadat et al 2004); XBACs, X-ray-brightest Abell-type clusters of galaxies, is an all-sky, X-ray flux-limited sample of 242 Abell clusters of galaxies compiled from ROSAT All-Sky Survey data (Ebeling et al. 1996a, 1996b).

We present our initial cluster sample in Table 3.1, in which we report the redshift and coordinates of the clusters, and their properties as given in Chen et al. (2007).

The emission measure weighted temperature T_X is mainly derived from a single temperature fit to the global X-ray spectrum of the clusters (Markevitch

et al. 1998; Reiprich 2001, and references therein), while in some clusters it is derived from using the L_X-T relation of Markevitch (1998).

The mass deposit rate are derived from a classical cooling flow model. r_{500} is the radius at which the average density of the enclosed region is 500 times the critical density of the universe.

Table 3.1: Cluster properties. (1) name (2) redshift (3),(4) right ascension and declination in the NED database (5),(6) right ascension and declination of the X-ray centroid (7) cluster mass (8) radius at which the mean density of the cluster is 500 times that of the critical density of the universe (9) emission measure weighted temperature (10) core radius (11) mass deposition rate (see text)

	name	**z**	**ra**	**dec**	**ra**$_X$	**dec**$_X$	**M**$_{500}$ (**10**^{14} $M_\odot$)	**r**$_{500}$ **(Mpc)**	**T**$_X$ **(keV)**	**r**$_c$ **(kpc)**	$\dot{M}$ **[M**$_\odot$**/yr]**
	(1)	(2)	(3)	(4)	(5)	(6)	(7)	(8)	(9)	(10)	(11)
1	A0335	0.0349	34.0320	-12.1518	34.032	-12.151	$2.79^{+1.09}_{-1.63}$	$1.20^{+0.14}_{-0.30}$	$3.01^{+0.07}_{-0.07}$	33^{+0}_{-0}	360^{+20}_{-17}
2	A0085	0.0556	10.4075	-9.3425	10.453	-9.318	$8.08^{+1.57}_{-3.51}$	$1.68^{+0.10}_{-0.29}$	$6.10^{+0.20}_{-0.20}$	82^{+3}_{-3}	200^{+33}_{-27}
3	A0119	0.0440	14.0890	-1.2629	14.054	-1.235	$8.98^{+1.20}_{-2.59}$	$1.76^{+0.07}_{-0.19}$	$5.80^{+0.60}_{-0.60}$	501^{+27}_{-26}	0^{+0}_{-0}
4	A0133	0.0569	15.6624	-21.9543	15.668	-21.880	$4.30^{+1.00}_{-2.08}$	$1.36^{+0.10}_{-0.27}$	$3.80^{+2.00}_{-0.90}$	45^{+1}_{-1}	108^{+55}_{-51}
5	A0262	0.0161	28.1560	-4.1371	28.191	36.157	$0.94^{+0.05}_{-0.12}$	$0.85^{+0.02}_{-0.04}$	$2.15^{+0.06}_{-0.06}$	41^{+11}_{-9}	14^{+4}_{-4}
6	A0399	0.0715	44.4851	13.0164	44.457	13.053	$7.74^{+2.15}_{-2.32}$	$1.63^{+0.14}_{-0.18}$	$7.40^{+0.70}_{-0.70}$	449^{+131}_{-99}	0^{+0}_{-0}
7	A0400	0.0240	44.4108	6.0333	44.412	6.006	$1.33^{+0.11}_{-0.16}$	$0.95^{+0.02}_{-0.04}$	$2.31^{+0.14}_{-0.14}$	154^{+9}_{-8}	0^{+0}_{-0}
8	A0401	0.0748	44.7373	13.5823	44.737	13.573	$8.38^{+1.22}_{-2.84}$	$1.67^{+0.08}_{-0.21}$	$8.30^{+0.50}_{-0.50}$	245^{+11}_{-10}	0^{+0}_{-0}
9	A0478	0.0900	63.3362	10.4764	63.359	10.466	$8.85^{+3.00}_{-4.69}$	$1.68^{+0.17}_{-0.37}$	$7.10^{+0.40}_{-0.40}$	98^{+2}_{-2}	645^{+137}_{-113}
10	A0496	0.0328	57.9943	-22.1680	68.397	-13.246	$4.81^{+0.89}_{-2.11}$	$1.44^{+0.08}_{-0.25}$	$4.13^{+0.08}_{-0.08}$	30^{+1}_{-1}	114^{+35}_{-28}
11	A0576	0.0381	110.3506	55.7389	110.382	55.764	$4.61^{+3.25}_{-2.39}$	$1.42^{+0.28}_{-0.30}$	$4.02^{+0.07}_{-0.07}$	394^{+221}_{-125}	0^{+0}_{-0}
12	A0754	0.0528	137.2087	-9.6366	137.256	-9.655	$13.86^{+4.40}_{-6.43}$	$2.02^{+0.19}_{-0.38}$	$9.00^{+0.50}_{-0.50}$	239^{+17}_{-16}	0^{+0}_{-0}
13	A1060	0.0114	159.2137	-27.5265	159.169	-27.521	$2.50^{+0.62}_{-1.02}$	$1.19^{+0.09}_{-0.19}$	$3.24^{+0.06}_{-0.06}$	94^{+15}_{-12}	0^{+0}_{-0}
14	A1367	0.0216	176.1231	19.8391	176.151	19.772	$7.42^{+1.11}_{-2.37}$	$1.69^{+0.08}_{-0.20}$	$3.55^{+0.08}_{-0.08}$	383^{+24}_{-22}	0^{+0}_{-0}
15	A1644	0.0474	194.3115	-17.3535	194.335	-17.381	$7.34^{+4.30}_{-4.40}$	$1.64^{+0.27}_{-0.43}$	$4.70^{+0.90}_{-0.70}$	299^{+127}_{-92}	0^{+0}_{-0}
16	A1650	0.0845	194.6926	-1.7530	194.674	-1.756	$6.53^{+2.17}_{-2.43}$	$1.52^{+0.15}_{-0.22}$	$5.60^{+0.60}_{-0.60}$	281^{+104}_{-70}	0^{+0}_{-0}
17	A1651	0.0860	194.8456	-4.1862	194.850	-4.189	$8.29^{+1.95}_{-3.60}$	$1.65^{+0.12}_{-0.28}$	$6.30^{+0.50}_{-0.50}$	180^{+9}_{-9}	81^{+30}_{-23}

Continued on next page

Table 3.1 – continued from previous page

	name	z	ra	dec	ra_X	dec_X	M_{500} ($10^{14}\ M_\odot$)	r_{500} (Mpc)	T_X (keV)	r_c (kpc)	$\dot{M}$ [$M_\odot$/yr]
	(1)	(2)	(3)	(4)	(5)	(6)	(7)	(8)	(9)	(10)	(11)
18	A1736	0.0461	201.7173	-27.1093	201.745	-27.125	$2.17^{+0.62}_{-0.69}$	$1.09^{+0.10}_{-0.13}$	$3.50^{+0.40}_{-0.40}$	374^{+177}_{-129}	0^{+0}_{-0}
19	A1795	0.0616	207.2522	26.5852	207.218	26.598	$9.87^{+3.85}_{-5.48}$	$1.79^{+0.21}_{-0.42}$	$6.00^{+0.30}_{-0.30}$	78^{+1}_{-1}	399^{+47}_{-39}
20	A2029	0.0767	227.7447	5.7617	227.729	5.720	$9.95^{+3.29}_{-5.16}$	$1.77^{+0.18}_{-0.38}$	$8.70^{+0.30}_{-0.30}$	83^{+2}_{-2}	514^{+93}_{-78}
21	A2052	0.0348	229.1896	7.0003	229.176	7.002	$2.70^{+0.57}_{-1.32}$	$1.19^{+0.08}_{-0.24}$	$3.03^{+0.04}_{-0.04}$	36^{+1}_{-1}	108^{+188}_{-49}
22	A2063	0.0354	230.7578	8.6394	230.757	8.580	$2.36^{+0.24}_{-0.59}$	$1.14^{+0.04}_{-0.10}$	$3.68^{+0.11}_{-0.11}$	110^{+6}_{-6}	21^{+2}_{-2}
23	A2065	0.0721	230.6776	27.7226	230.612	27.711	$11.19^{+9.57}_{-6.82}$	$1.84^{+0.42}_{-0.50}$	$5.40^{+0.30}_{-0.30}$	689^{+360}_{-186}	0^{+0}_{-0}
24	A2142	0.0899	239.5672	27.2246	239.592	27.233	$14.33^{+3.64}_{-6.83}$	$1.97^{+0.15}_{-0.38}$	$8.80^{+0.60}_{-0.60}$	153^{+5}_{-5}	337^{+82}_{-61}
25	A2147	0.0351	240.5716	15.8954	240.578	16.020	$2.31^{+0.40}_{-0.36}$	$1.13^{+0.06}_{-0.06}$	$4.91^{+0.28}_{-0.28}$	237^{+102}_{-64}	0^{+0}_{-0}
26	A2163	0.2010	243.8922	-6.1240	243.956	-6.150	$16.00^{+3.48}_{-4.86}$	$1.85^{+0.13}_{-0.21}$	$13.29^{+0.64}_{-0.64}$	519^{+30}_{-29}	0^{+0}_{-0}
27	A2199	0.0302	247.1540	39.5243	247.165	39.550	$4.29^{+1.18}_{-1.89}$	$1.39^{+0.12}_{-0.24}$	$4.10^{+0.08}_{-0.08}$	139^{+10}_{-9}	77^{+7}_{-6}
28	A2204	0.1523	248.1903	5.5785	248.195	5.574	$5.82^{+1.91}_{-2.98}$	$1.38^{+0.14}_{-0.29}$	$7.21^{+0.25}_{-0.25}$	67^{+3}_{-2}	1287^{+122}_{-129}
29	A2244	0.0970	255.6835	34.0468	255.667	34.063	$5.48^{+1.48}_{-2.23}$	$1.42^{+0.12}_{-0.23}$	$7.10^{+5.00}_{-2.20}$	125^{+10}_{-10}	129^{+199}_{-127}
30	A2255	0.0800	258.1294	64.0926	258.188	64.062	$7.86^{+0.92}_{-1.67}$	$1.63^{+0.06}_{-0.12}$	$6.87^{+0.20}_{-0.20}$	593^{+35}_{-32}	0^{+0}_{-0}
31	A2256	0.0601	255.9314	78.7174	256.010	78.632	$12.12^{+3.41}_{-4.12}$	$1.91^{+0.16}_{-0.25}$	$7.50^{+0.40}_{-0.40}$	587^{+39}_{-36}	0^{+0}_{-0}
32	A2589	0.0416	351.0022	16.8247	350.973	16.809	$3.24^{+0.54}_{-1.40}$	$1.26^{+0.07}_{-0.21}$	$3.70^{+2.20}_{-1.10}$	118^{+7}_{-7}	19^{+53}_{-19}
33	A2597	0.0852	351.3252	-12.1083	351.319	-12.124	$3.71^{+1.35}_{-2.22}$	$1.26^{+0.14}_{-0.33}$	$3.60^{+0.20}_{-0.20}$	57^{+2}_{-2}	501^{+58}_{-51}
34	A2634	0.0312	354.5766	27.0270	354.615	27.022	$4.51^{+0.67}_{-1.00}$	$1.42^{+0.07}_{-0.11}$	$3.70^{+0.28}_{-0.28}$	364^{+43}_{-38}	0^{+0}_{-0}
35	A2657	0.0404	356.2125	9.1443	356.237	9.201	$6.06^{+1.32}_{-2.57}$	$1.55^{+0.11}_{-0.26}$	$3.70^{+0.30}_{-0.30}$	119^{+5}_{-4}	2^{+5}_{-2}
36	A3112	0.0750	49.4683	-44.2429	49.485	-44.238	$4.36^{+1.26}_{-2.25}$	$1.34^{+0.12}_{-0.29}$	$4.70^{+0.40}_{-0.40}$	61^{+2}_{-2}	346^{+123}_{-97}
37	A3158	0.0590	55.6652	-53.6306	55.683	-53.641	$5.75^{+0.89}_{-1.66}$	$1.49^{+0.07}_{-0.16}$	$5.77^{+0.10}_{-0.05}$	268^{+19}_{-18}	0^{+0}_{-0}
38	A3266	0.0594	67.7997	-61.4063	67.856	-61.417	$19.24^{+4.76}_{-7.58}$	$2.23^{+0.17}_{-0.34}$	$7.70^{+0.80}_{-0.80}$	564^{+20}_{-19}	0^{+0}_{-0}
39	A3376	0.0455	90.1815	-40.0499	90.427	-39.986	$6.77^{+1.55}_{-1.99}$	$1.60^{+0.11}_{-0.17}$	$4.30^{+0.60}_{-0.60}$	754^{+68}_{-60}	0^{+0}_{-0}
40	A3391	0.0531	96.5643	-53.6812	96.608	-53.678	$6.04^{+0.74}_{-1.69}$	$1.53^{+0.06}_{-0.16}$	$5.70^{+0.70}_{-0.70}$	234^{+23}_{-21}	0^{+0}_{-0}

Continued on next page

Table 3.1 – continued from previous page

	name	z	ra	dec	ra_X	dec_X	M_{500} ($10^{14}\ M_\odot$)	r_{500} (Mpc)	T_X (keV)	r_c (kpc)	$\dot{M}$ [$M_\odot$/yr]
	(1)	(2)	(3)	(4)	(5)	(6)	(7)	(8)	(9)	(10)	(11)
41	A3395s	0.0498	96.8795	-54.3994	96.792	-54.469	$9.48^{+4.35}_{-4.29}$	$1.78^{+0.24}_{-0.32}$	$4.80^{+0.40}_{-0.40}$	604^{+172}_{-117}	0^{+0}_{-0}
42	A3526	0.0103	192.2158	-41.3058	192.230	-41.292	$3.41^{+0.60}_{-1.36}$	$1.32^{+0.07}_{-0.20}$	$3.68^{+0.06}_{-0.06}$	37^{+4}_{-4}	24^{+6}_{-5}
43	A3558	0.0480	201.9782	-31.4922	201.991	-31.488	$6.71^{+0.91}_{-2.12}$	$1.59^{+0.07}_{-0.19}$	$5.50^{+0.30}_{-0.30}$	223^{+5}_{-5}	0^{+0}_{-0}
44	A3562	0.0499	203.3825	-31.6729	203.460	-31.678	$3.51^{+0.43}_{-0.91}$	$1.28^{+0.05}_{-0.12}$	$5.16^{+0.16}_{-0.16}$	98^{+5}_{-5}	0^{+0}_{-0}
45	A3571	0.0397	206.8706	-32.8658	206.867	-32.854	$8.76^{+1.69}_{-3.43}$	$1.75^{+0.10}_{-0.27}$	$6.90^{+0.30}_{-0.30}$	181^{+6}_{-6}	35^{+11}_{-10}
46	A3581	0.0214	211.8645	-27.0207	211.877	-27.018	$0.93^{+0.19}_{-0.38}$	$0.84^{+0.05}_{-0.14}$	$1.83^{+0.04}_{-0.04}$	35^{+4}_{-4}	49^{+12}_{-11}
47	A3667	0.0560	303.1254	-56.8165	303.098	-56.813	$5.28^{+0.52}_{-1.15}$	$1.46^{+0.05}_{-0.11}$	$7.00^{+0.60}_{-0.60}$	279^{+10}_{-9}	0^{+0}_{-0}
48	A4038	0.0283	356.8797	-28.2029	356.919	-28.138	$2.58^{+0.49}_{-1.05}$	$1.18^{+0.07}_{-0.19}$	$3.15^{+0.03}_{-0.03}$	58^{+3}_{-3}	68^{+14}_{-12}
49	A4059	0.0460	359.1696	-34.6716	359.250	-34.752	$4.41^{+1.14}_{-2.03}$	$1.39^{+0.11}_{-0.26}$	$4.10^{+0.30}_{-0.30}$	89^{+5}_{-5}	69^{+20}_{-15}
50	COMA	0.0232	194.9531	27.9807	194.883	27.903	$9.95^{+2.10}_{-2.99}$	$1.86^{+0.12}_{-0.21}$	$8.38^{+0.34}_{-0.34}$	343^{+22}_{-20}	0^{+0}_{-0}
51	EXO0422	0.0390	66.4638	-8.5608	66.463	-8.560	$2.72^{+1.71}_{-1.45}$	$1.19^{+0.21}_{-0.27}$	$2.90^{+0.90}_{-0.60}$	142^{+40}_{-30}	48^{+59}_{-38}
52	FORNAX	0.0046	54.6289	-35.4545	54.628	-35.454	$1.29^{+0.44}_{-0.55}$	$0.96^{+0.10}_{-0.16}$	$1.20^{+0.04}_{-0.04}$	173^{+17}_{-15}	0^{+0}_{-0}
53	HYDRA-A	0.0538	159.2137	-27.5265	139.524	-12.095	$4.07^{+1.27}_{-2.14}$	$1.34^{+0.13}_{-0.29}$	$3.80^{+0.20}_{-0.20}$	50^{+1}_{-1}	293^{+150}_{-84}
54	IIIZw54	0.0311	55.3229	15.3975	55.322	15.397	$3.76^{+2.82}_{-2.26}$	$1.33^{+0.27}_{-0.35}$	$2.16^{+0.35}_{-0.30}$	289^{+123}_{-72}	0^{+0}_{-0}
55	MKW3S	0.0450	230.4660	7.7088	230.466	7.708	$3.22^{+0.92}_{-1.53}$	$1.25^{+0.11}_{-0.24}$	$3.50^{+0.20}_{-0.20}$	66^{+2}_{-2}	121^{+76}_{-44}
56	MKW4	0.0200	180.9905	1.8883	180.990	1.888	$0.69^{+0.04}_{-0.14}$	$0.76^{+0.01}_{-0.06}$	$1.71^{+0.09}_{-0.09}$	11^{+0}_{-0}	16^{+2}_{-2}
57	MKW8	0.0270	220.1796	3.4530	220.179	3.453	$2.00^{+0.46}_{-0.59}$	$1.08^{+0.08}_{-0.12}$	$3.29^{+0.23}_{-0.22}$	106^{+70}_{-42}	0^{+0}_{-0}
58	NGC1550	0.0123	64.9080	2.4099	64.908	2.409	$0.68^{+0.14}_{-0.24}$	$0.77^{+0.05}_{-0.10}$	$1.43^{+0.04}_{-0.03}$	45^{+15}_{-10}	20^{+10}_{-8}
59	NGC4636	0.0037	190.7078	2.6878	190.707	2.687	$0.18^{+0.03}_{-0.06}$	$0.49^{+0.03}_{-0.07}$	$0.76^{+0.01}_{-0.01}$	6^{+2}_{-1}	2^{+2}_{-1}
60	NGC5044	0.0090	198.8499	-16.3855	198.849	-16.385	$0.49^{+0.12}_{-0.25}$	$0.69^{+0.05}_{-0.15}$	$1.07^{+0.01}_{-0.01}$	11^{+0}_{-0}	28^{+1}_{-1}
61	NGC507	0.0165	20.9167	33.2556	20.916	33.255	$0.46^{+0.02}_{-0.07}$	$0.67^{+0.01}_{-0.04}$	$1.26^{+0.07}_{-0.07}$	19^{+1}_{-1}	14^{+2}_{-2}
62	S1101	0.0580	348.4938	-42.7275	348.493	-42.727	$2.94^{+1.57}_{-1.88}$	$1.20^{+0.18}_{-0.34}$	$3.00^{+1.20}_{-0.70}$	55^{+1}_{-1}	299^{+179}_{-112}
63	ZwCl1215	0.0750	184.4227	3.6590	184.422	3.659	$9.46^{+5.74}_{-4.87}$	$1.74^{+0.30}_{-0.37}$	$5.58^{+0.89}_{-0.78}$	431^{+27}_{-25}	0^{+0}_{-0}

Continued on next page

Table 3.1 – continued from previous page

	name	z	ra	dec	ra$_X$	dec$_X$	M_{500} ($10^{14}\ M_\odot$)	r_{500} (Mpc)	T_X (keV)	r_c (kpc)	$\dot{M}$ [$M_\odot$/yr]
	(1)	(2)	(3)	(4)	(5)	(6)	(7)	(8)	(9)	(10)	(11)
64	3C129	0.0223	72.2878	45.0109	72.287	45.010	$5.39^{+2.26}_{-2.33}$	$1.51^{+0.19}_{-0.26}$	$5.60^{+0.70}_{-0.60}$	318^{+178}_{-107}	0^{+0}_{-0}
65	A0539	0.0288	79.1464	6.4540	79.146	6.454	$2.68^{+0.32}_{-0.85}$	$1.19^{+0.05}_{-0.14}$	$3.24^{+0.09}_{-0.09}$	147^{+13}_{-12}	3^{+1}_{-1}
66	A0548e	0.0410	86.7573	-25.6163	86.366	-25.906	$1.49^{+0.13}_{-0.17}$	$0.97^{+0.03}_{-0.04}$	$3.10^{+0.10}_{-0.10}$	118^{+12}_{-11}	0^{+0}_{-0}
67	A0548w	0.0424	86.7573	-25.6163	87.169	-25.449	$1.00^{+0.58}_{-0.52}$	$0.85^{+0.14}_{-0.19}$	$1.20^{+0.19}_{-0.17}$	198^{+89}_{-61}	0^{+0}_{-0}
68	A0644	0.0704	124.3602	-7.5892	124.355	-7.528	$8.41^{+2.15}_{-3.81}$	$1.68^{+0.13}_{-0.31}$	$7.10^{+0.60}_{-0.60}$	202^{+6}_{-6}	16^{+29}_{-15}
69	A1413	0.1427	178.8288	23.4086	178.826	23.408	$9.77^{+2.78}_{-4.58}$	$1.65^{+0.14}_{-0.31}$	$7.32^{+0.26}_{-0.24}$	178^{+12}_{-11}	190^{+40}_{-32}
70	A1689	0.1840	197.8925	-1.3654	197.873	-1.336	$14.98^{+5.82}_{-8.38}$	$1.84^{+0.21}_{-0.44}$	$9.23^{+0.28}_{-0.28}$	162^{+6}_{-6}	683^{+239}_{-182}
71	A1775	0.0757	205.4816	26.3648	205.460	26.382	$4.19^{+1.36}_{-1.69}$	$1.32^{+0.13}_{-0.21}$	$3.69^{+0.20}_{-0.11}$	259^{+19}_{-17}	0^{+0}_{-0}
72	A1800	0.0748	207.4226	28.0690	207.346	28.091	$5.94^{+4.83}_{-3.59}$	$1.49^{+0.33}_{-0.40}$	$4.02^{+0.64}_{-0.56}$	391^{+223}_{-131}	0^{+0}_{-0}
73	A1914	0.1712	216.5124	37.8256	216.509	37.835	$11.84^{+3.65}_{-5.84}$	$1.72^{+0.16}_{-0.35}$	$0.53^{+0.51}_{-0.50}$	230^{+10}_{-10}	180^{+50}_{-40}
74	A2151w	0.0369	241.3125	17.7485	241.179	17.726	$1.60^{+0.35}_{-0.61}$	$1.00^{+0.07}_{-0.15}$	$2.40^{+0.06}_{-0.06}$	68^{+5}_{-4}	30^{+3}_{-3}
75	A2319	0.0564	290.1889	43.9619	290.274	43.964	$13.57^{+2.15}_{-4.59}$	$1.99^{+0.10}_{-0.26}$	$9.20^{+0.70}_{-0.70}$	284^{+14}_{-13}	0^{+0}_{-0}
76	A2734	0.0620	2.8339	-28.8718	2.829	-28.857	$4.82^{+0.85}_{-1.56}$	$1.40^{+0.08}_{-0.17}$	$3.85^{+0.62}_{-0.54}$	211^{+26}_{-23}	0^{+0}_{-0}
77	A2877	0.0241	17.4554	-45.9006	17.445	-45.901	$6.88^{+6.74}_{-3.79}$	$1.64^{+0.42}_{-0.38}$	$3.50^{+2.20}_{-1.10}$	189^{+18}_{-16}	0^{+0}_{-0}
78	A3395n	0.0498	96.8795	-54.3994	96.792	-54.469	$8.13^{+5.53}_{-4.69}$	$1.69^{+0.32}_{-0.42}$	$4.80^{+0.40}_{-0.40}$	672^{+383}_{-203}	0^{+0}_{-0}
79	A3528n	0.0540	193.5758	-29.0210	193.684	-29.265	$4.49^{+0.78}_{-1.53}$	$1.38^{+0.08}_{-0.18}$	$3.40^{+1.66}_{-0.64}$	177^{+16}_{-15}	0^{+0}_{-0}
80	A3528s	0.0551	193.5758	-29.0210	193.592	-29.011	$2.76^{+0.39}_{-0.44}$	$1.17^{+0.05}_{-0.07}$	$3.15^{+0.89}_{-0.59}$	100^{+8}_{-8}	1^{+11}_{-1}
81	A3530	0.0544	193.9037	-30.3540	193.922	-30.351	$4.34^{+1.09}_{-1.27}$	$1.37^{+0.11}_{-0.15}$	$3.89^{+0.27}_{-0.25}$	420^{+74}_{-61}	0^{+0}_{-0}
82	A3532	0.0539	194.3299	-30.3702	194.338	-30.396	$6.63^{+1.17}_{-2.84}$	$1.57^{+0.09}_{-0.27}$	$4.58^{+0.19}_{-0.17}$	281^{+26}_{-24}	0^{+0}_{-0}
83	A3560	0.0495	202.9604	-33.2237	203.107	-33.096	$2.77^{+1.85}_{-1.26}$	$1.18^{+0.22}_{-0.22}$	$3.16^{+0.51}_{-0.44}$	255^{+30}_{-27}	0^{+0}_{-0}
84	A3627	0.0163	243.8868	-60.9083	243.587	-60.871	$4.92^{+0.67}_{-0.91}$	$1.48^{+0.06}_{-0.10}$	$6.02^{+0.08}_{-0.08}$	299^{+56}_{-49}	0^{+0}_{-0}
85	A3695	0.0890	308.6990	-35.8274	308.694	-35.830	$7.03^{+4.66}_{-4.22}$	$1.55^{+0.29}_{-0.41}$	$5.29^{+0.85}_{-0.74}$	398^{+253}_{-149}	0^{+0}_{-0}
86	A3822	0.0760	328.5260	-57.8469	328.542	-57.867	$4.69^{+1.19}_{-1.46}$	$1.37^{+0.11}_{-0.16}$	$4.90^{+0.78}_{-0.69}$	350^{+159}_{-111}	0^{+0}_{-0}

Continued on next page

Table 3.1 – continued from previous page

	name	z	ra	dec	ra_X	dec_X	M_{500} ($10^{14}\ M_\odot$)	r_{500} (Mpc)	T_X (keV)	r_c (kpc)	$\dot{M}$ [$M_\odot$/yr]
	(1)	(2)	(3)	(4)	(5)	(6)	(7)	(8)	(9)	(10)	(11)
87	A3827	0.0980	330.4546	-59.9541	330.486	-59.954	$15.50^{+13.81}_{-9.76}$	$2.01^{+0.48}_{-0.56}$	$7.08^{+1.13}_{-0.99}$	593^{+247}_{-148}	0^{+0}_{-0}
88	A3888	0.1510	338.5960	-37.7247	338.637	-37.733	$29.81^{+24.98}_{-21.73}$	$2.38^{+0.54}_{-0.84}$	$8.84^{+1.41}_{-1.24}$	400^{+45}_{-39}	0^{+0}_{-0}
89	A3921	0.0936	342.4108	-64.3876	342.499	-64.431	$6.59^{+1.50}_{-2.32}$	$1.51^{+0.11}_{-0.20}$	$5.73^{+0.24}_{-0.23}$	328^{+25}_{-23}	0^{+0}_{-0}
90	AWM7	0.0172	43.6342	41.5861	43.634	41.586	$4.92^{+1.21}_{-2.26}$	$1.48^{+0.11}_{-0.27}$	$3.75^{+0.09}_{-0.09}$	173^{+17}_{-15}	6^{+3}_{-4}
91	HCG94	0.0417	349.3187	18.7197	349.318	18.719	$2.25^{+0.24}_{-0.60}$	$1.11^{+0.04}_{-0.11}$	$3.45^{+0.30}_{-0.30}$	86^{+4}_{-3}	6^{+3}_{-2}
92	IIZw108	0.0494	318.5247	2.5755	318.524	2.575	$3.85^{+2.60}_{-2.00}$	$1.32^{+0.25}_{-0.28}$	$3.44^{+0.55}_{-0.48}$	365^{+159}_{-105}	0^{+0}_{-0}
93	M49	0.0044	187.4448	8.0005	187.444	8.000	$0.67^{+0.40}_{-0.47}$	$0.77^{+0.13}_{-0.26}$	$0.95^{+0.02}_{-0.01}$	10^{+0}_{-0}	2^{+0}_{-0}
94	NGC499	0.0147	20.7979	33.4606	20.797	33.460	$0.33^{+0.25}_{-0.23}$	$0.60^{+0.12}_{-0.20}$	$0.72^{+0.03}_{-0.02}$	23^{+2}_{-1}	11^{+4}_{-3}
95	NGC5813	0.0064	225.2969	1.7020	225.296	1.702	$0.43^{+0.45}_{-0.33}$	$0.66^{+0.18}_{-0.26}$	$0.52^{+0.08}_{-0.07}$	24^{+8}_{-5}	9^{+11}_{-5}
96	NGC5846	0.0061	226.6220	1.6056	226.622	1.605	$0.18^{+0.11}_{-0.12}$	$0.49^{+0.08}_{-0.16}$	$0.82^{+0.01}_{-0.01}$	6^{+0}_{-0}	2^{+0}_{-0}
97	OPHIUCHU	0.0280	258.1115	-23.3634	258.111	-23.363	$38.76^{+21.59}_{-24.11}$	$2.91^{+0.46}_{-0.81}$	$10.26^{+0.32}_{-0.32}$	278^{+23}_{-21}	0^{+0}_{-0}
98	PERSEUS	0.0183	49.6517	41.5151	49.954	41.505	$6.08^{+1.55}_{-2.85}$	$1.58^{+0.12}_{-0.30}$	$6.79^{+0.12}_{-0.12}$	63^{+2}_{-1}	481^{+31}_{-32}
99	PKS0745	0.1028	116.8805	-19.2944	116.880	-19.294	$7.11^{+2.85}_{-3.91}$	$1.54^{+0.18}_{-0.36}$	$7.21^{+0.11}_{-0.11}$	71^{+2}_{-2}	1424^{+150}_{-133}
100	RXJ2344	0.0786	356.0723	-4.3776	356.072	-4.377	$8.89^{+5.48}_{-5.25}$	$1.70^{+0.29}_{-0.44}$	$4.73^{+0.76}_{-0.66}$	300^{+19}_{-18}	0^{+1}_{-0}
101	S405	0.0613	57.8867	-82.2209	57.886	-82.220	$4.62^{+3.14}_{-2.88}$	$1.39^{+0.26}_{-0.39}$	$4.21^{+0.67}_{-0.59}$	458^{+261}_{-158}	0^{+0}_{-0}
102	S540	0.0358	85.0258	-40.8415	85.025	-40.841	$2.52^{+1.55}_{-1.40}$	$1.16^{+0.20}_{-0.27}$	$2.40^{+0.38}_{-0.34}$	130^{+38}_{-28}	1^{+7}_{-1}
103	S636	0.0116	157.5146	-35.3234	157.514	-35.323	$1.56^{+0.44}_{-0.47}$	$1.01^{+0.09}_{-0.11}$	$1.18^{+0.19}_{-0.17}$	343^{+130}_{-86}	0^{+0}_{-0}
104	TRIANGUL	0.0510	249.5758	-64.3557	249.575	-64.355	$14.84^{+2.49}_{-5.28}$	$2.07^{+0.11}_{-0.28}$	$9.50^{+0.70}_{-0.70}$	278^{+10}_{-9}	0^{+0}_{-0}
105	UGC03957	0.0340	115.2429	55.4269	115.242	55.426	$3.32^{+2.76}_{-2.03}$	$1.28^{+0.28}_{-0.34}$	$2.58^{+0.41}_{-0.36}$	142^{+44}_{-33}	8^{+11}_{-8}
106	ZwCl1742	0.0757	266.0623	32.9893	266.062	32.989	$10.11^{+5.91}_{-6.30}$	$1.78^{+0.30}_{-0.49}$	$5.23^{+0.84}_{-0.73}$	231^{+45}_{-38}	0^{+23}_{-0}
107	2A0335+096	0.0349	54.6458	9.9650	54.645	9.965	0.00	0.00	0.00	0.00	-1.00
108	A0383	0.1883	42.0290	-3.4922	42.029	-3.492	0.00	0.00	0.00	0.00	-1.00
109	A0907	0.1603	149.5881	-11.0560	149.588	-11.056	0.00	0.00	0.00	0.00	-1.00

Continued on next page

Table 3.1 – continued from previous page

	name	**z**	**ra**	**dec**	**ra**$_X$	**dec**$_X$	**M**$_{500}$ (**10**^{14} $M_\odot$)	**r**$_{500}$ **(Mpc)**	**T**$_X$ **(keV)**	**r**$_c$ **(kpc)**	$\dot{M}$ **[M**$_\odot$**/yr]**
	(1)	(2)	(3)	(4)	(5)	(6)	(7)	(8)	(9)	(10)	(11)
110	A1991	0.0592	223.6259	18.6309	223.625	18.630	0.00	0.00	0.06	2.01	-1.00
111	A2390	0.2302	328.3942	17.6697	328.394	17.669	0.00	0.00	0.00	0.00	-1.00
112	RXJ1159+5532	0.0810	179.9641	55.5336	179.964	55.533	0.00	0.00	0.59	1.68	-1.00

3.2.1 r, g and u magnitudes

We matched the sample with the Sloan Digital Sky Survey database.

We have first selected for each cluster the 20 brigthest galaxies in r band whose distances from the center of the cluster were less than 0.5 Mpc and whose spectroscopic redshift difference with the cluster redshift was $\Delta z < 0.005$; if no spectroscopic redshift was available, we used a difference in photometric redshift of $\Delta z < 0.02$.

Of the initial sample of 112 clusters only 31 were observed in the SDSS, for a total of about 620 galaxies.

The query were written in SQL (Structured Query Language) and it is the following:

```
DECLARE @dz float SET @dz = 0.005
DECLARE @ra float, @dec float, @z float, @searchrad float, @name int
DECLARE my_cursor cursor read_only SCROLL
FOR
SELECT num, z, ra, dec, rad FROM MYDB.xray5
OPEN my_cursor
DECLARE @count int
DECLARE @interval int
SET @interval = 112
SET @count = 0*@interval
DECLARE @end int
SET @end = @count + @interval
WHILE(@count < @end)
BEGIN
SET @count = @count + 1
FETCH ABSOLUTE @count
from my_cursor into @name, @z, @ra, @dec, @searchrad
IF (@@fetch_status < 0) break
set @searchrad=@searchrad*1
INSERT mydb.xray_out_05Mpc_mag
SELECT TOP 20*
FROM
(
SELECT TOP 100000
@name as num, G.ra, G.dec, G.u, G.err_u, G.g, G.err_g, G.r, G.err_r
FROM
photoz pz,
dbo.fGetNearbyObjEq(@ra,@dec,@searchrad) as N,
Galaxy as G LEFT OUTER JOIN SpecObjAll as s on G.objID = s.BestObjID
WHERE
G.objID = N.objID
and G.objid = pz.objid
and ( ( isnumeric (s.z) = 1 and ( s.z > (@z - @dz) and s.z < (@z +@dz)
) )
or ( isnumeric (s.z) = 0 and ( (pz.z + 0.05) > (@z -@dz) and
(pz.z - 0.05) < (@z + @dz) ) )
)
```

```
and (G.flags_r & 0x0000080000000000) = 0
ORDER BY G.r
) T
END
CLOSE my_cursor
DEALLOCATE my_cursor
```

We retrieved thumbnails for each galaxy, and by visual inspection galaxies were classified as elliptical, lenticular, spiral, or with disturbed morphology or contaminated by nearby brigth stars. We are interested in galaxies with elliptical/lenticular morphology.

Using this subsample, a $M_g - M_r$ vs M_r plot for CCC and NCCC doesn't show any substantially difference for the two class of objects (Figure 3.1). Any consideration on the presence of some CCC galaxies with $M_g - M_r > 0.85$ mag, indicating a great amount of dust and hence of star formation, and also on the presence of a blue tail of CCC galaxies, evident in the upper panel of Figure 3.1, has to be taken with caution, since we are going to reanalyze the galaxy magnitudes, as we will explain in Section 3.3

The fits to the data are performed with the OLS Bisector, OR and RMA regression methods; in the following plots we will show the results from just the OR, for clarity, and we will explain our procedure in Section 3.4

We summarize the mean color differences found in this sample using the OLS Bisector, OR and RMA regression methods in Table 3.2.

Figure 3.1 show that the difference in the $g - r$ color is mostly due to blue CCC galaxies for which the spectroscopic redshift is unavailable, so we decided to choose a stronger limit on the distances of galaxies from the center of clusters.

As a matter of fact, as found by, e.g., Bildfell et al. (2008) and Rafferty et al. (2008), CCC galaxies show evidence of star formation only if they reside close to the center of the cluster.

In the second step, we identified galaxies close to the center of each cluster. We kept galaxies whose distance from the center was less than $6 * r_{180}$ along the line of sight and less than $0.05 * r_{180}$ (about 150 kpc) perpendicularly.

r_{180}, the radius at which the mean density of the enclosed region is 180 times the critical density of the universe, was computed as in Markevitch et al. (1998) as $r_{180} = 3.95[\mathrm{Mpc}](T_X/10\mathrm{keV})^{1/2}$. This radius typically corresponds to approximately the virial radius for clusters.

If no spectroscopic redshift was available, we retained the original constrain on the line of sight distance from the center of the cluster of $\Delta z < 0.02$.

Our request for a line of sight distance of less than $6 * r_{180}$ was chosen to take into account possible galaxy proper motions of galaxy inside clusters.

SDSS gives distances in arcminutes. We transformed these distances in Megaparsecs using the following equation:

$$d_{lum} = (1+z) * \int_0^z 1/\sqrt{(1+z)^2 * (1+\Omega_M * z) - z * (2+z) * \Omega_\Lambda} dz * c/\mathrm{H}_0 \tag{3.8}$$

$$d_{ang} = d_{lum}/(1+z)^2 \tag{3.9}$$

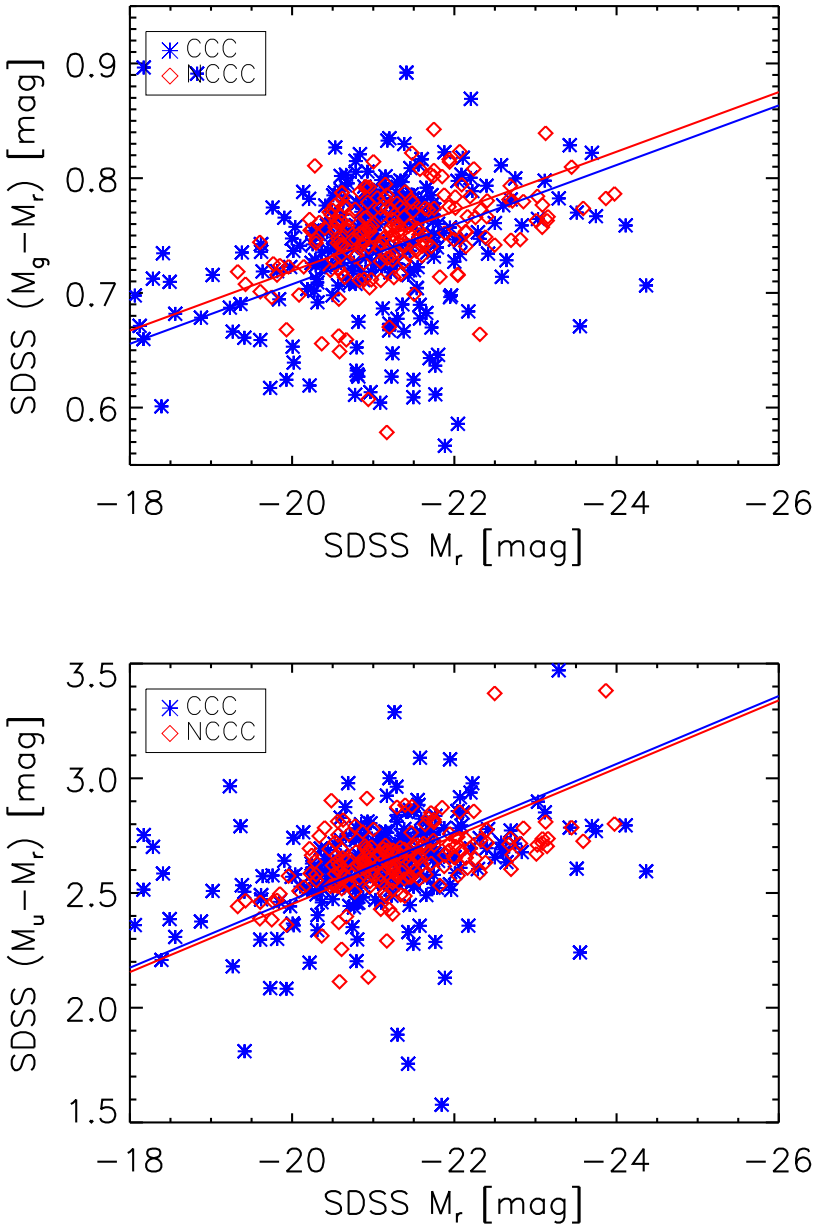

Figure 3.1: *Upper panel*: SDSS $M_g - M_r$ versus M_r magnitude for our initial sample, consisting of the 20 brightest galaxies in the r band for 112 clusters drawn from the Chen et al. (2007) sample. Blue asterisks represent galaxies in Cool Core Clusters, while red diamonds represent galaxies in Non Cool Core Clusters. The lines represent the fitted color-magnitude relations for the CCC (blue line) and NCCC (red line)samples. While the slope is fitted for the whole sample, the zero points are measured as zp= $\langle M_g - M_m \rangle$+slope$*\langle M_r \rangle$ separately for CCC and NCCC galaxies.*Bottom panel*: $M_u - M_r$ versus M_r magnitude.

Table 3.2: Mean color differences between CCC and NCCC galaxies in the first selected sample, and in the second one, drawn from the first after new, more restrictive, distance criteria.

	OLS Bisector	**OR**	**RMA**
$\Delta(zp)_{[g-r]}$ [first selection]	-0.036 ± 0.004	0.011 ± 0.001	-0.008 ± 0.005
$\Delta(zp)_{[u-r]}$ [first selection]	-0.07 ± 0.005	-0.019 ± 0.002	-0.05 ± 0.007
$\Delta(zp)_{[g-r]}$ [second selection]	-0.008 ± 0.08	0.029 ± 0.005	0.02 ± 0.09
$\Delta(zp)_{[u-r]}$ [second selection]	0.2 ± 0.005	-0.019 ± 0.002	0.039 ± 0.007

$$d_{\perp} = \mathrm{D[arcmin]} * 60 * d_{ang}/206265 \text{ [Mpc]} \tag{3.10}$$

In these equations, where the spectroscopic redshift were unavailable, we chose to use the cluster redshift rather than the photometric redshift.

Of the initial 20 galaxies selected for each cluster only 1-6 were found in these new range of distances. If we change our distance limits, e.g. if we vary the boundaries from $0.03 * r_{180}$ to $0.1 * r_{180}$ instead of $0.05 * r_{180}$, although changing the number of selected galaxies, it doesn't change results of this work.

We drawn in this way 80 galaxies from the original sample, of which 53 belong to Cool Core Clusters, and 27 belong to Non Cool Core Clusters.

We present this sample in Table 3.2.1.

In Figure 3.2 we show how the new constraints changed the $g-r$ and $u-m$ color magnitude diagram, and in Table 3.2 we report the measured mean color differences.

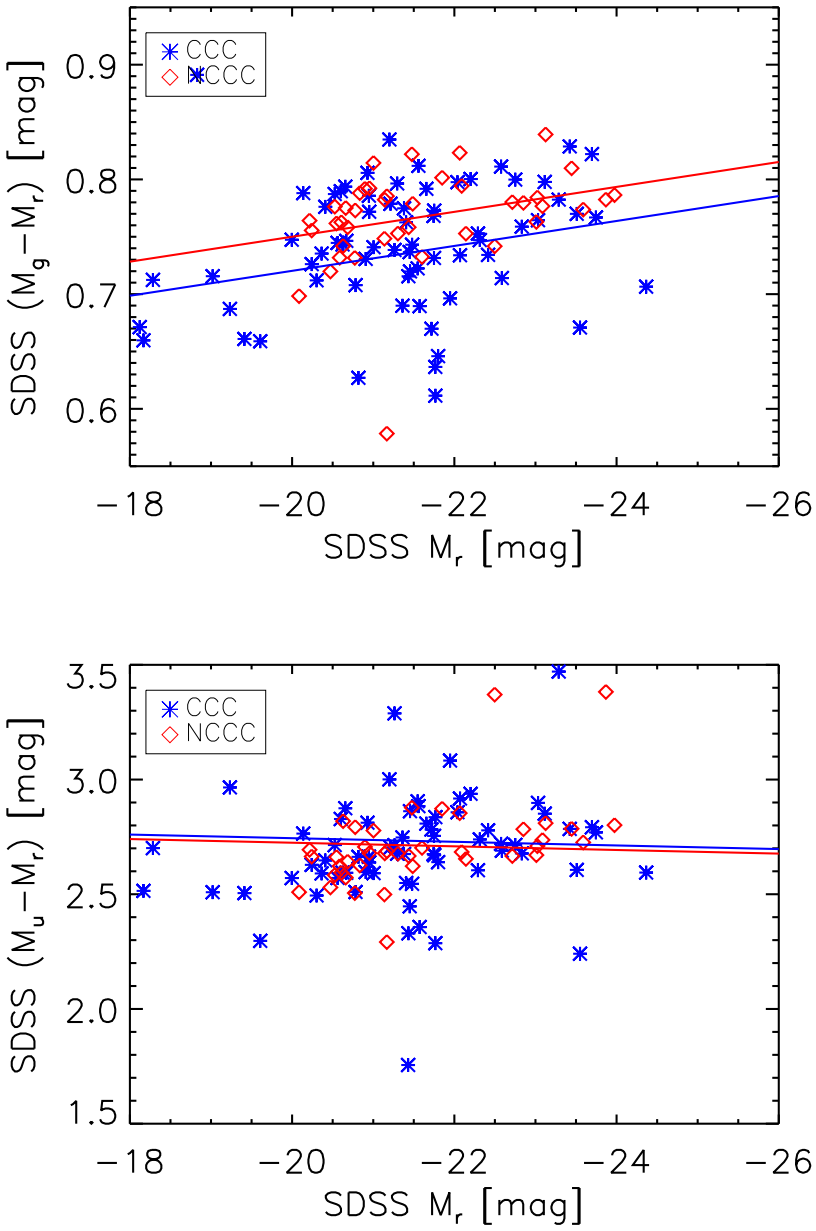

Figure 3.2: *Upper panel*: SDSS $M_g - M_r$ versus M_r magnitude for our reduced sample, consisting of 80 galaxies. Blue asterisks represent galaxies in Cool Core Clusters, while red diamonds represent galaxies in Non Cool Core Clusters. The lines represent the fitted color-magnitude relations for the CCC (blue line) and NCCC (red line)samples. While the slope is fitted for the whole sample, the zero points are measured as zp= $\langle M_g - M_m \rangle + \text{slope} * \langle M_r \rangle$ separately for CCC and NCCC galaxies (see text). *Bottom panel*: $M_u - M_r$ versus r magnitude.

Table 3.3: Galaxy properties. (1) Cluster name (2) redshift of thecluster (3),(4) right ascension and declination of the galaxy (5) apparent r model magnitude from the SDSS (6) spectroscopic redshift (7) (8) photometric redshift (9) projected distance from the center of the cluster

Cluster name	$\mathbf{z}_{cl}$	**ra**	**dec**	$\mathbf{mag}_r$	$\mathbf{z}_{sp}$	$\mathbf{z}_{ph}$	$\mathbf{d}_{perp}$ **[Mpc]**
(1)	(2)	(3)	(4)	(5)	(6)	(7)	(8)
A0085	0.0556	10.4603	-9.3031	13.389± 0.003	0.0553	0.0817± 0.0042	0.0639
A0085	0.0556	10.4510	-9.2842	15.228± 0.002	0.0528	0.0681± 0.0032	0.1254
A0085	0.0556	10.4172	-9.3043	15.714± 0.003	-999.	0.0722± 0.0079	0.1471
A1795	0.0616	207.2314	26.6168	15.652± 0.003	0.0628	0.0911± 0.0063	0.0966
A1795	0.0616	207.1876	26.5699	16.319± 0.003	0.0612	0.0973± 0.0120	0.1665
A1795	0.0616	207.1774	26.6169	16.667± 0.004	0.0618	0.0807± 0.0075	0.1759
A1795	0.0616	207.2103	26.5854	16.736± 0.004	0.0615	0.1007± 0.0106	0.0613
A1795	0.0616	207.2164	26.6120	16.897± 0.004	-999.	0.0657± 0.0138	0.0606
A1795	0.0616	207.2093	26.5591	17.020± 0.005	-999.	0.0550± 0.0093	0.1696
A2029	0.0767	227.7338	5.7448	13.474± 0.002	-999.	0.0802± 1.0000	0.1317
A2029	0.0767	227.7449	5.6919	16.835± 0.004	-999.	0.0793± 0.0056	0.1692
A2029	0.0767	227.7142	5.7080	16.933± 0.004	-999.	0.0773± 0.0070	0.0994
A2029	0.0767	227.7170	5.7530	17.057± 0.005	-999.	0.0734± 0.0058	0.1840
A2052	0.0348	229.1907	7.0044	14.040± 0.002	0.0310	0.0517± 0.0036	0.0332
A2052	0.0348	229.1735	7.0293	15.122± 0.002	0.0311	0.0379± 0.0044	0.0617
A2052	0.0348	229.1550	6.9653	15.208± 0.002	0.0367	0.0478± 0.0051	0.1107
A2063	0.0354	230.7721	8.6092	13.236± 0.001	-999.	0.0535± 1.0000	0.0832
A2063	0.0354	230.8126	8.5738	14.443± 0.002	0.0346	0.0367± 0.0055	0.1372
A2063	0.0354	230.7050	8.5605	15.424± 0.002	0.0350	0.0420± 0.0046	0.1380

Continued on next page

Table 3.3 – continued from previous page

Cluster name	$\mathbf{z}_c l$	**ra**	**dec**	$\mathbf{mag}_r$	$\mathbf{z}_{sp}$	$\mathbf{z}_p h$	$\mathbf{d}_{perp}$ **[Mpc]**
(1)	(2)	(3)	(4)	(5)	(6)	(7)	(8)
A2142	0.0899	239.5833	27.2334	14.826± 0.002	0.0908	0.1226± 1.0000	0.0467
A2142	0.0899	239.6027	27.2295	16.142± 0.004	0.0882	0.1099± 0.0053	0.0604
A2142	0.0899	239.5694	27.2367	17.008± 0.004	0.0892	0.1309± 0.0048	0.1230
A2142	0.0899	239.5965	27.2072	17.072± 0.005	0.0922	0.1205± 0.0087	0.1617
A2142	0.0899	239.5943	27.2567	17.582± 0.006	0.0903	0.1106± 0.0073	0.1446
A2199	0.0302	247.0971	39.5703	14.165± 0.002	0.0291	0.0527± 0.0042	0.1183
A2199	0.0302	247.1502	39.5338	14.949± 0.002	0.0283	0.0338± 0.0040	0.0407
A2199	0.0302	247.1852	39.5155	15.017± 0.002	0.0273	0.0529± 0.0043	0.0749
A2244	0.0970	255.6898	34.0611	16.052± 0.003	0.0932	0.1176± 0.0040	0.1185
A2244	0.0970	255.6508	34.0885	16.855± 0.004	0.0996	0.1242± 0.0028	0.1909
A1413	0.1427	178.8229	23.3913	17.156± 0.005	0.1391	0.1546± 0.0123	0.1488
A1413	0.1427	178.8179	23.4227	18.471± 0.011	-999.	0.1509± 0.0101	0.1489
A1689	0.1840	197.8839	-1.3297	17.974± 0.009	-999.	0.1925± 0.0076	0.1409
A1689	0.1840	197.8660	-1.3355	18.119± 0.009	-999.	0.1747± 0.0045	0.0778
A1689	0.1840	197.8676	-1.3454	18.154± 0.011	-999.	0.1949± 0.0062	0.1205
A1689	0.1840	197.8709	-1.3546	18.442± 0.012	-999.	0.1885± 0.0098	0.2094
A1689	0.1840	197.8682	-1.3329	18.489± 0.012	-999.	0.1919± 0.0098	0.0630
A1914	0.1712	216.4982	37.8278	17.417± 0.006	-999.	0.1848± 0.0091	0.1172
A1914	0.1712	216.5187	37.8415	17.983± 0.008	-999.	0.1815± 0.0039	0.1049
A1914	0.1712	216.5023	37.8360	18.013± 0.008	-999.	0.1577± 0.0138	0.0560
A1914	0.1712	216.5007	37.8195	18.182± 0.008	-999.	0.1695± 0.0129	0.1766
A1914	0.1712	216.4914	37.8248	18.277± 0.009	-999.	0.1808± 0.0090	0.1801
A1914	0.1712	216.5019	37.8221	18.369± 0.009	-999.	0.1656± 0.0097	0.1469
A2151w	0.0369	241.1492	17.7216	13.496± 0.001	0.0351	0.0746± 1.0000	0.0725

Continued on next page

Table 3.3 – continued from previous page

Cluster name (1)	$\mathbf{z}_c l$ (2)	**ra** (3)	**dec** (4)	$\mathbf{mag}_r$ (5)	$\mathbf{z}_{sp}$ (6)	$\mathbf{z}_p h$ (7)	$\mathbf{d}_{perp}$ **[Mpc]** (8)
A2151w	0.0369	241.1649	17.7008	13.813± 0.001	0.0356	0.0404± 0.0032	0.0727
A2151w	0.0369	241.1456	17.7174	14.788± 0.002	0.0378	0.0385± 0.0200	0.0891
A2151w	0.0369	241.1759	17.6837	15.592± 0.003	0.0324	0.0256± 0.0047	0.0991
NGC5813	0.0064	225.2959	1.6915	13.124± 0.003	-999.	0.0011± 1.0000	0.0050
NGC5813	0.0064	225.3014	1.7066	13.530± 0.004	-999.	0.0225± 0.0036	0.0034
NGC5846	0.0061	226.6217	1.5949	13.966± 0.002	-999.	0.0019± 1.0000	0.0046
A1991	0.0592	223.6312	18.6423	13.715± 0.002	-999.	0.0752± 0.0038	0.0515
RXJ1159+5532	0.0810	179.9674	55.5349	14.146± 0.002	0.0808	0.1003± 1.0000	0.0119
RXJ1159+5532	0.0810	179.9808	55.5390	18.289± 0.012	-999.	0.0793± 0.0182	0.0596
RXJ1159+5532	0.0810	179.9590	55.5484	18.485± 0.010	-999.	0.0613± 0.0134	0.0834
A0119	0.0440	14.0671	-1.2554	13.148± 0.001	0.0445	0.0733± 1.0000	0.0762
A0119	0.0440	14.0756	-1.2418	15.073± 0.002	0.0436	0.0845± 1.0000	0.0701
A0119	0.0440	14.0559	-1.2384	16.708± 0.006	0.0486	0.0313± 0.0076	0.0131
A1650	0.0845	194.6600	-1.7696	16.699± 0.004	-999.	0.0872± 0.0078	0.1114
A1650	0.0845	194.6532	-1.7481	16.852± 0.004	0.0841	0.1140± 0.0066	0.1270
A2065	0.0721	230.6001	27.7144	14.981± 0.002	-999.	0.0877± 0.0047	0.0544
A2065	0.0721	230.6185	27.6869	15.558± 0.003	-999.	0.0835± 0.0087	0.1228
A2065	0.0721	230.6158	27.6991	16.098± 0.003	-999.	0.0736± 0.0093	0.0610
A2147	0.0351	240.5583	16.0198	15.453± 0.002	-999.	0.0421± 0.0058	0.0474
A2147	0.0351	240.5733	16.0030	15.606± 0.002	0.0392	0.0444± 0.0051	0.0494
A2147	0.0351	240.5972	15.9965	15.801± 0.004	0.0347	0.0492± 0.0081	0.0747
A2147	0.0351	240.5440	15.9713	15.816± 0.003	0.0391	0.0243± 0.0055	0.1639
COMA	0.0232	194.8046	27.9770	13.574± 0.001	-999.	0.0350± 0.0047	0.1708
COMA	0.0232	194.8866	27.9836	14.138± 0.002	0.0194	0.0404± 0.0051	0.1145

Continued on next page

Table 3.3 – continued from previous page

Cluster name (1)	$\mathbf{z}_c l$ (2)	**ra** (3)	**dec** (4)	$\mathbf{mag}_r$ (5)	$\mathbf{z}_{sp}$ (6)	$\mathbf{z}_p h$ (7)	$\mathbf{d}_{perp}$ **[Mpc]** (8)
MKW8	0.0270	220.1626	3.4697	13.581± 0.001	0.0266	0.0674± 1.0000	0.0453
MKW8	0.0270	220.2195	3.4183	14.333± 0.002	0.0275	0.0499± 1.0000	0.1061
MKW8	0.0270	220.1225	3.4327	14.352± 0.002	0.0245	0.0626± 1.0000	0.1066
MKW8	0.0270	220.2419	3.4516	14.807± 0.002	0.0271	0.0439± 0.0978	0.1232
ZwCl1215	0.0750	184.4213	3.6558	14.690± 0.002	0.0767	0.1126± 0.0057	0.0166
ZwCl1215	0.0750	184.4116	3.6634	15.744± 0.003	0.0778	0.1217± 0.0032	0.0601
A1775	0.0757	205.4612	26.3690	15.234± 0.003	-999.	0.0882± 0.0106	0.0672
A1775	0.0757	205.4467	26.3809	16.999± 0.004	0.0771	0.1071± 0.0046	0.0631
A1775	0.0757	205.4409	26.3880	17.103± 0.005	-999.	0.0784± 0.0047	0.0939
A1775	0.0757	205.4753	26.3808	17.492± 0.006	0.0757	0.0819± 0.0069	0.0716
A1800	0.0748	207.3482	28.1073	14.122± 0.002	-999.	0.0843± 1.0000	0.0844
A1800	0.0748	207.3535	28.0974	16.544± 0.006	-999.	0.0641± 0.0189	0.0469
A1800	0.0748	207.3633	28.0790	17.213± 0.004	0.0763	0.0943± 0.0108	0.1007

3.2.2 NUV and IR magnitudes

We found NUV and K-band information for this sample by matching it with the Galaxy Evolution Explorer (GALEX) database (Martin et al. 2005; Morrissey et al. 2005) and the 2 Micron All Sky Survey (2MASS; Skrutskie et al. 2006).

GALEX is an orbiting space telescope observing galaxies in ultraviolet light. The GALEX mission is performing a series of imaging and spectroscopic sky surveys in two ultraviolet bands, FUV and NUV. The instrument consists of a 50 cm diameter modified Ritchey-Chrétien telescope providing a very wide field of view (1.25° diameter) with good astrometric quality across most of the field, and a resolution of 4.5"-6" [FUV-NUV]. The GALEX photometric data cover the wavelength range from 1344Å to 2831Å with the FUV passband (1344-1786Å) having λ_{eff}=1528Å and the NUV band (1771-2831Å) having λ_{eff}=2271Å. The FUV and NUV bands are obtained simultaneously using a dichroic beam splitter that also acts as a field aberration corrector.

Imaging surveys are carried out with different depth and coverage.

2MASS has uniformly scanned the entire sky in three near-infrared bands. It used two highly-automated 1.3-m telescopes, one at Mt. Hopkins, AZ, and one at Cerro Totolo/CTIO, Chile. Each telescope was equipped with a three-channel camera, each channel consisting of a 256×256 array of HgCdTe detectors, capable of observing the sky simultaneously at J (1.25μm), H (1.65μm), and Ks (2.17μm).

2MASS selected a 2"×2" pixel scale with 7.8 s of integration for each sky location, divided into six 1.3 s exposures.

The magnitude limits for extended sources are of 15.5, 14.3 and 13.5 mag respectively in the J, H and K_s band, with a completeness> 90%, for galaxies above a galactic latitude of |30| deg .

The 2MASS Extended Source Catalog contains sources that are extended with respect to the instantaneous PSF, such as galaxies and Galactic nebulae

Once identified, extended sources were then extracted directly from the Atlas Images. The galaxy flux is integrated using a suite of apertures, including large ones to capture the total flux of the source; photometry is so performed in a series of fixed circular apertures (50"-70"), circular and elliptical apertures defined by the source's J and K_s 20 and 21 mag arcsec^{-2} and Kron isophotes (a scaling of the intensity-weighted first moment radius), and multiple apertures yielding extrapolated "total" magnitudes. Elliptical fits is made to the isophotal contours, yielding basic source shape parameters such as semimajor axes, axial ratios, and position angles.

3.3 Photometric measures

Because of scattered light (see the Early Data Release paper Stoughton et al. 2002), the background sky in the SDSS images is non-uniform on arc-minute scales. The photometric pipeline determines the median sky value within each 100" square on a grid with 50" spacing, and bilinearly interpolates this sky value to each pixel. This biases the sky bright near large extended galaxies. In the Data Release 4 paper and in Mandelbaum et al. (2005) this effect is reported to causes a systematic decrease in the number density of faint objects near

bright galaxies. In addition, it also strongly affects the photometry of the bright galaxies themselves, as has been reported by Lauer et al. (2007), Bernardi et al. (2007), and Lisker et al. (2007). The amount of this effect was overestimated in Data Release 6 and was correctly measured in Data Release 7.

SDSS have quantified this effect by adding simulated galaxies with exponential or de Vaucouleurs profiles to SDSS images. The simulated galaxies ranged from apparent magnitude r=12 to r=19 in half-magnitude steps, with a one-to-one mapping from r to Sèrsic half-light radius determined using the mean observed relation between these quantities for Main sample galaxies with exponential and de Vaucouleurs profiles. Axis ratios of 0.5 and 1 were used, with random position angle for the non-circular simulated galaxies.

Results in the r band are shown in Figure 6 of Abazajian et al. (2009), here Figure 3.3, which presents the differences between the input magnitude and the model magnitude returned by the SDSS photometric pipeline as a function of r magnitude for galaxies with both exponential and de Vaucouleurs profiles.

On average the flux is underestimated by approximately 0.2 magnitudes at $r = 12.5$ mag and < 0.1 magnitudes at $r = 15$ mag for simulated galaxies with a Sérsic index of 1. For a Sérsic index of 4, the flux is underestimated by as much as 0.3 magnitudes at $r = 12.5$ mag. The scale sizes of galaxies are similarly underestimated by as much as 20% for simulated galaxies with Sérsic index of 1, and 30% for an index of 4. As pointed out by Abazajian et al.(2009), the most massive elliptical or cD galaxies will have more extended envelopes, producing a larger effect than found in these simulation (Lauer et al. 2007).

This is exactly our case, since we are working on massive cD galaxies, and in general with galaxies near cD and bright galaxies inside clusters with diffuse intra-cluster light.

To overcome this problem on bright galaxies we decided to perform a new analysis of the galaxy images.

3.3.1 The estimate of the sky

We start our analysis from the r-filter.

SDSS images are given in fits files with name in the form of *fpC-rrrrrr-bc-ffff.fit*, in which rrrrrr is the imaging run number, b is the filter used (u, g, r, i, z), c is the column location in the Imaging Array of the CCD which acquired the data (1-6), and $fffff$ is the field number within the run.

In Figure 3.4 we see the fits file with the image fpC-002821-r5-0184.fits, sampling the cluster RXJ1159+5532.

In each figure we have from one to 5 galaxies to examine, depending on the cluster. In this case we have three galaxies, zoomed and highlighted by the green circles in Figure 3.5.

Images were cutted with the *imcopy* IRAF task around the galaxies to be more easily treated. The cut depended from the position of the galaxies, so it changes from image to image.

We estimate the sky background using the *iraf* task *imstat* that give use the possibility to compute (between other parameters) the mean, median, standard deviation of the image.

We subtracted the median value of the whole image as a first estimate of the sky. Then we refined our choice of the sky by examining the subtracted image with the *imexam* package.

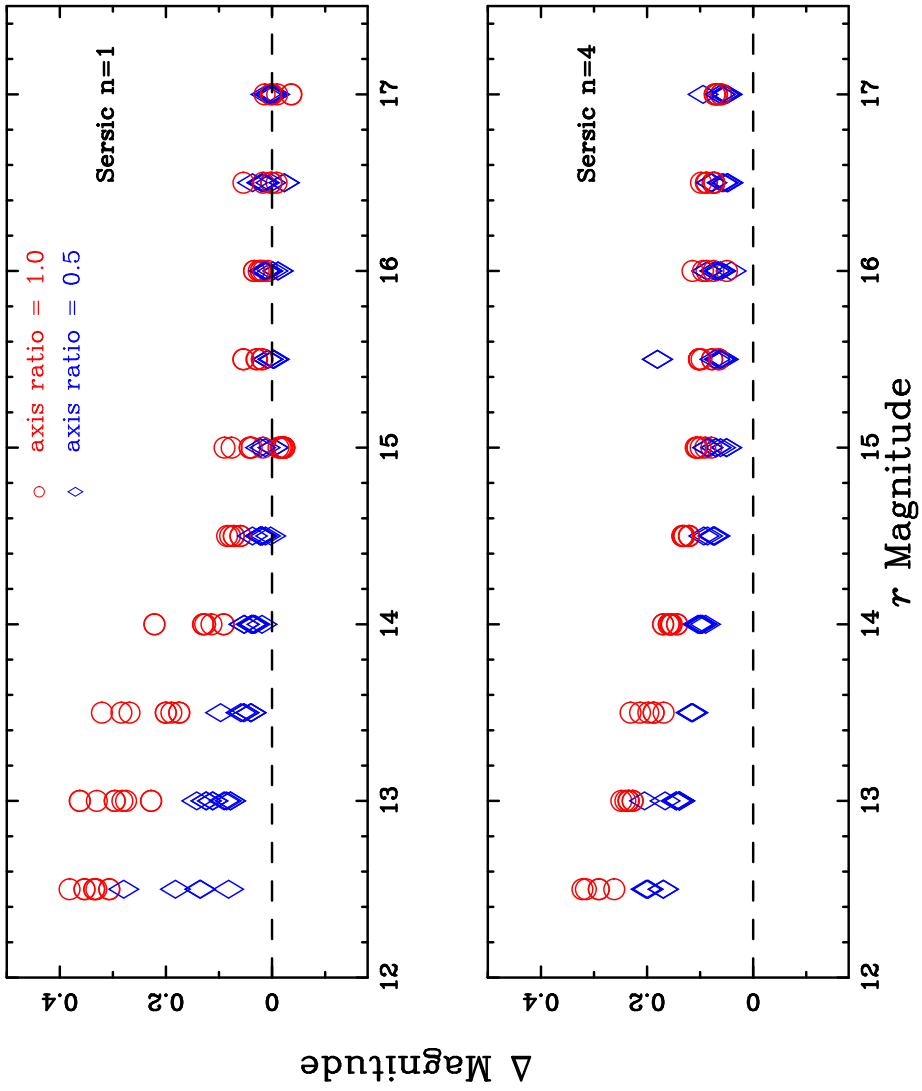

Figure 3.3: Differences between measured model and true r-band magnitudes of a series of simulated galaxies with Sèrsic index of 1 (disk galaxies; upper panel) and 4 (elliptical galaxies; lower panel), from Figure 6 of Abazajian et al.(2009)

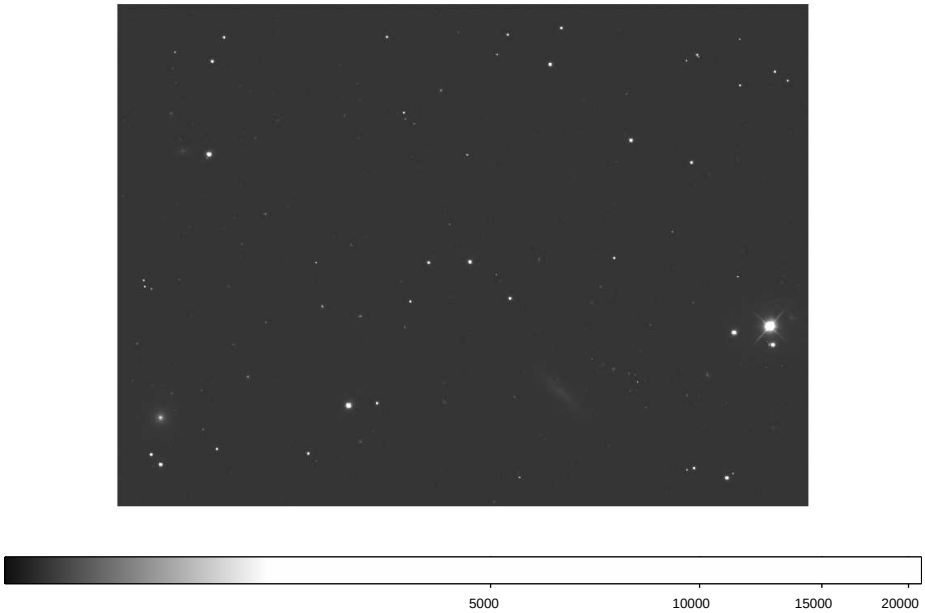

Figure 3.4: SDSS image fpC-002821-r5-0184.fits of the cluster RXJ1159+5532

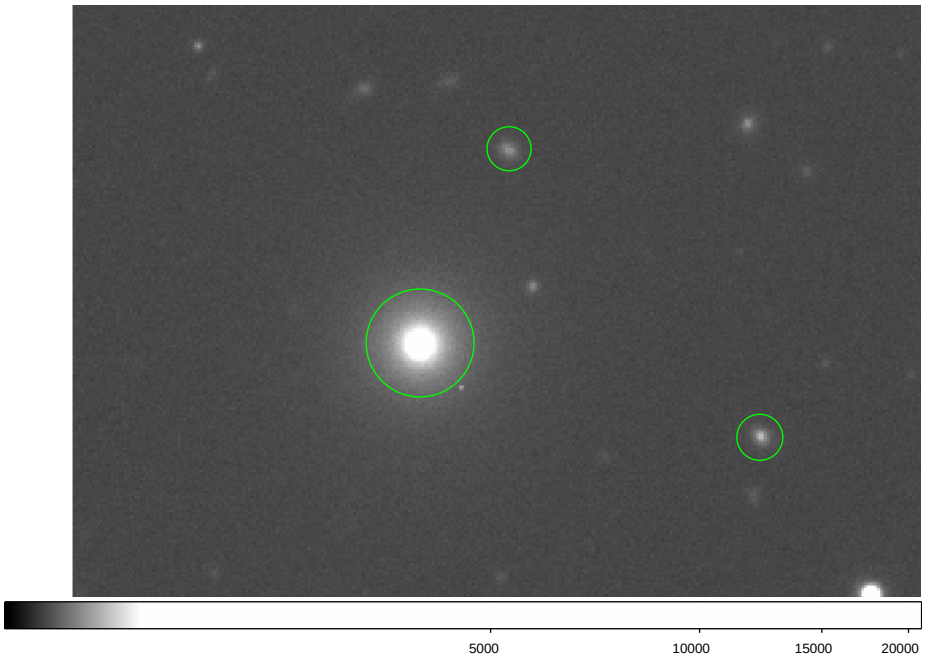

Figure 3.5: A cut of the SDSS image fpC-002821-r5-0184.fits with the green circles highlighting three galaxies of our sample, belonging to the cluster RXJ1159+5532

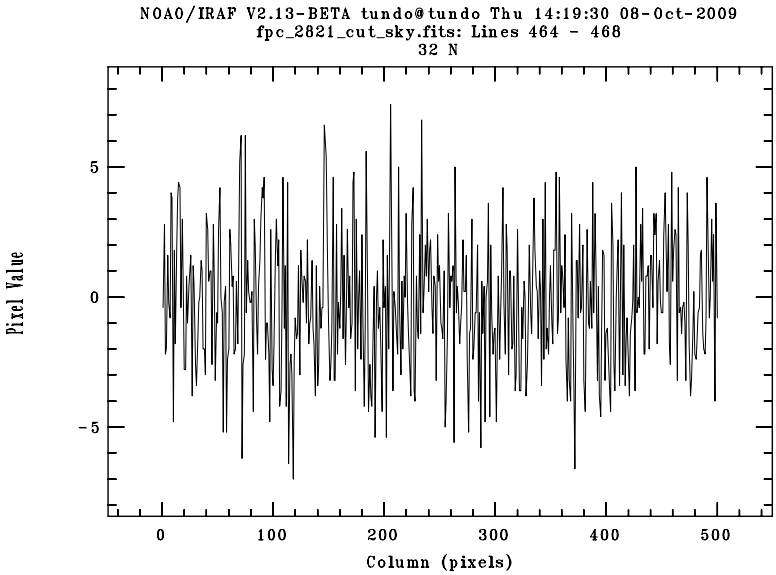

Figure 3.6: An example of the use of the "c" key of the IRAF *imexam* task, showing a plot of the lines from 464 to 460 (chosen for the absence of objects) in our sky-subtracted image of the cluster RXJ1159+5532.

With this task we can examine images using image display, plots, and text.

This task is generally intended for interactive use, and the image cursor is used to select points in the images to be examined and the key typed selects a particular operation.

In particular, the "l" key gives a plot of a line or average of lines with the column number as the ordinate and the pixel value as the abscissa. The averaging number and various graph options can be specified by the parameters from the *imexam* parameter set.

The "c" key gives a plot of a column or average of columns is made with the line number as the ordinate and the pixel value as the abscissa. The averaging number and various graph options are specified by the parameters from the cimexam parameter set.

An example of the use of the "l" and "c" keys used on the sky-subtracted image is shown in Figures 3.6 and 3.7.

We used these two keys to check if the mean value of the counts are zero in regions showing no objects, and if there are any dependence of the sky counts form the position in the image.

If the mean counts of the plots was higher or lower than zero we corrected for this difference and check again, till we are confident of our sky subtraction around our galaxies.

As an estimate of the uncertainty on the sky value we used the standard deviation of sky counts in a region of the image free of objects.

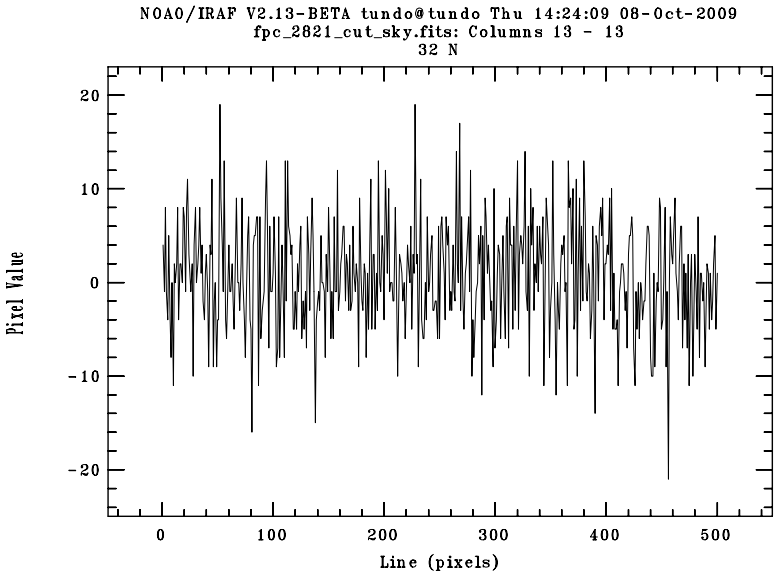

Figure 3.7: A plot of column 13 (chosen for the absence of objects) in our sky-subtracted image of the cluster RXJ1159+5532.

The task imsurfit for the estimate of the sky

As a test for the reliability of the above procedure in the estimate of the sky, we measured the sky counts on a subsample of images using the Iraf *imsurfit* task.

This task fit a surface to selected portions of the input image (the whole image, or selected rows/columns, or a border around the image, or, as in our case, image sections). The user may choose to use various functions in this fit (legendre polynomial, chebyshev polynomial, a cubic spline or a linear spline) and the order of the polynomials in both x and y.

In output the task will give the fitted image -the fitted sky in our case- the original minus the fitted image -the sky subtracted image- and others.

We tried different functions and order of the polynomials to test if the sky could be better fitted than by a constant. Even if the *imsurfit* task fit surfaces on the image, we find that the value of the sky around the galaxies of our interest is the same we measure with the procedure explained above. So, we decided that we could relay on the measure of the sky as given by the *imexam* task.

The measure of the seeing

After the removal of the sky counts we selected the bright stars in the image and performed a radial profile plot using the "r" task of the *imexam*. The "r" task gives the aperture magnitude and flux, the estimated background sky, the profile fit peak, the ellipticity and position angle from the moment analysis, and four estimates of the profile width.

The profile type is set by the fittype parameter. The choices are "gaussian" and "moffat", so that the profile equation are, respectively,

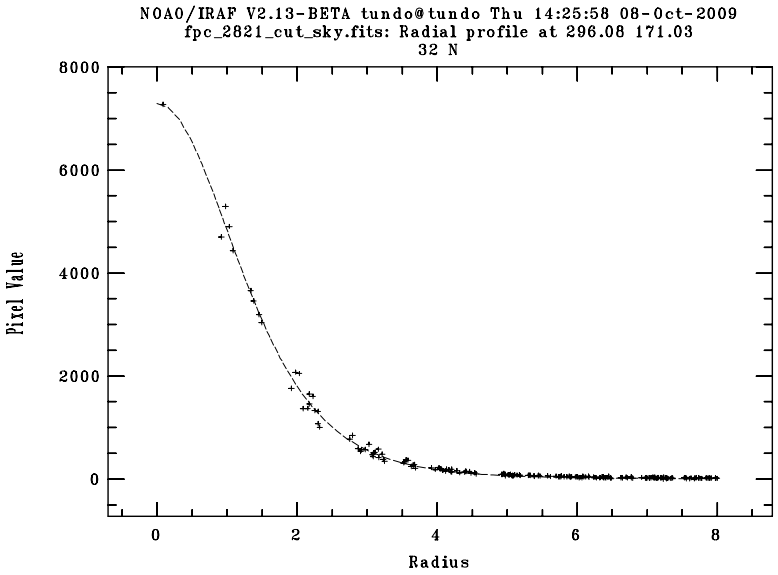

Figure 3.8: An example of the use of the "r" key of the IRAF *imexam* task, showing the radial profile of a bright star in our sky-subtracted image.

$$I = I_c \exp(-0.5(r/\sigma)^2) \tag{3.11}$$

$$I = I_c(1 + (r/\alpha)^2)^{-\beta} \tag{3.12}$$

We used the measure of the FWHM from the fit to a moffat profile to estimate the seeing of the image.

Since we are going to fit the surface brightness profile of the galaxies with a De Vaucouleur profile to find their magnitude, this measure is used to select the radius inside which the surface brightness profile of the galaxy must not be fitted.

An example of the radial fit of a star in our image is given in Figure 3.8

3.3.2 The *ellipse* task

Now we have a sky-subtracted image, on which we use the *ellipse* task of *iraf*.

The *ellipse* task fits elliptical isophotes to galaxy images. The task produces as main output one table which contains 40 or more parameters for each fitted isophote. The image is measured using an iterative method described by Jedrzejewski et al. (1987).

Each isophote is fitted at a pre-defined, fixed semi-major axis length. The task starts from a first guess elliptical isophote defined by approximate values for the X and Y center coordinates, ellipticity and position angle. Using these values, the image is sampled along an elliptical path producing a 1-dimensional intensity distribution as a function of position angle E. The harmonic content of this distribution is analyzed by least-squares fitting to the function:

$$y = y0 + A1 \times \sin E + B1 \times \cos(E) + A2 \times \sin(2\ E) + B2 \times \cos(2\ E) \quad (3.13)$$

Each one of the harmonic amplitudes A1, B1, A2, B2 is related to a specific ellipse geometric parameter, in the sense that it conveys information regarding how much the current parameter value deviates from the "true" one. To compute this deviation, the local image radial gradient has to be taken into account too. The algorithm picks up the largest amplitude among the four, estimates the local gradient and computes the corresponding increment in the associated ellipse parameter. That parameter is updated, and the image is resampled. This process is repeated until any one of the following criteria are met:

(1) The largest harmonic amplitude is less than a given fraction of the rms residual of the intensity data around the harmonic fit.

(2) A user-specified maximum number of iterations is reached.

(3) More than a given fraction of the elliptical sample points have no valid data in then, either because they lie outside the image boundaries or because they where flagged out from the fit.

At this point, the image data sample coming from the best fit ellipse is fitted by the following function:

$$y = y0 + An \times \sin(n\ E) + Bn \times \cos(n\ E) \quad (3.14)$$

with n = 3 and n = 4. The amplitudes (A3, B3, A4, B4), divided by the semi-major axis length and local intensity gradient, measure the isophote's deviations from perfect ellipticity (the amplitudes divided by semi-major axis and gradient, are the actual quantities written at the output table).

After fitting the ellipse that corresponds to a given value of the semi-major axis (by the process described above), the axis length is incremented or decremented following a pre-defined rule. At each step, the starting ellipse parameters are taken from the previously fitted ellipse that has the closest semi-major axis length to the current one.

Errors in intensity, magnitude and local gradient are obtained directly from the rms scatter of intensity data along the fitted ellipse. Ellipse geometry parameter errors are obtained from the internal errors in the harmonic fit, after removal of the first and second fitted harmonics.

Using cursor commands, the user can, at any time, list or modify most of the algorithm control parameters, as well as the current ellipse geometry.

Output is a table with one row for each isophote. Each row contains the following data: semi-major axis length, mean isophotal intensity and its rms, ellipticity and its error, position angle and its error, radial gradient relative error, number of valid data points used in the fit, number of flagged data points (either removed from the image or clipped out), number of iterations, and stop condition code.

The main output table also contains one row for each value of the semi-major axis length. The task can give: semi-major axis length (in pixel, SMA), the mean isophotal intensity, the error in isophotal intensity (RMS divided by the square root of the number of valid data points), the estimate of pixel variance, the root-mean-square RMS scatter around isophotal intensity, the ellipticity and ellipticity error, the position angle and position angle error, the ellipse center and ellipse center error, the local radial intensity gradient and the gradient

error, the mean isophotal magnitude, with lower and upper magnitude errors, the total flux enclosed by the ellipse and the total flux enclosed by a circle of radius equal to the semi-major axis length, the total flux enclosed by the ellipse, in magnitudes, the total flux enclosed by the circle, in magnitudes, the total number of valid pixels inside the ellipse, the total number of valid pixels inside the circle, and the A3, B3 (3rd harmonic deviations from ellipse), A4, B4 (4th harmonic deviations from ellipse) parameters, with errors.

The task has also the capability to read in a table previously generated by itself when applied to a given image, and use the ellipse geometry information in each table row to measure another (related) image. In this mode the fitting algorithm is disabled and the task just extracts photometry information from the image. This mode is activated by setting task parameter 'inellip' to the name of the table that contains the results of a former execution of the task. This feature is useful when measuring paired images e.g. as in a multicolor set to derive color indices and gradients.

Since we are interested in finding the colors $g - r$ and $u - r$ of our galaxies we fit the various parameter on the images in the r band, since it is the one in which galaxies are more luminous, and we use the capability of the *ellipse* task to use previously fitted parameters to fit galaxies in the g and u bands.

The *ellipse* task gives also the possibility to mask the stars and galaxies around the fitted galaxy. In the Figure 3.9 we show how does appear the image with the mask.

A zoomed particular of the image is shown in Figure 3.10 to show how the red rectangles that mask the image appear when they are imposed on the zoomed image.

Once given the starting guesses, the *ellipse* task performs the first fit of the first ellipse. We check by eye if the fit seems accurate and let *ellipse* go through the next ellipse.

In Figure 3.11 we show how the ellipses drawn by *ellipse* appear after the last ellipse is fitted. In this Figure the grey scale is driven to show the whole image as white to give more prominence to the red ellipses.

Plots of the parameters fitted by *ellipse* are shown by the task *isoplot* (see Figures 3.13 , 3.14).

In this case we forced *ellipse* to fit out to a radius where there were not enough valid point, because we needed to subtract the galaxy light out to the radius where the other two galaxies of our cluster lie. In Figure 3.13 we see that the points corresponding to the outer radii are fixed to the last value *ellipse* fitted with a valid stop code. In other words, the last ellipses are fixed to the center, shape, position angle of the last "good" ellipse, and are just scaled to the next semi-major axis length.

From the results of isophotal analysis generated by the isophote fitting task *ellipse* the *bmodel* task creates a 2-dimensional image file containing a noiseless photometric model of a source image.

The modelling interval can be specified by the user, so that one can built the model galaxy using the full range of semi-major axis lengths included in the ellipse table or using explicitly minimum and/or maximum values; in these cases outside the measured region the output image pixels are filled with a constant value.

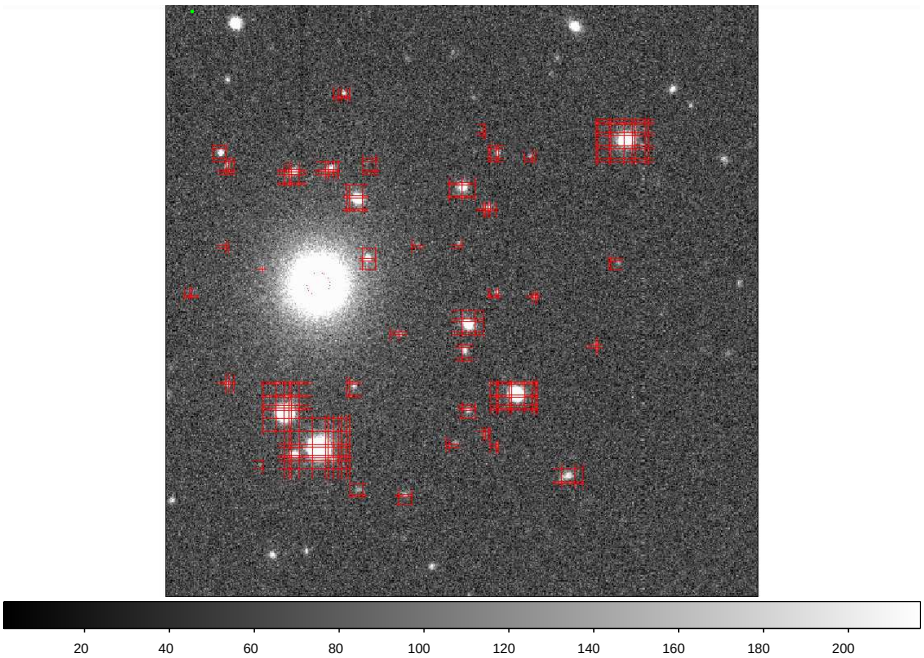

Figure 3.9: A zoom of our sky-subtracted image of the central galaxies of the cluster RXJ1159+5532. We see the red rectangles masking the objects around the galaxy to be fitted.

The model galaxy (see Figure 3.15) is then subtracted form the sky-subtracted image.

The result of this passage is shown in Figure 3.16. The green circle highlight the center of the subtracted galaxy.

To test if the galaxy is correctly modeled, we use again the task *imexam*.

In Figures 3.17 , 3.18 and 3.19 we show how a plot of a line and a column, respectively, appear after the model galaxy subtraction. We can see that the plots don't show any sharp step or gradient around the position of the galaxy, so indicating that the galaxy fitting is correct. In Figure 3.19 we plot a column shifted respect to the position of our galaxy, since the presence of a bright object at the same column position doesn't permit to appreciate how the plot of pixel counts appear around the subtracted galaxy.

A more complicated case

We have explained the basic process of fitting a single galaxy with the *ellipse* task. Even when there is more than one galaxy in a frame, we can simple identify by eye the brightest and biggest galaxy of the frame, fit (after masking the others) and subtract it, and proceed with the other galaxies.

Things complicate when we have to fit more than one galaxy in a frame, *and* when the galaxies are so close that their light mix.

In these cases we approach with the following steps:

- we chose the brightest galaxy of the frame. We mask the other(s) galaxy,

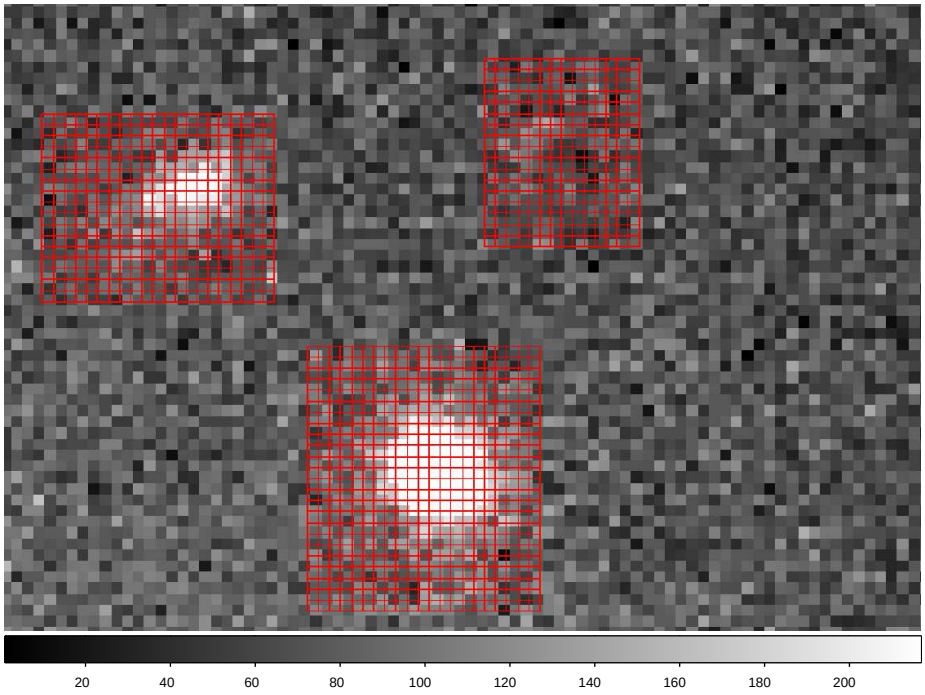

Figure 3.10: A closer view of the previous Figure, showing how the red rectangles look like when created.

and fit the first one.

- We subtract from the frame the model of the first galaxy, and fit the second galaxy
- We subtract the model of the second galaxy from the original sky-subtracted frame, and fit again the first galaxy
- Last, after subtracting the new model galaxy from the original frame, we perform a new fit on the second galaxy.

This procedure minimizes the pollution between the two galaxies.

The fitting in the *g* and *u* band

The *ellipse* task give the possibility to upload a previous output table with input ellipses for no-fit mode, in which case the task just extracts photometry information from the image.

We used this capability when fitting the g and u band images. The masks used in r band were also uploaded by the package.

We note that fixing the g and u ellipse properties to those of r band will tend to reduce the g and u surface brightness along the ellipses if the emissions in these bands have significantly different preferred ellipticities or position angles. As a consequence, the signatures of star formation would be diluted.

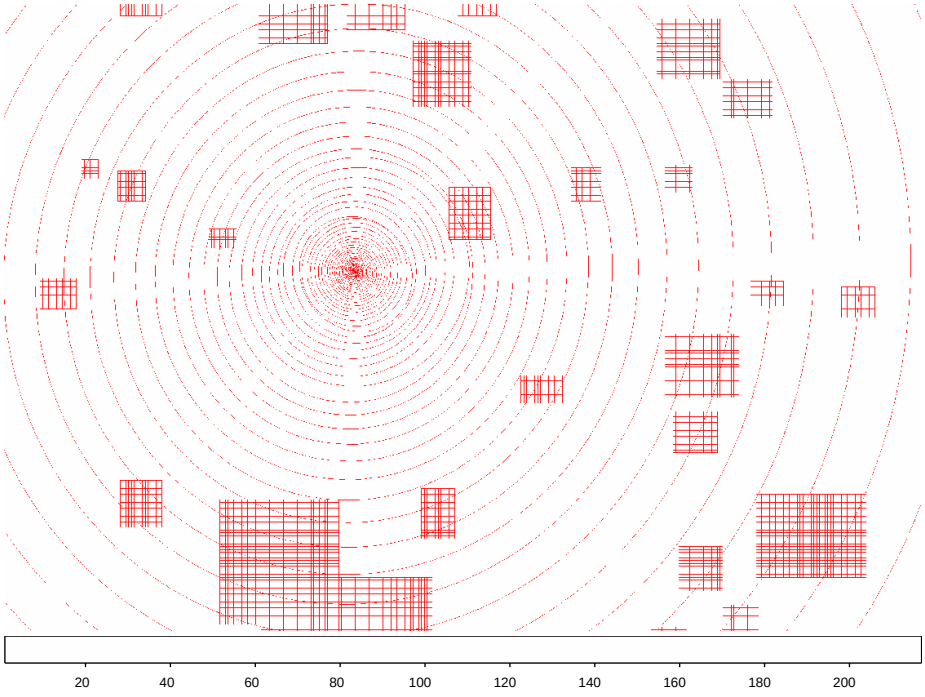

Figure 3.11: As in Figure 3.9 we show the galaxy with over imposed the ellipses fitted by the *ellipse* task. In this image we forced the galaxy to be completely white to make it easier to see the red ellipses.

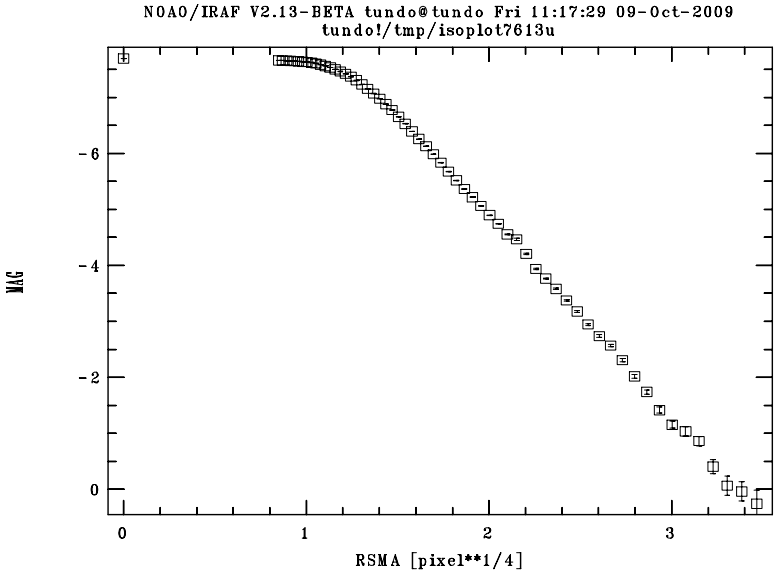

Figure 3.12: Surface brightness profile of the fitted galaxy versus the semi-major axis length (in pixel$^{1/4}$) of the fitted ellipses, plotted by the *isoplot* task

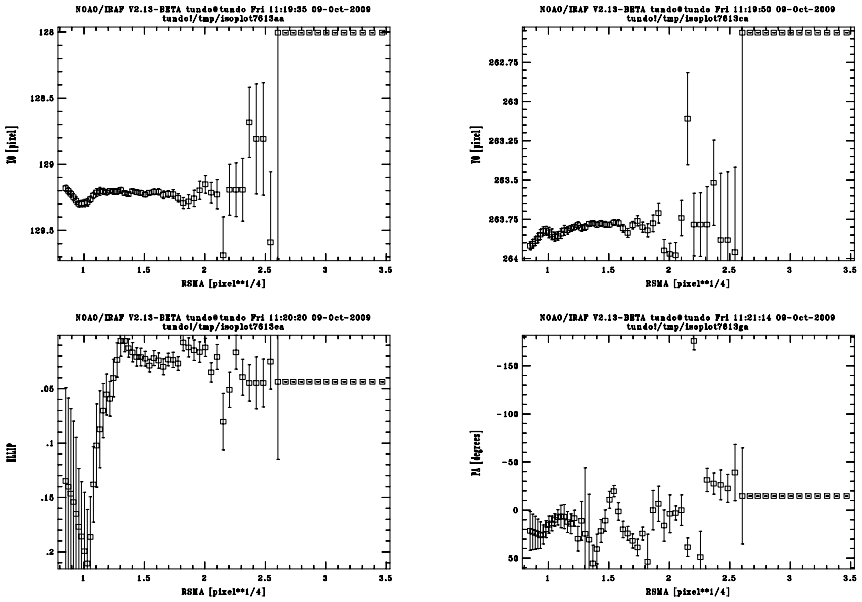

Figure 3.13: An example of the parameters fitted by the *ellipse* task. In the panels there are plotted, versus the ellipse semi-major axis length, respectively: the abscissa position of the center of the fitted ellipse (upper left panel), the ordinate position (upper right panel), the ellipticity b/a (bottom left panel) and the position angle (PA) (bottom right panel).

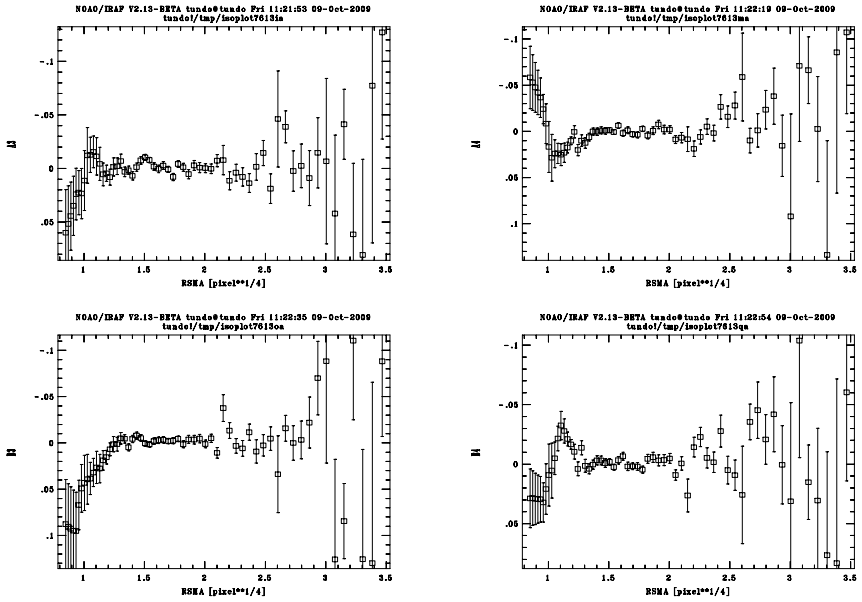

Figure 3.14: An example of the parameters fitted by the *ellipse* task versus the semi-major axis length of the fitted ellipses. From the left to the right, from up to down, the $A3$, $A4$, $B3$, $B4$ parameters.

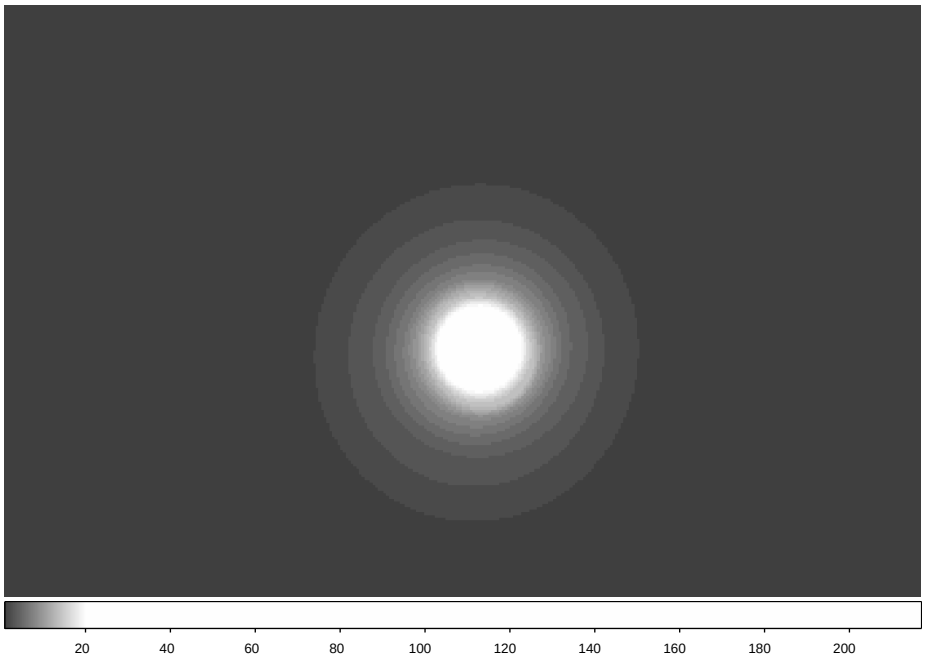

Figure 3.15: Model galaxy built by the *bmodel* task from the parameters fitted by the *ellipse* task.

3.3.3 The profile fitting

The calibration

With the Fpc fits file we downloaded the corresponding tsField fits files (*tsField-rrrrrr-c-v-ffff.fit*, where *rrrrrr* is the imaging run number, *c* is the camera column (1-6), *v* is the rerun number, and *ffff* is the field number for the first field in the file.) that contain all field information.

We retrieved the zero point (*aa*), extinction coefficient (*kk*) and the airmass for each galaxy in each band. Exposure time is the same for all objects, and it is t_{exp} =53.907456 s

We convert the observed number of counts to a count rate using the exposure time, then correct counts for atmospheric extinction using the extinction coefficient *kk* and the airmass, and finally divide by the zero-point count rate, which is given by $f_0 = 10^{-0.4*aa}$ counts/second.

In a single step

$$f/f_0 = (\text{counts}/\text{exptime})10^{0.4(aa+kk*airmass)} \tag{3.15}$$

The CCD report, obviously, counts in each pixel. Still, we are interested in surface brightness profile, and consequently we want measures in arcseconds square.

So we have to add a term that take into account the area of the pixel, that correspond to 0.396" in the sky.

Then the magnitude of the galaxy is simply derived using the following equation:

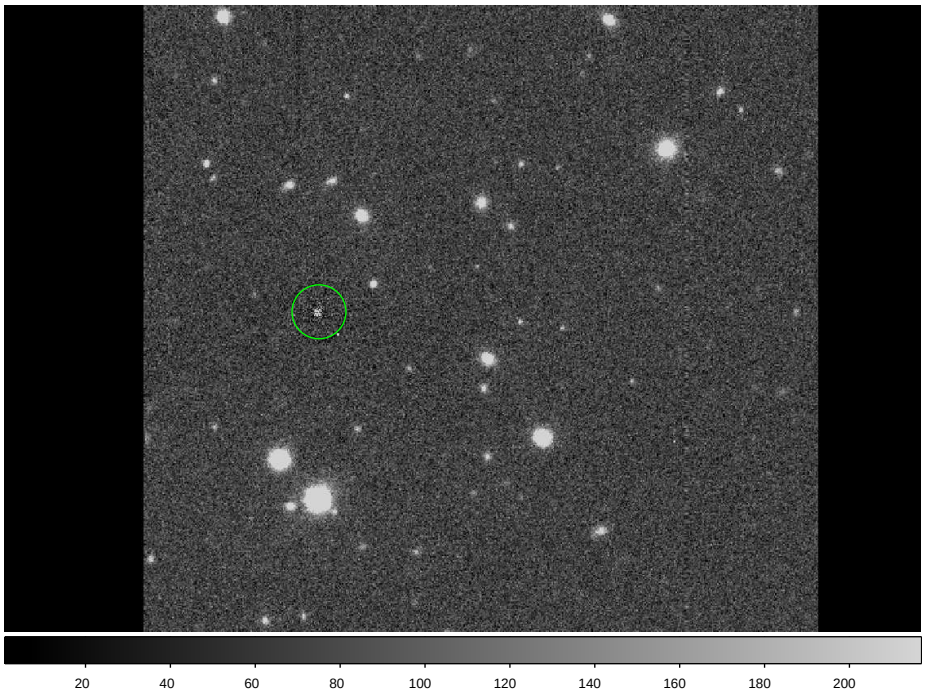

Figure 3.16: Our sky-subtracted image after subtracting the model galaxy built by the *bmodel* task. The green circle highlights the position of the original galaxy center.

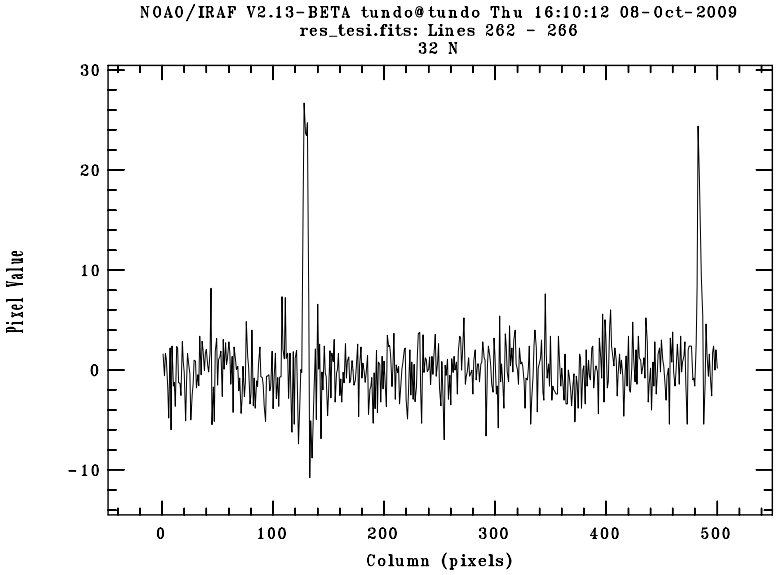

Figure 3.17: A plot of the lines 262-266, corresponding to the position of the center of the fitted galaxy.

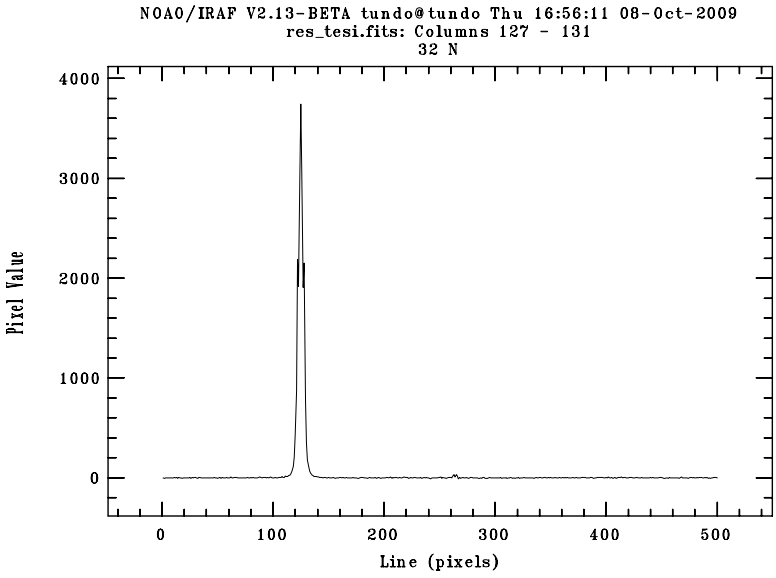

Figure 3.18: A plot of the columns 127-131, corresponding to the position of the center of the fitted galaxy.

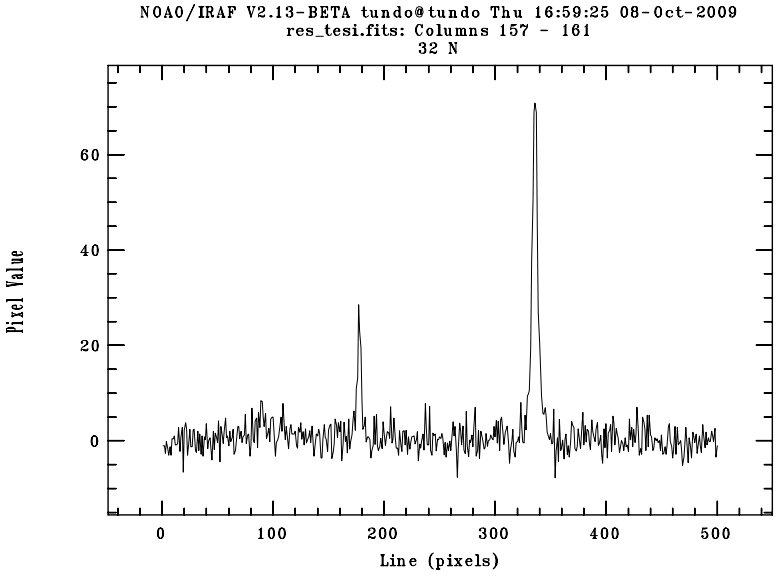

Figure 3.19: A plot of the columns 157-161, to avoid the bright galaxy presents in columns 127-131.

$$\text{mag} = -2.5 * \log(f/f_0) - 2.5 * \log(1./0.396^2) \tag{3.16}$$

The uncertainties that belongs to the magnitude are given by the following expression:

$$\text{error(mag)} = 2.5/\ln(10) * \text{error(counts)} \ / \ \text{counts} \tag{3.17}$$

The fpC (corrected frames) files report counts (or "data numbers", DN). However, it is the number of photo-electrons which is really counted by the CCD detectors and which therefore obeys Poisson statistics. The number of photo-electrons is related to the number of counts through the gain (which is really an inverse gain):

$$\text{photo-electrons} = \text{counts} * \text{gain} \tag{3.18}$$

The gain is reported in the headers of the tsField. The total noise contributed by dark current and read noise (in units of DN^2) is also reported in the tsField files in header keyword dark_variance.

Thus, the error in DN on a measured magnitude is given by the following expression:

$$\text{error(counts)} = \sqrt{\text{[counts+sky]/gain + Npix*(dark\_variance+skyErr)}} \tag{3.19}$$

where counts is the number of object counts, sky is the number of sky counts summed over the same area as the object counts, Npix is the area covered by the object in pixels, gain and dark_variance are the gain and dark variance from the corresponding tsField file, and skyErr is the error on the estimate of the average sky level in the frame.

The profile fitting

Since we selected our sample to be composed by early type galaxies, we want to fit now their surface brightness profile by a De Vaucouleur profile.

Even if this profile can give a poor fit for lenticular galaxies, the net effect on the *color* of the galaxy should be negligible. The magnitude itself, otherwise, can differ using the two profile models.

Anyway, in our sample of 80 galaxy just 7 present a lenticular morphology so that we could easily check that, while the mean color differences between CCC and NCCC galaxies may be slightly different, our final results and conclusions don't change if we include or not these 7 galaxies.

The De Vaucouleur profile is described by the following equation:

$$I(r) = I_0 * e^{-7.67 * \frac{r}{r_e}^{1/4}} \tag{3.20}$$

where I_0 is the central value of the surface brightness, and r_e is the effective radius.

When I_0 and r_e are known, the magnitude can be calculated with the following expression:

$$\mu_e = -2.5 * \log(I_0) + 8.3276 + C_0 \tag{3.21}$$

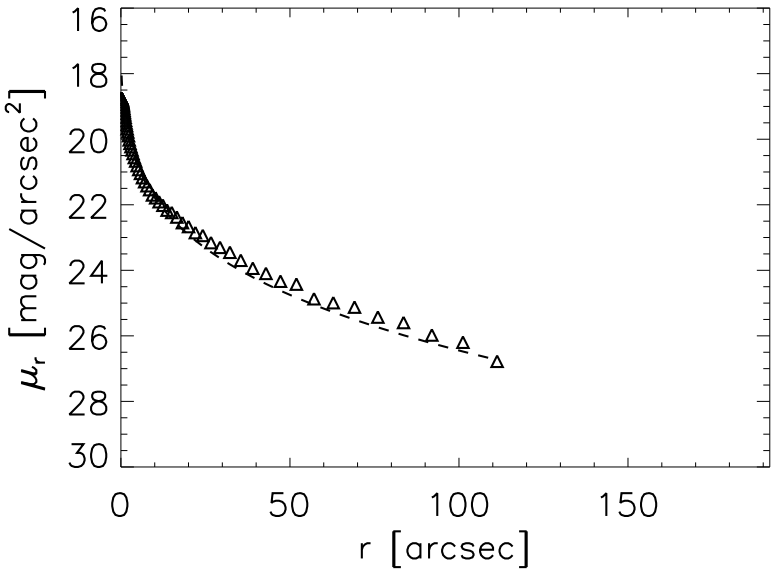

Figure 3.20: Surface brightness profile in magnitude versus the radius r in arcseconds for the brightest central galaxy in the A1991 cluster, in the r band. The dashed line represents the best De Vaucouleurs fit for the profile of the galaxy.

where C_0 represent the calibration constant. Hence, the magnitude is given by

$$\text{mag} = \mu_e - 5 * \log(r_e) - 3.388 \tag{3.22}$$

or

$$\text{mag} = -2.5 * \log(I_0 * r_e^2) + C_0 - 4.939 \tag{3.23}$$

But we have still to take into account the ellipticity $e = 1 - b/a$ of the galaxies, where a and b represent the minor and major axis of the galaxy.

The correct equation to calculate the magnitude of the galaxy will hence need a further term, and it is now given by the following:

$$\text{mag} = -2.5 * \log(I_0 * r_e^2 * (1 - e)) + C_0 - 4.939 \tag{3.24}$$

The SDSS gives numerous methods to measure the ellipticity, including the Stokes parameters, the adaptive moments, the isophotal parameters, and measures of the axis ratio from the De Vaucouleurs profiles and the exponential profiles. We chose to use the estimate given by the model De Vaucouleurs fit, also because the model fits do correctly account for the effect of the seeing, while the other methods do not.

We chose to use the SDSS ellipticity instead of the one measured by the *ellipse* task because, as it is shown in Figure 3.13 (bottom left panel), the value of $1 - b/a$ can vary at each radius. In situations like this it can be difficult to

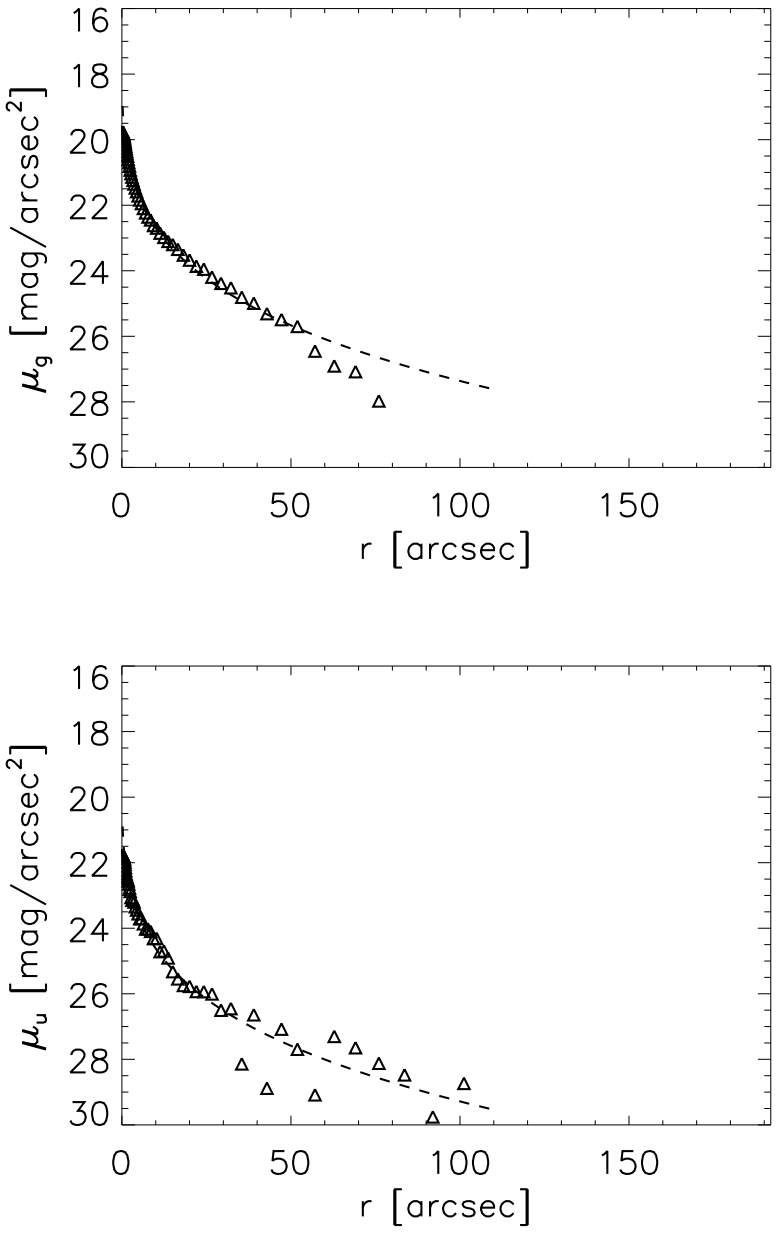

Figure 3.21: *Upper panel*: Surface brightness profile in magnitude versus the radius r in arcseconds for the brightest central galaxy in the A1991 cluster, in the g band. The dashed line represents the best De Vaucouleurs fit for the profile of the galaxy. The effective radius is fixed to the one fitted in the r band, and just the central intensity is fitted. *Bottom panel*: as in the upper panel, in the u band.

evaluate an objective criterion to chose the correct ellipticity to assign to the galaxy.

We show in Figure 3.20 an examples of our profile fitting in the r band.

The fit was performed with the *curvefit* IDL routine.

Once the effective radius r_e in the r band is fitted, we can proceed to measure the magnitudes in the g and u band. We fix the effective radius r_e as found in the r band, and fit just the intensity I_0.

An example of our fits in g and u bands is shown in Figure 3.21.

Some galaxies could not be fitted in a meaningful way, in the u or g band, or even in r band. It is still possible to get a value for the magnitude, but the surface brightness profile is disturbed or the galaxy is too small to have enough valid points to be fitted beyond the seeing.

So, after checking one by one the single fits, we decided to reduce our sample to 47 galaxies, of which 27 belonging to Cool Core Clusters and 20 belonging to Non Cool Core Clusters.

While we didn't use an objective criterion to exclude galaxies from our final sample, we checked that our "subjective" choice don't influence our final results.

We present in Table 3.3.3 the magnitudes for our sample. Uncertainties on magnitudes are given by the following Equation:

$$\epsilon(\mathrm{mag}) = \frac{2.5}{\ln(10)} * \frac{\epsilon(I_0)}{I_0} + \frac{5}{\ln(10)} * \frac{\epsilon(R_e)}{R_e} \tag{3.25}$$

where $\epsilon(I_0)$ and $\epsilon(R_e)$ are given by the *curvefit* IDL routine.

Table 3.4: Fitted magnitudes in r, g and u band, for our sample of cluster galaxies.

Cluster name	**ra [deg]**	**dec [deg]**	***r* [mag]**	***g* [mag]**	***u* [mag]**
A0085	10.4603	-9.3031	10.7797 ± 0.01	11.1805 ± 0.01	13.21 ± 0.01
A0085	10.4510	-9.2842	14.9582 ± 0.01	15.6149 ± 0.01	17.65 ± 0.01
A0085	10.4172	-9.3043	15.5354 ± 0.01	16.0733 ± 0.01	18.11 ± 0.01
A1795	207.2314	26.6168	15.4836 ± 0.03	17.9293 ± 0.02	20.84 ± 0.09
A1795	207.1876	26.5699	16.1788 ± 0.01	16.3112 ± 0.01	18.25 ± 0.02
A1795	207.1774	26.6169	15.5433 ± 0.1	15.9131 ± 0.07	17.90 ± 0.07
A1795	207.2103	26.5854	15.8498 ± 0.04	15.4950 ± 0.07	17.46 ± 0.03
A1795	207.2164	26.6120	16.5237 ± 0.03	17.4983 ± 0.04	19.98 ± 0.05
A1795	207.2093	26.5591	16.7543 ± 0.02	17.5681 ± 0.02	19.29 ± 0.02
A2029	227.7338	5.7448	12.1879 ± 0.01	13.1396 ± 0.01	15.15 ± 0.01
A2029	227.7449	5.6919	16.0218 ± 0.05	16.8722 ± 0.03	18.75 ± 0.04
A2029	227.7142	5.7080	16.5556 ± 0.09	17.5666 ± 0.06	19.38 ± 0.07
A2029	227.7170	5.7530	16.8671 ± 0.3	17.3633 ± 0.2	18.9 ± 0.1
A2052	229.1907	7.0044	13.1169 ± 0.008	13.3294 ± 0.01	15.18 ± 0.01
A2052	229.1735	7.0293	14.5634 ± 0.009	14.8390 ± 0.02	16.66 ± 0.01
A2052	229.1550	6.9653	15.0322 ± 0.01	15.9421 ± 0.01	17.77 ± 0.01
A2063	230.7721	8.6092	12.5633 ± 0.01	13.7549 ± 0.01	15.79 ± 0.01
A2063	230.8126	8.5738	14.1752 ± 0.006	15.2035 ± 0.01	17.046 ± 0.008
A2063	230.7050	8.5605	15.2784 ± 0.01	15.8050 ± 0.01	17.74 ± 0.01
A2142	239.5833	27.2334	14.1299 ± 0.01	15.8321 ± 0.02	18.12 ± 0.01
A2142	239.6027	27.2295	15.4893 ± 0.01	16.3764 ± 0.01	19.6 ± 0.1
A2142	239.5694	27.2367	16.7694 ± 0.02	17.5369 ± 0.02	20.28 ± 0.06
A2142	239.5965	27.2072	16.5782 ± 0.02	17.1955 ± 0.02	19.39 ± 0.05

Continued on next page

Table 3.4 – continued from previous page

Cluster name	ra [deg]	dec [deg]	mag_r [mag]	mag_g [mag]	mag_u [mag]
A2142	239.5943	27.2567	17.1052 ± 0.1	18.8735 ± 0.08	25 ± 10
A2199	247.0971	39.5703	14.0075 ± 0.01	14.9530 ± 0.008	16.822 ± 0.008
A2199	247.1502	39.5338	14.7543 ± 0.01	14.8722 ± 0.01	16.58 ± 0.01
A2199	247.1852	39.5155	14.8498 ± 0.05	15.5944 ± 0.03	17.40 ± 0.03
A2244	255.6898	34.0611	15.8363 ± 0.02	16.7243 ± 0.02	18.46 ± 0.01
A2244	255.6508	34.0885	16.6877 ± 0.06	17.1439 ± 0.04	20.08 ± 0.07
A1413	178.8229	23.3913	16.9453 ± 0.06	17.9992 ± 0.04	19.32 ± 0.07
A1413	178.8179	23.4227	12.4135 ± 0.08	16.2274 ± 0.08	18.8 ± 0.5
A1689	197.8839	-1.3297	17.1913 ± 0.1	17.2973 ± 0.1	29. ± 8.
A1689	197.8660	-1.3355	16.0989 ± 0.6	16.6961 ± 0.4	18.4 ± 0.2
A1689	197.8676	-1.3454	15.4744 ± 0.2	15.8548 ± 0.2	18.3 ± 0.1
A1689	197.8709	-1.3546	17.7477 ± 0.5	17.8805 ± 0.3	29 ± 13
A1914	216.4982	37.8278	16.9798 ± 0.08	18.1605 ± 0.06	19.95 ± 0.07
A1914	216.5187	37.8415	17.2188 ± 0.05	18.3645 ± 0.05	27.5 ± 0.7
A1914	216.5023	37.8360	17.7909 ± 0.3	19.8465 ± 0.1	30. ± 7.
A1914	216.5007	37.8195	16.9082 ± 0.2	17.8877 ± 0.1	19.8 ± 0.1
A1914	216.4914	37.8248	17.5725 ± 0.07	18.6658 ± 0.07	29. ± 2.
A1914	216.5019	37.8221	17.7536 ± 0.07	18.6292 ± 0.08	19.40 ± 0.09
A2151w	241.1492	17.7216	13.1607 ± 0.02	14.6717 ± 0.01	16.60 ± 0.01
A2151w	241.1649	17.7008	13.6639 ± 0.006	14.8735 ± 0.007	16.718 ± 0.007
A2151w	241.1456	17.7174	15.0622 ± 0.04	15.7796 ± 0.02	17.5513± 0.02
A2151w	241.1759	17.6837	15.3218 ± 0.08	15.6419 ± 0.05	17.3506± 0.05
NGC5846	226.6217	1.5949	12.8031 ± 0.01	12.9864 ± 0.01	14.8232± 0.01
A1991	223.6312	18.6423	13.2585 ± 0.01	14.4258 ± 0.01	16.3507± 0.01
RXJ1159+	179.9674	55.5349	13.8775 ± 0.01	14.8273 ± 0.01	16.8307± 0.01

Continued on next page

Table 3.4 – continued from previous page

Cluster name	ra [deg]	dec [deg]	mag_r [mag]	mag_g [mag]	mag_u [mag]
RXJ1159+	179.9808	55.5390	18.1396 ± 0.1	19.3248 ± 0.09	29.8595± 6.
RXJ1159+	179.9590	55.5484	17.8359 ± 0.2	18.2008 ± 0.1	19.0307± 0.1
A0119	14.0671	-1.2554	12.5474 ± 0.007	13.7092 ± 0.009	15.6872± 0.006
A0119	14.0756	-1.2418	14.8712 ± 0.009	15.5789 ± 0.009	17.3908± 0.009
A0119	14.0559	-1.2384	16.6808 ± 0.08	17.5174 ± 0.05	19.3218± 0.05
A1650	194.6600	-1.7696	16.9235 ± 0.03	17.1606 ± 0.04	19.0312± 0.03
A1650	194.6532	-1.7481	16.5554 ± 0.02	17.1772 ± 0.02	19.3773± 0.04
A2065	230.6001	27.7144	14.8191 ± 0.009	16.1334 ± 0.009	18.1675± 0.01
A2065	230.6185	27.6869	15.4713 ± 0.01	16.7392 ± 0.01	18.7308± 0.01
A2065	230.6158	27.6991	15.7891 ± 0.01	15.8278 ± 0.01	17.8037± 0.01
A2147	240.5733	16.0030	15.3874 ± 0.1	15.8614 ± 0.08	17.6285± 0.08
A2147	240.5972	15.9965	15.4448 ± 0.1	15.8048 ± 0.08	17.5657± 0.08
A2147	240.5440	15.9713	15.6428 ± 0.09	16.0204 ± 0.05	18.0438± 0.06
COMA	194.8046	27.9770	13.3386 ± 0.05	13.9310 ± 0.03	15.7749± 0.03
COMA	194.8866	27.9836	13.5811 ± 0.008	14.1252 ± 0.007	15.8682± 0.007
MKW8	220.1626	3.4697	12.3025 ± 0.01	13.2714 ± 0.01	15.1950± 0.01
MKW8	220.2195	3.4183	14.0604 ± 0.02	14.5706 ± 0.01	16.5592± 0.01
MKW8	220.1225	3.4327	14.0850 ± 0.1	14.7473 ± 0.07	16.7366± 0.06
MKW8	220.2419	3.4516	14.5481 ± 0.009	15.0343 ± 0.008	16.8196± 0.008
wCl1215	184.4213	3.6558	14.0681 ± 0.07	15.4348 ± 0.04	17.3869± 0.04
wCl1215	184.4116	3.6634	15.4233 ± 0.04	16.3670 ± 0.02	18.3571± 0.03
A1775	205.4612	26.3690	16.8160 ± 1.	21.1267 ± 1.	29.5333± 8.
A1775	205.4467	26.3809	16.1244 ± 0.1	17.1398 ± 0.06	19.4966± 0.07
A1775	205.4409	26.3880	16.7435 ± 0.07	17.6070 ± 0.04	19.6140± 0.08
A1775	205.4753	26.3808	16.9086 ± 0.03	17.5110 ± 0.03	19.4484± 0.03

Continued on next page

Table 3.4 – continued from previous page

Cluster name	ra [deg]	dec [deg]	mag_r [mag]	mag_g [mag]	mag_u [mag]
A1800	207.3482	28.1073	12.4055 ± 0.01	13.0701 ± 0.01	15.0307± 0.01
A1800	207.3535	28.0974	16.3103 ± 0.3	16.7476 ± 0.1	18.1804± 0.1
A1800	207.3633	28.0790	16.4187 ± 0.03	17.2250 ± 0.03	20.6813± 0.04

3.3.4 Tests on the quality of the magnitude fitting

Mono and bidimensional reduction

Our reduction is based on a mono-dimensional fit of the surface brightness profile of the galaxies.

To test the goodness of ours fit, we performed a bi-dimensional fit of a subsamples of 10 galaxies chosen to have different size and magnitude, using the GALMORPH software (Hyde et al. 2008), that performs two-dimensional χ^2 minimization, using simulated annealing as the search algorithm.

Figure 3.22 (upper panel) shows the differences between r magnitudes between the SDSS data, and the mono and bidimensional fit magnitudes (that we will call from now on Tundo and Hyde magnitudes), versus the SDSS magnitudes. Different symbols refers to different fitting procedure, as in the legend. We see that the mono and bidimensional fit as performed in this work give results in remarkably agreement, except for one single object, while SDSS usually find magnitudes fainter than in ours measurements. Figure 3.22 (bottom panel) shows the same data versus the effective radius as measured by the SDSS.

We should expect to see a correlation between $\Delta(r)$ and the r magnitude or R_e, but we just observe that for the two brightest galaxies (SDSS $r < 13.5$) $\Delta(r)$ is much greater than for fainter galaxies. Probably we don't observe any trend in $\Delta(r)$ with the r magnitude or R_e since our sample is composed mostly by galaxies fainter than $r = 15$ and smaller than $R_e = 4$ arcmin, with a gap between these values and the ones belonging to the two galaxies with bigger magnitude and size.

Comparation with SDSS magnitudes

In Figures 3.23 ,3.24 and 3.25 we show our model r, g and u magnitude versus the SDSS model magnitudes. We see, as expected, that SDSS magnitudes tend to be fainter.

In Figure 3.26 we plot the differences $r_{SDSS} - r$ versus ours r magnitudes. Compared with Figure 3.3 (Figure 6 of Abazajian et al. 2009) it indicates that we correctly estimated the effect of the overestimated sky in SDSS measures.

In fact, we see that the differences $r_{SDSS} - r$ show the same trend as in Figure 3.3, with $r_{SDSS} - r$ increasing at grater r_{SDSS}. In the simulations of Abazajian et al. (2009) $r_{SDSS} - r$ <0.1 mag at r_{SDSS} >16 mag, while in Figure 3.26 we see that the data points at r_{SDSS} >16 mag have a mean of >0.2 mag, and show higher dispersion than in Abazajian et al. (2009). Still, we notice that we are plotting actual data of cluster galaxies, for which it is predicted to have higher $r_{SDSS} - r$ than in simulations of isolated galaxies. Moreover, we are looking at relatively faint galaxies in usually crowded fields, so that the galaxy fitting strongly depends on the subtraction of the other galaxies. This explains why $r_{SDSS} - r$ shows a greater dispersion at r_{SDSS} >16 mag than at 14< r_{SDSS} >16 mag respect to the simulations of Abazajian et al. (2009).

We report the mean uncertainties on our fitted magnitude to be $\langle \Delta r \rangle$ =0.04 mag, $\langle \Delta g \rangle$ =0.03 mag, $\langle \Delta u \rangle$ =0.04 mag. In comparison, the mean uncertainties on the SDSS magnitudes for the galaxies in our sample are: $\langle \Delta r \rangle$ =0.003 mag, $\langle \Delta g \rangle$ =0.004 mag, $\langle \Delta u \rangle$ =0.03 mag.

We notice that our uncertainties are usually greater than the ones reported in the SDSS database.

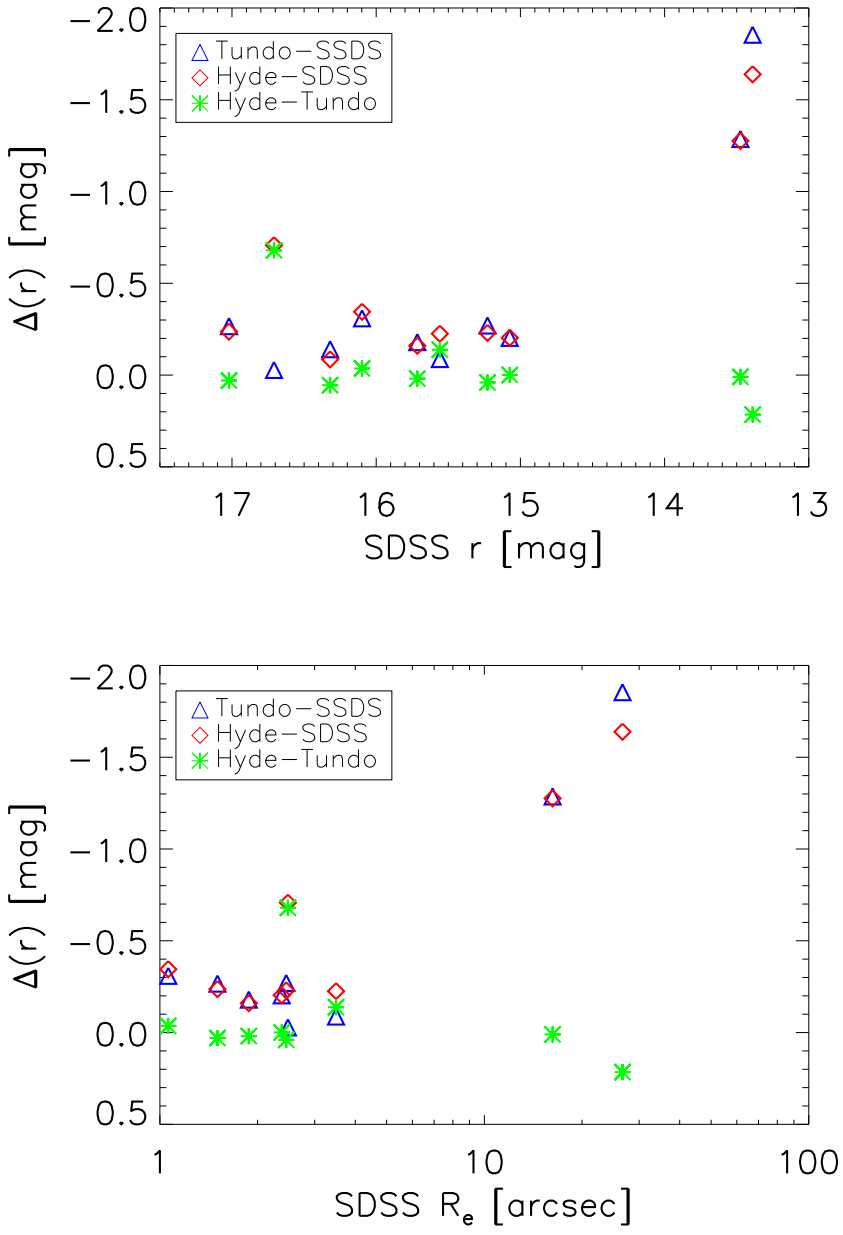

Figure 3.22: *Upper panel*: Differences between SDSS, Tundo and Hyde fitted r magnitudes for a subsample of 10 galaxies (see text). Blue triangles, red diamonds and green asterisks represent respectively the differences between SDSS and Tundo, between SDSS and Hyde, and between Tundo and Hyde magnitudes, as in the legend. *Bottom panel*: as in the upper panel, with the data plotted versus the SDSS effective radius.

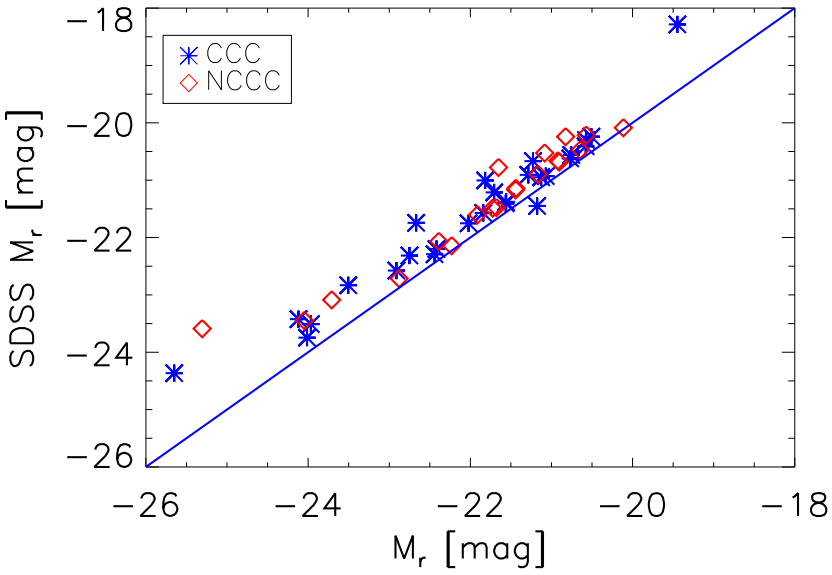

Figure 3.23: SDSS M_r magnitudes versus our fitted magnitudes. Blue line represent an unitary relation. Galaxies are divided in CCC and NCCC galaxies as in the legend.

In fact, in SDSS measure, errors on model magnitudes are based only on photon statistics, while in our case we add the uncertainties coming from the fitting itself, so that a galaxy with a contribution of the intracluster light will have greater uncertainties, since its surface brightness profile will differ from a pure De Vaucouleur one.

3.4 The Color-Magnitude relation

The K-correction and the absolute magnitude

The K-correction between a bandpass R used to observe a galaxy at redshift z and the desired bandpass Q is defined by the equation (Oke & Sandage 1968; Hogg et al. 2002):

$$m_R = M_Q + \mathrm{DM}(z) + K_{QR}(z) - 5\log_{10} h \tag{3.26}$$

where $\mathrm{DM}(z) = 25 - 5\log_{10}(d_L/(h^{-1}\ \mathrm{Mpc}))$ is the bolometric distance modulus calculated from the luminosity distance d_L, and M_Q is the absolute magnitude.

In order to find the adequate k-correction, we use the IDL code *kcorrect* (Blanton et al. 2003). The exact description of the algorithm would take too much space, and we refer to Blanton et al. (2003) for that, nevertheless we can say that the code, given the observations and uncertainties available for each galaxy, finds the nonnegative linear combination of N template star-formation histories which best predict those observations in the χ^2 sense.

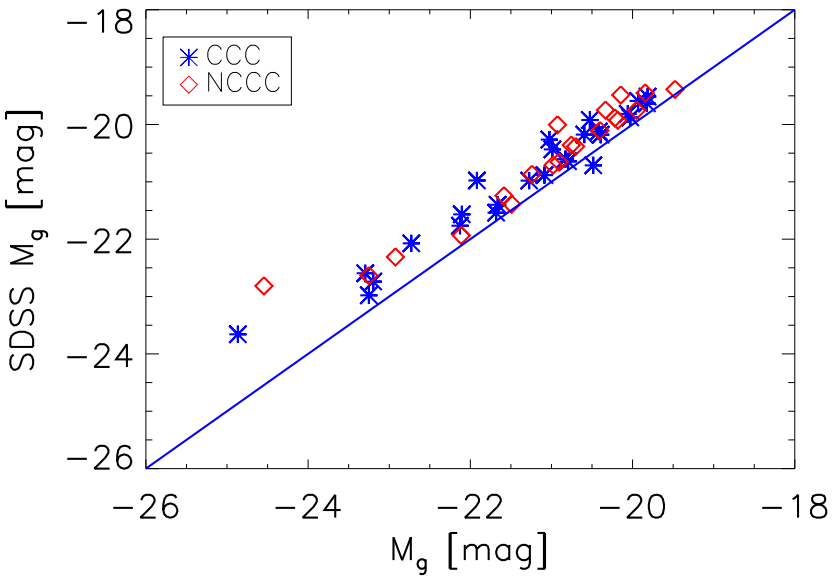

Figure 3.24: As in Figure 3.23 plotting g band magnitudes.

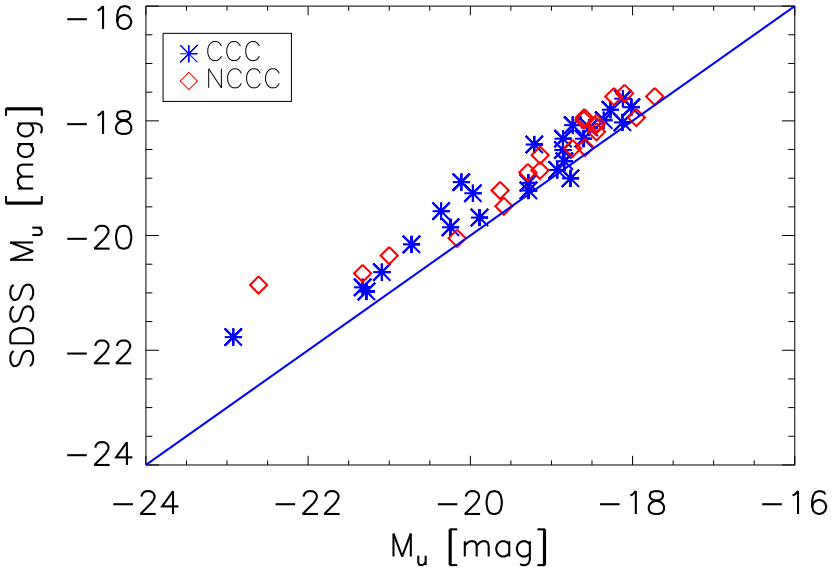

Figure 3.25: As in Figure 3.23 plotting u band magnitudes.

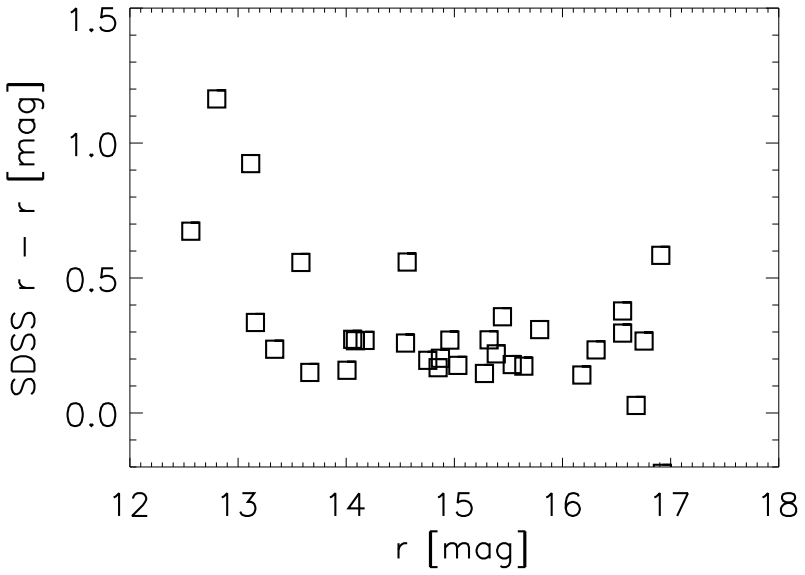

Figure 3.26: Differences between SDSS r magnitudes and our fitted magnitudes versus the SDSS r magnitudes.

The method is designed to work well for a wide range of data sets. It uses photometry and spectroscopy of the Sloan Digital Sky Survey, the Galaxy Evolution Explorer in the ultraviolet, and the Two-Micron All Sky Survey in the near infrared (NIR).

Since a model spectrum for the galaxy is given, the K-correction between a bandpass R used to observe a galaxy at redshift z and the desired bandpass Q is defined by Equation 3.26 where K_{QR} is

$$K_{QR} = -2.5 \log_{10} \left[\frac{1}{[1+z]} \frac{\int \mathrm{d}\lambda_o \, \lambda_o \, L_\lambda\left(\frac{\lambda_o}{1+z}\right) R(\lambda_o) \int \mathrm{d}\lambda_e \, \lambda_e \, g^Q_\lambda(\lambda_e) \, Q(\lambda_e)}{\int \mathrm{d}\lambda_o \, \lambda_o \, g^R_\lambda(\lambda_o) \, R(\lambda_o) \int \mathrm{d}\lambda_e \, \lambda_e \, L_\lambda(\lambda_e) \, Q(\lambda_e)} \right] . \tag{3.27}$$

Here, $R(\lambda)$ and $Q(\lambda)$ represent the response of the instrument per unit photon entering the Earth's atmosphere (or the telescope aperture for a space instrument). g^R_λ is the flux density per unit wavelength (e.g. ergs s^{-1} cm^{-2} $\mathrm{\AA}^{-1}$) for the standard source for band R, and similarly for band Q.

When $R = Q$:

$$K_R(z) = -2.5 \log_{10} \left[\frac{1}{[1+z]} \frac{\int \mathrm{d}\lambda_o \, \lambda_o \, L_\lambda\left(\frac{\lambda_o}{1+z}\right) R(\lambda_o)}{\int \mathrm{d}\lambda_e \, \lambda_e \, L_\lambda(\lambda_e) \, R(\lambda_e)} \right] . \tag{3.28}$$

Reddening corrections in magnitudes are applied to our magnitudes using the extinction computed in the SDSS database at the position of each object, following Schlegel, Finkbeiner & Davis (1998).

Luminosity evolution

Galaxies are fainter at the present day, owing mostly to passive evolution. In the picture of galaxy formation all the stars in a galaxy that are formed in an inital burst, thereafter evolves only in a passive, quiescent manner as they make their journey along the main sequence. This results in a gradual dimming of the stars, and consequently the galaxy. Any further episodes in the evolution of galaxies, such as secondary bursts of (or gradual) star-formation activity must take place against this background of the passive evolution of the pre-existing stars.

Bell (2003) finds mean evolution corrections by comparison of galaxy *ugrizK* magnitudes with galaxy evolution models at each galaxy's redshift in their sample drawn from the SDSS and 2MASS databases. He finds evolution corrections of $\sim$(2.3,1.6,1.3,1.1,1.0,0.8)z in *ugriz*K, while Blanton et al. (2003c) report the evolution by fitting for it explicitly in their LF estimation, and find an evolution of $\sim$(4.2$\pm$0.9,2.0$\pm$0.5,1.6$\pm$0.3,1.6$\pm$0.4,0.8$\pm$0.3)z in *ugriz*. Independently, Bernardi et al. (2003a) find evolution of $\sim$(1.2,0.9,0.8,0.6)z in *griz* for early type galaxies using a similar (but totally independent) technique to Blanton et al. (2003c).

We chose to use the evolution correction from Bell (2003), that are in agreement with other works and that have the advantage of incorporate the multi-passband information.

The redshift and magnitude distributions

We show in Figure 3.27 the magnitude distribution of our sample. The black line represent the distribution for the whole sample, while the red and blue lines are for the NCCC and CCC sample. In Figure 3.28 we show the redshift distribution for our samples. The color code is the same as in Figure 3.27. We see that the distributions of the CCC and NCCC sample are comparable. Any differences in color between the two samples won't be due to differences in magnitude or redshift distribution.

In Figure 3.29 we show the magnitudes of our galaxies versus their redshifts. In this Figure it is more easily appreciated that the two samples have similar distribution.

The color magnitude relations

Figures 3.30 and 3.31 show the color-magnitude diagram $g-r$ and $u-m$ versus M_r for CCC and NCCC samples.

Since we are interested in the mean color difference between the two samples, we are going to fit the $g-r$ and $u-m$ versus M_r relation using the *sixlin.pro* routine of IDL (Isobe et al. 1990)

As discussed in the first Chapter, when the scatter of data points in a relation is non negligible, the theoretical results of different regression methods will be different. As in the previous Chapter we chose to show the results of

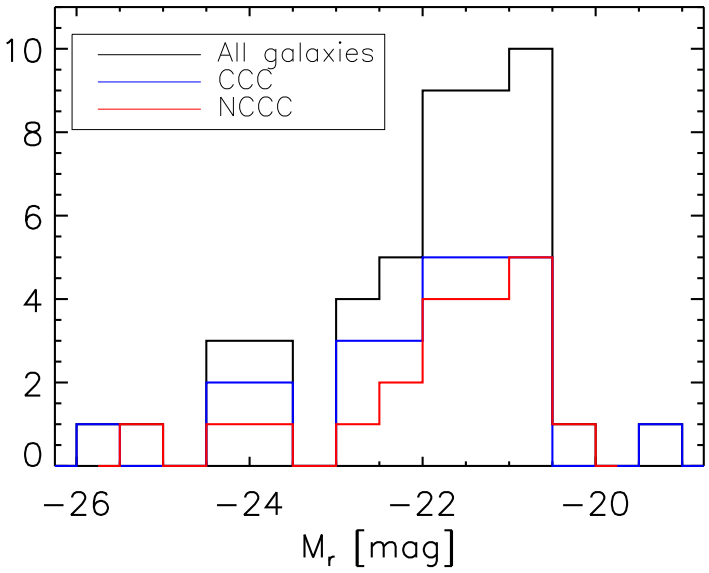

Figure 3.27: Magnitude distribution of our sample. The black line represent the distribution for the whole sample, while the red and blue lines are for the NCCC and CCC sample.

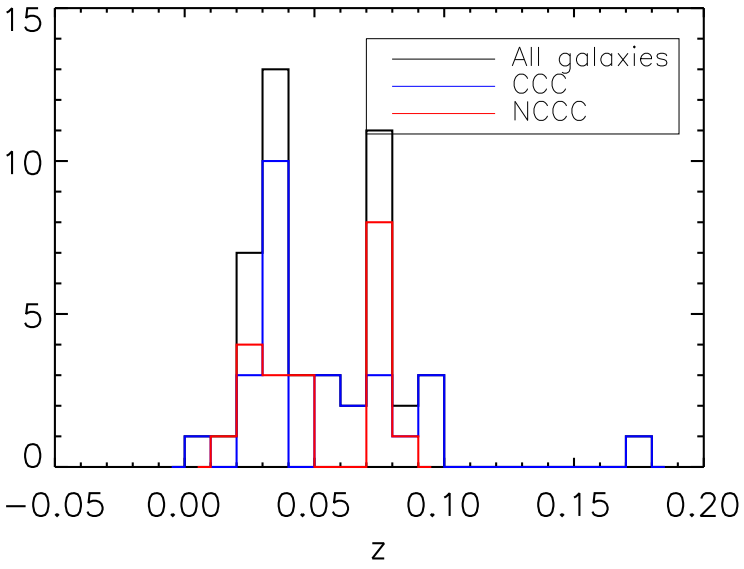

Figure 3.28: Redshift distribution for our samples.The black line represent the distribution for the whole sample, while the red and blue lines are for the NCCC and CCC sample.

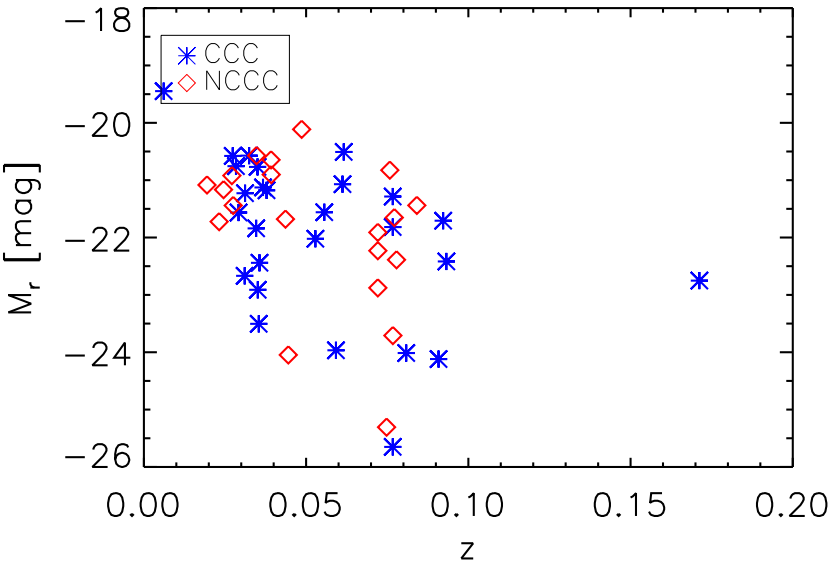

Figure 3.29: M_r magnitude versus redshift for our sample. CCC galaxies are represented by blue asterisks, while NCCC galaxies are represented by red diamonds, as in the legend.

three different regression methods, namely the Orthogonal Least Square Bisector (OLS Bisector), the Orthogonal Regression (OR) and the Reduced Major Axis (RMA).

For each of these methods, we fitted the color-magnitude relation for all the data points to retrieved the slopes b_{gmr} and b_{umr} for the $g-r$ and $u-r$ versus r relations.

We then derived the zero points using the following equations separately for CCC and NCCC galaxies:

$$\mathrm{zp}_{gmr} = \langle (M_g - M_r) \rangle - \langle M_r \rangle * \mathrm{b}_{gmr} \tag{3.29}$$

$$\mathrm{zp}_{umr} = \langle (M_u - M_r) \rangle - \langle M_r \rangle * \mathrm{b}_{umr} \tag{3.30}$$

This procedure assume the hypothesis that galaxies both in CCC and NCCC follow the same color-magnitude relation, and that the two samples differ just for the mean colors, hence for the zero points.

Figures 3.30 and 3.31 show the relations found using the OR method only, for clarity. In Table 3.4 we show the differences between zero points ($\mathrm{zp}_{CCC} - \mathrm{zp}_{NCCC}$) for the $M_g - M_r$ and $M_u - M_r$ color magnitude relation using the three regression methods.

In Figure 3.34, 3.33 and 3.32 we plot the $M_{NUV} - M_r$ versus M_r, the $M_{NUV} - M_K$ versus K and the $M_r - M_K$ versus M_K diagram.

We summarize our results in Table 3.4; we see that in as many as half of the cases the mean color differences are null within uncertainties.

Table 3.5: Mean color differences between CCC and NCCC galaxies, using OLS Bisector, OR and RMA regression methods.

	OLS Bisector	**OR**	**RMA**
$\Delta(zp)_{[g-r]}$	0.003± 0.003	0.002 ± 0.002	0.003 ± 0.002
$\Delta(zp)_{[u-r]}$	0.07 ± 0.01	0.067 ± 0.005	0.072 ± 0.008
$\Delta(zp)_{[g-r]}SDSS$	0.022± 0.003	0.0157± 0.0005	0.0185± 0.0004
$\Delta(zp)_{[u-r]}SDSS$	0.1 ± 0.3	0.041 ± 0.006	0.052 ± 0.009
$\Delta(zp)_{[r-K]}$	0.08 ± 0.3	0.05 ± 0.1	0.06 ± 0.05
$\Delta(zp)_{[NUV-r]}$	0.2 ± 0.1	0.14 ± 0.09	0.16 ± 0.1
$\Delta(zp)_{[NUV-K]}$	0.2 ± 0.9	0.02 ± 0.4	0.14 ± 0.4

These results point to the conclusion that mean color difference in optical band cannot quantify the differences in SFR between galaxies in Cool Core Clusters and Non cool Core Clusters.

Still, we observe that if the zero points were really equall to zero, if, in consequence, there were no differences between CCC and NCCC galaxies, we should observe values of $\mathrm{zp}_{ccc}-\mathrm{zp}_{Nccc}$ both positive and negative, while in our case all values except one are greater than zero.

This indicate, in our opinion, that the mean differences in color we found actually indicate a physical differences between CCC and NCCC galaxies.

We want to notice, moreover, that our reported errors on magnitudes are very conservative, since they include not only photon statistic but also the uncertainties on the profile fitting. Hence, even the uncertainties on zero point differences are very conservative.

As a further test on the reliability of our measures we compute the $M_g - M_r$ and $M_u - M_r$ color magnitude relations using SDSS data, to see how much the final mean color difference differ from the one we measured.

In Figure 3.37 upper left and right panels we show the color magnitude diagrams using the SDSS magnitudes. As in Figures 3.30 and 3.31 we only show the results from the OR method, for clarity.

Results of this procedure are shown in table 3.4. The use of SDSS data gives mean color differences that can be higher or lower than the one we measured, while uncertainties are understandably lower.

We want to notice, moreover, that we have not treated our galaxies for possible dust reddening.

We know that the dust is a product of star formation, so that galaxies with an high rate of star formation will have a greater amount of dust, and their colors will be redder than if due only to their galaxies.

Still, since our goal in the work is mainly to asses if broad band colors can be used to see the differences between CCC and NCCC galaxies, we notice that dust reddening will *reduce* the mean color difference we are seeking, in the hypothesis that this difference is due mainly to difference in the galaxy population and not to different ages.

K band should be less affected by this problem, so that the $M_r - M_K$ color should be quite unaffected, and give a good estimate of the actual color difference between CCC and NCCC galaxies.

We note also that we cannot rely on results from the $M_{NUV} - M_K$ colors,

since we see in Figure 3.33 that due to the match between GALEX and 2MASS data in this plot CCC and NCCC galaxies don't span the same range of magnitude, so that at magnitude brighter than $M_K = -25$ mag we observe only CCC galaxies.

As a further test on the reliability of our procedure we compare our fitted color magnitude relation $M_g - M_r$ with the one found by Roche et al.(2009); they studied a sample of E/SO galaxies from the SDSS DR4 (Adelman-McCarthy et al. 2006) and two different samples of BCG (one selected from the C4 BCGs, a subsample of the first-ranked galaxies within the catalog of clusters detected using a C4 cluster-detection algorithm on the SDSS-DR2 data (Miller et al. 2005), further selected following the indications of Bernardi et al. (2007) and excluding any spiral or disk component. The second one from the max-BCG catalog of Koester et al. (2007)).

They report a slope and zero point in the whole E/SO sample of $b_{E/SO} = 0.01735 \pm 0.00046$ and $\mathrm{zp}_{E/SO} = 0.3794 \pm 0.0093$, while in the C4 BCG and max-BCG they give $b_{C4BCG} = 0.0056 \pm 0.0047$, $\mathrm{zp}_{C4BCG} = 0.6604 \pm 0.1084$ (not including an evolution term), and $b_{max-BCG} = 0.0082 \pm 0.0018$, $\mathrm{zp}_{max-BCG} = 0.5877 \pm 0.0403$.

In our sample we have $b = -0.0174 \pm 0.0006$, zp= 0.362 ± 0.001 (we report results from OR regression only, for simplicity), while the SDSS data give $b_{SDSS} = -0.0074 \pm 0.0002$, $zp_{SDSS} = 0.6042 \pm 0.0004$.

We observe that we are not looking at BCG galaxies only, so that a slope of $b = -0.0174 \pm 0.0006$ is quite in good agreement with the estimates of Roche et al.(2009), while the one from the SDSS magnitudes is not.

3.4.1 The Mass deposit rate versus color

If colors trace the SFR due to the mass deposit rate predicted by the cooling flow models, we should observe a correlation between colors and $\dot{M}$.

We plotted in Figures 3.35 and 3.36 the $M_g - M_r$ and $M_u - M_r$ colors of ours galaxies versus the mass deposit rate $\dot{M}$ =dM/dt [$M_\odot$/year] as reported by Chen et al. (2007).

We divided our galaxies in two bin of magnitude, splitted around r =-21.5 mag. This value was chosen to assure a similar number of galaxies in both bins.

Figure 3.37 (left and right bottom panels) show the $M_g - M_r$ and $M_u - M_r$ colors using SDSS values versus $\dot{M}$. In this case one could see a trend between $M_u - M_r$ color and $\dot{M}$. Anyway, a *fit* to the relation reveals that any correlation's slope have an uncertainties that makes the slope itself compatible with zero (we have $\mathrm{b}_{OLSB} = -0.003 \pm 0.02$, b_{OR}=-0.0004±0.004, b_{RMS} =-0.001±0.02 for galaxies with r >-21.5 and $\mathrm{b}_{OLSB} = 0.006 \pm 0.08$, b_{OR}=-0.0002±0.002, b_{RMS} =0.007±0.08 for galaxies with r <-21.5). Moreover, if we remove the data point with the highest value of $M_u - M_r$ for the galaxies in the lowest bin of magnitude and the data point with the lowest value of $u - r$ for the galaxies in the highest bin of magnitude we see that the apparent correlation completely disappears.

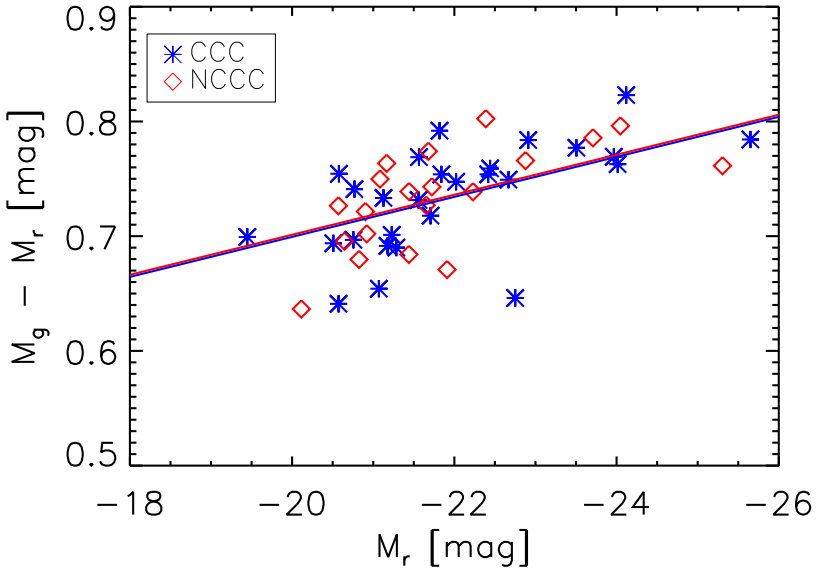

Figure 3.30: $M_g - M_r$ versus M_r diagram for our sample. Blue asterisks represent galaxies in Cool Core Clusters, while red diamonds represent galaxies in Non Cool Core Clusters. The lines represent the fitted color-magnitude relations for the CCC (blue line) and NCCC (red line)samples (see text)

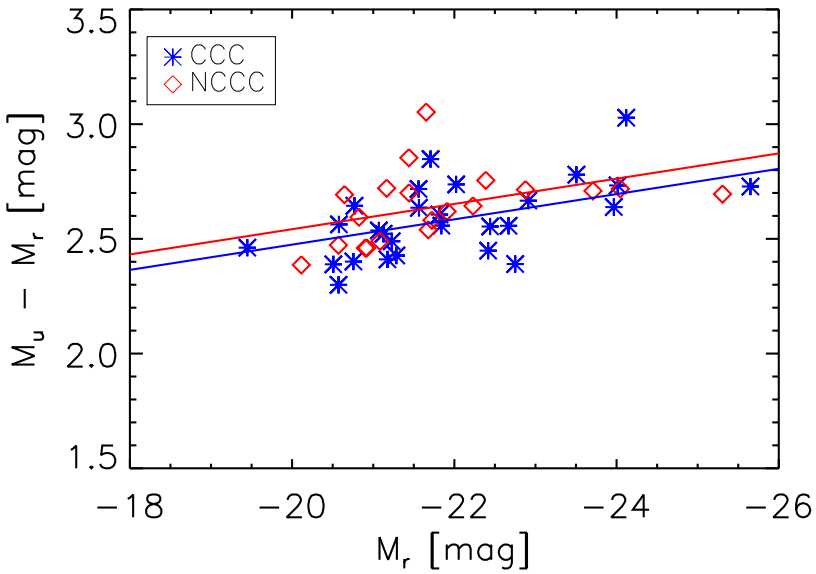

Figure 3.31: $M_u - M_r$ versus M_r diagram for our sample. Symbols are as in Figure 3.30.

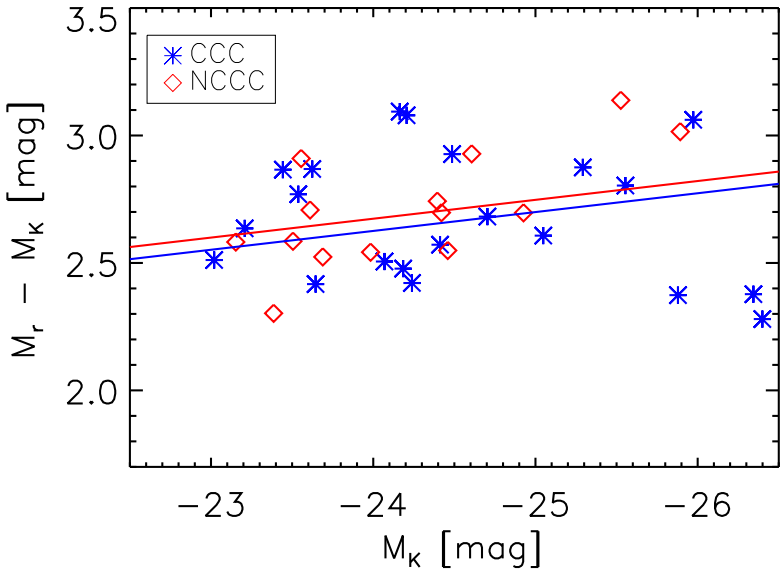

Figure 3.32: $M_r - M_K$ versus M_K diagram. Blue asterisks represent CCC galaxies, while red diamonds represent NCCC galaxies. The lines represent the fitted color-magnitude relations for the CCC (blue line) and NCCC (red line)samples (see text).

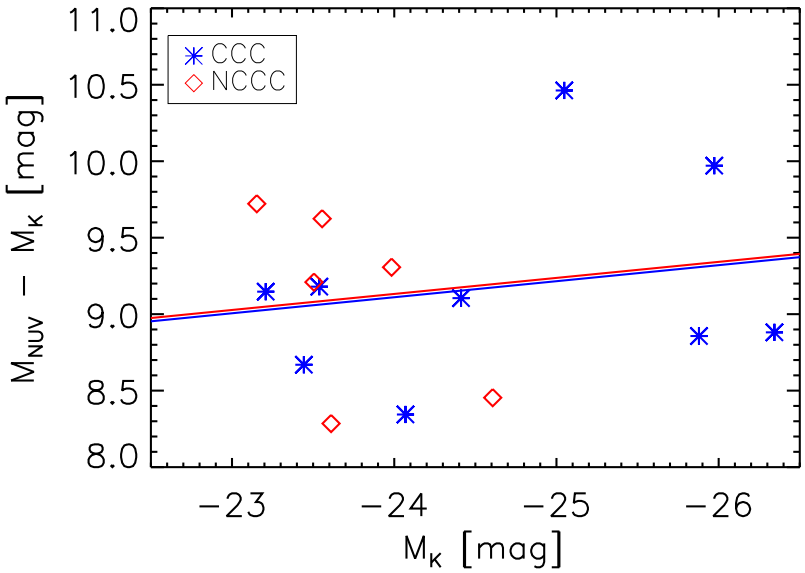

Figure 3.33: $M_{NUV} - M_K$ versus M_K magnitudes. Symbols are as in Figure 3.34.

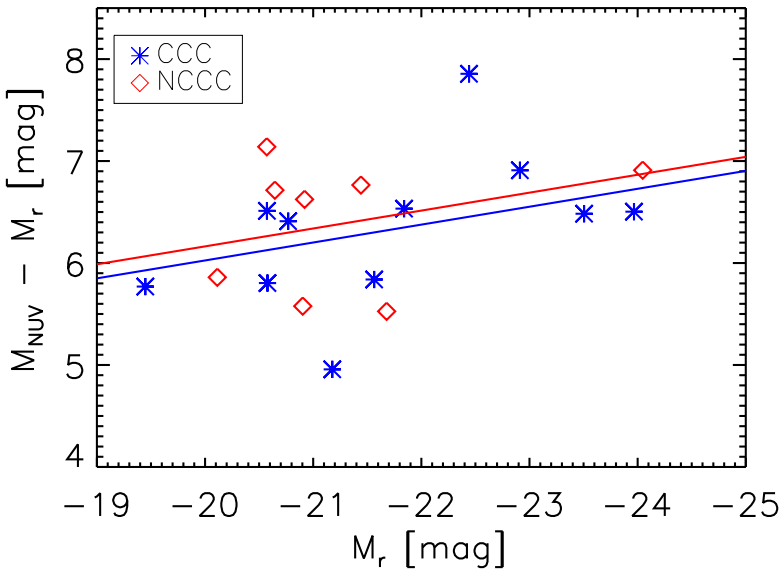

Figure 3.34: $M_{NUV} - M_r$ versus M_r diagram. Symbols are as in Figure 3.34.

3.5 The mean star formation

A color difference between galaxies can be thought as a difference in age, if we assume pure luminosity evolution between them. Alternatively, is perhaps more reasonable to assume that the overall population in CCC and NCCC galaxies is of the same age and type, and to calculate consequentelly the SFR needed to account for the CCC galaxies to be bluer.

In order to translate color information into constraints on the underlying ages of the stellar populations, the colors must be compared with stellar population synthesis models. In their most basic form, commonly referred to as simple stellar populations (SSPs), these models provide evolutionary information for a coeval population of stars born with a given composition and initial mass function (IMF). The closest physical analog to such SSPs are globular cluster systems from which the SSP models are calibrated.

The approximation of a single evolved stellar population clearly does not apply to evolved, complex stellar populations of galaxies. However, if one assumes that galaxies are composed of a superposition of SSPs, born at different epochs, rates, and metallicities, one can use the SSPs to develop model grids that mimic the range of plausible galactic stellar populations and these can be compared with galaxy color profiles. The stellar population model grids are created by taking the single burst SSPs, with constant stellar IMF and fixed metallicity, and convolving them with a given star formation history (SFH).

Several such SSP models have been produced by a number of independent groups and are in a constant state of modification as improvements to many of the input parameters (e.g. stellar libraries, model atmospheres, convection,

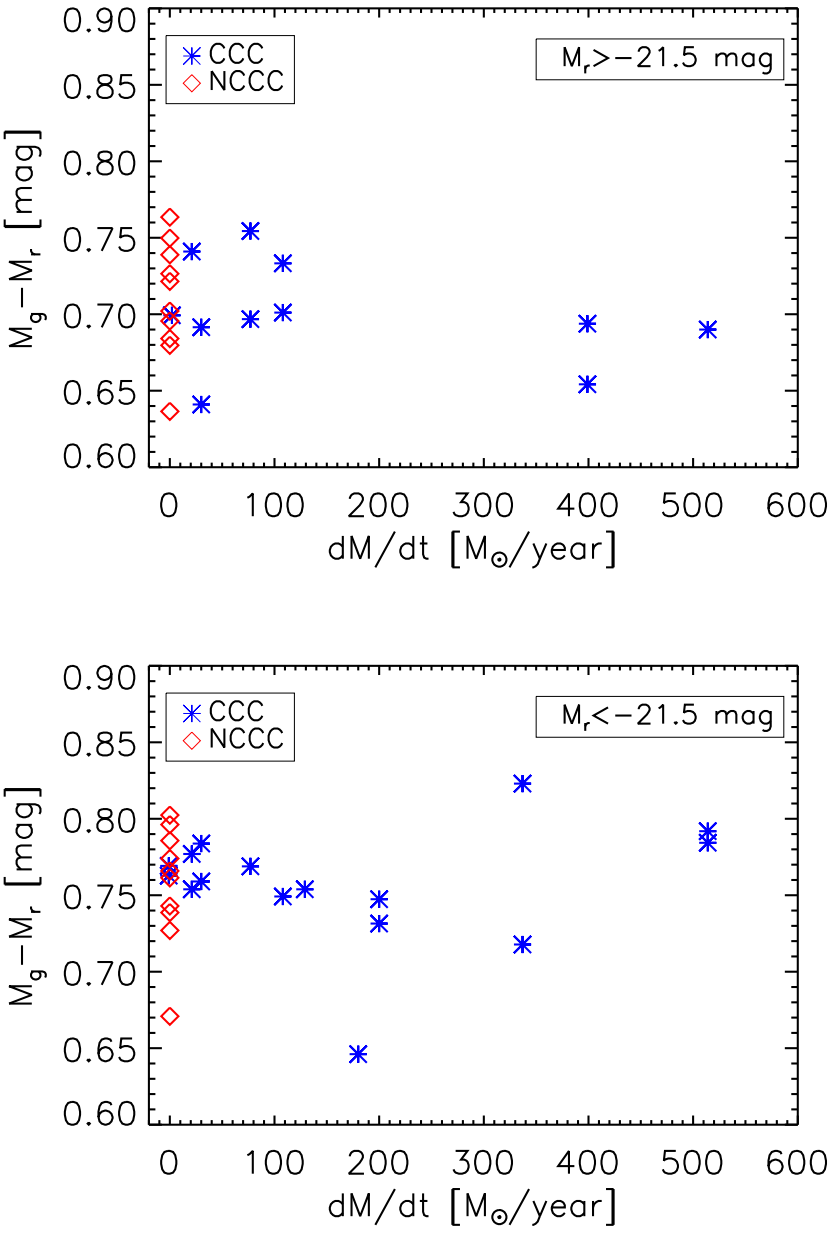

Figure 3.35: *Upper panel*: $M_g - M_r$ colors versus the mass deposit rate $\dot{M}$ as given by Chen et al. (2007) for galaxies in the lowest bin of magnitude (M_r >-21.5). Galaxies in Non Cool Core clusters are plotted according to their colors with a null value for $\dot{M}$.*Bottom panel*: the same as in the upper panel, with galaxies in the highest bin of magnitude (M_r <-21.5) mag.

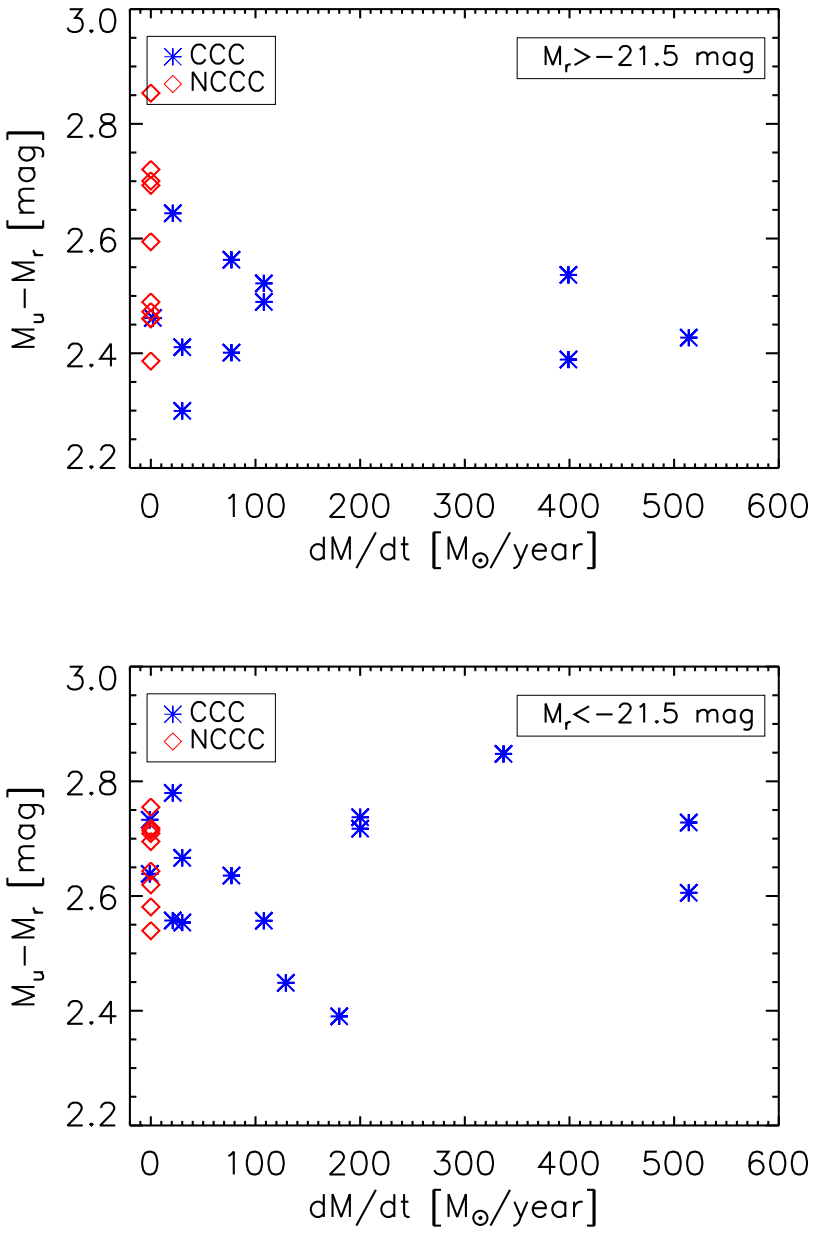

Figure 3.36: As in Figure 3.35 plotting $u-r$ colors. *Upper panel*: $M_g - M_r$ colors versus the mass deposit rate $\dot{M}$ for galaxies with M_r >-21.5 mag *Bottom panel*: $M_g - M_r$ versus $\dot{M}$ for galaxies with M_r <-21.5 mag.

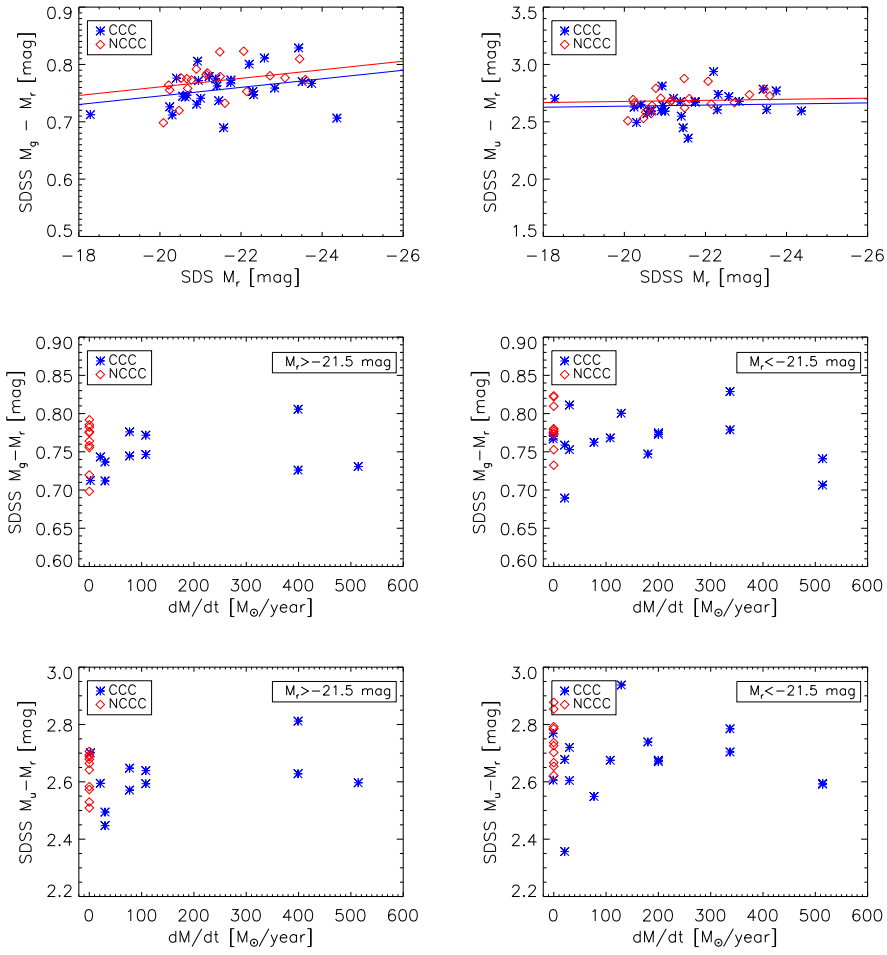

Figure 3.37: Using SDSS magnitude measures, we show: *Upper Left panel:* $M_g - M_r$ versus M_r magnitude. *Upper Right panel:* $M_u - M_r$ versus M_r magnitude. *Middle Left panel:* $M_g - M_r$ versus $\dot{M}$ for the lowest bin in M_r magnitude *Middle Right panel:* $M_g - M_r$ versus $\dot{M}$ for the highest bin in M_r magnitude.*Bottom Left panel:* $M_u - M_r$ versus $\dot{M}$ for the lowest bin in M_r magnitude. *Bottom Right panel:* $M_u - M_r$ versus $\dot{M}$ for the highest bin in M_r magnitude.

mass loss, mixing) come to light.

Bruzual & Charlot (2003) stellar population synthesis models gives the possibility for computing the spectral evolution of stellar populations of different metallicities at ages.

Others evolutionary population synthesis models for a wide range of metallicities, ages, star formation histories, and Horizontal Branch morphologies, including blue morphologies at high metallicity are given in Maraston (2005).

We will use our broad band optical, NUV and NIR colors, together with an assumption for the IMF, and for the metallicity of CCC and NCCC clusters.

Generally speaking, the UV light is sensitive to young stellar populations or very old stellar populations like core-helium burning low mass stars. Since the UV-optical color is more sensitive to young stars than the optical color, the UV information is useful to constrain the mean stellar ages of galaxies (Yi et al. 1999; Dorman et al. 2003). The NIR light is sensitive to the old stellar population and metal abundance in a galaxy (Smail et al. 2001). Since the optical light is sensitive both to the age and metallicity of galaxies, the combination of the information in the optical and NIR bands is useful to estimate the mean stellar age and mean stellar metallicity of galaxies (Smail et al. 2001; Chang et al. 2006; Lee et al. 2008a).

The sensitivity of the near-UV to small amounts of young stellar populations makes it the ideal tool to quantify any young populations, or to rule out their presence down to very small levels. And the old bulk stellar populations of massive early-type galaxies should makes the measuring small young components easier.

The evolution of the NUV-r color, as a function of the age of the young component for a range of parameters, reveals that the young population dominates the UV wavelengths for even small young populations, with a weak dependence on the mass fraction, as shown, e.g., by Schawinski (2009).

In practice, since the determination of the age and metallicity are beyond the aim of this work, we will fix the metallicity and age of two "model" galaxies, one representing the "average" NCCC galaxy, and the other one representing the average CCC galaxy.

We will perform a comparison of the observed photometric SED to a library of SEDs from Maraston (2005) and will compute the appropriate model SED, for different star formation history (a constant star formation of different lengths, or a declining star formation).

Table 3.5 report our preliminary calculation for an hypothetical mean color difference of $M_g - M_r$ =0.02 mag, using the stellar population synthesis models of Maraston (2005), using a Salpeter IMF (Salpeter 1955) and a metallicity, respectively, of Z=0.3*$Z_\odot$ and Z=0.5*$Z_\odot$ for NCCC and CCC (De Grandi & Molendi 2001).

In this example we used a constant star formation with three different star formation length, respectively of 10, 100 and 500 Myr.

Once the mass fraction of the last significant starburst that occurred in a galaxy is determined, the SFR is given by the following equation:

$$\mathrm{SFR} = \Delta \mathrm{M}_{tot}/\mathrm{SFL} \times \mathrm{M}_{tot} \tag{3.31}$$

where $\Delta \mathrm{M}_{tot}$ is the mass fraction involved in the star formation, SFL is the star formation length used in the fit, and M_{tot} is the total mass of our model

galaxy.

Table 3.6: Derived star formation rates given different star formation lengths, for a galaxy of 10^{12}M$_\odot$ and an hypothetical color difference of $M_g - M_r$ =0.02 mag. (1) Adopted Star Formation Length (2) Fraction of the total mass of the galaxy involved in the star formation (3) Derived Star Formation Rate.

SFL [Myr] **(1)**	Δ **M**$_{tot}$ **(2)**	**SFR [M**$_\odot$**/yr] (3)**
10	5×10^{-5}	5
100	2×10^{-4}	2
500	1.7×10^{-3}	3.4

We see that in this first example we obtain SFR that are far away from the estimates of hundreds to thousands M$_\odot$/yr from a pure cooling flow models.

We will compare our final findings with the actual SFR measured in the literature for some of the galaxies in our sample.

3.6 Discussion and conclusions

Galaxy clusters are very important giant astrophysical laboratories providing us with a well characterized physical environment compared to field galaxies; they also allow the study of large coeval galaxy populations and enable the investigation of their evolution in connection with the chemical and thermal evolution of the embedding intracluster medium; given moreover the importance of clusters as a test in cosmological models, they represent a key field of research in the modern studies of formation and evolution of galaxies.

A key topic in nowadays astrophysics is represented by the so called AGN feedback.

AGN feedback is invoked to quench star formation in massive galaxies, and in particular it is required in galaxy formation and evolution models to prevent the so called "cooling flow problem".

In fact, it is long known that in most clusters the central cooling time of the hot ICM is lower than the age of the cluster. Moreover, there is an observed drop of the gas temperature toward the center of the cluster. Put together, these evidences suggest that there should be a strong cooling flow of gas in these clusters, with consequent formation of new stars (Fabian 1994).

Even if the mass deposit rate derived in "pure" cooling flow model have been reduced from the initial hundreds to thousands M$_\odot$/year of first ROSAT observations, there is still no agreement between the cooling flow prediction and the modern high quality Chandra and XMM-Newton spectra.

The most suitable explanation is that the cooling gas is reheated and the mechanism is believed nowadays to be AGN feedback. Even if it is not yet clear the way in which energy released by gas infalling to the central supermassive black hole (SMBH) can heat the gas, energetic argument, and the presence of SMBH in almost every galaxy, lead to the conclusion that AGN feedback could solve the cooling flow problem, quenching star formation.

Still, even if much efforts have been made in the comprehension of the AGN feedback effect on star formation in CCC galaxies, and several studies (e.g.

Cardiel et al. 1998, Edge 2001, Goto 2005, Pipino et al. 2009, Crawford et al. 1999, Hicks & Mushotzky 2005 , Bildfell et al. 2008, Rafferty et al. 2008, McNamara et al 2006, Wilman et al. 2006, O'Dea et al. 2008) showed that at least some amount of star formation does exist in the central galaxies of cool core clusters, it is still missing a quantification of the mean difference in SF between CCC and NCCC galaxies.

Moreover, the methods used in such studies are usually time consuming, and while they give vital clues for the understanding of galaxy cluster physics, they lack the need of larger samples.

We want to assess if broad band optical, NIR and UV colors can retain the differences in star formation between cool core and non cool core galaxies.

We retrieved from the extended HIFLUGCS sample (Reiprich 2001, Reiprich & Böhringer 2002) the 20 brighter galaxies in the r band from the SDSS DR6 for each cluster.

Cluster properties, included the mass deposit rate in a pure cooling flow model, are taken from Chen et al. (2007).

A further selection on this initial sample was performed by picking galaxies whose distance from the center was less than $6 * r_{180}$ along the line of sight and less than $0.05 * r_{180}$ (about 150 kpc) perpendicularly.

We rejected galaxies that, after a visual inspection, revealed a spiral morphology, or contamination by bright stars.

Of the initial 20 galaxies selected for each cluster only 1-6 were found in these new range of distances – changing the limits of our selection doesn't change the main results of this work.

Our final sample consist of 80 galaxies, of which 53 belong to cool core clusters and 27 belong to non cool core cluster.

We found NUV and K-band information for this sample by matching it with GALEX (Martin et al. 2005; Morrissey et al. 2005) and 2MASS data (Skrutskie et al. 2006). Our final sample consists of 80 galaxies (27 NCCC galaxies and 53 CCC galaxies), of which just 54 have a 2MASS counterpart and only 21 have a GALEX counterpart.

A new analysis of SDSS images is needed because the SDSS sky estimate is biased high near bright galaxies (Abazajian et al. 2009) and this effect leads to underestimation of flux and size of as much as 30%, possibly more in the case of cD and cluster galaxies.

We used the IRAF packages to perform sky subtraction and galaxy fitting (imsurfit and ellipse packages, mostly.)

The surface brightness profile from the images in r filter were fitted with a De Vaucouleur profile; once retrieved, the effective radius r_e is kept fix while fitting the r and r surface brightness profile.

Some of the galaxies could not be reliably fitted in u and/or g band, and were rejected. Our final sample consist of 47 galaxies (20 NCCC and 27 CCC galaxies).

We compared our measurements with the prediction of Abazajian et al. (2009) for a set of simulated galaxies, and the differences $r_{SDSS} - r$ versus ours r magnitudes indicate that we correctly estimated the effect of the overestimated sky in SDSS measures.

K-correction is performed following the method of Blanton et al. (2003), using the IDL routine *kcorrect.pro*.

We notice that the two classes of object span the same range of magnitude, so that any differences would not due to an offset in the mean magnitude.

Figures 3.30, 3.31, 3.32, 3.33 and 3.34 show respectively our color-magnitude diagram $M_g - M_r$ and $M_u - M_r$ versus M_r, $M_r - M_K$ and $M_{NUV} - M_K$ versus M_K, and $M_{NUV} - M_r$ versus M_r for CCC and NCCC galaxies, showed as blue asterisks and red diamonds.

Since we are interested in the mean color difference between the two samples, we fitted the color-magnitude relation for all the data points to retrieve the slopes b for each color-magnitude relations.

We then derived the zero points using the $zp = \langle color \rangle - \langle mag \rangle * b$ separately for the two CCC and NCCC sample.

This is under the hypothesis that galaxies both in CCC and NCCC follow the same color-magnitude relation, and that the two samples differ just for the mean colors – so for the zero points.

Table 3.4 summarizes the differences between zero points ($\Delta zp = zp_{CCC} - zp_{NCCC}$) between CCC and NCCC samples for the various color magnitude relations; as many as half of the cases show values that are compatible with no differences within uncertainties.

This would mean that broad band colors are not enough sensible to quantify the differences in star formation between CCC and NCCC galaxies.

However, we observe that the zero points are systematically positive, therefore the differences in mean colors are probably physically different in our samples; we notice that, while for example SDSS magnitude uncertainties are computed just from photon statistic, we add also the uncertainties coming from the fitting itself.

We should add that we didn't correct in any way for the reddening due to the dust in star forming galaxies, so that the differences in color we found are really lower limits to the real differences.

The color differences we found are compatible with CCC central galaxies to have recent or ongoing SF. Still, a pure cooling flow model is excluded by our findings.

Figures 3.35, 3.36, show the colors of ours galaxies versus the mass deposit rate $\dot{M}$ =dM/dt [$M_\odot$/year]. We divided our galaxies in two bin of magnitude, around M_r =-21.5 mag. This value was chosen to assure a similar number of galaxies in both bins.

In a pure cooling flow model, we should observe a correlation between the mass deposit rate calculated from X-ray observations and the colors of galaxies, since the star formation due to the cooling gas falling on the central galaxies should give bluer colors in galaxies undergoing stronger star formation. In our case, we don't see any correlation.

In the hypothesis of a pure passive luminosity evolution, one can interpreter a mean color difference as a difference in age.

For example, CCC galaxies, bluer than NCCC, should be younger.

Alternatively, it is perhaps more reasonable to assume that the overall population in CCC and NCCC galaxies is of the same age and type, and to calculate consequently the SFR needed to account for the CCC galaxies to be bluer.

SFR will be derived from single stellar population models (SSP) of Maraston (2005).

Preliminary calculations are shown in Table 3.5.

SFR are predicted assuming a test $\Delta(g-r) = 0.02$ difference in mean color for three different length of star formation (10, 100 and 500 Myr), and using metallicity, respectively, of Z=0.3*$Z_\odot$ and Z=0.5*$Z_\odot$ for NCCC and CCC galaxies.

We see that for a galaxy of $10^{12} M_\odot$ we obtain a maximum SFR of 5 $M_\odot$/yr, well below the predicted one from mass deposit rate from pure cooling flow models of hundreds of $M_\odot$/yr.

3.6.1 Future work

Future work include the treatment of dust, and the actual measure of the SFR in CCC and NCCC galaxies.

Distance constraints will be re examined and more galaxies will be probably included in the sample, so to study how rapidly the SF differences disappear with the radius, between CCC and NCCC clusters.

We will compare our findings with the results of the studies that obtain the SF in single galaxies, to test the reliability of broad band colors in assessing the mean SF differences between CCC and NCCC clusters.

A further step will be done by matching our sample with that of Rafferty et al. (2006) that present the most extensive cluster sample with radio cavity properties.

We will test if the difference between the SFR in individuals objects and the mean SFR measured using the mean color differences shows any correlation with the estimated age of the last AGN episode, as traced by the radio cavities.

Chapter 4

Conclusions

One of the main themes in extragalactic astronomy for the next decade will be the evolution of galaxies over cosmic time. It has, however, become clear that the properties and evolution of galaxies are intimately linked to the growth of their Supermassive Black Holes (SMBH). Understanding the formation of galaxies, and their subsequent evolution, will therefore be incomplete without clearifing the connection between the SMBHs and their host galaxies.

The formation, assembly history, and environmental impact of the SMBHs that are ubiquitous in the nuclei of luminous galaxy today remain some of the main unsolved problems in cosmic structure formation studies.

In this thesis work we want to give our contribution to this exciting frontier of astronomy.

To understand galaxy evolution we need both tools that can help us to trace the behavior of SMBHs and their host galaxies at high redshift and in active galaxies, and to understand how AGN feedback acts.

So, this thesis work had two different goals, all pointing to the same main topic.

The first part of the work was devoted to find a tracer for the stellar velocity dispersion σ_* in order to give a tool in the study of the $M_\bullet - \sigma_*$ relation even in active or high redshift galaxies, were the σ_* cannot be measured directly.

The second part focused on the determination of the extent of the AGN feedback ability in re-heating the cooling gas in cluster galaxies; this is the subject of considerable interest today since theoretical models still presents AGN feedback that produces red and dead ellipticals while recent observations suggest that AGN feedback cannot be as efficient as to completely suppress star formation

4.1 Stellar velocity dispersion and the ionized gas kinematic

The stellar velocity dispersion σ_* is a key parameter in studying galaxies and galaxy evolution, since it trace the bulge stellar mass and the kinematics of stars inside the host galaxy, and since it is tightly connected with the circular velocity V_c (Pizzella et al. 2005) and with the mass of the super massive black holes at the center of galaxies.

There is considerable interest in the abundance of supermassive black holes in the local universe (e.g. Yu & Tremaine 2002; Marconi et al. 2004; McLure & Dunlop 2004; Shankar et al. 2004; Yu & Lu 2004; Ferrarese & Ford 2005; Bernardi et al. 2007; Tundo et al. 2007), the evolution of the mass density in SMBHs over cosmic times (e.g., Monaco et al. 2000; Kauffmann & Haehnelt 2000; Granato et al. 2001; Cattaneo & Bernardi 2003; Haiman et al. 2004; Hopkins et al. 2006; Lapi et al. 2006; Haiman et al. 2007; Shankar et al. 2008 and references therein), and in the question of whether or not $M_\bullet - \sigma_*$ relation evolves.

Unfortunately, σ_* is difficult to measure both in high redshift and active galaxies, where stellar absorption features can be overwhelmed by nonstellar emission from the nucleus. In these cases it has become common to use secondary indicators, such as the width of the ionized gas emission lines from the Narrow Line Region (NLR). The NLR is thought to be near enough to the active nucleus to be illuminated by the central engine, and big enough to be dominated by the gravitational potential of the bulge (Wilson & Heckman 1985; Whittle 1992a,b). The [OIII]λ5007 line is strong and ubiquitous in active galaxies, and its high ionization potential assures us of the fact that it is near the central engine. This has suggested its use as a proxy for σ_*.

However, direct comparison of [OIII]λ5007 and σ_* shows large scatter (e.g. Nelson & Whittle 1996). And indirect comparisons, which are typically based on asking if the slope of the $M_\bullet - \sigma_*$ relation changes when σ_* is replaced with $\sigma_{[\rm OIII]}$, show that although some AGN populations have the same slope (Nelson 2000; Boroson 2003; Shields et al. 2003), others, particularly Narrow Line Seyfert1s, do not (Grupe & Mathur 2004; Botte et al. 2005; Bian, Yuan & Zhao 2006). Recently, Greene & Ho (2005) have shown that because the [OIII] line can be asymmetric, there is some subtlety about which measure of its width is the best proxy for σ_*. But perhaps more worrying, they also found that the difference $\Delta\sigma = \sigma_{[\rm OIII]} - \sigma_*$ correlates with the Eddington ratio L_{bol}/L_{EDD} (which measures the accretion rate of the central engine) and this last quantity acts as a third parameter. This suggests that [OIII] is more affected by the AGN than one expects σ_* to be, limiting its usefulness as a reliable tracer of σ_* for all galaxy types.

Since it is known that blueshifts and blue wings correlate with the Ionization Potential (IP) of the line (de Robertis & Osterbrock 1984; Komossa et al. 2008; Rice et al. 2006), we want to test the feasibility of using a line that has a lower IP than the [OIII] line as a tracer of σ_*. The [NII] and Hα emission lines are good candidates, having IPs of 14.5 eV and 13.6 eV, respectively, compared to 35.1 eV for [OIII]. Moreover, since our goal is to trace the gravitational potential of the bulge – and not to find a proxy for $M_\bullet$ – there is no compelling reason to rely on a tracer coming from the NLR.

We used the SDSS Main Galaxy Sample to select our sample of emission line galaxies, divided in three subsamples of AGN, Transition (TR) and Star Forming (SF) galaxies using the diagnostic of Kewley et al. (2006).

We performed a linear regression using three different methods, namely, the Orthogonal Least Square Bisector (OLS Bisector), the Orthogonal Reduction (OR), and the Reduced Major Axis (RMA) as delined in Isobe et al. (1990). Since in our sample the intrinsic scatter in the data is high, the different methods will give results that are *theoretically* different. Our subsequent discussion is

nevertheless valid for each of the three methods.

We computed then the slope, zero point, intrinsic scatter and the correlation of the relations using the method outlined in Tundo et al. (2007), since the methods from Isobe et al. (1990) doesn't take into account measurements errors in both variables while our method does.

What's more, while orthogonal methods are the best choice when one is willing to understand the underling relation between two variables, when the goal is to find the actual relation that enable to transform the observed variable in another one, one should pick a method that minimize the residuals of the dependent variable at a fixed value of the independent one, as it does the OLS (Y|X) method –and our, with the advantage of including the effect of measurement errors in both variables.

We showed that [OIII] line do have a correlation with σ_*; this correlation is poor, with a Pearson correlation coefficient ranging from 0.42 to 0.55 in the different subsamples (see Table 2.3). The slope of the relation is statistically *lower* than unity, and the AGN sample shows the lowest value (see Table 2.4.3).

Our results agree with the findings of other studies, that indicated slopes lower than unity. Gaskell (2009) proposes an equation for the $\sigma_{gas} - \sigma_*$ relation that appears to be in agreement with ours.

Hα and [NII] show a tighter relation, with a Pearson correlation coefficient of 0.60 and 0.62, respectively, in the AGN subsample (see Tables 2.3).

Nevertheless, even in the cases of Hα and [NII] lines we found slopes that are lower than unity, even if they are usually steeper than the slope of the $\sigma_* - \sigma_{[OIII]}$ relation (Table 2.4.3).

While with [OIII] and Hα lines we find that the slopes in the SF and TR samples are usually steeper than in the AGN sample, with [NII] we find in the three subsamples slopes that agree within uncertainties.

All results from our measures of the intrinsic scatter and of the correlation coefficient do show that [NII] and Hα lines are more tightly tied to σ_* than [OIII].

In particularly, we find an intrinsic scatter using the [NII] emission line that is about 20% lower than in the case of [OIII].

We observe that the mean value of the ratio σ_{gas}/σ_* is enhanced in AGN rather than in StarForming or Transition galaxies, as reported in Table 2.4.2.

The fact that in the AGN sample the mean value of σ_{gas}/σ_* is close to unity must not confuse. We have $\sigma_{gas} < \sigma_*$ below $\sigma_{gas} \sim 100$ km s^{-1}, and $\sigma_{gas} > \sigma_*$ above, and this effect is much more evident in AGN than in StarForming or Transition galaxies.

This is caused by different reasons. One is the fact that StarForming and StarBurst galaxies reach lower values of magnitude –and so, very roughly, of mass and of velocity dispersion–, so that the numbers of points that are below the limits for which $\sigma_{gas}/\sigma_* < 1$ is greater than for AGN galaxies.

The more important reason is that in StarForming or Transition galaxies the ionized gas is probably less perturbed by non-gravitational effects from the central engine, so the measured σ_{gas} is subvirial as observed in quiescent galaxies.

The reason for the slope in the $\sigma_* - \sigma_{[OIII]}$ relation to be lower than in the cases of [NII] or Hα lines could reside in the fact that [OIII] is nearer to the central engine in AGN, and consequently can be more subject to its non

gravitational acceleration; $\sigma_{[OIII]}$ is then more broadened respect to [NII] or Hα and its position in a $\sigma_* - \sigma_{gas}$ plot migrate toward higher value of σ_{gas}, so lowering the slope of the relation.

It is interesting to study the behavior of the Transition sample. $\sigma_{[NII]}$ and $\sigma_{H\alpha}$ show slopes that are similar than in the case of the StarForming , while for the [OIII] we see that the slope for the TR sample is intermediate between AGN and SF samples.

This is explained by the proximity of [OIII] to the AGN respect to [NII] or Hα. Since TR galaxies can have a certain amount of nuclear activity, any acceleration effect on the ionized gas will be more efficient on the gas in the NLR. So, in TR galaxies we effectively see that [NII] and Hα lines are less affected by AGN activities.

We still see a slope lower than unity in SF galaxies probably due to two effects. One is the perturbation to the gas kinematic due to the star formation itself. Shocks and heating from the burst of star formation can accelerate the gas even if the outcome of these accelerations will be obviously small respect to that of an AGN, and probably they would be diluted in an integrated spectrum.

The second reason is that in SF galaxies we could still see the effects of possible past nuclear activity. In fact, even if diagnostic diagram can assure us that a galaxy is undergoing star formation and in not an AGN *now*, nothing preclude that the galaxy could have experienced some activity in the past, since the idea that galaxies may have had multiple, periodic episode of AGN burst are nowadays commonly accepted.

We want to notice that the slope of the SF sample is higher in the case of the [OIII]. This effect is primarily due to our constraints in the minimum σ_{gas} and σ_* allowed (actually, 50 km s^{-1}). In fact, as we already noticed, lowering our limits results in steeper slopes, so we checked that *increasing* the limit to, e.g., 70 km s^{-1} causes the slopes in the SF sample to become shallower in the case of the [OIII] line, while they remain almost unchanged using [NII] and Hα lines.

Another clue of the fact that the differences in the slope and scatter in the $\sigma_{gas} - \sigma_*$ relation is due to the fact that [OIII] is more subject to acceleration from the AGN activity, come from the comparison of the [NII], Hα and [OIII] measures.

In effect, if we look at Figures 2.23 we see that [NII] and Hα clearly describe the same kinematics, with a Pearson correlation coefficient for the $\sigma_{[H\alpha]} - \sigma_{[]NII}$ relation of R_P =0.95, while the relation between $\sigma_{[OIII]}$ and $\sigma_{[NII]}$ or $\sigma_{H\alpha}$ shows a poorer correlation with $R_P \sim$0.70 (see also Figures 2.25 and 2.24).

We would expect in Figures 2.29, 2.30 and 2.31, since rotation should tend to increase the σ of emission lines, an increase in the relative difference $(\sigma_{gas} - \sigma_*)/\sigma_*$ at higher b/a, so for galaxies seen face-on.

This is not observed. So, since b/a should be a parameter that play at least some role in the $\sigma_{gas} - \sigma_*$ relation we decided to test it.

Our samples were divided in four bin of inclination, and we derived the best fit parameters of the $\sigma_{gas} - \sigma_*$ relation in each bin.

As Nelson & Whittle (1996), we found that b/a is not correlated with σ_{gas}, as if the velocity field of the ionized gas is completely random respect to the inclination of the galaxy.

A conclusive test of [NII] being a better tracer for the stellar velocity disper-

sion respect to the [OIII] line is represented by the fact that in a $M_\bullet - \sigma_{gas}$ plot (see Figure 2.44, 2.45 and 2.46) the $M_\bullet - \sigma_{[NII]}$ presents the lowest scatter.

This is true when looking at moderately active galaxies, while in low redshift QSO and X-ray bright AGN (see Figure 2.47, 2.48 and 2.49) the correlation is poor in both [NII] and [OIII] lines, while it seems to be slightly stronger using Hα line.

This effect could be due to a correlation between the accretion of the SMBH and the FWHM of the broad emission lines, and hence of a correlation between the activity of the AGN and the derived SMBH mass (Xu & Cao 2007), so that galaxies with an accreting SMBHs have $M_\bullet$ overestimated respect to galaxies with a moderately active nucleus.

Still, we cannot completely rule out the hypothesis that this effect is due instead to an underestimation of our line width measures, but if this is the case we should observe such bias even in the samples of quiescent or moderately active AGN.

This aspects needs further study.

We suggest that in using a ionized gas as a tracer for the stellar velocity dispersion, one should take into account two points.

The first one is that in any case the slope of the relation between the gas and the stars is lower than unity, and that it must be calibrated depending on the class of galaxies studied.

The second point is that Hα and especially [NII] show less scatter and higher correlation with stars than [OIII], and a lower contamination from nuclear effects.

We propose an equation for the σ_{gas}/σ_* for each of the three line, in the different subsamples, using different regression methods.

It has to be noticed that due to its higher wavelength the [NII] line is observable in the optical up to a lower redshift than [OIII] line (see Table 2.7 for the observed wavelengths of the emission lines at various redshifts); nevertheless, [NII] can be also observable in NIR spectra.

4.1.1 Future work

Since the use of the [OIII] line was proposed to trace the stellar velocity dispersion in active and far galaxies, it has to be remembered that the tracer for σ_*should: 1-be observable in far galaxies 2-be used also in individual cases and not just statistically.

It would be interesting to put together the three emission lines and to perform a Principal Component Analysis to find if a combination of different lines could indicate a way to predict in a reliable way the stellar velocity dispersion.

Another point of interest is to find other lines that could be used as a tracer for the stellar velocity dispersion; in fact, since the need for a proxy for σ_*come for both active galaxies and high redshift galaxies, we will need different lines that could permit us to reach higher redshift.

In future studies we will also retrieve more samples of galaxies with measured $M_\bullet$; we will search for different types of galaxies to explore to which extent we can use the ionized gas as a tracer for the stellar velocity dispersion in different class of AGN, and to have some clues on the different behavior of the $M_\bullet - \sigma_{gas}$ relation in such galaxies.

4.2 AGN feedback and the cooling flow problem

Galaxy clusters are very important giant astrophysical laboratories providing us with a well characterized physical environment compared to field galaxies; they also allow the study of large coeval galaxy populations and enable the investigation of their evolution in connection with the chemical and thermal evolution of the embedding intracluster medium; given moreover the importance of clusters as a test in cosmological models, they represent a key field of research in the modern studies of formation and evolution of galaxies.

A key topic in nowadays astrophysics is represented by the so called AGN feedback.

AGN feedback is invoked to quench star formation in massive galaxies, and in particular it is required in galaxy formation and evolution models to prevent the so called "cooling flow problem".

In fact, it is long known that in most clusters the central cooling time of the hot ICM is lower than the age of the cluster. More, there is an observed drop of the gas temperature toward the center of the cluster. Put together, these evidences suggest that there should be a strong cooling flow of gas in these clusters, with consequent formation of new stars (Fabian 1994).

Even if the mass deposit rate derived in "pure" cooling flow model have been reduced from the initial hundreds to thousands $M_{\odot}$/year of first ROSAT observations, there is still no agreement between the cooling flow prediction and the modern high quality Chandra and XMM-Newton spectra.

The most suitable explanation is that the cooling gas is reheated and the mechanism is believed nowadays to be AGN feedback. Even if it is not yet clear the way in which energy released by gas infalling to the central supermassive black hole (SMBH) can heat the gas, energetic argument, and the presence of SMBH in almost every galaxy, lead to the conclusion that AGN feedback could solve the cooling flow problem, quenching star formation.

Still, even if much efforts have been made in the comprehension of the AGN feedback effect on star formation in CCC galaxies, and several studies (e.g. Cardiel et al. 1998, Edge 2001, Goto 2005, Pipino et al. 2009, Crawford et al. 1999, Hicks & Mushotzky 2005 , Bildfell et al. 2008, Rafferty et al. 2008, McNamara et al 2006, Wilman et al. 2006, O'Dea et al. 2008) showed that at least some amount of star formation does exist in the central galaxies of cool core clusters, it is still missing a quantification of the mean difference in SF between CCC and NCCC galaxies.

Moreover, the methods used in such studies are usually time consuming, and while they give vital clues for the understanding of galaxy cluster physics, they lack the need of larger samples.

We want to assess if broad band optical, NIR and UV colors can retain the differences in star formation between cool core and non cool core galaxies.

We retrieved from the extended HIFLUGCS sample (Reiprich 2001, Reiprich & Böhringer 2002) the 20 brighter galaxies in the r band from the SDSS DR6 for each cluster.

Cluster properties, included the mass deposit rate in a pure cooling flow model, are taken from Chen et al. (2007).

A further selection on this initial sample was performed by picking galaxies whose distance from the center was less than $6 * r_{180}$ along the line of sight and

less than $0.05 * r_{180}$ (about 150 kpc) perpendicularly.

We rejected galaxies that, after a visual inspection, revealed a spiral morphology, or contamination by bright stars.

Of the initial 20 galaxies selected for each cluster only 1-6 were found in these new range of distances – changing the limits of our selection doesn't change the main results of this work.

Our final sample consist of 80 galaxies, of which 53 belong to cool core clusters and 27 belong to non cool core cluster.

We found NUV and K-band information for this sample by matching it with GALEX (Martin et al. 2005; Morrissey et al. 2005) and 2MASS data (Skrutskie et al. 2006). Our final sample consists of 80 galaxies (27 NCCC galaxies and 53 CCC galaxies), of which just 54 have a 2MASS counterpart and only 21 have a GALEX counterpart.

A new analysis of SDSS images is needed because the SDSS sky estimate is biased high near bright galaxies (Abazajian et al. 2009) and this effect leads to underestimation of flux and size of as much as 30%, possibly more in the case of cD and cluster galaxies.

We used the IRAF packages to perform sky subtraction and galaxy fitting (imsurfit and ellipse packages, mostly.)

The surface brightness profile from the images in r filter were fitted with a De Vaucouleur profile; once retrieved, the effective radius r_e is kept fix while fitting the r and r surface brightness profile.

Some of the galaxies could not be reliably fitted in u and/or g band, and were rejected. Our final sample consist of 47 galaxies (20 NCCC and 27 CCC galaxies).

We compared our measurements with the prediction of Abazajian et al. (2009) for a set of simulated galaxies, and the differences $r_{SDSS} - r$ versus ours r magnitudes indicate that we correctly estimated the effect of the overestimated sky in SDSS measures.

K-correction is performed following the method of Blanton et al. (2003), using the IDL routine *kcorrect.pro*.

We notice that the two classes of object span the same range of magnitude, so that any differences would not due to an offset in the mean magnitude.

Figures 3.30, 3.31, 3.32, 3.33 and 3.34 show respectively our color-magnitude diagram $M_g - M_r$ and $M_u - M_r$ versus M_r, $M_r - M_K$ and $M_{NUV} - M_K$ versus M_K, and $M_{NUV} - M_r$ versus M_r for CCC and NCCC galaxies, showed as blue asterisks and red diamonds.

Since we are interested in the mean color difference between the two samples, we fitted the color-magnitude relation for all the data points to retrieve the slopes b for each color-magnitude relations.

We then derived the zero points using the $zp = \langle color \rangle - \langle mag \rangle * b$ separately for the two CCC and NCCC sample.

This is under the hypothesis that galaxies both in CCC and NCCC follow the same color-magnitude relation, and that the two samples differ just for the mean colors – so for the zero points.

Table 3.4 summarizes the differences between zero points ($\Delta zp = zp_{CCC} - zp_{NCCC}$) between CCC and NCCC samples for the various color magnitude relations; as many as half of the cases show values that are compatible with no differences within uncertainties.

This would mean that broad band colors are not enough sensible to quantify the differences in star formation between CCC and NCCC galaxies.

However, we observe that the zero points are systematically positive, therefore the differences in mean colors are probably physically different in our samples; we notice that, while for example SDSS magnitude uncertainties are computed just from photon statistic, we add also the uncertainties coming from the fitting itself.

We should add that we didn't correct in any way for the reddening due to the dust in star forming galaxies, so that the differences in color we found are really lower limits to the real differences.

The differences we found are compatible in our opinion with CCC central galaxies to have recent or ongoing SF. Still, a pure cooling flow model is excluded by our findings.

Figures 3.35, 3.36, show the colors of ours galaxies versus the mass deposit rate $\dot{M}$ =dM/dt [$M_\odot$/year]. We divided our galaxies in two bin of magnitude, around M_r =-21.5 mag. This value was chosen to assure a similar number of galaxies in both bins.

In a pure cooling flow model, we should observe a correlation between the mass deposit rate calculated from X-ray observations and the colors of galaxies, since the star formation due to the cooling gas falling on the central galaxies should give bluer colors in galaxies undergoing stronger star formation. In our case, we don't see any correlation.

In the hypothesis of a pure passive luminosity evolution, one can interpreter a mean color difference as a difference in age.

For example, CCC galaxies, bluer than NCCC, should be younger.

Alternatively, it is perhaps more reasonable to assume that the overall population in CCC and NCCC galaxies is of the same age and type, and to calculate consequently the SFR needed to account for the CCC galaxies to be bluer.

SFR will be derived from single stellar population models (SSP) of Maraston (2005).

Preliminary calculations are shown in Table 3.5.

SFR are predicted assuming a test $\Delta(M_g - M_r) = 0.02$ difference in mean color for three different length of star formation (10, 100 and 500 Myr), and using metallicity, respectively, of Z=0.3*$Z_\odot$ and Z=0.5*$Z_\odot$ for NCCC and CCC galaxies.

We see that for a galaxy of $10^{12} M_\odot$ we obtain a maximum SFR of 5 $M_\odot$/yr, well below the predicted one from mass deposit rate from pure cooling flow models of hundreds of $M_\odot$/yr.

4.2.1 Future work

Future work include the treatment of dust, and the actual measure of the SFR in CCC and NCCC galaxies.

Distance constraints will be re examined and more galaxies will be probably included in the sample, so to study how rapidly the SF differences disappear with the radius, between CCC and NCCC clusters.

We will compare our findings with the results of the studies that obtain the SF in single galaxies, to test the reliability of broad band colors in assessing the mean SF differences between CCC and NCCC clusters.

A further step will be done by matching our sample with that of Rafferty et al. (2006) that present the most extensive cluster sample with radio cavity properties.

We will test if the difference between the SFR in individuals objects and the mean SFR measured using the mean color differences shows any correlation with the estimated age of the last AGN episode, as traced by the radio cavities.

Bibliography

Abazajian, K. N., et al. 2009, ApJS , 182, 543

Abell, G. O. 1958, ApJS , 3, 211

Adams, F. C., Graff, D. S., & Richstone, D. O. 2001, ApJL, 551, L31

Adelman-McCarthy, J. K., et al. 2006, ApJS , 162, 38

Aller, M. C., & Richstone, D. 2002, AJ, 124, 3035

Arnaud, M., & Evrard, A. E. 1999, MNRAS, 305, 631

Balogh, M. L., Baldry, I. K., Nichol, R., Miller, C., Bower, R., & Glazebrook, K. 2004, ApJL, 615, L101

Bîrzan, L., Rafferty, D. A., McNamara, B. R., Wise, M. W., & Nulsen, P. E. J. 2004, ApJ , 607, 800

Beifiori, A., Sarzi, M., Corsini, E. M., Dalla Bontà, E., Pizzella, A., Coccato, L., & Bertola, F. 2009, ApJ , 692, 856

Bell, E. F. 2003, ApJ , 586, 794

Bell, E. F. 2003, ApJ , 586, 794

Bender, R., & Saglia, R. P. 1999, Galaxy Dynamics - A Rutgers Symposium, 182, 113

Bernardi, M., Hyde, J. B., Sheth, R. K., Miller, C. J., & Nichol, R. C. 2007, AJ, 133, 1741

Bernardi, M., et al. 2003, AJ, 125, 32

Bernardi, M., et al. 2003, AJ, 125, 1849

Bettoni, D., Falomo, R., Fasano, G., & Govoni, F. 2003, A&A, 399, 869

Bian, W., Yuan, Q., & Zhao, Y. 2006, MNRAS, 367, 860

Bildfell, C., Hoekstra, H., Babul, A., & Mahdavi, A. 2008, MNRAS, 389, 1637

Binney, J., & Tabor, G. 1995, MNRAS, 276, 663

Blandford, R. D. 1998, ApSS , 261, 245

Blanton, M. R., et al. 2003, AJ, 125, 2348

Borgani, S., et al. 2001, ApJ , 561, 13

Boroson, B., Vrtilek, S. D., Kallman, T., & Corcoran, M. 2003, ApJ , 592, 516

Boroson, T. A. 2003, ApJ , 585, 647

Botte, V., Ciroi, S., di Mille, F., Rafanelli, P., & Romano, A. 2005, MNRAS, 356, 789

Bregman, J. N., Otte, B., Miller, E. D., & Irwin, J. A. 2006, ApJ , 642, 759

Brüggen, M., & Kaiser, C. R. 2002, Nature , 418, 301

Branduardi-Raymont, G., Fabricant, D., Feigelson, E., Gorenstein, P., Grindlay, J., Soltan, A., & Zamorani, G. 1981, ApJ , 248, 55

Brighenti, F., & Mathews, W. G. 2003, ApJ , 587, 580

Brinchmann, J., Charlot, S., White, S. D. M., Tremonti, C., Kauffmann, G., Heckman, T., & Brinkmann, J. 2004, MNRAS, 351, 1151

Bromley, B. C., Press, W. H., Lin, H., & Kirshner, R. P. 1998, ApJ , 505, 25

Brotherton, M. S. 1996, ApJS , 102, 1

Brotherton, M. S. 1996, ApJS , 102, 1

Bruzual, G., & Charlot, S. 2003, MNRAS, 344, 1000

Burns, J. O., Gregory, S. A., & Holman, G. D. 1981, ApJ , 250, 450

Burns, J. O., Gregory, S. A., & Holman, G. D. 1981, ApJ , 250, 450

Butcher, H., & Oemler, A., Jr. 1978, ApJ , 226, 559

Canizares, C. R. 1988, Nature , 336, 309

Canizares, C. R., Clark, G. W., Jernigan, J. G., & Markert, T. H. 1982, ApJ , 262, 33

Cardiel, N., Gorgas, J., & Aragon-Salamanca, A. 1998, MNRAS, 298, 977

Cattaneo, A., & Bernardi, M. 2003, MNRAS, 344, 45

Cavaliere, A., & Fusco-Femiano, R. 1976, A&A, 49, 137

Cavaliere, A., & Vittorini, V. 2002, ApJ , 570, 114

Cavagnolo, K. W., Donahue, M., Voit, G. M., & Sun, M. 2008, ApJL, 683, L107

Chen, Y., Reiprich, T. H., Böhringer, H., Ikebe, Y., & Zhang, Y.-Y. 2007, A&A, 466, 805

Ciotti, L., Ostriker, J. P., & Proga, D. 2009, ApJ , 699, 89

Ciotti, L., & Ostriker, J. P. 1997, ApJL, 487, L105

Coil, A. L., et al. 2008, ApJ , 672, 153

Connolly, A. J., Szalay, A. S., Bershady, M. A., Kinney, A. L., & Calzetti, D. 1995, AJ, 110, 1071

Cowie, L. L., Songaila, A., Hu, E. M., & Cohen, J. G. 1996, AJ, 112, 839

Crawford, C. S., Allen, S. W., Ebeling, H., Edge, A. C., & Fabian, A. C. 1999, MNRAS, 306, 857

Croton, D. J. 2006, MNRAS, 369, 1808

Chang, R., Shen, S., Hou, J., Shu, C., & Shao, Z. 2006, MNRAS, 372, 199

Churazov, E., Sunyaev, R., Forman, W., & Böhringer, H. 2002, MNRAS, 332, 729

Croton, D. J., et al. 2006, MNRAS, 365, 11

David, L. P., Nulsen, P. E. J., McNamara, B. R., Forman, W., Jones, C., Ponman, T., Robertson, B., & Wise, M. 2001, ApJ , 557, 546

De Grandi, S., & Molendi, S. 2001, ApJ , 551, 153

De Lucia, G., Springel, V., White, S. D. M., Croton, D., & Kauffmann, G. 2006, MNRAS, 366, 499

De Robertis, M. M., & Osterbrock, D. E. 1984, ApJ , 286, 171

De Robertis, M. M., & Osterbrock, D. E. 1986, ApJ , 301, 727

Di Matteo, T., Springel, V., & Hernquist, L. 2005, Nature , 433, 604

Donahue, M., Horner, D. J., Cavagnolo, K. W., & Voit, G. M. 2006, ApJ , 643, 730

Dorman, B., O'Connell, R. W., & Rood, R. T. 2003, ApJ , 591, 878

Dressler, A., et al. 1997, ApJ , 490, 577

Dressler, A. 1980, ApJ , 236, 351

Dunn, R. J. H., & Fabian, A. C. 2006, MNRAS, 373, 959

Ebeling, H., Voges, W., Bohringer, H., Edge, A. C., Huchra, J. P., & Briel, U. G. 1996, MNRAS, 281, 799

Ebeling, H., Voges, W., Bohringer, H., Edge, A. C., Huchra, J. P., & Briel, U. G. 1996, MNRAS, 283, 1103

Edge, A. C. 2001, MNRAS, 328, 762

Edge, A. C. 2001, MNRAS, 328, 762

Efstathiou, G., & Fall, S. M. 1984, MNRAS, 206, 453

Eisenstein, D. J., et al. 2003, ApJ , 585, 694

Ellingson, E., Lin, H., Yee, H. K. C., & Carlberg, R. G. 2001, ApJ , 547, 609

Fabian, A. C., & Nulsen, P. E. J. 1977, MNRAS, 180, 479

Fabian, A. C., et al. 2000, MNRAS, 315, L8

Fabian, A. C., Sanders, J. S., Allen, S. W., Crawford, C. S., Iwasawa, K., Johnstone, R. M., Schmidt, R. W., & Taylor, G. B. 2003, MNRAS, 344, L43

Fabian, A. C. 1994, ARA&A , 32, 277

Ferrarese, L., & Ford, H. 2005, Space Science Reviews, 116, 523

Ferrarese, L., & Merritt, D. 2000, ApJL, 539, L9

Ferrarese, L., & Merritt, D. 2000, ApJL, 539, L9

Finn, R. A., Balogh, M. L., Zaritsky, D., Miller, C. J., & Nichol, R. C. 2008, ApJ , 679, 279

Forman, W., & Jones, C. 1982, ARA&A , 20, 547

Fukugita, M., Ichikawa, T., Gunn, J. E., Doi, M., Shimasaku, K., & Schneider, D. P. 1996, AJ, 111, 1748

Gültekin, K., et al. 2009, ApJ , 698, 198

Gaskell, C. M. 2009, New Astronomy Review, 53, 140

Gebhardt, K., et al. 2000, AJ, 119, 1157

Gebhardt, K., et al. 2000, ApJL, 539, L13

Gerke, B. F., et al. 2007, MNRAS, 376, 1425

Gnedin, N. Y. 2000, ApJ , 542, 535

Goto, T. 2005, MNRAS, 356, L6

Graham, A. W., Erwin, P., Caon, N., & Trujillo, I. 2001, ApJL, 563, L11

Granato, G. L., Silva, L., Monaco, P., Panuzzo, P., Salucci, P., De Zotti, G., & Danese, L. 2001, MNRAS, 324, 757

Greene, J. E., & Ho, L. C. 2006, ApJL, 641, L21

Greene, J. E., & Ho, L. C. 2005, ApJ , 627, 721

Greene, J. E., & Ho, L. C. 2005, ApJ , 630, 122

Grupe, D., & Mathur, S. 2004, ApJL, 606, L41

Gu, Q., Melnick, J., Fernandes, R. C., Kunth, D., Terlevich, E., & Terlevich, R. 2006, MNRAS, 366, 480

Gull, S. F., & Northover, K. J. E. 1973, Nature , 244, 80

Gunn, J. E., & Gott, J. R., III 1972, ApJ , 176, 1

Gunn, J. E., et al. 1998, AJ, 116, 3040

Gunn, J. E., et al. 2006, AJ, 131, 2332

Häring, N., & Rix, H.-W. 2004, ApJL, 604, L89

Haehnelt, M. G., & Kauffmann, G. 2000, MNRAS, 318, L35

Haiman, Z., Ciotti, L., & Ostriker, J. P. 2004, ApJ , 606, 763

Hao, L., et al. 2005, AJ, 129, 1783

Hasinger, G., Miyaji, T., & Schmidt, M. 2005, A&A, 441, 417

Heckman, T. M., Miley, G. K., van Breugel, W. J. M., & Butcher, H. R. 1981, ApJ , 247, 403

Heckman, T. M. 1981, ApJL, 250, L59

Heinz, S., Choi, Y.-Y., Reynolds, C. S., & Begelman, M. C. 2002, ApJL, 569, L79

Henry, J. P., Evrard, A. E., Hoekstra, H., Babul, A., & Mahdavi, A. 2009, ApJ , 691, 1307

Henry, J. P. 2004, ApJ , 609, 603

Hicks, A. K., & Mushotzky, R. 2005, ApJL, 635, L9

Hicks, A. K., & Mushotzky, R. 2005, ApJL, 635, L9

Ho, L. C. 2009, ApJ , 699, 638

Hoeft, M., Yepes, G., Gottlöber, S., & Springel, V. 2006, MNRAS, 371, 401

Hogg, D. W., et al. 2002, AJ, 124, 646

Hopkins, P. F., Hernquist, L., Cox, T. J., Di Matteo, T., Robertson, B., & Springel, V. 2006, ApJS , 163, 1

Hyde, J. B., Bernardi, M., Sheth, R. K., & Nichol, R. C. 2008, MNRAS, 391, 1559

Hyde, J. B., & Bernardi, M. 2009, MNRAS, 396, 1171

Isobe, T., Feigelson, E. D., Akritas, M. G., & Babu, G. J. 1990, ApJ , 364, 104

Jedrzejewski, R. I., Davies, R. L., & Illingworth, G. D. 1987, AJ, 94, 1508

Johnstone, R. M., Fabian, A. C., & Nulsen, P. E. J. 1987, MNRAS, 224, 75

Jorgensen, I., Franx, M., & Kjaergaard, P. 1995, MNRAS, 276, 1341

Kaiser, C. R., & Binney, J. 2003, MNRAS, 338, 837

Kaspi, S., Smith, P. S., Netzer, H., Maoz, D., Jannuzi, B. T., & Giveon, U. 2000, ApJ , 533, 631

Kaspi, S., Maoz, D., Netzer, H., Peterson, B. M., Vestergaard, M., & Jannuzi, B. T. 2005, ApJ , 629, 61

Kauffmann, G., & Haehnelt, M. 2000, MNRAS, 311, 576

Kauffmann, G., White, S. D. M., & Guiderdoni, B. 1993, MNRAS, 264, 201

Kauffmann, G., et al. 2003, MNRAS, 341, 33

Kewley, L. J., Geller, M. J., Jansen, R. A., & Dopita, M. A. 2002, AJ, 124, 3135

Kewley, L. J., Groves, B., Kauffmann, G., & Heckman, T. 2006, MNRAS, 372, 961

King, A. 2003, ApJL, 596, L27

Koester, B. P., et al. 2007, ApJ , 660, 221

Komossa, S., Xu, D., Zhou, H., Storchi-Bergmann, T., & Binette, L. 2008, ApJ , 680, 926

Kormendy, J., & McClure, R. D. 1993, AJ, 105, 1793

Kormendy, J., & Richstone, D. 1995, ARA&A , 33, 581

La Franca, F., et al. 2005, ApJ , 635, 864

Lacey, C., & Cole, S. 1993, MNRAS, 262, 627

Lahav, O., Naim, A., Sodré, L., Jr., & Storrie-Lombardi, M. C. 1996, MNRAS, 283, 207

Lapi, A., Shankar, F., Mao, J., Granato, G. L., Silva, L., De Zotti, G., & Danese, L. 2006, ApJ , 650, 42

Larson, R. B., Tinsley, B. M., & Caldwell, C. N. 1980, ApJ , 237, 692

Lauer, T. R., et al. 2007, ApJ , 662, 808

Lee, J. H., Lee, M. G., Park, C., & Choi, Y.-Y. 2008, MNRAS, 389, 1791

Lin, Y.-T., Mohr, J. J., & Stanford, S. A. 2003, ApJ , 591, 749

Lisker, T., Grebel, E. K., Binggeli, B., & Glatt, K. 2007, ApJ , 660, 1186

Loh, Y.-S., Ellingson, E., Yee, H. K. C., Gilbank, D. G., Gladders, M. D., & Barrientos, L. F. 2008, ApJ , 680, 214

Mac Low, M.-M., & Ferrara, A. 1999, ApJ , 513, 142

Madau, P., Ferguson, H. C., Dickinson, M. E., Giavalisco, M., Steidel, C. C., & Fruchter, A. 1996, MNRAS, 283, 1388

Magorrian, J., et al. 1998, AJ, 115, 2285

Mandelbaum, R., et al. 2005, MNRAS, 361, 1287

Maraston, C. 2005, MNRAS, 362, 799

Marconi, A., & Hunt, L. K. 2003, ApJL, 589, L21

Marconi, A., Risaliti, G., Gilli, R., Hunt, L. K., Maiolino, R., & Salvati, M. 2004, MNRAS, 351, 169

Markevitch, M., Forman, W. R., Sarazin, C. L., & Vikhlinin, A. 1998, ApJ , 503, 77

Martin, D. C., et al. 2005, ApJL, 619, L1

Mazzotta, P., Kaastra, J. S., Paerels, F. B., Ferrigno, C., Colafrancesco, S., Mewe, R., & Forman, W. R. 2002, ApJL, 567, L37

McIntosh, D. H., Rix, H.-W., Rieke, M. J., & Foltz, C. B. 1999, ApJL, 517, L73

McLure, R. J., & Dunlop, J. S. 2002, MNRAS, 331, 795

McLure, R. J., & Dunlop, J. S. 2004, MNRAS, 352, 1390

McNamara, B. R., & Nulsen, P. E. J. 2007, ARA&A , 45, 117

McNamara, B. R., et al. 2006, ApJ , 648, 164

McNamara, B. R., Nulsen, P. E. J., Wise, M. W., Rafferty, D. A., Carilli, C., Sarazin, C. L., & Blanton, E. L. 2005, Nature , 433, 45

McNamara, B. R., et al. 2001, ApJL, 562, L149

McNamara, B. R., et al. 2000, ApJL, 534, L135

McNamara, B. R., & O'Connell, R. W. 1989, AJ, 98, 2018

Miller, C. J., et al. 2005, AJ, 130, 968

Monaco, P., Salucci, P., & Danese, L. 2000, MNRAS, 311, 279

Moore, B., Quinn, T., Governato, F., Stadel, J., & Lake, G. 1999, MNRAS, 310, 1147

Moore, B., Katz, N., Lake, G., Dressler, A., & Oemler, A. 1996, Nature , 379, 613

Morrissey, P., et al. 2005, ApJL, 619, L7

Navarro, J. F., Frenk, C. S., & White, S. D. M. 1995, MNRAS, 275, 720

Nelson, C. H., & Whittle, M. 1996, ApJ , 465, 96

Nelson, C. H. 2000, ApJL, 544, L91

Nulsen, P. E. J., McNamara, B. R., Wise, M. W., & David, L. P. 2005, ApJ , 628, 629

O'Dea, C. P., et al. 2008, ApJ , 681, 1035

Oegerle, W. R., Cowie, L., Davidsen, A., Hu, E., Hutchings, J., Murphy, E., Sembach, K., & Woodgate, B. 2001, ApJ , 560, 187

Oemler, A., Jr. 1974, ApJ , 194, 1

Oke, J. B., & Sandage, A. 1968, ApJ , 154, 21

Omma, H., Binney, J., Bryan, G., & Slyz, A. 2004, MNRAS, 348, 1105

Ostriker, J. P. 2000, Physical Review Letters, 84, 5258

Panter, B., Heavens, A. F., & Jimenez, R. 2003, MNRAS, 343, 1145

Peres, C. B., Fabian, A. C., Edge, A. C., Allen, S. W., Johnstone, R. M., & White, D. A. 1998, MNRAS, 298, 416

Peterson, J. R., & Fabian, A. C. 2006, Physics Reports , 427, 1

Peterson, J. R., Kahn, S. M., Paerels, F. B. S., Kaastra, J. S., Tamura, T., Bleeker, J. A. M., Ferrigno, C., & Jernigan, J. G. 2003, ApJ , 590, 207

Phillips, M. M., Jenkins, C. R., Dopita, M. A., Sadler, E. M., & Binette, L. 1986, AJ, 91, 1062

Piffaretti, R., Jetzer, P., Kaastra, J. S., & Tamura, T. 2005, A&A, 433, 101

Pipino, A., Kaviraj, S., Bildfell, C., Babul, A., Hoekstra, H., & Silk, J. 2009, MNRAS, 395, 462

Pizzella, A., Corsini, E. M., Vega Beltrán, J. C., & Bertola, F. 2004, A&A, 424, 447

Pizzella, A., Corsini, E. M., Dalla Bontà, E., Sarzi, M., Coccato, L., & Bertola, F. 2005, ApJ , 631, 785

Poggianti, B. M., et al. 2006, ApJ , 642, 188

Poole, G. B., Babul, A., McCarthy, I. G., Sanderson, A. J. R., & Fardal, M. A. 2008, MNRAS, 391, 1163

Postman, M., & Geller, M. J. 1984, ApJ , 281, 95

Postman, M., et al. 2005, ApJ , 623, 721

Quilis, V., Moore, B., & Bower, R. 2000, Science, 288, 1617

Quinn, T., Katz, N., & Efstathiou, G. 1996, MNRAS, 278, L49

Rafferty, D. A., McNamara, B. R., Nulsen, P. E. J., & Wise, M. W. 2006, ApJ , 652, 216

Rafferty, D. A., McNamara, B. R., & Nulsen, P. E. J. 2008, ApJ , 687, 899

Reiprich, T. H., , H.& Böhringer 2002, ApJ , 567, 716

Reiprich, T. H. 2001, Ph.D. Thesis,

Rice, M. S., Martini, P., Greene, J. E., Pogge, R. W., Shields, J. C., Mulchaey, J. S., & Regan, M. W. 2006, ApJ , 636, 654

Richstone, D., et al. 1998, Nature , 395, A14

Roche, N., Bernardi, M., & Hyde, J. 2009, MNRAS, 398, 1549

Ruszkowski, M., & Begelman, M. C. 2002, ApJ , 581, 223

Sadat, R., Blanchard, A., Kneib, J.-P., Mathez, G., Madore, B., & Mazzarella, J. M. 2004, A&A, 424, 1097

Salucci, P., Szuszkiewicz, E., Monaco, P., & Danese, L. 1999, MNRAS, 307, 637

Salpeter, E. E. 1955, ApJ , 121, 161

Sanders, D. B., Soifer, B. T., Elias, J. H., Madore, B. F., Matthews, K., Neugebauer, G., & Scoville, N. Z. 1988, ApJ , 325, 74

Sarazin, C. L. 1989, ApJ , 345, 12

Sarzi, M., et al. 2002, ApJ , 567, 237

Schawinski, K. 2009, MNRAS, 397, 717

Schindler, S., Castillo-Morales, A., De Filippis, E., Schwope, A., & Wambsganss, J. 2001, A&A, 376, L27

Schlegel, D. J., Finkbeiner, D. P., & Davis, M. 1998, ApJ , 500, 525

Schuecker, P., Böhringer, H., Collins, C. A., & Guzzo, L. 2003, A&A, 398, 867

Shankar, F., Salucci, P., Granato, G. L., De Zotti, G., & Danese, L. 2004, MNRAS, 354, 1020

Shaver, P. A., Wall, J. V., Kellermann, K. I., Jackson, C. A., & Hawkins, M. R. S. 1996, Nature , 384, 439

Shields, G. A., Gebhardt, K., Salviander, S., Wills, B. J., Xie, B., Brotherton, M. S., Yuan, J., & Dietrich, M. 2003, ApJ , 583, 124

Silk, J., & Rees, M. J. 1998, A&A, 331, L1

Silk, J., & Rees, M. J. 1998, A&A, 331, L1

Silverman, J. D., et al. 2008, ApJ , 679, 118

Skrutskie, M. F., et al. 2006, AJ, 131, 1163

Smail, I., Kuntschner, H., Kodama, T., Smith, G. P., Packham, C., Fruchter, A. S., & Hook, R. N. 2001, MNRAS, 323, 839

Smith, J. A., et al. 2002, AJ, 123, 2121

Soltan, A. 1982, MNRAS, 200, 115

Springel, V., Di Matteo, T., & Hernquist, L. 2005, MNRAS, 361, 776

Stoughton, C., et al. 2002, AJ, 123, 485

Stoughton, C., et al. 2002, AJ, 123, 485

Strauss, M. A., et al. 2002, AJ, 124, 1810

Tabor, G., & Binney, J. 1993, MNRAS, 263, 323

Tabor, G., & Binney, J. 1993, MNRAS, 263, 323

Toomre, A., & Toomre, J. 1972, ApJ , 178, 623

Tremaine, S., et al. 2002, ApJ , 574, 740

Tremaine, S., et al. 2002, ApJ , 574, 740

Tremonti, C. A., et al. 2004, ApJ , 613, 898

Tran, K.-V. H., van Dokkum, P., Illingworth, G. D., Kelson, D., Gonzalez, A., & Franx, M. 2005, ApJ , 619, 134

Tran, K.-V. H., Simard, L., Zabludoff, A. I., & Mulchaey, J. S. 2001, ApJ , 549, 172

Treu, T., Ellis, R. S., Kneib, J.-P., Dressler, A., Smail, I., Czoske, O., Oemler, A., & Natarajan, P. 2003, ApJ , 591, 53

Tundo, E., Bernardi, M., Hyde, J. B., Sheth, R. K., & Pizzella, A. 2007, ApJ , 663, 53

Ueda, Y., Akiyama, M., Ohta, K., & Miyaji, T. 2003, ApJ , 598, 886

Véron-Cetty, M.-P., Véron, P., & Gonçalves, A. C. 2001, A&A, 372, 730

van der Marel, R. P. 1999, AJ, 117, 744

Vikhlinin, A., et al. 2009, ApJ , 692, 1060

Vikhlinin, A., et al. 2003, ApJ , 590, 15

Vikhlinin, A., Kravtsov, A., Forman, W., Jones, C., Markevitch, M., Murray, S. S., & Van Speybroeck, L. 2006, ApJ , 640, 691

Voigt, L. M., & Fabian, A. C. 2004, MNRAS, 347, 1130

Voit, G. M., & Donahue, M. 2005, ApJ , 634, 955

Wang, R., Wu, X.-B., & Kong, M.-Z. 2006, ApJ , 645, 890

White, R. L., Becker, R. H., Helfand, D. J., & Gregg, M. D. 1997, ApJ , 475, 479

Whitmore, B. C., & Gilmore, D. M. 1991, ApJ , 367, 64

Whittle, M. 1985, MNRAS, 213, 1

Whittle, M. 1992, ApJ , 387, 109

Whittle, M. 1992, ApJ , 387, 121

Whittle, M. 1992, ApJS , 79, 49

Wilman, R. J., Edge, A. C., & Swinbank, A. M. 2006, MNRAS, 371, 93

Wilman, R. J., Edge, A. C., & Swinbank, A. M. 2006, MNRAS, 371, 93

Wilson, A. S., & Heckman, T. M. 1985, Astrophysics of Active Galaxies and Quasi-Stellar Objects, 39

Wilson, A. S., & Willis, A. G. 1980, ApJ , 240, 429

Wise, M. W., McNamara, B. R., Nulsen, P. E. J., Houck, J. C., & David, L. P. 2007, ApJ , 659, 1153

Xu, Y., & Cao, X.-W. 2007, Chinese Journal of Astronomy and Astrophysics, 7, 63

Yi, S., Lee, Y.-W., Woo, J.-H., Park, J.-H., Demarque, P., & Oemler, A., Jr. 1999, ApJ , 513, 128

Yip, C. W., et al. 2004, AJ, 128, 2603

York, D. G., et al. 2000, AJ, 120, 1579

Yu, Q., & Lu, Y. 2004, ApJ , 610, 93

Yu, Q., & Tremaine, S. 2002, MNRAS, 335, 965

Yu, Q., & Tremaine, S. 2002, MNRAS, 335, 965

Zabludoff, A. I., & Mulchaey, J. S. 1998, ApJ , 496, 39